

ABSTRACT

Title of dissertation: Remote and Local
Entanglement of Ions
using Photons and Phonons

David Lee Hayes, Doctor of Philosophy, 2012

Dissertation directed by: Professor Christopher Monroe
Joint Quantum Institute,
University of Maryland Department of Physics and
National Institute of Standards and Technology

The scaling of controlled quantum systems to large numbers of degrees of freedom is one of the long term goals of experimental quantum information science. Trapped-ion systems are one of the most promising platforms for building a quantum information processor with enough complexity to enable novel computational power, but face serious challenges in scaling up to the necessary numbers of qubits. In this thesis, I present both technical and operational advancements in the control of trapped-ion systems and their juxtaposition with photonic modes used for quantum networking. After reviewing the basic physics behind ion trapping, I then describe in detail a new method of implementing Raman transitions in atomic systems using optical frequency combs. Several different experimental setups along with simple theoretical models are reviewed and the system is shown to be capable of full control of the qubit-oscillator system. Two-ion entangling operations using optical frequency combs are demonstrated along with an extension of the operation

designed to suppress certain experimental errors. I then give an overview of how spatially separated ions can be entangled using a photonic interconnect. Experimental results show that pulsed excitation of trapped ions provide an excellent single photon source that can be used as a heralded entangling gate between macroscopically separated systems. This heralded entangling gate is used to show a violation of a Bell inequality while keeping the detection loophole closed and can be used as a source of private random numbers. Finally, the coherent Coulomb force-based gates are combined with the probabilistic photon-based gates in a proof of concept experiment that shows the feasibility of a distributed ion-photon network.

Remote and Local Entanglement of Ions using Photons and Phonons

by

David Lee Hayes

Dissertation submitted to the Faculty of the Graduate School of the
University of Maryland, College Park in partial fulfillment
of the requirements for the degree of
Doctor of Philosophy
2012

Advisory Committee:
Professor Chris Monroe, Chair/Advisor
Professor Steve Rolston, Co-Advisor
Professor Luis Orozco
Professor Eite Tiesinga
Professor Edo Waks

© Copyright by
David Lee Hayes
2012

To Kate

Graduate school has been a challenging time for me and I would like to thank the many people that have helped me along the way. First, I need to thank my parents for making sure that I was able to eventually find my way onto this road. Thanks for the math tutor Mom. Once I found myself buried deep in the physics clan, there were many people I worked with who have helped me see the light that I needed to either clarify my thinking or just brighten my day. While I was in graduate school in New Mexico, I had some luck in finding my way into the quantum information group headed by Ivan Deutsch. While it was quickly apparent to me that Ivan was an incredible physicist, I eventually came to know that I could always trust that he always had my well being in mind and couldn't have been a better advisor. Once I got to Maryland, I started working closely with what would become a long list of great people. Steve Olmschenk, Peter Maunz, Dzmitry Matsukevich, Dave Hucul, Qudsia Quraishi, Kenny Lee, Susan Clark, Shantanu Debnath, Daniel Brennan and finally Volkan Inlek have all worked closely with me and have all been instrumental in my success. Although I didn't work on the same projects as the other members of the group, I immensely enjoyed the company of Ming-Shien Chang, Brian Fields, Rajibul Islam, Kihwan Kim, Andrew Manning, Emily Edwards, Simcha Korenblit, Le Lou, Jonathan Mizrahi, Crystal Senko, Jon Sterk, Chenglin Cao, Taeyoung Choi, Kale Johnson and Jake Smith. I would like to especially thank Wes Campbell for letting me come into his office to bug him and answering late night emails about weird ideas of his or mine and showing me a good time when I needed it. But most importantly, I want to thank my advisor Chris Monroe. Chris has been a great mentor while I've been here. He has the wisdom to

know when to speak and when not to. By that, I mean that there has been times when the best thing for me was to go off on my own and think about something, but there are also times for brainstorming or a little reassurance and Chris always seems to know what time it is.

Table of Contents

List of Tables	vii
List of Figures	viii
1 Introduction	1
1.1 Ion-photon networks	1
2 Ytterbium ions	9
2.1 The Paul Trap	9
2.1.1 Trapping charged particles	9
2.1.2 Dynamics in the Paul trap	12
2.2 Trapping Yb^+	18
2.2.1 The $^{171}\text{Yb}^+$ hyperfine qubit	29
2.2.2 State initialization and detection	30
2.2.3 Qubit rotations with resonant microwaves	39
2.3 Multiple Ions	43
3 Control through Raman transitions	50
3.1 Stimulated Raman transitions driven by an optical frequency comb	50
3.1.1 Raman Transitions in a three-level atom using a single pulse train	50
3.1.2 Control of the $^{171}\text{Yb}^+$ clock qubit	63
3.1.3 Control of the qubit-oscillator system	66
3.1.4 Error Suppression in Raman Transitions	83
3.2 Light Shifts	91
4 Phonon mediated entanglement of ions	98
4.1 Spin-Dependent Forces	98
4.2 Two Atom Entanglement	105
4.2.1 Experimental Implementation of the Mølmer-Sørensen Gate	108
4.3 Coherent Error Suppression in Mølmer-Sørensen Operations	117
4.4 Two Ion Walsh Gates	126
5 Photon mediated entanglement of ions	132
5.1 Entangling atoms by detecting a single photon	133
5.2 Entangling atoms through the detection of two photons	143
5.2.1 Errors in the Type II protocol	153
5.3 Bell's theorem and private random numbers	156
6 Integrating Phonon and Photon based entangling operations	164
6.1 The Quantum Repeater	164
6.1.1 $2 + 1$ Quantum Repeater Elementary Unit	167
6.1.2 $2 + 1$ Experiment	168
6.2 Conclusions and Outlook	178

A	Paraboloidal Ion Trap	181
B	Probability amplitude for Raman transitions in a three-level atom using an optical frequency comb	187
C	Walsh function Identity	191
	Bibliography	194

List of Tables

2.1	Resonant transition frequencies for neutral Ytterbium isotopes	20
2.2	Relevant parameters for $^{171}\text{Yb}^+$	49
3.1	Rabi frequencies for different pulse shapes	57
5.1	Photonic gate experiment results	151
5.2	Bell inequality experiment results	161

List of Figures

1.1	Quantum version of Moore’s law	2
1.2	Concept drawing of an ion-photon network	4
2.1	Schematic of the four rod trap	11
2.2	Comparison of a numerical integration of the Matheiu equation with an approximate analytic solution	15
2.3	RF resonator can	18
2.4	Neutral Ytterbium Energy Diagram	19
2.5	Ionized Ytterbium Energy Diagram	22
2.6	Doppler-free saturated absorption laser lock	24
2.7	Five-ion crystal ICCD camera image	27
2.8	Axial trap frequency as a function of endcap voltages	29
2.9	Asymptotic optical pumping efficiencies.	33
2.10	Single ion state detection	34
2.11	Cooling a PMT to suppress dark counts.	34
2.12	Diagrams showing which laser frequencies are present for Doppler cooling, optical pumping and state detection protocols	35
2.13	Bayesian inference state detection with multiple ions and multiple detectors	38
2.14	Single ion rotations using resonant microwaves.	40
2.15	Single ion microwave Ramsey experiment	43
2.16	Two ion motional mode illustration	47
2.17	Motional mode structure for 10 ions	48
3.1	An illustration of a Raman transition	51
3.2	An energy diagram illustrating a stimulated Raman transition driven by an optical frequency comb	58
3.3	Driving Rabi oscillations using a single pulse train	60
3.4	The relevant Clebsch-Gordan coefficients for Raman transitions in $^{171}\text{Yb}^+$	65
3.5	Co-propagating Raman beams setup	68
3.6	Carrier transition line shape	69
3.7	Driving Raman transitions with counter-propagating beams	70
3.8	An illustration of the resonance condition for Raman transitions using frequency shifted frequency combs	75
3.9	Using Raman transitions for an autocorrelation measurement	77
3.10	Raman spectroscopy of the qubit-oscillator system	84
3.11	Ramsey experiments with and without a beat note lock	86
3.12	Noise eater data	87
3.13	Suppressing errors due to laser intensity fluctuations	88
3.14	Sideband cooling measurement	90
3.15	Stark shift to Rabi frequency measurement with the femtosecond laser	95
3.16	Intensity autocorrelation for the femtosecond laser	96

4.1	Illustration of a spin-dependent force acting on a single ion	103
4.2	Spin-dependent force experiments with a single ion	106
4.3	Spin-dependent force experiments with a single ion	108
4.4	Symmetric detuning scan for calibrating the Mølmer-Sørensen Gate .	112
4.5	Time scan for calibrating the Mølmer-Sørensen Gate	113
4.6	Parity measurement of two entangled ions	116
4.7	Phase space picture of detuning errors in the Mølmer-Sørensen gate .	118
4.8	Illustration of the error suppression in the Mølmer-Sørensen gate . . .	119
4.9	Some Walsh functions	123
4.10	Walsh modulated spin-dependent force operations with a single ion .	125
4.11	Walsh modulated Mølmer Sørensen gates with two ions	130
5.1	W-state scattering pattern	141
5.2	A schematic of the type II experiment	145
5.3	An illustration of the protocol to entangle the clock qubit with photonic frequency qubits	147
5.4	Bounds on the randomness generated in a Bell Inequality Experiment	160
5.5	Bounds on the randomness generated by remote entangled ions	162
6.1	Repeater Architecture	165
6.2	Schematic of the blade trap	170
6.3	Flowchart for the 2 + 1 experiment	171
6.4	Schematics showing the optical setup for the 2 + 1 experiment	173
6.5	Individual addressing data	174
6.6	Measured populations of the 2 + 1 experiment	177
A.1	Paraboloidal ion trap schematic	182
A.2	Parabolic coordinate system	182
A.3	Graphical analysis of paraboloidal ion trap design parameters	186

Chapter 1

Introduction

1.1 Ion-photon networks

The emergence of quantum information science has spurred the development of quantum mechanical devices with ever increasing degrees of complexity and control. With the long term goal of building a quantum computer, researchers have made tremendous progress since the first demonstration of an entangling logic gate [1] to recent experiments demonstrating “a combination of all of the fundamental elements required to perform scalable quantum computing” [2] and small scale quantum simulations of magnetism [3, 4] and field theories [5]. The number of qubits that experimentalists have been able to entangle has been obeying a quantum version of Moore’s law, effectively doubling every 5.7 years as shown in Fig. 1.1 with the current record being 14 qubits [6]. A wide variety of quantum information processing platforms are being developed simultaneously including neutral atoms [7], electron spins [8], superconductor qubits [9] and optical fields [10] to name a few and techniques developed for quantum information processing have started being used in other fields such as metrology [11], imaging [12], communication networks [13] and condensed matter theory [14]. Despite all of the progress going on around the world, it is generally thought that fault-tolerant quantum computing is years, if not decades away because of the challenges foreseen in scaling the prospective systems

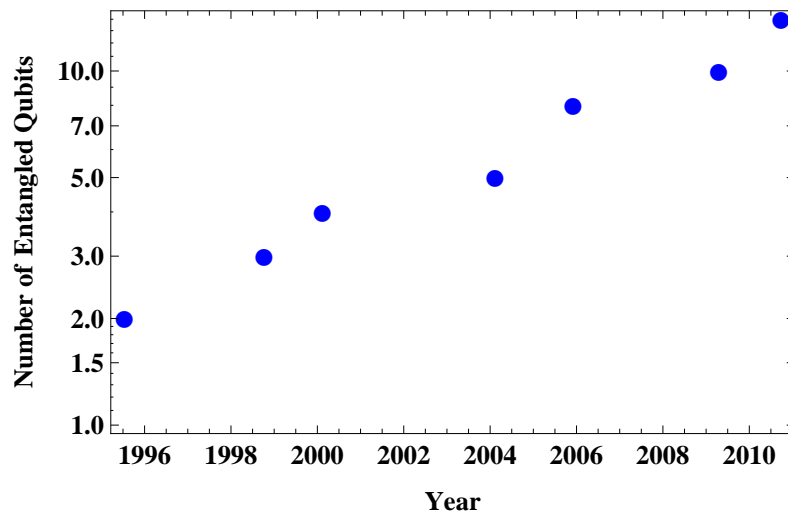


Figure 1.1: This log plot shows that number of qubits are able to be faithfully entangled in the laboratory is roughly doubling every 5.7 years. This data was shared courtesy of [15].

to large numbers of qubits. The minimum requirements for a universal quantum computer have been compiled into the now famous DiVincenzo requirements [16] which state that the system needs,

- well characterized qubits which can be easily scaled to large numbers
- the ability to initialize the qubits to a simple fiducial state
- long coherence times compared to the time scale of gate operations
- a universal set of quantum gates
- a qubit-specific measurement capability

As will be discussed in this thesis, trapped ions are close to demonstrating all of these criteria with outstanding exception being the scalability issue. In order for a quantum computer to outperform a classical computer and do something “interesting,” it is generally accepted that at least 1000 logical qubits will be needed. Because

a quantum computer will require error correction [17] in order to fight decoherence, there will be additional overhead and likely require several, if not many, physical qubits for every logical qubit. Given the enormity of the task, it will be crucial that physicists and engineers think hard about how to optimize both the control and the layout of such a device.

At its most basic level, a quantum computer will require a quantum memory for storage and manipulation of information and a quantum data bus for transfer of information. The internal atomic states of trapped ions have been shown to provide an excellent quantum memory with coherence times of several minutes being demonstrated [18] and systems of many trapped ions have demonstrated the use of phonons as a natural quantum data bus for entangling operations [19, 1, 20, 21]. The first proposal for trapped ion quantum computing envisioned a large ion crystal that was controlled through laser interactions with individual ions [19]. This approach runs into several complicating issues when scaled to very large numbers of ions. One problem with using a single ion crystal of N qubits is the increased mass leads to a decrease in the motional coupling parameter $\eta \propto \frac{1}{\sqrt{N}}$ which leads to slower gate speeds. Other problems include a decrease in the inter-ion spacing resulting in addressability problems and the increased stray excitations from the spectral crowding of the motional-mode structure. It might, therefore, be advantageous to design a complex trapped ion system around a modular design philosophy in which the system is made up of separated ion traps of manageable complexity that are connected through a quantum channel that can be turned on and off like a switch. One possible way to do this is by building an ion trap that consists of many

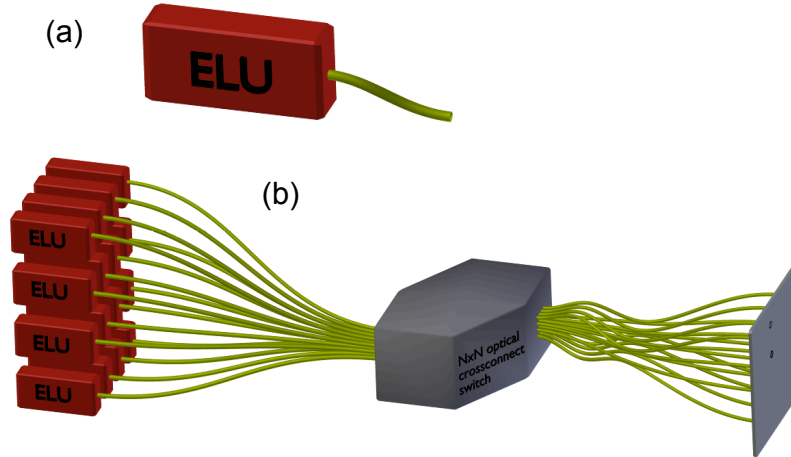


Figure 1.2: A concept drawing of a proposed ion-photon network. (a) The elementary logic unit (ELU) represents a single trapped ion register where quantum information is stored and manipulated through Coulomb force mediated gates. (b) Using an optical cross-connect switch, the different registers can be connected using ion-photon entangling operations along with entanglement swapping measurements on the photons.

trapping regions that can be connected by shuttling individual ions using dynamic control voltages [22] and there has been a lot of progress made in recent years toward realizing this architecture [23, 24]. Another possible way to do this is to use a photonic interconnect between the ion registers as depicted in Fig. 1.2 [25]. In this modular architecture, the elementary logic units (ELUs) contain trapped ion registers where information is stored and manipulated using coherent interactions while the interconnections are established through an entanglement swapping apparatus that involves a measurement of photon pairs that are entangled with respective registers.

A closely related emerging quantum technology is the quantum communication network. Not long after the power of quantum computers had been shown to be capable of cracking state of the art encryption codes, [26], it was realized that

privacy among communicating parties could be guaranteed by the laws of physics if one has access to a quantum communication network [27]. It wasn't long after the community became familiar with DiVincenzo's criteria that he added two more requirements to his list for the construction of a quantum network [16];

- the ability to interconvert stationary and flying qubits
- the ability to faithfully transmit flying qubits between specified locations

These additional criteria are not only crucial to quantum communication networks, but will likely be needed for distributed quantum computing and for error correction which might require communication between different pieces of the computer. Photons, being the fastest way to transmit information, are one obvious choice for flying qubits and researchers are currently studying different methods of interfacing stationary and flying qubits. In tradition with the conventional circuit model of quantum computing [28], much of the effort is geared toward engineering deterministic interactions between stationary and flying qubits with the goal being the production of a single photon in the desired mode on demand. This approach implies that an atom trapped in free space will not suffice and one must resort to engineering a strong coupling environment through the interaction with a cavity [29, 30, 31], with reflective optics [32] or with high numerical aperture lenses [33]. Another approach, however, has shown that it possible to establish interconnects between free space atoms through a heralded probabilistic photonic channel [34], albeit at the cost of lower efficiency.

Besides the difficulties involved with interfacing photonic and matter qubits, photons will be subject to a host of destructive processes in transit between different quantum memories. For example, any optical fiber used as a quantum channel for photons has an attenuation length associated with it that causes the amount of transmitted light to be depleted in an exponential fashion. Classical communication networks also suffer from attenuation of signals and use repeater stations to amplify signals before the attenuation leads to any serious deterioration of the signal. A quantum communication network's advantage, however, stems from the inability of an eavesdropper to gain information about the transmission without being detected [35] as enforced by the quantum no-cloning theorem [36] which has the added consequence that amplification of the signal is not possible. Nonetheless, it is still possible to construct a quantum repeater that is capable of faithful transmission of quantum information in the presence of attenuation through the use of distributed entanglement [37]. As discussed in more detail in Chapter 6, an ion-photon quantum repeater can be constructed through a series of memory nodes that are connected through photonic channels.

While all of the necessary components of such an architecture have been extensively studied independently, the complexities of merging these technologies are only beginning to be understood and dealt with. This thesis aims to show experimental advances in both the coherent control of individual trapped ion registers and their integration with a photonic interconnect channel.

The thesis is organized as follows;

Chapter 2 begins with a brief review of basic ion trapping physics along with a detailed description of the experimental apparatus. The procedure for loading Ytterbium ions is detailed along with a description of the relevant atomic structure of $^{171}\text{Yb}^+$ and basic characteristics of the system. The definition of the qubit subspace is given along with an overview of state initialization, manipulation and detection techniques.

Chapter 3 describes a new technique of controlling trapped ion hyperfine qubits using mode locked pulsed lasers. Simple models are developed for the description of the interaction between the atomic system and the pulsed laser and experimental data showing full control over the system is shown.

Chapter 4 gives an overview of the technique commonly used to implement coherent interactions between neighboring ions. Experimental data is presented demonstrating the entanglement of two trapped $^{171}\text{Yb}^+$ ions. An extension of this entangling gate that is designed to be more resistant to certain errors is described and experimentally demonstrated.

Chapter 5 is an overview of photon mediated entangling operations amongst stationary matter qubits. Two basic types of photonic gates are described along with their inherent advantages and disadvantages and some relevant scaling laws. A Bell inequality experiment is demonstrated and used as random number generator.

Chapter 6 presents our progress toward the construction of an ion-photon network. Using the coherent entangling operations among neighboring ions in one trap along with a photonic connection that is shared with another distant trap, we demonstrate a correlation between the qubit state in one register and collective state

of another register.

Chapter 2

Ytterbium ions

2.1 The Paul Trap

Trapped ions have been at the forefront of experimental quantum information science since at least 1995 [1] when the first demonstration of an entangling gate between two qubits took place. The trapped ion platform was well positioned to take the lead in experimental quantum information science after having benefited from decades of development by researchers interested in mass spectrometry and atomic clocks. The development of ion traps was largely motivated by the long confinement times and the extreme isolation of particles that is desired by precision measurement experiments. The overlap of these desiderata in precision measurements and the search for the perfect qubit is what led to the ion trap being the most successful platform in these early days of quantum information science. In this chapter, some basic tools of an ion trap laboratory are reviewed.

2.1.1 Trapping charged particles

One consequence of Maxwell's laws of electromagnetism is that static electric fields can not produce a stable trap for a charged particle. This statement can be derived using the fact that electric fields are divergenceless in free space, $\nabla \cdot \vec{E} = 0$, as shown by Earnshaw's theorem. Because the field can be written as the gradient

of a conservative field that satisfies Laplace's equation, the potential can possess no maxima or minima, only saddle points, implying that a field that generates a trap in one-dimension will necessarily create an anti-trap in another dimension. But by considering dynamic fields, a stable trap can be generated in a configuration now referred to a Paul trap [38, 39]. Most experiments described in this thesis were performed using a four rod trap like the one shown in Fig. 2.1. In the simplest configuration, a trap is formed by applying DC voltages to the needle shaped endcap electrodes and an oscillating radio frequency voltage to two opposing rods, with the other two rods and the endcap electrodes being RF grounded through shunting capacitors. The DC voltages provide a restoring force for a charged particle in the z direction, but as dictated by Maxwell's equation form an anti-trap in the $x-y$ plane. Near the center of the trap, the field can be linearized and the electric potential can be approximated by,

$$\phi(x, y, z) = V_0 \frac{\eta_{rf}}{2} \frac{x^2 - y^2}{R^2} \cos \Omega_T t + U_0 \frac{\eta_{dc}}{R^2} \left(z^2 - \frac{1}{2} (\epsilon_{dc} x^2 + (1 - \epsilon_{dc}) y^2) \right), \quad (2.1)$$

where $V_0 \cos \Omega_T t$ is the applied RF voltage, U_0 is the DC voltage, R is the distance from the electrode to the trapping region and $\eta_{rf}, \eta_{dc}, \epsilon_{dc}$ are geometric factors that must be found through experiment or simulation. In the ideal case where the RF electrodes are hyperbolic and the DC endcaps are far enough away as to be negligible, the factor η_{rf} limits to one. We have ignored the small RF field in the z direction due to the endcaps which allows the motion along the z direction to be approximated

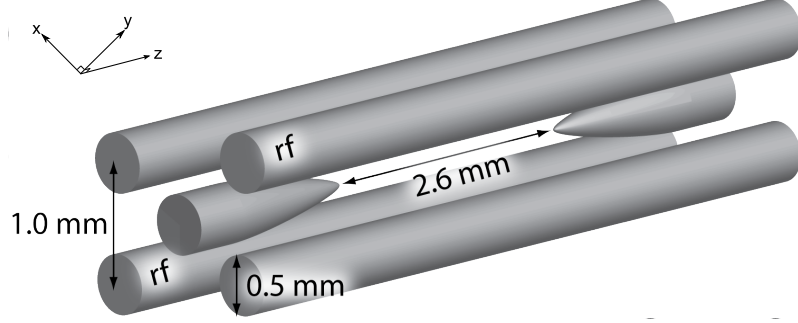


Figure 2.1: A schematic of the four rod trap is shown indicating where the static and time-dependent voltages are applied.

as purely harmonic motion with a secular frequency,

$$\omega_z = \sqrt{eU_0\eta_{dc}/R^2m}. \quad (2.2)$$

The motion in the x direction is described by the Mathieu equation,

$$m \frac{d^2x}{dt^2} = eV_0\eta_{rf} \frac{x}{R^2} \cos\Omega_T t - eU_0 \frac{\eta_{dc}}{R^2} \epsilon_{dc} x, \quad (2.3)$$

with the motion along y obeying a similar differential equation. To understand how a force like the one described in Eq. (2.3) creates a stable trap, consider a particle interacting with the field,

$$E(x, t) = E_0(x) \sin(\Omega_T t). \quad (2.4)$$

For simplicity, assume the form $E_0(x) = kx$ and that at $t = 0$ the particle is located $x_0 > 0$. During the first half of the field cycle, $0 < t < 2\pi/\Omega_T$, a positively charged particle will feel a positive force and accelerate away from the origin. However,

during the second half of the cycle the particle will feel a negative force and accelerate toward the origin. Since the gradient of $E_0(x)$ is positive, the particle feels a larger impulse in the second half of the cycle and therefore acquires a net negative change in momentum over the entire cycle. This effectively creates a restoring force in the x direction. This idea is implemented in a variety of designs in different ion traps around the world.

2.1.2 Dynamics in the Paul trap

In this section, I will review the classical version of this problem, but will omit many of the mathematical details as they are extensively covered in many other texts [40]. Since the potential in Eq. (2.1) is separable in x, y and z , and z is well approximated by purely harmonic motion, the rest of the picture can be filled in by considering the effect of the field in the x direction. Eq. (2.3) can be rewritten in dimensionless form as,

$$\frac{d^2x}{d\tau^2} + (a + 2q\cos 2\tau)x = 0, \quad (2.5)$$

where we have defined the following parameters; $\tau = \Omega_T t/2$, $a = \frac{2eU_0\eta_{dc}\epsilon_{dc}}{m\Omega_T^2 R^2}$ and $q = \frac{2eV_0\eta_{rf}}{m\Omega_T^2 R^2}$. Solutions to the Mathieu equation can be found using Floquet theory, which is familiar to most physicists in the form of Bloch's theorem concerning solutions to the time-independent Schrödinger equation with a periodic potential. Floquet's theorem states that the differential equation (2.5) has solutions of the form, $x(\tau) = \zeta(\tau)e^{i\beta\tau}$ where $\zeta(\tau + \pi) = \zeta(\tau)$ and β is a constant. In analogy with the solutions to Bloch's problem, the solution is the product of a function ζ that has the same

periodicity as the drive function and time dependent phase with the quantity β sometimes referred to as the quasi-energy. The general solution to Eq. (2.5) is expressed as,

$$x(\tau) = e^{\pm i\beta\tau} \zeta(\tau). \quad (2.6)$$

Because $\zeta(\tau)$ is periodic, the function admits a Fourier decomposition,

$$\zeta(\tau) = \sum_{n=-\infty}^{\infty} c_n e^{in\tau}. \quad (2.7)$$

Plugging Eq. (2.7) into the differential equation (2.5) and using the orthogonality of the different Fourier components yields an expression for β ,

$$(\beta - n)^2 = \frac{a + q(c_{n+2} + c_{n-2})}{c_n}. \quad (2.8)$$

The parameter a comes from the static voltages in the z direction and in our case is quite small compared to the effect of the RF voltages. If a is assumed to be small compared to q , the expression in Eq. (2.8) becomes $\beta^2 = q \left(\frac{c_2}{c_0} + \frac{c_{-2}}{c_0} \right)$. The fractions $\frac{c_2}{c_0}$ and $\frac{c_{-2}}{c_0}$ can be found to lowest order by rewriting Eq. (2.8) as,

$$\frac{c_n}{c_{n+2}} = \frac{1}{\frac{(\beta-n)^2}{q} - \frac{c_{n-2}}{c_n}} = \frac{1}{\frac{(\beta-n)^2}{q} - \left(\frac{1}{\frac{(\beta-n+2)^2}{q} - \frac{c_{n-4}}{c_{n-2}}} \right)}. \quad (2.9)$$

The second equality is reached by using the expression for $\frac{c_n}{c_{n+2}}$ with the substitutions $n \rightarrow n - 2$ and $n - 2 \rightarrow n - 4$. This process can be continued to yield an expression in terms of a continued fraction, and similar expressions can be derived for $\frac{c_n}{c_{n-2}}$,

which to lowest order yield,

$$\frac{c_n}{c_{n\pm 2}} \approx \frac{q}{(\beta - n)^2}. \quad (2.10)$$

Putting it all together implies,

$$\beta \approx \left(q \left(\frac{c_2}{c_0} + \frac{c_{-2}}{c_0} \right) \right)^{1/2} \quad (2.11)$$

$$\approx \left(q \left(\frac{q}{(\beta - 2)^2} + \frac{q}{(\beta - 2)^2} \right) \right)^{1/2} \quad (2.12)$$

$$\approx \frac{q}{\sqrt{2}}. \quad (2.13)$$

An approximate solution can then be written down by ignoring Fourier components where $|n| > 2$ and using $c_2 \approx c_0 \frac{q}{2}$ to write,

$$x(\tau) \approx x_0 e^{i(\beta\tau + \phi)} \left(1 + \frac{q}{2} \cos 2\tau \right). \quad (2.14)$$

We see that the motion is comprised of pieces, one that describes an oscillation at the frequency $\omega_s = \beta\tau/t = \frac{\beta\Omega_T}{2}$ with an amplitude x_0 and another that describes an oscillation at the frequency $\omega_\mu = 2\tau/t = \Omega_T$ with an amplitude $x_0 \frac{q}{2}$. Remembering that both $\beta \ll 1$ and $q \ll 1$ means that the motion can be thought of as harmonic motion together with small fast oscillations at the RF drive frequency Ω_T as illustrated in Fig. 2.2.

A complimentary analysis [38] that considers the force on the charged particle averaged over the time $2\pi/\Omega_T$, leads to the following expression for the average force

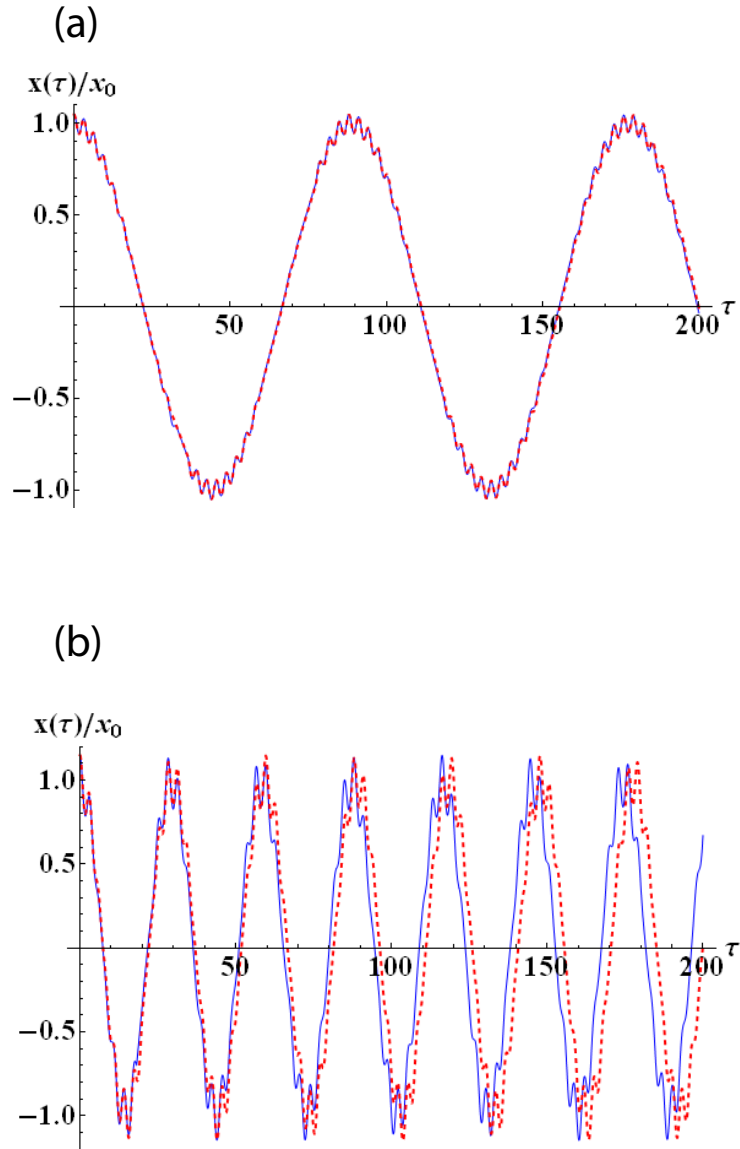


Figure 2.2: The approximate solution to the Matheiu equation (2.14), (red), is compared to a numerical integration of Eq. (2.3), (blue). In figure (a) the value of $a = 0$ and $q = 0.1$ and in figure (b) the values are $a = 0$ and $q = 0.3$.

felt by the particle,

$$\bar{F} = -\frac{e^2}{4m\Omega_T^2} \frac{\partial}{\partial x} E_0^2(x). \quad (2.15)$$

This implies that the particle exhibits nearly harmonic motion when it is trapped in a region where the field $E_0(x)$ is well described by a linear function. This analysis provides a useful picture in which the ion is trapped by a potential well that is proportional to the square of the electric field, with the proportionality factor being determined by the charge and mass of the particle and the frequency of the RF drive. By assuming the potential in Eq. (2.1) and that the geometric factor is approximately 1, the transverse secular frequency of Yb^+ is,

$$\frac{\omega_x}{2\pi} \approx 10\text{MHz} \frac{V_0(\text{kV})}{\Omega_T/2\pi(\text{MHz})R^2(\text{mm})} \quad (2.16)$$

$$\frac{\omega_x^{(4\text{-rod})}}{2\pi} \approx 48\text{MHz} \frac{V_0(\text{kV})}{\Omega_T/2\pi(\text{MHz})}, \quad (2.17)$$

with $R \approx 0.46$ mm in the four-rod trap. The expression in Eq. (2.17) is not always valid since the Mathieu equation solutions are only stable in limited regimes, with the case of $a = 0$ yielding stable orbits when $0 < q < q_{max} = 0.93$ [39]. Using Eq. (2.15), one finds that the secular frequency is related to the RF drive frequency as,

$$\omega_x = \frac{\Omega_T}{2\sqrt{2}} q, \quad (2.18)$$

meaning that the secular frequency must be approximately $2\sqrt{2}$ times smaller than the RF drive frequency in order to create a stable trap. If the voltage applied to the electrodes is limited to 1 kV, this restriction, along with Eq. (2.17), dictates that

the RF drive frequency must be no less than ≈ 10 MHz. In the lab, the RF potential is typically generated using drive frequencies of 10 – 40 MHz with the large voltage being generated through the use of a helical resonator [41] like the one shown in fig. 2.3. The voltage on the trap electrodes is given by $V_0 = \epsilon\sqrt{PQ}$, where $\epsilon \approx 20$ is determined by the geometry of the helical resonator, P is the input RF power and Q is the quality factor of the resonator. The trap was successfully loaded using a can with a resonance frequency of 35 MHz, $Q = 270$ and driven with $P = 9$ W, resulting in a trapping frequency of 1.3 MHz. A second can was constructed in hopes of achieving a higher trapping frequency by using a lower RF drive frequency of 12 MHz, but it was found that the trap was not stable for more than one ion unless the RF input power was reduced to $P = 2$ W, resulting in a trapping frequency of 1.8 MHz. The trap is made complete by the application of the DC voltages to the needles, which is typically on the order of 10 – 600 V. These parameters yield trapping frequencies on the order of 1 – 3 MHz in the $x - y$ plane and 0.01 – 1 MHz in the z direction. Numerical simulations of the trapping environment reveal that the depth of the four-rod trap is on the order of 10 eV, or 10^5 K [42]. This ion trap resides in an ultra-high vacuum environment whose pressure is measured to be $\approx 10^{-11}$ Torr by an ion gauge and has been observed to hold a single ion for several weeks.

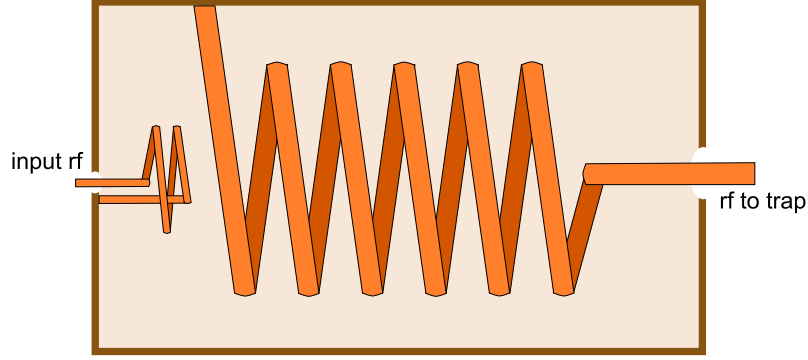


Figure 2.3: A helical resonator can is shown schematically to illustrate the inductive coupling between the RF input antenna and the trap electrodes.

2.2 Trapping Yb^+

To load the trap, an atomic oven source is placed a few centimeters away from the center of the trap and resistively heated for 1 – 5 minutes. Neutral Ytterbium is ionized in a two-photon process in which an atom that is initially in the ground $^1\text{S}_0$ state is excited to the $^1\text{P}_1$ state and then to a state where one of the valence electrons becomes unbound. The $^1\text{S}_0 \Leftrightarrow ^1\text{P}_1$ transition has a resonance frequency of $c/(398.9\text{nm})$ and the transition from the excited $^1\text{P}_1$ state to the continuum requires a photon with an energy of at least $ch/(394.1\text{nm})$. As will be discussed later, the main dipole transition used in the Yb^+ system has a resonant frequency of $c/(369.5\text{nm})$ which corresponds to a photon energy that is more than enough to free the valence electron. The photoionization procedure is therefore achieved by focusing two laser beams, 398.9 nm and 369.5 nm, in the center of the trap. Since the atomic oven generates a thermal cloud of atoms streaming toward the center of the trap, it important to take into account Doppler shifts seen by the atom if isotope selectivity is desired. The chamber holds two atomic oven sources, one being packed

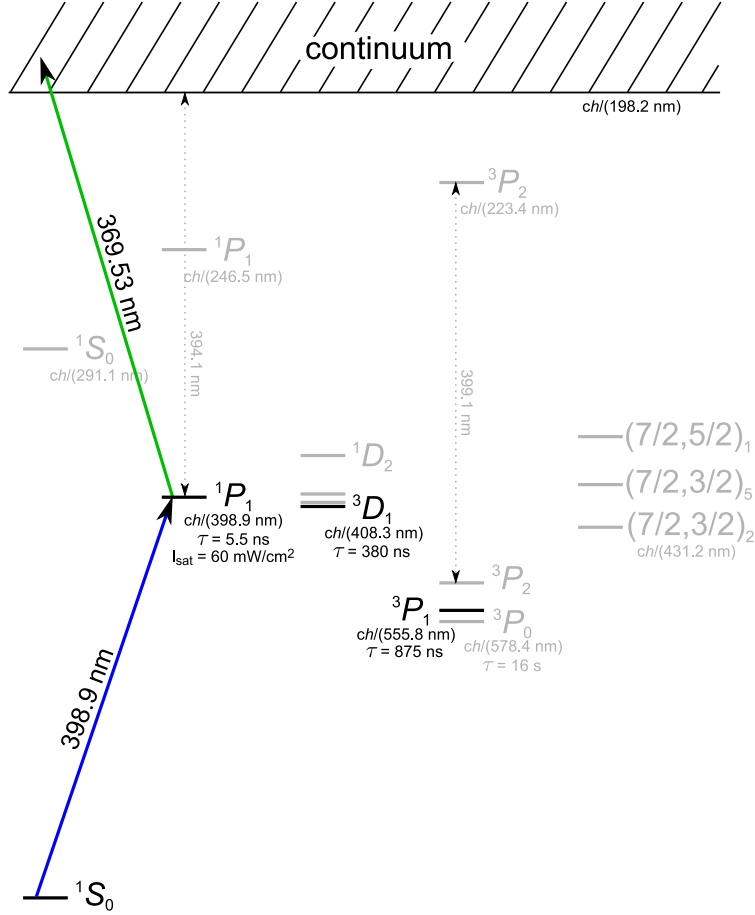


Figure 2.4: The relevant energy level structure for ionizing neutral Ytterbium. Ytterbium is ionized in a two-photon process with the first photon resonantly driving the $^1S_0 \leftrightarrow ^1P_1$ and the second photon liberating the electron from the atom.

with all the different isotopes of Ytterbium in their natural abundance ratios and the other being a purified source with higher than 90% being ^{171}Yb . A list showing the resonances of the $^1S_0 \leftrightarrow ^1P_1$ for the different Ytterbium isotopes is shown in table 2.1.

The ions are imaged using a $\text{NA} = 0.23$ triplet lens that has a working distance of 13 mm. The lens is placed ≈ 3 mm from the vacuum chamber window which is 3.3 mm thick and whose vacuum side surface is 8.5 mm from the center of the ion trap. The triplet lens stack generates an image plane ≈ 300 mm from the ion where

Isotope	Shift from ^{174}Yb (MHz)	absolute λ in nm
^{176}Yb	-509.310(50)	398.91190
$^{173}\text{Yb}(F = 5/2)$	-253.418(50)	398.91177
$^{173}\text{Yb}(F = 3/2)$	515.975(200)	398.91136
^{172}Yb	533.309(53)	398.91135
$^{173}\text{Yb}(F = 7/2)$	587.986(56)	398.91132
$^{171}\text{Yb}(F = 3/2)$	832.436(50)	398.91119
$^{171}\text{Yb}(F = 1/2)$	1153.696(61)	398.91102
^{170}Yb	1192.393(66)	398.91100
^{168}Yb	1887.400(50)	398.91063
$^{173}\text{Yb}(\text{centroid})$	291.516(54)	398.91147
$^{171}\text{Yb}(\text{centroid})$	939.523(39)	398.91113

Table 2.1: This shows the resonant frequencies for the $^1\text{S}_0 \leftrightarrow ^1\text{P}_1$ transition for the different neutral Ytterbium isotopes as taken from [43]. The resonance frequency for ^{174}Yb is 751,525,987.761(60) MHz or 398.91163 nm.

a 500 μm pinhole is placed to reduce the background light created by light scattered from the trap electrodes. After the pinhole, a doublet lens stack refocuses the image onto either a photo-multiplier tube (PMT) or an intensified CCD camera (ICCD) depending on the position of flip mirror. The PMTs used in these experiments are Hamamatsu PMTs with quantum efficiencies ranging from 0.2 – 0.4 and dark count rates on the order of 10 Hz and the camera is the Princeton Instruments PI-MAX ICCD. The camera is only used for imaging and trouble-shooting and not for quantitative measurements as the read out time and noise characteristics are inferior to that of the PMT. In addition to the pinhole, interference filters designed to pass 369 nm light made by Semrock inc. are placed in front of the PMT and camera.

The ion is localized by being Doppler cooled on the ${}^2\text{S}_{1/2} \leftrightarrow {}^2\text{P}_{1/2}$ transition. The D_1 transition is not a closed cycling transition since the atom has a 0.5% chance of decaying to the low lying ${}^2\text{D}_{3/2}$ state from the ${}^2\text{P}_{1/2}$ state. Because of the relatively long lifetime of the ${}^2\text{D}_{3/2}$ state, 53 ms, a second laser is used to depopulate this state through the ${}^3[3/2]_{1/2}$ state with resonant 935.2 nm light.* The combination of the 369.5 nm and 935.2 nm light results in a closed bow-tie configuration cycling transition as depicted in fig. 2.5. An added complication comes from the presence

*The bracket notation used for the ${}^3[3/2]_{1/2}$ state is a reference to an angular momentum coupling scheme that differs from the usual Russell-Saunders (L-S) coupling. When the atom is excited to the ${}^3[3/2]_{1/2}$ state, a second electron is excited to the valence shell from the f shell, resulting in a hole that carries angular momentum. The L-S coupled core has a total angular momentum J_c which is then coupled to the angular momentum of the two valence electrons to give the angular momentum $K = L + J_c$, which is the value contained in the brackets. The spin of the two valence electrons are coupled together and denoted by the multiplicity superscript. Finally the spin is coupled to K to give the total angular momentum $J = K + S$, which is denoted by the subscript [44].

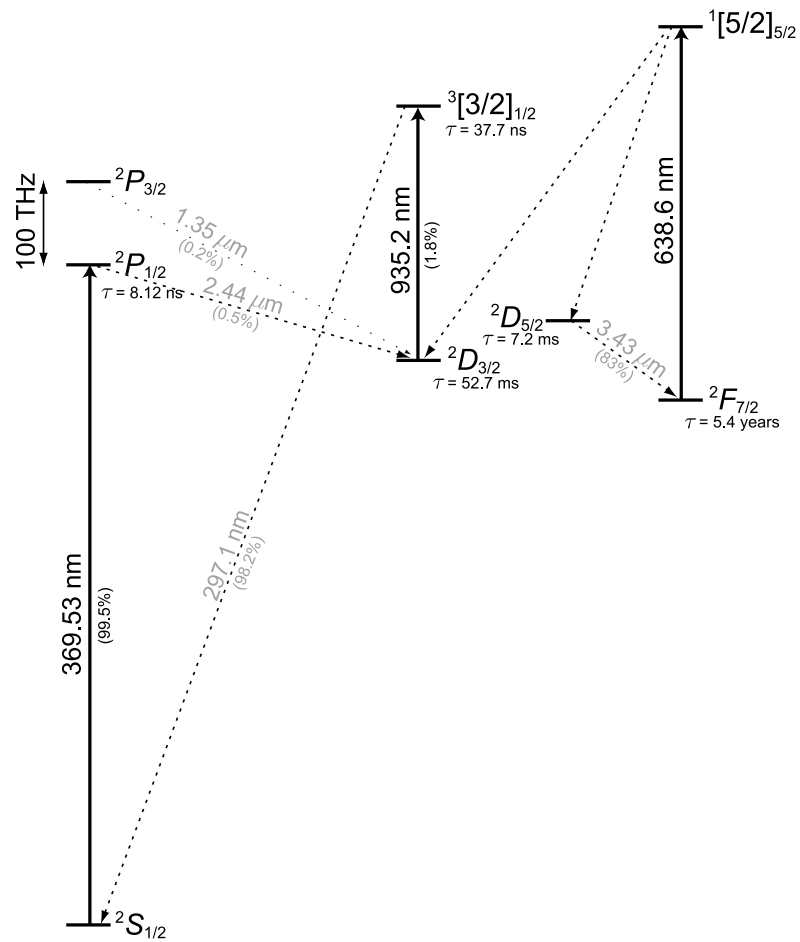


Figure 2.5: The energy level structure for Yb^+ .

of the low lying ${}^2F_{7/2}$ state that has a lifetime of approximately 6 years [45]. When the ion is being cooled, it is possible for the atom to make the transition to the ${}^2F_{7/2}$ state through collisions with the background gas, which is observed to occur on the timescale of tens of minutes. For this reason, an addition laser tuned near 638.6 nm is directed toward the ion to depopulate the ${}^2F_{7/2}$ state through ${}^1[5/2]_{5/2}$ which has a decay channel to ${}^2D_{3/2}$.

This cooling scheme is most easily implemented using a Yb^+ isotope that has no nuclear spin and, therefore, a simple energy level structure. In this case, both the ${}^2S_{1/2}$ and ${}^2P_{1/2}$ manifolds consist of only two Zeeman levels split by ~ 5 MHz by the presence of a small magnetic field of ~ 4 G. In the case of ${}^{171}\text{Yb}^+$, which has a spin 1/2 nucleus, the hyperfine structure of the $\left\{ {}^2S_{1/2}, {}^2P_{1/2}, {}^2D_{3/2}, {}^3[3/2]_{1/2} \right\}$ manifolds must be considered to avoid optically pumping the ion into a dark state. The ${}^{171}\text{Yb}^+$ ion is cooled with light that is nearly resonant with the ${}^2S_{1/2}|F=1\rangle \leftrightarrow {}^2P_{1/2}|F=0\rangle$ transition, but off-resonant scattering from the $F=1$ manifold in the excited state will eventually pump the atom to the $F=0$ ground state. To clean out the population in the $F=0$ state, the 369.5 nm light is phase modulated with an EOM at 7.35 GHz so that the second sideband at 14.4 GHz will be nearly resonant with the ${}^2S_{1/2}|F=0\rangle \leftrightarrow {}^2P_{1/2}|F=1\rangle$ transition. Likewise, the 935.2 nm light is also phase modulated at 3.07 GHz, which is the sum of the hyperfine splittings of the ${}^2D_{3/2}$ and ${}^3[3/2]_{1/2}$ states. The cooling beam is positioned so as to have a projection on all three principal axes of the trap so that the ion is cooled along all directions and a biasing DC voltage is applied to two of the electrodes to ensure that there are no degeneracies in the trapping frequencies.

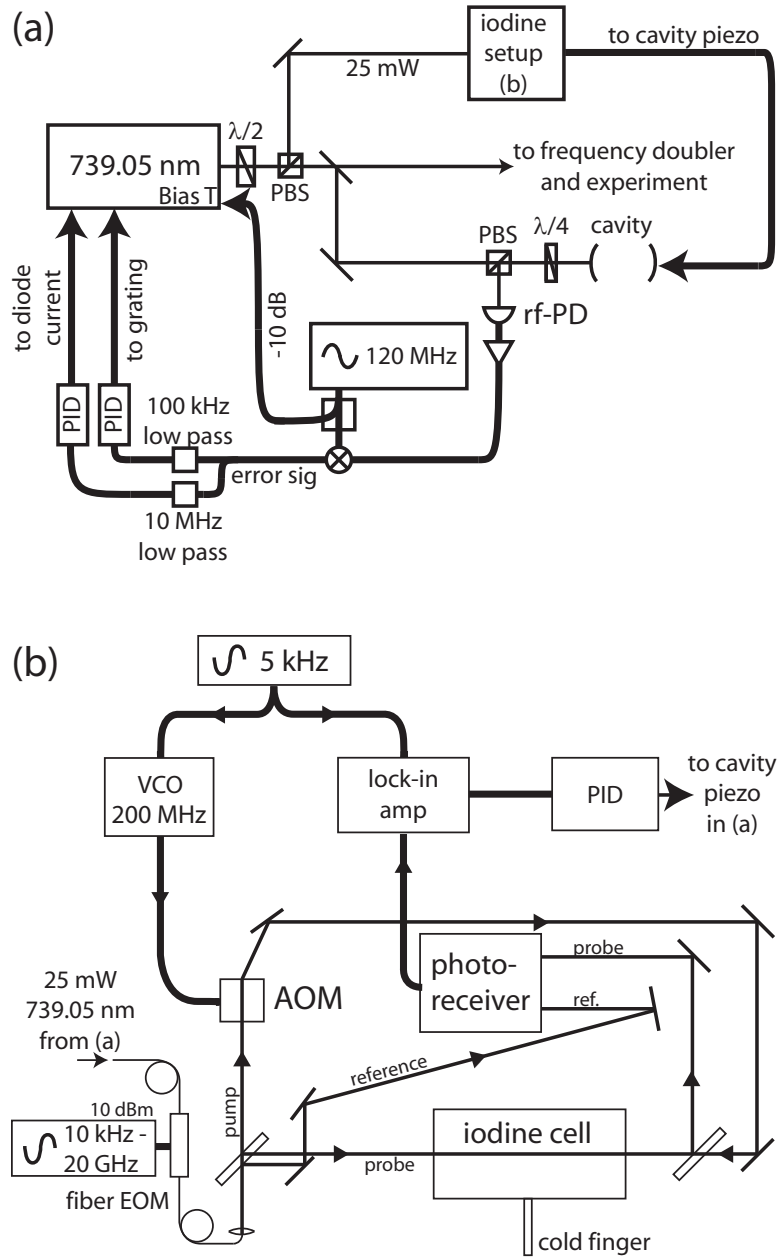


Figure 2.6: (a) The laser is locked to an external cavity using a Pound-Drever-Hall scheme [46]. (b) The cavity is locked to the Doppler free saturated absorption signal inside an iodine cell.

Because of the small branching ratios in the bow-tie cycling transition, the maximum scatter rate is well approximated by neglecting the time the atom spends in the $^2D_{3/2}$ and $^3[3/2]_{1/2}$ states. The maximum scattering rate of $^{171}\text{Yb}^+$ is diminished due to the presence of coherent dark states. Populating the coherent dark states is avoided by the application of the small magnetic field which has the adverse effect of making the cooling laser slightly off resonant for the σ^\pm transitions in the D_1 line. The optimization of this effect versus the desire to avoid population trapping in the coherent dark states results in a reduction of the scatter rate by about a factor of 3.

The minimum temperature of the Yb^+ ion is found by considering the steady state solution of the optical Bloch equations and the theory of Doppler cooling. The optical Bloch equations can be derived from a master equation describing the coherent interaction of a two-level atom with a monochromatic light source and effects of spontaneous emission,

$$\frac{d\rho}{dt} = -\frac{i}{\hbar} [H, \rho] - \frac{\Gamma}{2} (\sigma^+ \sigma^- \rho + \rho \sigma^+ \sigma^-) + \Gamma \sigma_- \rho \sigma^+, \quad (2.19)$$

where H includes the unperturbed two-level atom Hamiltonian and the interaction with the laser and Γ is the spontaneous emission rate. If the Rabi frequency of the dipole transition is Ω and the detuning of the laser from resonance is δ , the steady-state solution of Eq. (2.19) shows that the population in the excited state is given by,

$$\rho_{ee} = \frac{s_0/2}{1 + s_0 + (2\delta/\Gamma)^2}, \quad (2.20)$$

where the on-resonance saturation parameter $s_0 \equiv 2\Omega^2/\Gamma^2$. Because the scattering rate is proportional to the population of the excited state, the scatter rate is,

$$\gamma_p = \Gamma \rho_{ee}. \quad (2.21)$$

In the case of a traveling wave, the optical Bloch equations can be modified to estimate the optical force on a atom moving with velocity v ,

$$F = \hbar k \frac{s\Gamma/2}{1+s} \left(1 + \frac{2\delta vk}{(1+s)(\delta^2 + \Gamma^2/4)} \right) \equiv F_0 - \beta v, \quad (2.22)$$

where the generalized saturation parameter $s \equiv \frac{s_0}{1+(2\delta/\Gamma)^2}$ and the damping coefficient for the velocity dependent part of the optical force is,

$$\beta = -\hbar k^2 \frac{4s_0(\delta/\Gamma)}{(1+s_0 + (2\delta/\Gamma)^2)^2}. \quad (2.23)$$

The maximum damping coefficient is achieved when $\delta = -\Gamma/2$ and $s_0 = 2$, which yields $\beta_{max} = \hbar k^2/4$. The constant force F_0 in Eq. (2.22) can be removed by considering the effect of an externally applied trapping potential and in the case of low intensities, $s \ll 1$, one can estimate a minimum temperature achievable using Doppler cooling. By first defining the recoil energy, E_r , as the amount of kinetic energy an atom at rest would gain through spontaneous emission as,

$$E_r = \frac{\hbar^2 k^2}{2M} = \hbar \omega_r, \quad (2.24)$$

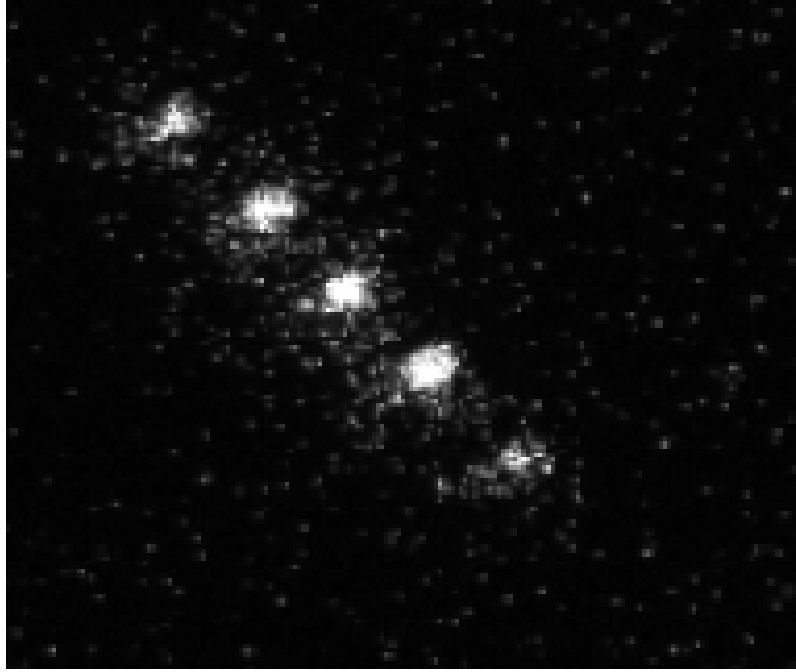


Figure 2.7: An image taken with an intensified CCD camera showing a 5 ion crystal being Doppler cooled. The ion spacing is approximately $10 \mu\text{m}$, showing that our imaging resolution is on the order of $1 \mu\text{m}$.

the average frequency of each absorbed photon is $\omega_{abs} = \omega_a + \omega_r$ whereas the average frequency of each emitted photon is $\omega_{abs} = \omega_a - \omega_r$. The atom, therefore, gains an average energy of $2\hbar\omega_r$ from each scattering induced recoil, which occurs at a rate γ_p . By equating the cooling rate $\vec{F} \cdot \vec{v}$ with the heating rate $\gamma_p 2\hbar\omega_r$, one finds that the minimum kinetic energy is achieved when $\delta = -\Gamma/2$ and a minimum temperature $T_D = \hbar\Gamma/2k_B$. For Yb, the maximum scatter rate and minimum temperature are $\Gamma/2 \approx 61 \text{ MHz}$ and $470 \mu\text{K}$. Once the ion is cooled to Doppler temperature they can easily be seen on the camera as shown in fig. 2.7. The localization of the particle can be estimated as $\sqrt{\langle x^2 \rangle}$ for a harmonic oscillator obeying a Boltzmann distribution.

For the Hamiltonian $H = \hbar\omega(a^\dagger a + 1/2)$, the partition function is,

$$Z = \sum_{n=0}^{\infty} e^{-\hbar\omega(n+1/2)/k_B T} = e^{-\beta\hbar\omega/2} \frac{1}{1 - e^{-\beta\hbar\omega}}. \quad (2.25)$$

The density matrix is then used to calculate $\langle x^2 \rangle$,

$$\langle x^2 \rangle = \text{Tr}[\hat{x}^2 \rho] \quad (2.26)$$

$$= \frac{1}{Z} \frac{\hbar}{2m\omega} \sum_{n=0}^{\infty} e^{-\beta\hbar\omega(n+1/2)} \langle n | (a + a^\dagger)^2 | n \rangle \quad (2.27)$$

$$= \frac{2}{Z} \frac{\hbar}{2m\omega} \frac{e^{-\beta\hbar\omega/2}(1 + e^{-\beta\hbar\omega})}{2(1 - e^{-\beta\hbar\omega})^2} \quad (2.28)$$

$$= x_0^2 \coth(\beta\hbar\omega/2), \quad (2.29)$$

where $x_0 = \sqrt{\hbar/2m\omega}$ is the characteristic length scale and is equal to the spread in the ground state wavefunction. Substituting the Doppler temperature into the last equation, we can estimate the localization of a trapped ion,

$$\Delta x = \sqrt{\frac{\hbar}{2m\omega} \coth(\omega/\Gamma)}. \quad (2.30)$$

The experiments described in this text were all done with trap frequencies ranging from 300kHz to 4MHz which corresponds to a localization ranging from 81nm to 6nm, a range which beyond the precision of our imaging system (1 μm).

Once an ion is trapped and laser cooled so as to be sufficiently localized for observation on a camera, the secular frequency of the trap can be measured directly. One method of measuring this quantity is to apply a relatively small oscillating

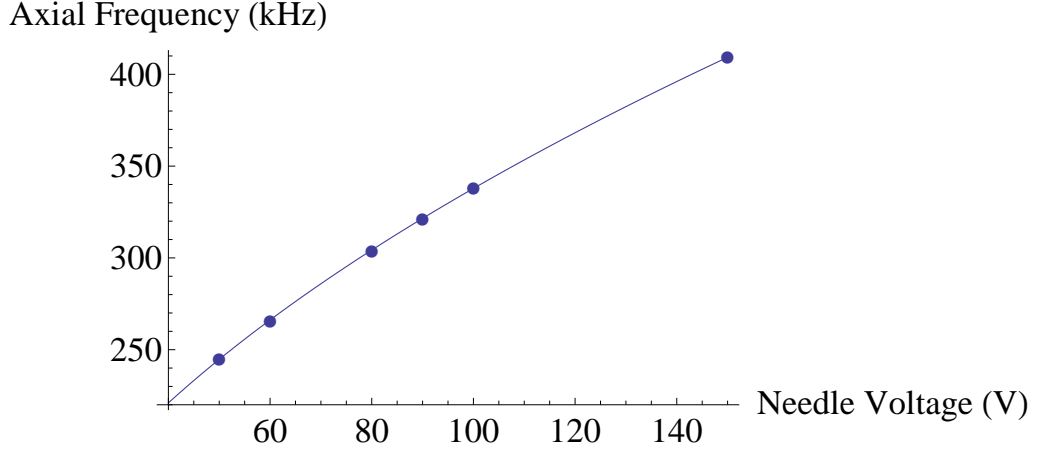


Figure 2.8: A measurement of the axial frequency as a function of the DC voltage U_0 that is applied the endcap needles. The function fit to the data is $\nu_{axial} = m\sqrt{U_0} + b$, where the fit parameters are $m = 31.8\text{kHz}/\text{V}^{1/2}$ and $b = 20.0\text{kHz}$. The small constant offset is likely due to the weak RF trap that exists in the axial direction due to the endcap needles being RF grounded. Note the error bars for the data points are small enough to be obscured by the size of the points.

voltage, (1-10 V), to one of the trap electrodes while observing the response of the ion on the camera. If the frequency of this applied voltage is brought into resonance with the secular motion, the ion will be parametrically driven leading to an observable delocalization of the ion. The resonance frequency's dependence on the applied DC voltages is observed to scale like the square root of the needle voltage, fig. 2.8, as is to be expected as shown by Eq. (2.2).

2.2.1 The $^{171}\text{Yb}^+$ hyperfine qubit

We have so far limited our discussion of the control of the Ytterbium ion to that of its motional degrees of freedom and its electronic structure. The $^{171}\text{Yb}^+$ isotope possesses a spin 1/2 nucleus and, therefore, hyperfine structure within the electronic structure. In particular, $^2\text{S}_{1/2} |F = 0, m_f = 0\rangle \equiv |0\rangle$ and $^2\text{S}_{1/2} |F = 1, m_f = 0\rangle \equiv |1\rangle$

form an especially attractive qubit. As we now begin to discuss in detail, this system has been shown to fulfill all of DiVincenzo's criteria for a suitable qubit.

The $m_f = 0$ states in the ${}^2S_{1/2}$ manifold are primarily chosen for the exceptionally long coherence time that is observed. The frequency splitting for these two states has been measured to be $\nu_0 = 12.642812118466 + \delta_{2z}$ GHz, where $\delta_{2z} = (310.8)B^2$ Hz with B in Gauss [18].

2.2.2 State initialization and detection

The Ytterbium ion lends itself to simple state initialization and detection protocols as described in [47]. State initialization is achieved through an optical pumping procedure that prepares the ion in $|0\rangle$. This is done by illuminating the ion with laser light that is resonant with ${}^2S_{1/2}|F=1\rangle \leftrightarrow {}^2P_{1/2}|F=1\rangle$ transition. If the polarization of the laser has $\hat{\pi}$, $\hat{\sigma}^+$ and $\hat{\sigma}^-$ components, the ion will eventually be pumped to $|0\rangle$ since every state in the ${}^2P_{1/2}|F=1\rangle$ manifold decays to $|0\rangle$ with a probability of 1/3. This procedure is ultimately limited by an off-resonant process that happens when an ion in $|0\rangle$ absorbs a photon from the pumping beam and then falls into the ${}^2S_{1/2}|F=1\rangle$ manifold. The hyperfine splitting of the ${}^2S_{1/2}$ results in the optical pumping beam being 12.6 GHz detuned from the resonance of this process. An estimate of the theoretical limit of the state initialization protocol can be made by looking at the steady state solution of a simple rate equation for the population of the bright state. If we consider all of the population in ${}^2S_{1/2}|F=1\rangle$ to be represented by $P_1(t)$ and the population of the ${}^2S_{1/2}|F=0\rangle$ state to be $P_0(t)$,

then the state initialization protocol can be modeled with the following differential equation,

$$\dot{P}_1(t) = -\Omega_{1,0}P_1(t) + \Omega_{0,1}P_0(t), \quad (2.31)$$

where $\Omega_{i,j}$ is the pumping rate from P_i to P_j . If the laser is tuned to be on resonance with the ${}^2S_{1/2}|F=1\rangle \leftrightarrow {}^2P_{1/2}|F=1\rangle$ transition, then the pumping rates can be estimated to be,

$$\Omega_{1,0} = \frac{1}{3} \frac{\Gamma}{2} \frac{s}{1+s} \quad (2.32)$$

$$\Omega_{0,1} = \frac{2}{3} \frac{\Gamma}{2} \frac{s}{1+s+4\left(\frac{\omega_{hf}}{\Gamma}\right)^2}, \quad (2.33)$$

where the factors of $1/3$ and $2/3$ account for the Clebsch-Gordan coefficients. Eq. (2.31) can be simplified by using the normalization condition $P_0 + P_1 = 1$. If the differential equation is then recast in terms of the dimensionless time $\tau = \Omega_{0,1}t$ and the ratio of the pumping rates $R \equiv \Omega_{1,0}/\Omega_{0,1}$, and the ion is assumed to be initially in the ${}^2S_{1/2}|F=1\rangle$ manifold, the solution to Eq. (2.31) is,

$$P_1(\tau) = \frac{1}{1+R} (1 + Re^{-(1+R)\tau}). \quad (2.34)$$

This leads to the steady state solution,

$$P_1(\infty) = \frac{1}{1+R}. \quad (2.35)$$

Because of power broadening, the optimal state preparation is in the limit $s \rightarrow 0$, giving a minimum of $\lim_{s \rightarrow 0} P_1(\infty) = \frac{2}{3+4(\omega_{hf}/\Gamma)^2}$. The actual $^{171}\text{Yb}^+$ hyperfine splitting and D_1 linewidth give an estimate of $\sim 10^{-6}$ for the minimum state preparation error. Fig. 2.9 shows how the state preparation error scales with the saturation parameter and how long the optical pumping light is on.

The qubit state is read out using a state-dependent fluorescent technique which takes advantage of the fact that $^2S_{1/2}|F=0\rangle \leftrightarrow ^2P_{1/2}|F=0\rangle$ is a forbidden transition. Therefore, light that is resonant with the $^2S_{1/2}|F=1\rangle \leftrightarrow ^2P_{1/2}|F=0\rangle$ will cause an ion in $|1\rangle$ to scatter many photons, while an ion in $|0\rangle$ will scatter very few photons as shown in fig. 2.10. The large difference in the number of photons scattered means that a simple discriminator method can be used for state detection. Because of a finite background, we ascribe the events where 0 or 1 photons are detected to a projection onto $|0\rangle$ and the events where more than 1 photon is detected to a projection onto $|1\rangle$. This protocol is limited by the off-resonant process that populates the $^2P_{1/2}|F=1\rangle$ manifold which can decay into $|0\rangle$. See [48] for a detailed description of the limits of this protocol. Another source of noise in this protocol comes from background light and dark counts on the PMT. Background light is minimized by using a well focused beam to avoid unwanted scatter off of the trap electrodes in combination with an optical filter from Semrock inc. that blocks light that has a larger wavelength than 370nm. Dark counts on the PMT can be minimized by cooling the PMT module as shown in fig. 2.12.

The fast readout of the PMT makes it ideal for state detection of a single ion, but unless individual addressing is used, a multi-qubit register requires more than

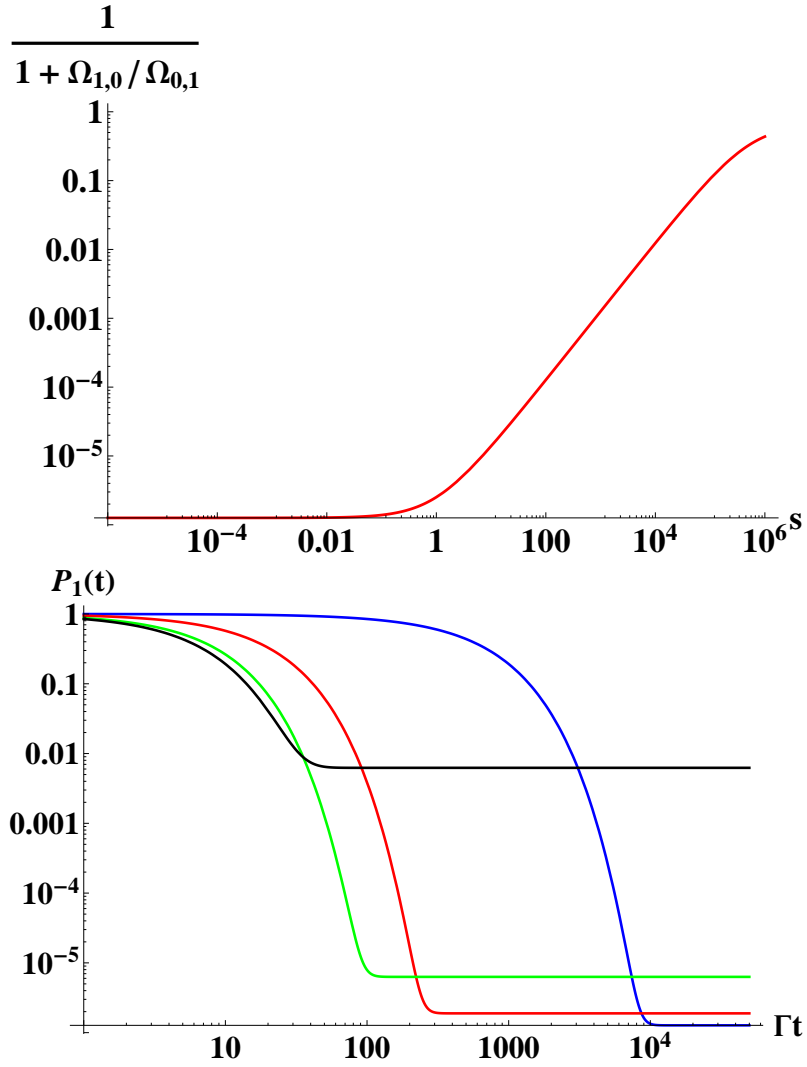


Figure 2.9: The first plot shows the steady state solution of Eq. (2.31) as a function of the saturation parameter. The second plot shows $P_1(t)$ for different intensities; $s = 0.01$ (blue), $s = 0.5$ (red), $s = 4$ (green), $s = 5000$ (black)

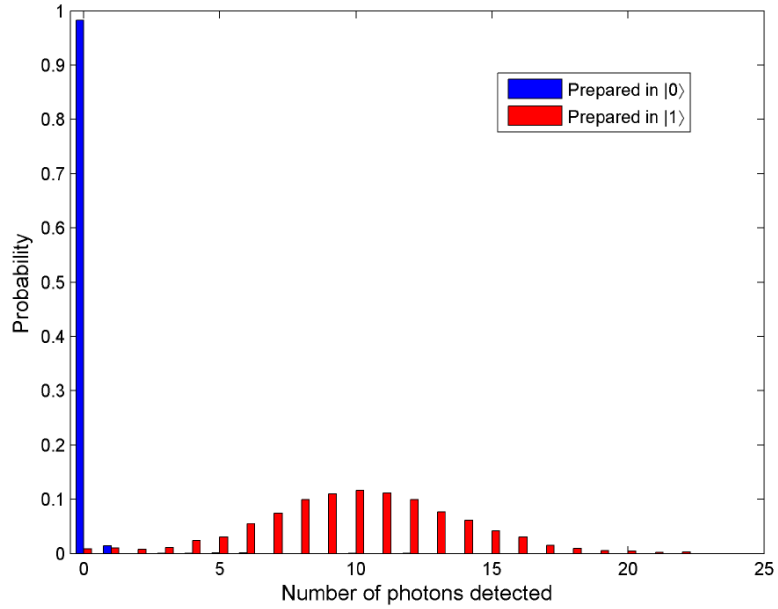


Figure 2.10: The histograms show the probability of detecting different numbers of photons for the two different qubit states. If the ion is optically pumped to $|0\rangle$, we usually only detect one or two photons upon shining laser light onto the ion. If instead, we apply a π pulse before applying the detection beam, we see an average of 10 photons. If we ascribe the events where we detect zero or one photons to a projection onto $|0\rangle$ and more than one photon to a projection onto $|1\rangle$, then our state detection fidelity is 98%.

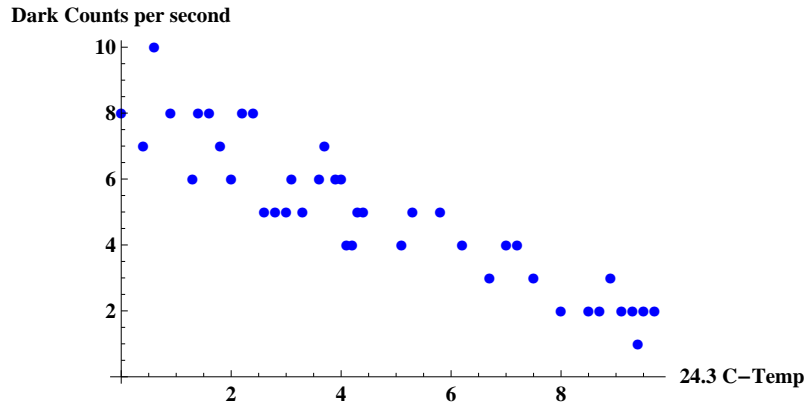


Figure 2.11: The data shows the minimization of dark counts on the PMT being used for state detection. As the module is cooled with a thermo-electric cooler by about 10°C the dark counts are seen to decrease by about a factor of 4. The PMT was operating in the dark and dark counts were recorded for a minute and then rounded to the nearest integer to calculate the counts per second. The temperature of the module was recorded by attaching a thermocouple to the outside casing. The temperature was not taken lower than shown in order to avoid condensation on the electronics.

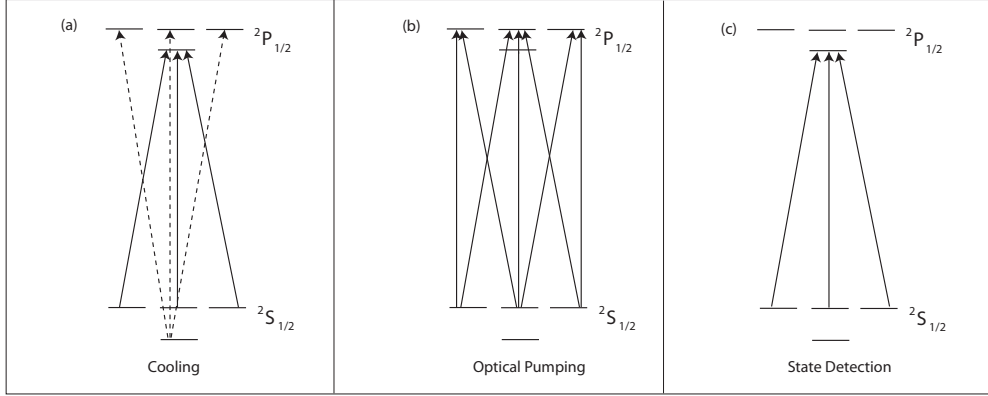


Figure 2.12: The laser frequencies present for Doppler cooling, optical pumping and state detection protocols are shown. (a) The solid lines show the carrier frequency of $c/(369.5261 \text{ nm})$ and the dashed line shows the carrier plus the sum of the two hyperfine splittings, (14.7 GHz), imparted by passing the beam through an EOM. (b) For the optical pumping routine, the laser is modulated at 2.1 GHz to couple the two $F = 1$ manifolds. We do not shown the carrier frequency here. (c) The state detection protocol used an unmodulated beam.

one detector for readout. This can be done with either a ICCD camera or an array of PMTs, but one must take care to minimize the cross-talk between detectors. One way to do this is to use a Bayesian inference method which takes into account information from neighboring detectors. For example, if detector A sees one photon and the neighboring detector B sees many photons, depending on the amount of cross-talk, the photon seen by detector A might be ascribed to the ion that is lined up with detector B instead of assuming that ion A emitted a photon. The number of photons detected by detector A and B will be labeled d_a and d_b . Using Bayes' rule, the probability that a certain distribution of detected photons, $\{d_a, d_b\}$, was produced by a pair of ions in the state $|\psi\rangle$ is,

$$P(|\psi\rangle|d_a, d_b) = \frac{P(d_a, d_b||\psi\rangle)P(|\psi\rangle)}{\sum_{\mu, \nu} P(d_a, d_b||\mu\nu\rangle)P(|\mu\nu\rangle)}, \quad (2.36)$$

where the sum is over all possible spin states of the two ions. In order to calculate $P(d_a, d_b || \psi\rangle)$ we need to know the probability of a single ion emitting N photons and the probability that a single photon emitted by ion A will be detected by detector B. We define the probability of a single ion in the state $|\mu\rangle$ emitting N photons as $P(\mu, N)$, the probability of a detected photon being seen by the wrong detector as P_w and the probability of a detected photon being seen by the correct detector as P_c . If $|\psi\rangle = |\mu\nu\rangle$, then,

$$P(d_a, d_b || \mu\nu\rangle) = \sum_{j=0}^{d_a+d_b} \sum_{i=0}^j P(\mu, j) P(\nu, d_a+d_b-j) P_w^{d_a+2i-j} P_c^{d_b-2i+j} \binom{j}{i} \binom{d_a+d_b-j}{d_b+i-j}. \quad (2.37)$$

The index j represents how many photons ion A contributed to the total number seen and the index i represents how many of those were detected by the detector aligned with ion B. Using these definitions, one can easily see that the first binomial coefficient comes from the multiplicity of the photons emitted from ion A seen by detector B, while the second binomial coefficient is the multiplicity of the photons from ion B seen by detector A.

As a numerical test of this detection method, we can calculate the expected state detection error for an ideal system of two ions and two detectors. For simplicity, we will assume that an ion generates a Poisson distribution in the number of detected photons in an ensemble of experiments with the average number of photons for the dark state being 0.01 and 10 for the bright state, which resembles the situation in for $^{171}\text{Yb}+$ in the sense that the optimal discriminator choice is to assign $|0\rangle$ to the events where 0 or 1 photons are detected and $|1\rangle$ to all other events. By choosing

Poisson distributions, the overlap of the two distributions is smaller than what is actually the case and therefore the single ion state detection is more efficient, but it should be sufficient for demonstrating the power of Bayesian inference in suppressing crosstalk errors. For the numerical simulation, we assume that the system is perfectly calibrated in the sense that the probability of a photon emitted from ion A was detected by the wrong detector is known and equal to the probability of a photon from ion B being detected by the wrong detector. As an example, we can calculate the likelihood that one dark ion and one bright ion would result in n photons being seen by detector A and 10 photons being seen by detector B. As shown in fig. 2.13, in the case of 10% detector crosstalk, the Bayesian method tells us that unless detector A sees 5 or more photons, the best bet is to say that the measurement record was generated by ion A being in the dark state and ion B being in the bright state. This particular case would contribute to the overall state detection error by $\frac{1}{4}(P(2, 5||01) + P(3, 5||01) + P(4, 5||01)) = 0.004$ with the factor of $1/4$ coming from there being 4 basis states in the case of two qubits. However, this calculation of the error for the discriminator method is an overestimate since the optimal cutoff for a single ion is not necessarily the same as the optimal cutoff for two ions in the presence of cross talk. By summing over all possible photon count records and picking out the events that result in a state detection error, the optimal discriminator can be chosen. In the case of 10% crosstalk, the state detection is optimized when $|0\rangle$ is assigned to all events that register less than 4 photons. By summing over all possible photon records, the optimized discriminator method is found to result in an error rate of 2.5% while the Bayesian inference method results

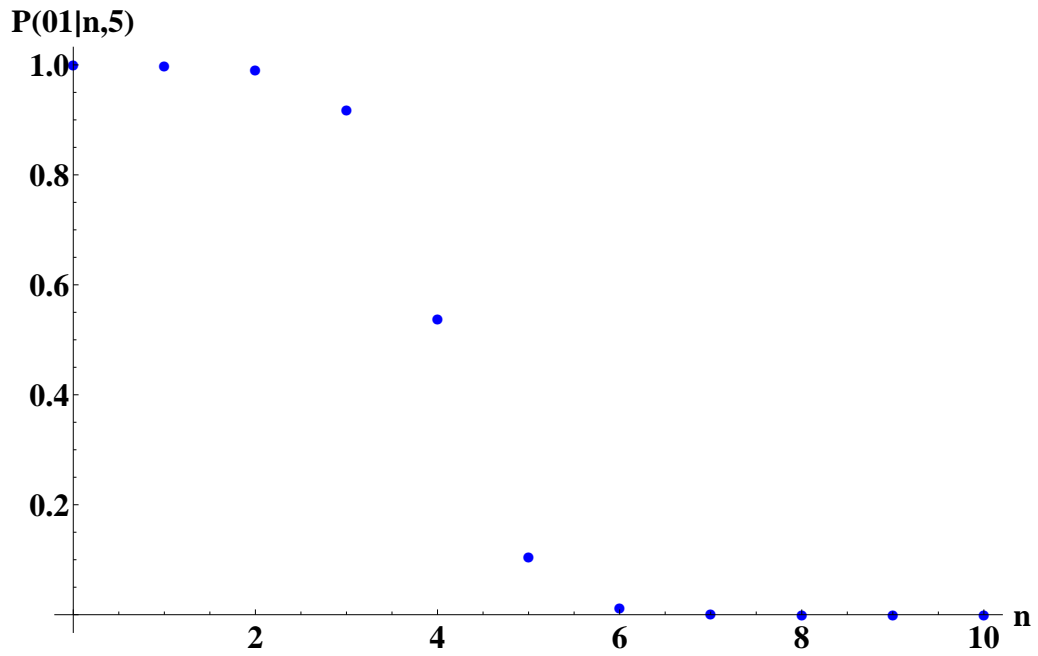


Figure 2.13: A plot of $P(|01\rangle|n, 5)$ as defined by Eq. (2.36) and Eq. (2.37). This calculation assumes Poisson distributions for the individual ion photon distributions and that 10% of the photons generated by each ion are detected by the wrong detector. As seen in the plot, when detector B registers 5 photons, the best bet for the state of the ions is $|01\rangle$ when detector A registers fewer than 5 photons.

in an error rate of 1.6%. See [49, 50, 51] for related methods of state detection using spatio and temporal photon distribution information.

2.2.3 Qubit rotations with resonant microwaves

Single qubit rotations can easily be achieved through the application of microwaves near the resonant frequency 12.6 GHz. If we consider a single qubit interacting with a monochromatic source of microwaves, the Hamiltonian is given by,

$$H_0 = -\frac{\omega_0}{2}\sigma_z + \mu B \cos(\omega_\mu t + \phi)(|0\rangle\langle 1| + |1\rangle\langle 0|), \quad (2.38)$$

where the units are chosen such that $\hbar = 1$. By transforming to the interaction picture, the Hamiltonian becomes,

$$H_1 = \frac{\mu B}{2}(e^{-i((\omega_0 - \omega_\mu)t + \phi)}|0\rangle\langle 1| + e^{i((\omega_0 - \omega_\mu)t + \phi)}|1\rangle\langle 0|), \quad (2.39)$$

where we have taken advantage of the rotating wave approximation. The dynamics can now be solved for easily by transforming to yet another frame where the Hamiltonian takes the time-independent form,

$$H_2 = -\frac{\omega_0 - \omega_\mu}{2}\sigma_z + \frac{\mu B}{2}(\cos(\phi)\sigma_x - \sin(\phi)\sigma_y) \quad (2.40)$$

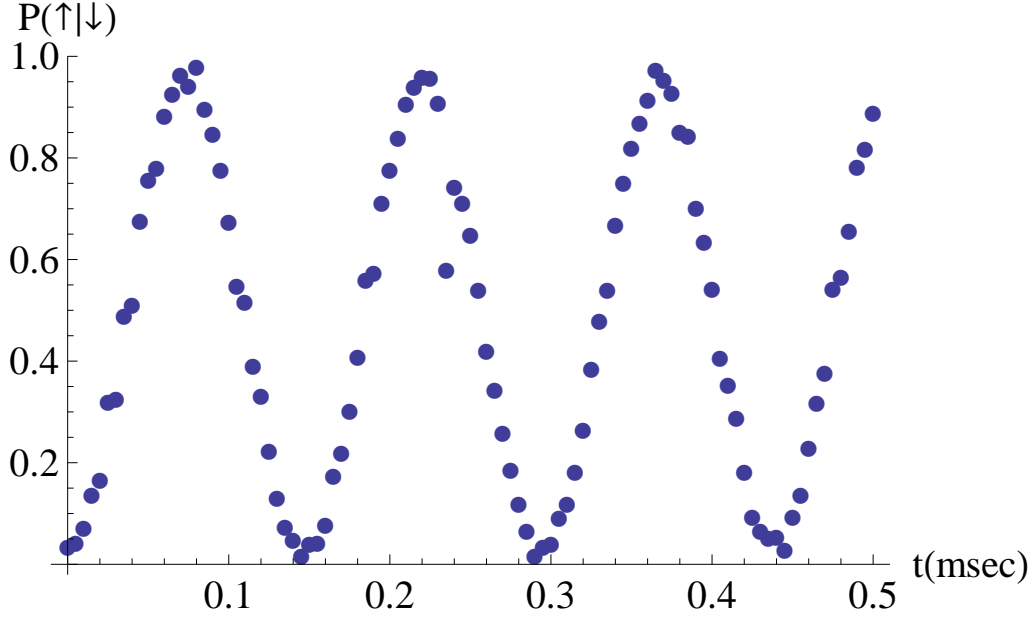


Figure 2.14: The data shows the evolution of $\langle |\uparrow\rangle\langle\uparrow| \rangle$ as a function of the time resonant microwaves are directed toward trapped $^{171}\text{Yb}^+$ after initializing the state to $|\downarrow\rangle\langle\downarrow|$.

Defining $\delta \equiv \omega_0 - \omega_\mu$, $\Omega \equiv \mu B$ and $\sigma_\phi \equiv \cos(\phi)\sigma_x - \sin(\phi)\sigma_y$, the rotation axis σ_r and Rabi frequency $\tilde{\Omega}$, is given by,

$$\sigma_r = \frac{\delta\sigma_z + \Omega\sigma_\phi}{\sqrt{\delta^2 + \Omega^2}} \quad (2.41)$$

$$\tilde{\Omega} = \sqrt{\delta^2 + \Omega^2}, \quad (2.42)$$

and the evolution operation is then given by,

$$U_2 = e^{-i\frac{\tilde{\Omega}t}{2}\sigma_r}. \quad (2.43)$$

The decoherence of the qubit states can be related to fluctuations in the local

magnetic field by considering the Hamiltonian $H = -\frac{\omega_0 + \omega_\Delta(t)}{2}\sigma_z$ where the constant frequency $\omega_0 = 2\pi\nu_0$ and the fluctuating $\omega_\Delta(t)$ is determined by the magnetic field. Since the change in the splitting is proportional to the square of the magnetic field, we can estimate the change in the splitting as $\omega_\Delta(t)/2\pi = 310B^2 \text{ Hz} \approx 310(B_0^2 + 2B_0\Delta B(t))$ where we have ignored the presumably small term proportional to $\Delta B(t)^2$. To keep the notation simple, we can add the constant contribution from the magnetic field to ω_0 and redefine $\omega_\Delta(t)$ to only include the time dependent fluctuations of the magnetic field. Because the Hamiltonian describing this situation commutes with itself at different times, only one term in the Magnus expansion is non-zero and the time evolution operator is given by,

$$U = e^{\frac{i}{2} \int_0^t dt' (\omega_0 + \Delta\omega(t'))\sigma_z}. \quad (2.44)$$

If the qubit is prepared in superposition state $|\psi\rangle = (|0\rangle + |1\rangle)/\sqrt{2}$, then the time evolved state is given by,

$$\rho(t) = U |\psi\rangle \langle\psi| U^\dagger \quad (2.45)$$

$$= \frac{1}{2} (|0\rangle \langle 0| + |1\rangle \langle 1|) \quad (2.46)$$

$$+ e^{-i(\omega_0 t + \int_0^t dt' \Delta\omega(t'))} |0\rangle \langle 1| + e^{i(\omega_0 t + \int_0^t dt' \Delta\omega(t'))} |1\rangle \langle 0| \quad (2.47)$$

The last expression is only true in the context of a single experiment. In order to calculate a density matrix that is useful for describing the state made in the lab, we need to calculate an ensemble average. Before taking the ensemble average, the

expression can be simplified by going to a frame that rotates at ω_0 through the unitary $U_0 = e^{i\frac{\omega_0}{2}\sigma_z}$. In the rotating frame the density matrix is given by,

$$\tilde{\rho} = \frac{1}{2} (|0\rangle\langle 0| + |1\rangle\langle 1| + \langle e^{-i\int_0^t dt' \Delta\omega(t')} \rangle |0\rangle\langle 1| + \langle e^{i\int_0^t dt' \Delta\omega(t')} \rangle |1\rangle\langle 0|) \quad (2.48)$$

If the random acquired phase $\phi(t) = \int_0^t dt' \Delta\omega(t')$ has a Gaussian distribution, then the density matrix can be written as,

$$\tilde{\rho} = \frac{1}{2} (|0\rangle\langle 0| + |1\rangle\langle 1| + e^{-\frac{1}{2}\langle \phi(t)^2 \rangle} (|0\rangle\langle 1| + |1\rangle\langle 0|)) \quad (2.49)$$

If the noise is Gaussian, the ensemble average is given by [52],

$$\langle \phi(t)^2 \rangle = \int_0^t dt_1 \int_0^t dt_2 \langle \Delta\omega(t_1)\Delta\omega(t_2) \rangle. \quad (2.50)$$

In the case of a white noise spectrum, the noise is delta correlated, i.e. $\langle \Delta\omega(t_1)\Delta\omega(t_2) \rangle = \gamma\delta(t_1 - t_2)$, where γ is the standard deviation of $\Delta\omega$ from zero. This implies that the coherence decays exponentially in time with a rate given by the standard deviation of $\Delta\omega$.

The coherence time of our clock qubit is measured by performing a Ramsey experiment using coherent microwaves. If two near resonant microwave pulses are applied sequentially with a time delay between them, the pulses will add constructively when the time delay is equal to an integer multiple of the inverse of the detuning. However, the qubit splitting or the phase of the microwaves are fluctuating randomly, this Ramsey oscillation will decay. Fig. 2.15 shows that a microwave

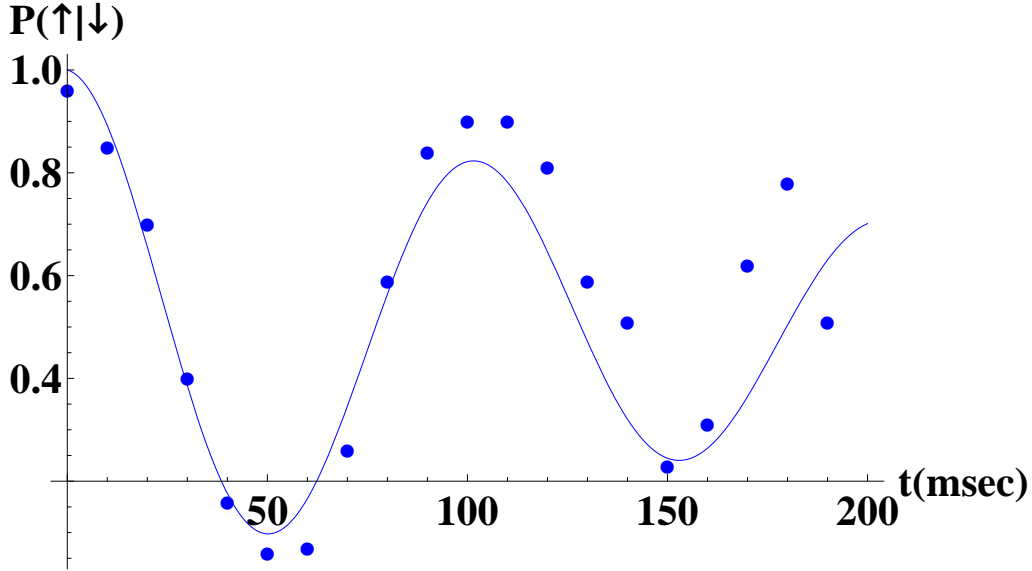


Figure 2.15: By applying two $\pi/2$ microwave pulses near resonance with a variable delay t between them reveals a coherence time of approximately 200 msec. This coherence time is likely due to phase noise on the microwave source as opposed to fluctuations in the qubit splitting [47]. The function that is fit to the data assumes an exponential decay.

Ramsey experiment with a single ion reveals a coherence time of approximately 200 msec. As shown in [47], these measurements are typically limited by phase noise in the microwave source which can be eliminated in an experiment that uses two ions in separate traps and compares the parity of the two ions to reveal a coherence time of 2.5 sec, which is probably limited by differential magnetic field noise.

2.3 Multiple Ions

When multiple ions are in the trap, the mutual repulsive Coulomb interactions must be considered in the potential energy of the system,

$$V(r_i) = \sum_{i=1}^N \sum_{j=1}^3 \frac{m\omega_j^2}{2} x_j^2 + \frac{1}{2} \sum_{i,j=1, i \neq j}^N \frac{e^2}{|r_i - r_j|}. \quad (2.51)$$

The motion of the collection of particles is commonly described by assuming the ions can be cooled down to a temperature such that the ions do not move far from the positions that minimize the energy of the system. In that regime, the forces felt by the ions can be linearized by expanding the potential about the equilibrium positions. If $\frac{\omega_{x,y}}{\omega_z} > 0.73N^{0.86}$, where N is the number of ions in the trap, the ions will tend to line up in the z direction when they are cooled to low temperatures [53]. For the case of two Yb^+ ions, the equilibrium positions are $(0, 0, \pm l)$, where we have introduced the length scale $l^3 = e^2/4m\omega_z^2$. This implies that two ions in a trap with a 300 kHz axial frequency will be about $7.7 \mu\text{m}$ apart and about $3.4 \mu\text{m}$ apart for a 1 MHz trap. The ions' displacement coordinates from these equilibrium positions, \vec{r}_i , are defined as,

$$\vec{R}_1(t) = (0, 0, -l) + \vec{r}_1(t) \quad (2.52)$$

$$\vec{R}_2(t) = (0, 0, l) + \vec{r}_2(t) \quad (2.53)$$

$$\vec{r}_i = x_i\hat{x} + y_i\hat{y} + z_i\hat{z}. \quad (2.54)$$

We then linearize the Coulomb interaction by considering the force of repulsion between the two ions,

$$\vec{F}_c = \frac{e^2}{(\vec{R}_1 - \vec{R}_2)^3}(\vec{R}_1 - \vec{R}_2) \quad (2.55)$$

Now we introduce the vector $\vec{D} = \vec{R}_1 - \vec{R}_2 = (D_x, D_y, D_z)$ and expand the force components around the point $\vec{D}_0 = (0, 0, -2l)$.

$$F_c^x = \frac{e^2}{(D_x^2 + D_y^2 + D_z^2)^{3/2}} D_x \quad (2.56)$$

$$= \frac{e^2}{(2l)^3} (x_1 - x_2) + \dots \quad (2.57)$$

$$F_c^y = \frac{e^2}{(D_x^2 + D_y^2 + D_z^2)^{3/2}} D_y \quad (2.58)$$

$$= \frac{e^2}{(2l)^3} (y_1 - y_2) + \dots \quad (2.59)$$

$$F_c^z = \frac{e^2}{(D_x^2 + D_y^2 + D_z^2)^{3/2}} D_z \quad (2.60)$$

$$= \frac{e^2}{(2l)^2} - 2 \frac{e^2}{(2l)^3} (z_1 - z_2) \dots \quad (2.61)$$

We see that to lowest order the three spatial dimensions are not coupled to each other and can be analyzed separately. If we transform to a coordinate system such that $\tilde{z}_1(t) = -l + z_1(t)$ and $\tilde{z}_2(t) = l + z_2(t)$ so that z_1 and z_2 are just the excursions from the equilibrium points, then we can write Newton's second law in simple matrix form,

$$m \frac{d^2}{dt^2} \begin{pmatrix} z_1 \\ z_2 \end{pmatrix} = \begin{pmatrix} -m\omega_z^2 - \frac{e^2}{4l^3} & \frac{e^2}{4l^3} \\ \frac{e^2}{4l^3} & -m\omega_z^2 - \frac{e^2}{4l^3} \end{pmatrix} \begin{pmatrix} z_1 \\ z_2 \end{pmatrix}. \quad (2.62)$$

The normal modes, b_i^j , can be found by assuming their dynamics are described by simple harmonic motion so that they have the form,

$$b_z^j = e^{\pm i\omega_{z,j}t} \begin{pmatrix} \mu_j \\ \nu_j \end{pmatrix}, \quad (2.63)$$

where μ_j and ν_j are constants. If this simple time dependence is assumed then Eq. (2.62) can be recast as an eigenvalue equation. Remembering that $e^2/4ml^3 = \omega_z^2$, the eigensystem is found to be,

$$b_z^1 = \frac{e^{\pm i\omega_z t}}{\sqrt{2}} \begin{pmatrix} 1 \\ 1 \end{pmatrix} \quad b_z^2 = \frac{e^{\pm i\sqrt{3}\omega_z t}}{\sqrt{2}} \begin{pmatrix} 1 \\ -1 \end{pmatrix}. \quad (2.64)$$

In general, the solution is described by superposing the \pm solutions in order to fit the initial conditions. The equations for x are given by,

$$m \frac{d^2}{dt^2} \begin{pmatrix} x_1 \\ x_2 \end{pmatrix} = \begin{pmatrix} -m\omega_x^2 + \frac{e^2}{8l^3} & -\frac{e^2}{8l^3} \\ -\frac{e^2}{8l^3} & -m\omega_x^2 + \frac{e^2}{8l^3} \end{pmatrix} \begin{pmatrix} x_1 \\ x_2 \end{pmatrix}, \quad (2.65)$$

and the eigensystem is found to be,

$$b_x^1 = \frac{e^{\pm i\omega_{x,1} t}}{\sqrt{2}} \begin{pmatrix} 1 \\ 1 \end{pmatrix} \quad b_x^2 = \frac{e^{\pm i\omega_{x,2} t}}{\sqrt{2}} \begin{pmatrix} 1 \\ -1 \end{pmatrix}, \quad (2.66)$$

where $\omega_{x,1} = \omega_x$ and $\omega_{x,2} = \sqrt{\omega_x^2 - \omega_z^2}$. The eigenmodes of motion in the y direction are identical in form to that of the x direction. The symmetric mode is referred to as the center-of-mass mode, while the antisymmetric mode is referred to as the breathing mode when describing the axial motion and is referred to as the tilt mode when describing the transverse motion. See fig. 2.16 for an illustration of these eigenmodes.

In finding the general mode structure of a linear chain of N ions, we follow

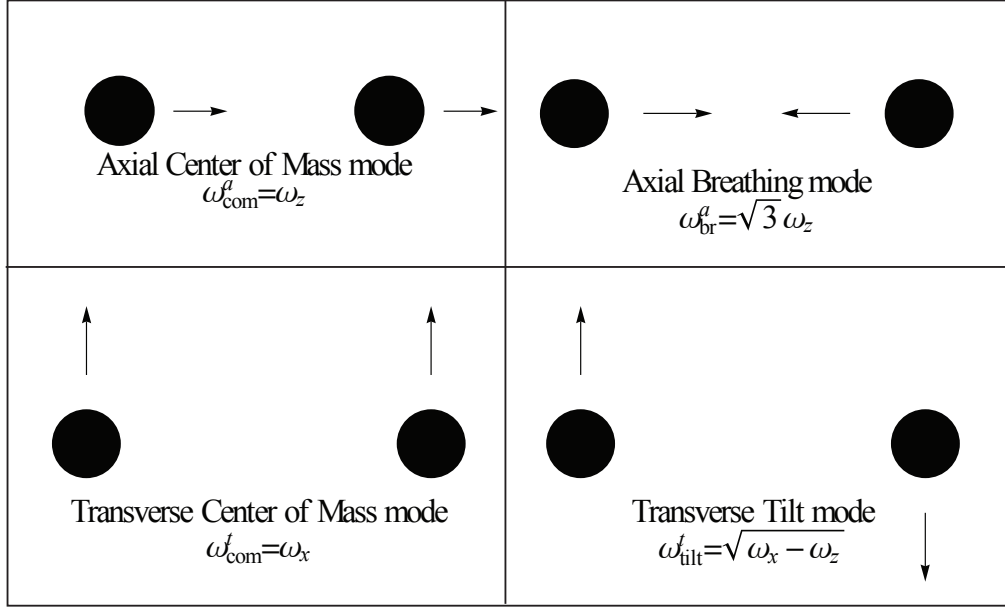


Figure 2.16: The illustrations show the relative motion of two ions in their normal modes of motion along with the characteristic frequencies of those modes.

the notation used in [54] and start by solving for the equilibrium positions given the potential in Eq. (2.51). By assuming that the ions line up along the z direction in their ground state, the gradient of the potential with respect to each ion's z coordinate gives N expressions for the net force felt by each ion. By setting the net force of each ion to be zero, the set of N coupled algebraic equations that must be satisfied is,

$$u_j - \sum_{n=1}^{j-1} \frac{1}{(u_j - u_n)^2} + \sum_{n=j+1}^N \frac{1}{(u_j - u_n)^2} = 0, \quad (2.67)$$

where u_j is the position of the j^{th} ion in units of $l = (e^2/4m\omega_z^2)^{1/3}$. The normal modes of motion can then be found by expanding the potential about these equilibrium

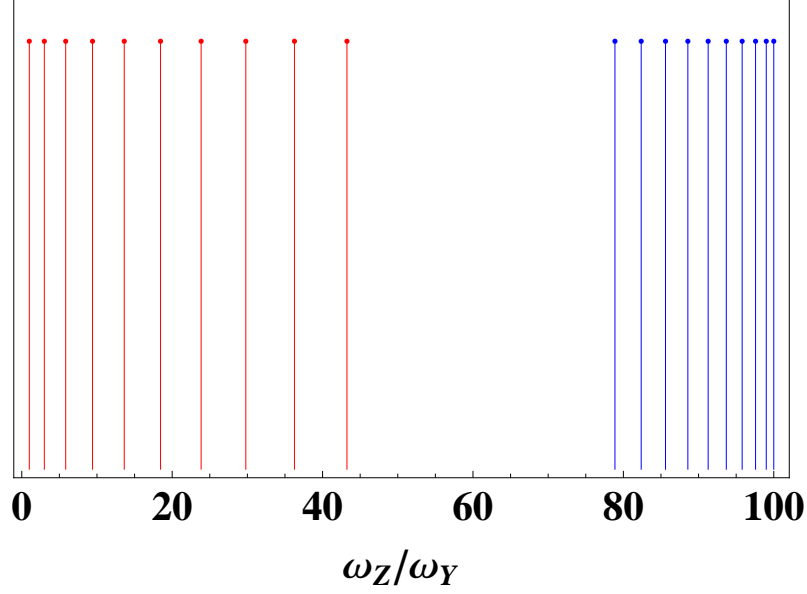


Figure 2.17: The figure shows the mode structure for 10 ions with the axial modes represented in red and the transverse modes represented in blue. The lowest frequency mode is the axial center-of-mass mode, while the highest frequency mode is the transverse center-of-mass mode.

positions and finding the eigenvectors and eigenvalues of the matrix defined by,

$$A_{n,j}^{\xi} = \begin{cases} \epsilon_{\xi}^2 + \sum_{p=1, p \neq j}^N a_{\xi} / |u_j - u_p|^3 & (n = j) \\ -a_{\xi} / |u_j - u_n|^3 & (n \neq j) \end{cases}, \quad (2.68)$$

where $\epsilon_{\xi} = \omega_{\xi} / \omega_z$, $a_x = a_y = -1$, and $a_z = 2$ and the eigenfrequencies being $\omega_{\xi,k} = \sqrt{\lambda_{\xi,k}} \omega_{\xi}$ where $\lambda_{\xi,k}$ are the eigenvalues of A^{ξ} . The mode structure for a 10 ion crystal is shown in Fig. 2.17.

The description of the ion crystal through the normal modes of motion provides an elegant means for understanding how control over a large collection of ions might be possible. However, it also presents a challenge in terms of the scalability of ion crystals to the large numbers that are needed for quantum information processors. As can be seen in Fig. 2.17, the addition of more ions will lead to spectral crowding

that will eventually make addressing single modes of motion difficult from a practical point of view. This problem is, in principle, able to be circumvented by using a modular architecture as described in the first chapter of this thesis.

We conclude this chapter with a table useful experimental parameters for $^{171}\text{Yb}+$ shown in table 2.2.

Parameter	Expression	Value
Doppler temperature	$\frac{\hbar\Gamma}{2k_b}$	470 μK
Recoil energy	$\frac{\hbar k^2}{4\pi m}$	8.5 kHz
Saturation Intensity	$\frac{\pi\hbar c\Gamma}{2\lambda^3 R_{br}}$	51 mW/cm ²
Ground state localization	$\sqrt{\frac{\hbar}{2m\omega}}$	$\frac{5 \text{ nm}}{\sqrt{\omega/2\pi(\text{MHz})}}$
Thermal state localization	$\sqrt{\frac{\hbar\Gamma}{2m\omega^2}}$	$\frac{24 \text{ nm}}{\omega/2\pi(\text{MHz})}$
Ion spacing	$2\left(\frac{e^2}{4m\omega^2}\right)^{1/3}$	$\frac{3.5 \mu\text{m}}{(\omega/2\pi(\text{MHz}))^{2/3}}$

Table 2.2: A table of relevant parameters for $^{171}\text{Yb}+$. Note that the parameter R_{br} that appears in the saturation intensity is the branching ratio from $^2\text{P}_{1/2}$ to $^2\text{S}_{1/2}$, which is ≈ 0.995 . It should also be noted that this formula for the saturation intensity assumes a two level atom and ignores the hyperfine and Zeeman structure. The formula given for the localization of an ion in a thermal state is derived by assuming the Doppler temperature, expanding Eq. (2.29) around $\beta\hbar\omega = 0$ and keeping only the leading term.

Chapter 3

Control through Raman transitions

3.1 Stimulated Raman transitions driven by an optical frequency comb

A natural approach toward coherent entangling interactions among neighboring ions is to use the strong Coulomb force shared between them. In order to generate entanglement between spins using the position dependent Coulomb interaction, one must engineer a control set capable of addressing and entangling the spin and motional degrees of freedom. This approach was pioneered in [19] Cirac and Zoller in which they proposed using the shared collective motion of the ions as a quantum data bus between separated qubits. In this chapter, I will review how these forces can be made using stimulated Raman transitions and how they can be implemented using a mode-locked pulsed laser. Many of the results reviewed in this chapter were presented in [55].

3.1.1 Raman Transitions in a three-level atom using a single pulse train

As shown in the previous chapter, the qubit state can be controlled through the application of the electromagnetic radiation tuned to the resonance frequency of the

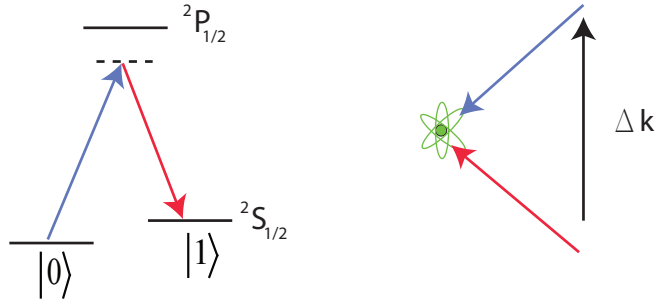


Figure 3.1: The two hyperfine levels in the ground state can be coupled by two phase locked laser beams whose beat note is equal to the qubit energy splitting. The momentum transfer in such a transition is proportional to the difference in the two wavevectors Δk .

qubit splitting. The absorption of microwave photons does impart a momentum kick to the ion, but the coupling as quantified by the Lamb-Dicke parameter, $\eta = kx_0 = \frac{2\pi}{\lambda} \sqrt{\frac{\hbar}{2m\omega}}$ is on the order of 10^{-6} for a 1 MHz trap. The coupling to the motional degree of freedom can be enhanced by many orders of magnitude by using a two photon transition that employs optical photons. In a lambda system, a coupling between the two ground states can be engineered by applying two phase locked laser beams that have a beat note equal to the ground state energy splitting as depicted in fig. 3.1. Because this is a two photon process, the coupling parameter η is proportional to the difference in wave vectors of the two photons. If, for example, the two beams are counter propagating and have a wavelength that is close to the $^2S_{1/2} \leftrightarrow ^2P_{1/2}$ transition, the Lamb-Dicke parameter is on the order of 10^{-1} . High fidelity qubit operations through Raman transitions are typically achieved by either phase locking two monochromatic lasers or by modulating a single cw laser with an AOM or an EOM. However, the technical demands of phase-locked lasers and the limited bandwidths of the modulators hinder their application to experiments.

By using a pulsed laser, we can exploit the large bandwidth to easily bridge large frequency gaps to gain control over complex atomic systems.

In driving transitions between hyperfine levels using optical fields, one must consider the coupling to the excited ${}^2P_{1/2}$ and ${}^2P_{3/2}$ states. However, most of the important physics can be gleaned from a much simpler analysis which only considers the coupling to one of these excited states. We start this chapter with a derivation of the effective Hamiltonian that arises from the mutual coupling of the qubit states to only one excited state through an interaction with a mode-locked pulsed laser.

In the regime where a single pulse has a negligible effect on the ion, we consider an ideal train of N pulses that produce an electric field at a fixed point in space described by,

$$E(t) = \sum_{n=0}^{N-1} f(t - nT - t_0) e^{i\omega_c t}. \quad (3.1)$$

We have ignored any carrier-envelope phase shift [56] since, as we will see, this phase is irrelevant for a two photon transition. The frequency domain picture is captured by the non-unitary Fourier transform of Eq. (3.1).

$$\mathcal{F}[f(t)] = \int_{-\infty}^{\infty} dt e^{-i\omega t} f(t) \quad (3.2)$$

$$\tilde{E}(\omega) = \int_{-\infty}^{\infty} dt e^{-i\omega t} \sum_{n=0}^{N-1} f(t - nT - t_0) e^{i\omega_c t} \quad (3.3)$$

$$= \sum_{n=0}^{N-1} e^{-i(\omega - \omega_c)(nT + t_0)} \tilde{f}(\omega - \omega_c) \quad (3.4)$$

In the limit of an infinite number of pulses, a simple picture arises with the help of

the following identity,

$$\sum_{n=-\infty}^{\infty} e^{-in\omega T} = \omega_r \sum_{k=-\infty}^{\infty} \delta(\omega - k\omega_r) \quad (3.5)$$

$$\omega_r = \frac{2\pi}{T} \quad (3.6)$$

$$\nu_r = \frac{1}{T}, \quad (3.7)$$

where ν_r is the repeating frequency of the laser. Therefore, the pulsed laser produces the following spectrum;

$$\tilde{E}^{(0)}(\omega) = \lim_{N \rightarrow \infty} \tilde{E}(\omega) = \tilde{f}(\omega - \omega_c) \omega_r \sum_{k=-\infty}^{\infty} \delta(\omega - \omega_c - k\omega_r) \quad (3.8)$$

Eq. (3.8) describes a frequency comb whose envelope function $\tilde{f}(\omega)$ is centered around the carrier frequency ω_c . Note that there is an offset frequency given by $\omega_c \bmod \omega_r$. The inverse Fourier transform of Eq. (3.8) gives,

$$\mathcal{F}^{-1}[\tilde{f}(\omega)] = \frac{1}{2\pi} \int_{-\infty}^{\infty} d\omega e^{i\omega t} \tilde{f}(\omega) \quad (3.9)$$

$$E^{(0)}(t) = \sum_{k=-\infty}^{\infty} E_k e^{i\omega_k t} e^{-i(\omega_k - \omega_c)t_0} \quad (3.10)$$

$$E_k \equiv \frac{\omega_r}{2\pi} \tilde{f}(\omega_k - \omega_c) \quad (3.11)$$

$$\omega_k \equiv \omega_c + k\omega_r \quad (3.12)$$

Eq. (3.10) is just the infinite pulse train written as a Fourier series. This expression can now be used to describe the dynamics in a lambda system driven by a long pulse train. Consider the Hamiltonian describing a three-level atom interacting with the

pulsed laser,

$$i\hbar\frac{\partial}{\partial t}\psi = H\psi \quad (3.13)$$

$$H = H_0 + H_{int}(t) \quad (3.14)$$

$$H_0 = \hbar \begin{pmatrix} \omega_1 & & \\ & \omega_2 & \\ & & \omega_3 \end{pmatrix} \quad (3.15)$$

$$H_{int}(t) = -\mu(r) \cdot E(t) \quad (3.16)$$

$$H = H_0 - \sum_k \mu \cdot E_k \text{Re} [e^{i\omega_k t} e^{-i(\omega_k - \omega_c)t_0}], \quad (3.17)$$

where $\omega_1 < \omega_2 \ll \omega_3$ and $\mu(r)$ is the atomic dipole operator. A complete solution to the Schrödinger equation with this Hamiltonian can be studied using multi-mode Floquet theory [57], but I will restrict the following analysis to the perturbative regime. Since the Raman transitions use the excited P states to establish a coupling between the qubit states, it is important to use a far-detuned light source in order to avoid building up significant population in the unstable electronic level where spontaneous emission of a photon can erase the quantum information in the qubit and even carry the atom out of the computational states. While detuning the laser from resonance results in a weaker coupling between the qubit states, it will be shown that the relative strength of this coupling as compared to the rate of spontaneous emission grows favorably with larger detunings. In the regime where the optical fields are tuned far enough off resonance as to only establish a minuscule population in the excited electronic state, the dynamics are accurately described by an effective

Hamiltonian that couples the qubit states directly. In this section, I will follow the method outlined in ref. [58]. For a Hamiltonian that can be written in the following way,

$$H_I = \sum_{n=1}^M \hat{h}_n e^{-i\omega_n t} + \hat{h}_n^\dagger e^{-i\omega_n t}, \quad (3.18)$$

it can be shown that second order perturbation theory predicts the following effective Hamiltonian,

$$H_{eff} = \sum_{n,m=1}^M \frac{1}{\hbar\bar{\omega}_{m,n}} \left[\hat{h}_m^\dagger, \hat{h}_n \right] e^{i(\omega_m - \omega_n)t} \quad (3.19)$$

$$\frac{1}{\bar{\omega}_{m,n}} = \frac{1}{2} \left(\frac{1}{\omega_m} + \frac{1}{\omega_n} \right). \quad (3.20)$$

Using the Hamiltonian describing the interaction between the frequency comb and the three level atomic system, the commutators in Eq. (3.19) generate four distinct operators, $|3\rangle\langle 3| - |1\rangle\langle 1|$, $|3\rangle\langle 3| - |2\rangle\langle 2|$, $|2\rangle\langle 1|$ and $|1\rangle\langle 2|$. The first and second operators describe Stark shifts while the third and fourth describe the coupling between the qubit states. If we ignore the Stark shift terms for now, the effective Hamiltonian is,

$$H_{eff} = -\frac{\mu^2}{4} \sum_{m,n=1}^{M/2} \frac{1}{\hbar\bar{\omega}_{m,n}} \tilde{E}_m \tilde{E}_n (|2\rangle\langle 1| e^{i(\omega_m - \omega_n)t} e^{-i(m-n)\omega_r t_0} \quad (3.21)$$

$$+ |1\rangle\langle 2| e^{-i(\omega_m - \omega_n)t} e^{i(m-n)\omega_r t_0}) \quad (3.22)$$

$$\omega_m = \Delta - \omega_r(k_0 - m + 1) \quad (3.23)$$

$$\omega_n = \Delta - \omega_{hf} - \omega_r(k_0 - n + 1), \quad (3.24)$$

where $\Delta = \omega_3 - \omega_c$ and k_0 is an artificial cut off imposed by the bandwidth of the laser. In writing these expressions, I have set ω_1 to be “sea-level,” i.e. $\omega_1 = 0$ and $\omega_2 = \omega_{hf}$. The sum in Eq. (3.18) is assumed to be finite in the derivation of Eq. (3.19), which is naturally imposed by the finite bandwidth of the laser that restricts the number of significant comb teeth. Even this effective Hamiltonian would require multi-mode Floquet theory for an exact solution, but an approximate solution can be found by considering the resonant terms where the time-dependence in the exponential functions vanishes. These so called stationary terms are picked out by requiring $\omega_m - \omega_n = 0$, which implies that the ratio $\frac{\omega_{hf}}{\omega_r} \equiv q$ is an integer. This is simply the mathematical description of the physical requirement that the two-photon Raman transition can only be driven if there exists optical frequency differences that match the energy difference of the qubit states. The stationary terms can then be picked out of the sum by inserting a Kronecker delta function $\delta_{m,n-q}$, in which case the effective Hamiltonian is reduced to,

$$H_{eff} \approx -(|2\rangle\langle 1|e^{iq\omega_r t_0} + |1\rangle\langle 2|e^{iq\omega_r t_0}) \sum_n^{M/2} \frac{\mu}{4\hbar\bar{\omega}_{n,n-q}} \tilde{E}_n \tilde{E}_{n-q}. \quad (3.25)$$

Eq. (3.25) shows that the effective Hamiltonian is a coupling between the qubit states, with a Rabi frequency that depends on the bandwidth of the laser and the detuning Δ while the phase of the induced rotation is determined by the arrival time of the pulse train. The sum in Eq. (3.25) is difficult to evaluate analytically, but it can be approximated by an integral if the repetition rate is small compared to the bandwidth of a single pulse. In general, the integral is difficult to evaluate

f(t)	Ω
$\sqrt{\frac{\pi}{2}} E_0 \text{sech}(\pi t/\tau)$	$\frac{\nu_r \tau \mu ^2 E_0^2}{\Delta} \frac{\omega_{hf} \tau}{e^{\omega_{hf} \tau/2} - e^{-\omega_{hf} \tau/2}}$
$\frac{E_0}{(4\pi)^{1/4}} e^{-\frac{1}{2}(\frac{t}{\tau})^2}$	$\frac{\nu_r \tau \mu ^2 E_0^2}{\Delta} e^{-(\omega_{hf} \tau)^2/4}$
$\frac{E_0}{\sqrt{2\pi}} \text{sinc}(t/\tau)$	$\frac{\nu_r \tau \mu ^2 E_0^2}{\Delta} \text{tri}(\omega_{hf} \tau/2)$

Table 3.1: This table shows different expressions for the Rabi frequency when different functional forms are chosen for the pulse envelope when evaluating Eq. (3.26) within the approximation that the sum can be replaced by an integral. The function $\text{tri}(t) \equiv \max(1 - |t|, 0)$ is the triangular distribution and τ is the characteristic time of the pulse.

for any realistic pulse shape with the exception flat-top spectrum. To simplify the expression, we can use the fact that the detuning Δ is usually large compared to both the hyperfine splitting and the bandwidth of the frequency comb and use an expansion of $\frac{1}{\bar{\omega}_{n,n-q}}$ in ω_{HF}/Δ and ω_r/Δ . The lowest order approximation is simply $\frac{1}{\bar{\omega}_{n,n-q}} \approx 1/\Delta$, allowing the following simple expression for the Rabi frequency,

$$\frac{\Omega}{2} \equiv \frac{|\mu|^2 \sum_k \tilde{E}_k \tilde{E}_{k-q}}{2\Delta}, \quad (3.26)$$

where $\Omega/2$ is defined in the same way as in Eq. (2.40). The expression for the Rabi frequency invites a simple picture of a three level system interacting with an ensemble of continuous wave lasers as illustrated in fig. 3.2. If the sum in Eq. (3.26) is approximated by an integral, analytic expressions for the Rabi frequency can be calculated in the case of several common spectra found in mode-locked pulsed lasers, some of which are shown in table 3.1. This result predicts Rabi oscillations when the repetition rate of the laser is a multiple of the qubit splitting. As an alternative to the frequency domain picture where photons are absorbed from one comb tooth

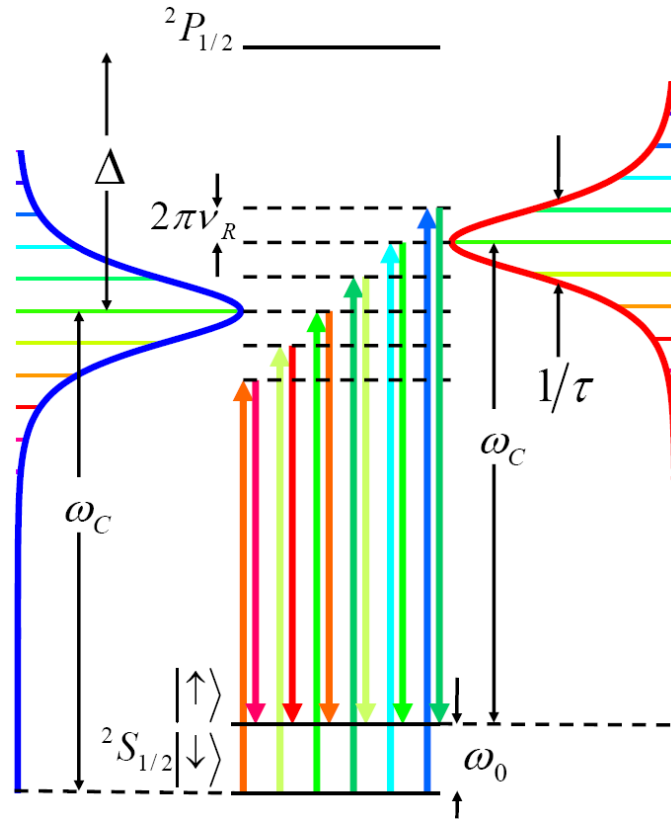


Figure 3.2: The Stokes Raman process driven by frequency combs is shown here schematically. An atom starting in $|\downarrow\rangle$ can be excited to a virtual level by absorbing a photon from the blue comb and then driven to the $|\uparrow\rangle$ state by emitting a photon into the red comb. Although drawn here as two different combs, if the pulsed laser's repetition rate or one of its harmonics is in resonance with the hyperfine frequency, the absorption and emission can both be stimulated by the same frequency comb. Because of the even spacing of the frequency comb, all of the comb teeth contribute through different virtual states which result in indistinguishable paths that add constructively.

and emitted into another, one can also think of the time domain picture. If the dynamics are confined to the qubit space, one can imagine the Bloch vector rotating on a sphere and is periodically kicked by sequential laser pulses. If the q parameter is an integer, then the Bloch vector will have the same azimuthal angle every time it is kicked by another laser pulse, allowing all of the kicks to add constructively.

This effect was demonstrated using a Ti:Sapph laser that is frequency doubled and detuned from the D_1 resonance by 9 THz so as to have a center wavelength of 373.5 nm. A thin-film polarizer followed by a $\lambda/4$ waveplate was used to prepare the beam with circular polarization so that the qubit states were coupled through the ${}^2P_{1/2}|F = 1, m_f = 1\rangle$ state. The repetition rate of the laser was measured to be 80.78 MHz, making the q parameter of the pulsed laser almost exactly a half integer. The pulse picker was then used to extinguish every other pulse, at which point the q parameter was nearly an integer and the qubit state was observed to oscillate as illustrated by the data in fig. 3.3. To tune the q parameter to be exactly on resonance, a mirror on a translation stage inside the laser cavity was adjusted by a few millimeters.

The Rabi frequency can be written in terms of the intensity of the pulse train by starting with the formula for the intensity of a monochromatic wave,

$$I = c\epsilon_0 \langle |E(t)|^2 \rangle = \frac{c\epsilon_0}{2} |E_0|^2, \quad (3.27)$$

where the average is done over one or many optical cycles and the factor of 1/2 comes from the average of \cos^2 . If the envelope of the pulse varies slowly compared

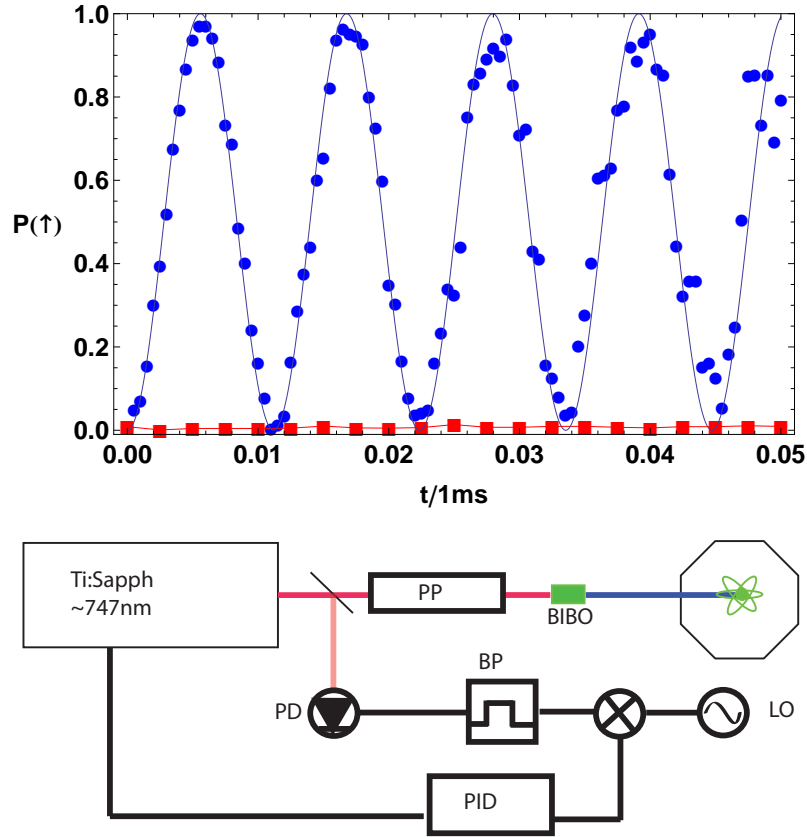


Figure 3.3: (a) The data shows the qubit evolution due to a single pulse train. The pulsed laser used in the experiment has a repetition rate of 80.78 MHz, meaning the parameter $q = 156.5$ and does not meet the resonance condition. By using a pulse picker, (PP), to extinguish every other pulse, the parameter $q = 313$ and fulfills the resonance condition and causes the qubit state to oscillate as shown by the blue circles. By only letting every third pulse through, the parameter $q = 469.5$ and is again far from resonance causing the qubit to stay in the initialized state as shown by the red squares. Each data point is the result of 300 experiments, giving a typical statistical error of ± 0.03 . (b) A Ti:Sapph laser with a center wavelength of 747 nm is doubled using a non-linear crystal and directed onto a single ion. By adjusting the cavity length inside the laser and using a pulse picker, the repetition rate is made commensurate with the qubit splitting to drive coherent Raman transitions. A small amount of the beam is picked off and directed onto a fast photodiode to generate an RF comb which is then band-pass filtered to select a single comb tooth. The comb tooth is then mixed with a stable local oscillator to generate an error signal which is then fed to a PID loop to stabilize the repetition rate of the laser via a piezo mounted behind one of the cavity mirrors inside the laser cavity. When locked, the repetition rate is stable to within 1 Hz for more than an hour.

to the optical frequency, then we should be able to write the average intensity as,

$$\bar{I} = \nu_R \frac{c\epsilon_0}{2} \int_{-\infty}^{\infty} dt |f(t)|^2. \quad (3.28)$$

Now we can write a formula for the base Rabi frequency in terms of the saturation parameter $s = I/I_{sat}$,

$$I_{sat} = \frac{\gamma^2 \epsilon_0 c}{4\mu^2} \quad (3.29)$$

$$\Omega_0 = \nu_R \tau \frac{|E_0|^2 \mu^2}{\Delta} \quad (3.30)$$

$$= \frac{\gamma^2 s}{2\Delta}, \quad (3.31)$$

where τ is the characteristic time of the pulse as shown in table 3.1. The Rabi frequency of oscillations in the qubit driven by the comb is a factor of two larger than the frequency of oscillations for the case of two cw lasers. In the cw case, if the qubit is initialized to the $|\downarrow\rangle$ state and hit with a π pulse, one of the lasers drives the atom to the excited state while the other laser drives the atom from the excited state back down to the $|\uparrow\rangle$ state. In the case of the frequency comb that is on resonance, each comb tooth can participate in both of those processes, since there is always another comb tooth that is the right distance away because of the even spacing. The frequency comb, therefore, uses the power twice as efficiently when $\frac{\omega_{hf}}{\omega_r}$ is an integer.

An estimate of the off-resonant scattering rate can be made by first calculating the population of the eliminated excited state. An alternative to the effective

Hamiltonian theory is to calculate the differential equations governing the evolution of the different states' probability amplitudes and adiabatically eliminate the excited state from the system. This approach is more cumbersome than the effective Hamiltonian theory but allows for an estimation of the excited state population. As shown in App. B, the excited state probability amplitude is approximately given by,

$$\tilde{c}_3 \approx \frac{\mu}{\Delta} \sum_k \tilde{E}_k [e^{i\omega_k t} + e^{-i\omega_k t}] (\tilde{c}_1 e^{i\omega_c t} + \tilde{c}_2 e^{i(\omega_c - \omega_{HF})t}) \quad (3.32)$$

$$\approx \frac{\mu}{\Delta} \sum_k \tilde{E}_k [e^{i\omega_k t} + e^{-i\omega_k t}] e^{i\delta t} \left((A_1 e^{i\frac{\Omega}{2}t} + B_1 e^{-i\frac{\Omega}{2}t}) e^{i\omega_c t} \quad (3.33)$$

$$+ (A_2 e^{i\frac{\Omega}{2}t} + B_2 e^{-i\frac{\Omega}{2}t}) e^{i(\omega_c - \omega_{HF})t} \right) \quad (3.34)$$

Now assume the pulses have very little overlap in order to write down an expression for the probability of being in the excited state as,

$$|\tilde{c}_3|^2 \approx 2 \left| \frac{\mu}{\Delta} \right|^2 \sum_n f^2(t - nT) [1 + \cos(2\omega_c t)] [1 + \sin(\Omega t) \sin(\omega_{HF} t)] \quad (3.35)$$

The average of this expression will be dominated by the ‘‘DC’’ term,

$$\langle |\tilde{c}_3|^2 \rangle = 2 \left| \frac{\mu}{\Delta} \right|^2 \left\langle \sum_n f^2(t - nT) \right\rangle \quad (3.36)$$

$$= 2 \left| \frac{\mu}{\Delta} \right|^2 \nu_r \int_{-\infty}^{\infty} dt f^2(t) \quad (3.37)$$

$$= 2 \left| \frac{\mu}{\Delta} \right|^2 \nu_r |E_0|^2 \tau \quad (3.38)$$

$$= 2 \frac{\Omega_0}{\Delta} \quad (3.39)$$

This result suggests a scattering rate of,

$$R_s = \frac{2\gamma}{\Delta} \Omega_0 \quad (3.40)$$

$$\Omega = \frac{\mu^2}{\Delta} \sum_k E_k E_{k-q} \quad (3.41)$$

$$= \frac{\mu^2 \nu_R}{\Delta} \tilde{f}^2(\omega_{HF}) \quad (3.42)$$

$$\frac{R_s}{\Omega} = \frac{2\gamma}{\Delta} \frac{\tilde{f}^2(0)}{\tilde{f}^2(\omega_{HF})} \quad (3.43)$$

For the hyperbolic secant pulse,

$$\frac{R_s}{\Omega} = \frac{2\gamma}{\Delta} \frac{\sinh\left(\frac{\omega_{HF}\tau}{2}\right)}{\omega_{HF}\tau/2}. \quad (3.44)$$

For a Gaussian pulse,

$$E(t) = E_0 e^{-(t/\tau)^2} \quad (3.45)$$

$$\frac{R_s}{\Omega} = \frac{2\gamma}{\Delta} e^{(\omega_{HF}\tau)^2/8}. \quad (3.46)$$

This result shows that the decoherence induced by off-resonant scattering can be suppressed by detuning the laser farther from resonance while increasing the power to maintain a given Rabi frequency.

3.1.2 Control of the $^{171}\text{Yb}^+$ clock qubit

The previous section used a simplified model in order to build intuition about the physics behind Raman transitions driven by an optical frequency comb and we

now seek to provide a more accurate description that includes the effects of both 2P states and the embedded Clebsch-Gordan structure. The Clebsch-Gordan algebra that must be considered will only result in overall scaling factors for the previously derived Rabi frequency and spontaneous scattering rate, but the inclusion of the second excited state leads to quantum interference between the different processes. The main result from the previous section is that the Rabi frequency resulting from the optical frequency comb is essentially that of the continuous wave laser case with the amplitude being proportional to the autocorrelation of the pulse spectrum evaluated at the qubit splitting. For this section, we will assume that the bandwidth of the pulse is large compared to the qubit splitting, meaning that this prefactor can be approximated as the average power in the beams. In this approximation, the Rabi frequency, Stark shifts and scattering rates for the Raman transition control using a single pulse train that is circularly polarized are given by [59],

$$\frac{\Omega}{2} = \frac{1}{3}g^2 \left(\frac{1}{\Delta} + \frac{1}{\Delta_{fs} - \Delta} \right) \quad (3.47)$$

$$\delta_0 = \frac{g^2}{12} \left(\frac{1}{\Delta} - \frac{2}{\Delta_{fs} - \Delta} \right) \quad (3.48)$$

$$\delta_1 = \frac{g^2}{12} \left(\frac{1}{\Delta + \nu_{hf}} - \frac{2}{\Delta_{fs} - \Delta - \nu_{hf}} \right) \quad (3.49)$$

$$R_s = \gamma \frac{g^2}{3} \left(\frac{1}{\Delta^2} + \frac{2}{(\Delta_{fs} - \Delta)^2} \right), \quad (3.50)$$

where g is equal to the Rabi frequency of the resonant one-photon $^2S_{1/2} \longleftrightarrow ^2P_{3/2}$ transition and Δ_{fs} is the fine-structure splitting. The ratio of this Rabi frequency to scattering rate is identical to the ratio of Eq. (3.44) and Eq. (3.46) in the

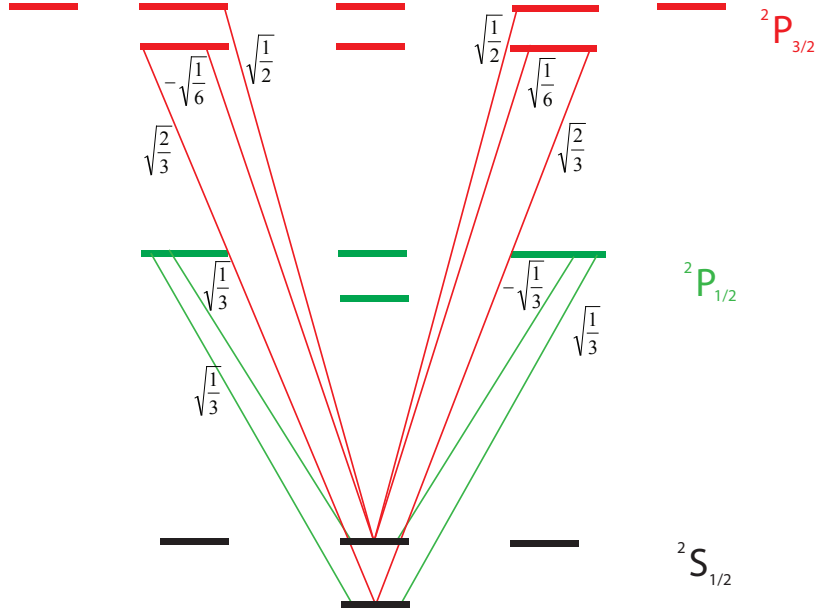


Figure 3.4: Using these Clebsch-Gordon coefficients, one can easily understand the relative weights for the different excited state contributions appearing in the expressions for the Rabi frequency and Stark shifts in Eq. (3.47,3.48,3.49). The contributions from the two 2P states are equal because $\left(\sqrt{\frac{1}{3}}\right)^2 = \sqrt{\frac{2}{3}}\sqrt{\frac{1}{6}}$, noting that the $F = 2$ states do not contribute since they do not couple to $|0\rangle$. The Stark shift terms from the ${}^2P_{1/2}$ level are proportional to $\left(\sqrt{\frac{1}{3}}\right)^2$ for both qubit states whereas the contributions from the ${}^2P_{3/2}$ level are proportional to $\left(\sqrt{\frac{2}{3}}\right)^2$ and $\left(\sqrt{\frac{1}{6}}\right)^2 + \left(\sqrt{\frac{1}{2}}\right)^2$ for the qubit states $|0\rangle$ and $|1\rangle$ respectively.

limits $\Delta_{fs} \gg \Delta$ and $\omega_{hf}\tau \approx 1$. The different weights appearing in the equations for the Rabi frequency, Stark shifts and scattering rates originate from the relevant Clebsch-Gordon coefficients that are shown in fig. 3.4.

The experiments done using the Ti:Sapph laser that was detuned from the D_1 line by 9 THz are expected to have a scattering rate to Rabi frequency ratio at the 10^{-4} level. By going to a 355 nm pulsed laser system, where the laser is blue detuned from the ${}^2P_{1/2}$ state by 33 THz and red detuned from the ${}^2P_{3/2}$ state, the ratio of the of the scattering rate to Rabi frequency is approximately 10^{-6} , meaning that

spontaneous emission induced decoherence is a negligible effect in our experiments. Also, the differential AC Stark shift to Rabi frequency ratio for the 355 nm system is approximately 10^{-4} , meaning that frequency fluctuations due to changes in the laser intensity are also negligible.

3.1.3 Control of the qubit-oscillator system

Starting with the optical frequency comb provided by a mode-locked laser, linear optical elements can be used to shape the spectrum into one that is suitable to gain full control over the qubit-oscillator system. With the four different hyperfine levels in the ground state of the Ytterbium ion and the three different degrees of freedom of the oscillator system, come many different transitions that are available depending on the beam geometry. In the previous section, it was shown that Raman transitions can be driven when the repetition rate was commensurate with the energy splitting of the two states of interest. Since the repetition rate of a laser is not capable of being changed on a fast time scale, full control over the qubit-oscillator system is simplest when the optical spectrum is shaped by linear elements outside of the laser cavity. In contrast to the previous section, it will now be desirable that the repetition rate be incommensurate with any transition energy in order to isolate different transitions spectroscopically.

The simplest way to resolve the different transitions in the system is to use a single AOM that is driven at two different frequencies as shown in fig. 3.5, thereby generating two co-propagating pulse trains. In this case, the two frequency combs

seen by the ion are frequency shifted relative to one another so that the beat note between the different combs is resonant with the energy splitting of interest, meaning that the new requirement for driving a transition between the qubit states is given by $|n\omega_r + \Delta\omega_{aom}| = \omega_{hf}$ where n is an integer. This method allows for more control over the qubit since the phase of the AOM drive can now be used to choose the rotation axis for the qubit instead of the arrival time of the pulse train. However, this method can be impractical for some setups given the finite bandwidth of the AOM being used. Depending on the repetition rate, one might have to use a AOM that has a bandwidth comparable to $\omega_r/2$. To demonstrate this control setup, we use a 355 nm pulsed laser system called the Vanguard, which was manufactured by Spectra-Physics. The Vanguard laser used in this setup has a repetition rate of 80.566 MHz and is capable of producing 3.5 W of average power. The repetition rate of this laser is such that the single AOM can be driven near 77.58 MHz and 71.48 MHz to generate the correct beat note since $157 \times 80.566 + (71.48 - 77.58) = \omega_{hf}/2\pi$. As shown in fig. 3.6, the carrier transition can then be brought into resonance with the beat note of the frequency combs by tuning one of the drive frequencies of the AOM.

The small angle between the two beams in the co-propagating geometry results in a negligible momentum transfer meaning that the coupling to the motional degree of freedom is highly suppressed. In order to address the motional states of the ion, the beam is sent through a beam splitter and then each arm is sent through separate AOM's and directed onto the ion from different angles as shown in fig. 3.7. The two beams are directed onto the ion from orthogonal directions and both beams are

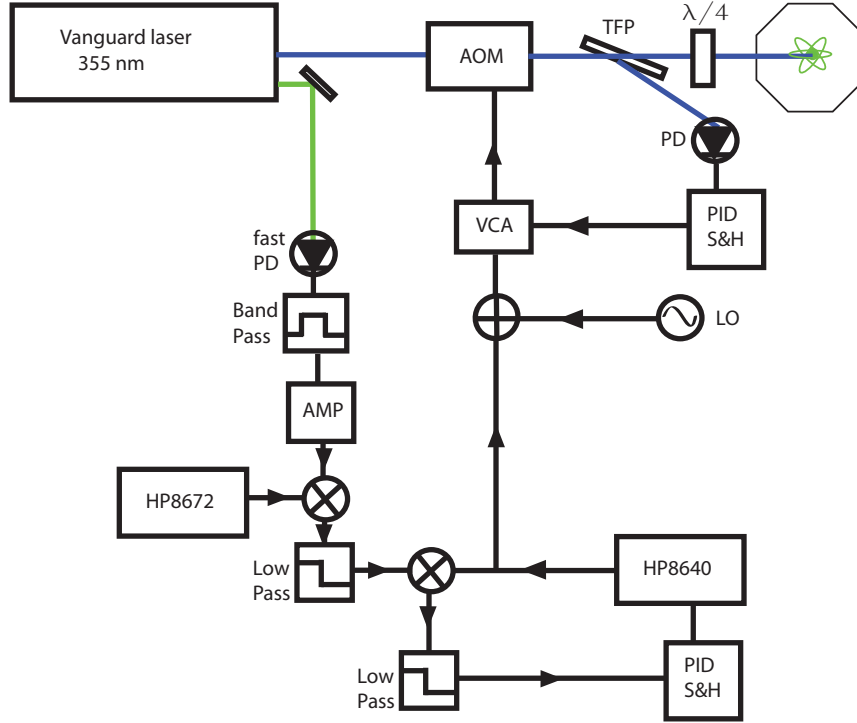


Figure 3.5: A co-propagating beam geometry setup is shown. Since the repetition rate of the Vanguard laser is not able to be locked, a feed-forward locking scheme is used instead in which the quantity $n2\pi f_{rep} - \Delta\omega_{aom}$ is stabilized. The 532 nm light that is generated by the Vanguard system is sent onto a fast photodetector in order to generate an RF comb which is then bandpass filtered and amplified to generate a single comb tooth. A local oscillator, (HP8672), is detuned from the frequency nf_{rep} by ϵ and mixed with the comb tooth. The mixed signal is low-pass filtered and mixed with the HP8640 which is tuned to ω_1 to generate an error signal that is fed to a PID to stabilize $nf_{rep} - \omega_1$. This signal is then summed with a second oscillator that can be tuned so that $|n2\pi f_{rep} - \Delta\omega_{aom}| = \omega_{HF}$ where $\Delta\omega_{aom}$ is the difference between the two RF frequencies driving the AOM. A thin-film-polarizer, (THP), is inserted after the AOM to polarize the beam and the deflected beam is used to stabilize the intensity of the beam with a PID sample and hold circuit. The sample and hold circuit is implemented digitally with an FPGA board that is triggered right before any experiment and shut off before the experiment begins in order to avoid any phase shifts coming from the voltage controlled attenuator, (VCA). A $\lambda/4$ waveplate is inserted after the TFP in order to couple to the $m_f = 1$ Zeeman states in the excited P manifolds.

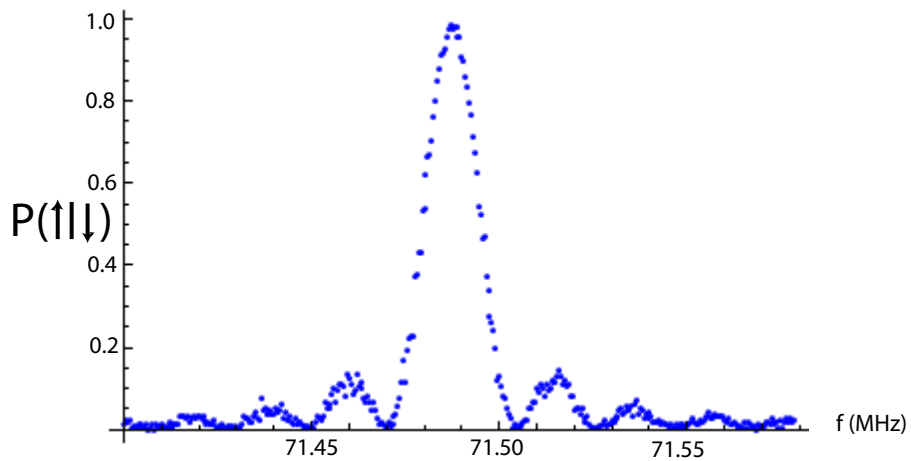


Figure 3.6: By scanning the frequency of the local oscillator, (LO), in the co-propagating geometry shown in fig. 3.5, the line shape of the carrier transition is seen. The oscillator that is locked to the frequency comb is run near 77.58 MHz and the repetition rate of the laser is measured to be 80.566 MHz, so that when the second generator is tuned to 71.48 MHz, the resonance condition $|157 \times 80.566 - 77.58 + 71.48| = \omega_{hf}/2\pi$ is satisfied. The typical statistical error for the data is ± 0.03 .

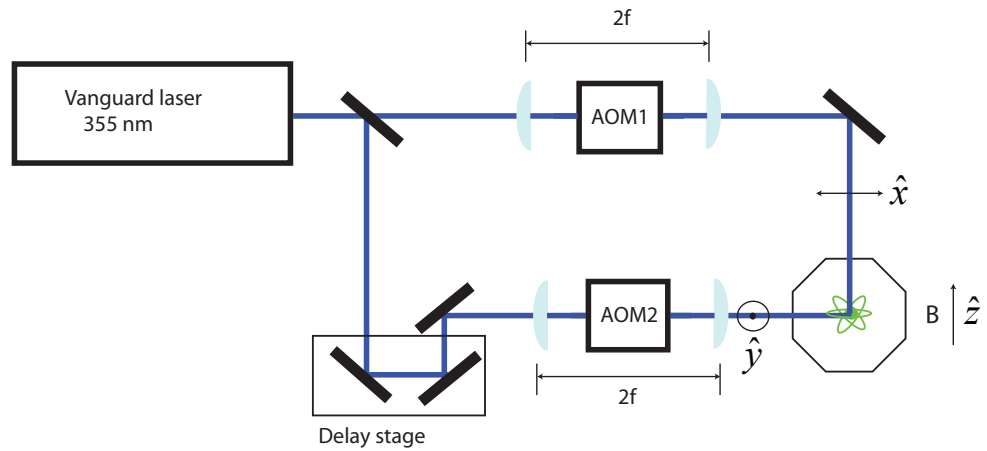


Figure 3.7: By splitting the pulsed laser beam and sending each arm through different AOMs, we can address the motional degree of freedom of the ion. A delay stage is inserted into one of the arms in order to ensure that the two path lengths are matched to better than 0.1 mm. As shown in fig. 3.5, one of the AOM's is driven with an RF generator that is locked to one of the RF comb teeth generated by the pulsed laser while the other AOM frequency can be tuned in order to single out a desired transition. The power in both arms are stabilized using digital sample and hold circuits as shown in fig. 3.5. In order to combat frequency dependent beam steering, lens of focal length f are placed before and after the AOMs so that a collimated beam focuses inside the AOM and then gets recollimated. The focal length of the lens used is in principle irrelevant, but in practice needs to be long enough so that the first order diffracted beam can be separated.

linearly polarized and mutually orthogonally to the small magnetic field, (lin-perp-lin). Each beam is passed through a separate AOM to shift its carrier frequency so that the electric fields from the beams at the location of the ion can be written as,

$$\vec{E}_1(t) = \frac{\hat{x}}{\sqrt{2}} \sum_n f(t - nT) e^{-i(\vec{k}_1 \cdot \vec{x} - (\omega_c + \omega_{ao1})t)} \quad (3.51)$$

$$\vec{E}_2(t) = \frac{\hat{y}}{\sqrt{2}} \sum_n f(t - nT - \Delta T) e^{-i(\vec{k}_2 \cdot \vec{x} - (\omega_c + \omega_{ao2})(t - \Delta T))}, \quad (3.52)$$

where ΔT accounts for any delay between the two pulse trains. Because of the Clebsch-Gordan coefficients, \hat{x} couples $|\downarrow\rangle$ to the symmetric superposition of the ${}^2P_{1/2}$ $|F = 1, m_f = 1\rangle$ and $|F = 1, m_f = -1\rangle$ states and couples $|\uparrow\rangle$ to the antisymmetric combination. The opposite is true for \hat{y} . The same is true for the coupling to the ${}^2P_{3/2}$ states, but their contribution will be neglected in the following analysis. We call the symmetric superposition $|+\rangle$ and the antisymmetric superposition $|-\rangle$. In this case, the interaction Hamiltonian is,

$$\begin{aligned} H_{\text{int}}(t) &= -\hat{\mu} \cdot \text{Re} \left[\vec{E}_1(t) + \vec{E}_2(t) \right] \quad (3.53) \\ &= -\frac{\mu}{\sqrt{2}} \sum_n f(t - nT) \cos \left(\vec{k}_1 \cdot \vec{x} - (\omega_c + \omega_{ao1})t \right) \times \\ &\quad (|\downarrow\rangle \langle +| + |+\rangle \langle \downarrow| + |\uparrow\rangle \langle -| + |-\rangle \langle \uparrow|) \\ &\quad -\frac{\mu}{\sqrt{2}} \sum_n f(t - nT - \Delta T) \cos \left(\vec{k}_2 \cdot \vec{x} - (\omega_c + \omega_{ao2})(t - \Delta T) \right) \\ &\quad (|\uparrow\rangle \langle +| + |+\rangle \langle \uparrow| + |\downarrow\rangle \langle -| + |-\rangle \langle \downarrow|) \quad (3.54) \end{aligned}$$

If the position of the ion is considered to be a classical variable for now, the wavefunction can be expanded in terms of the eigenstates of the unperturbed atomic

Hamiltonian and one finds the following set of differential equations for the evolution of the probability amplitudes,

$$\mathcal{E}(t) \equiv \frac{\mu}{\sqrt{2}} \sum_n f(t - nT) \quad (3.55)$$

$$\begin{aligned} \dot{c}_\downarrow + i\omega_\downarrow c_\downarrow &= i\mathcal{E}(t) \cos\left(\vec{k}_1 \cdot \vec{x} - (\omega_c + \omega_{ao1})t\right) c_+ \\ &\quad + i\mathcal{E}(t + \Delta T) \cos\left(\vec{k}_2 \cdot \vec{x} - (\omega_c + \omega_{ao2})(t + \Delta T)\right) c_- \end{aligned} \quad (3.56)$$

$$\begin{aligned} \dot{c}_\uparrow + i\omega_\uparrow c_\uparrow &= i\mathcal{E}(t) \cos\left(\vec{k}_1 \cdot \vec{x} - (\omega_c + \omega_{ao1})t\right) c_- \\ &\quad + i\mathcal{E}(t + \Delta T) \cos\left(\vec{k}_2 \cdot \vec{x} - (\omega_c + \omega_{ao2})(t + \Delta T)\right) c_+ \end{aligned} \quad (3.57)$$

$$\begin{aligned} \dot{c}_+ + i\omega_e c_+ &= i\mathcal{E}(t) \cos\left(\vec{k}_1 \cdot \vec{x} - (\omega_c + \omega_{ao1})t\right) c_\downarrow \\ &\quad + i\mathcal{E}(t + \Delta T) \cos\left(\vec{k}_2 \cdot \vec{x} - (\omega_c + \omega_{ao2})(t + \Delta T)\right) c_\uparrow \end{aligned} \quad (3.58)$$

$$\begin{aligned} \dot{c}_- + i\omega_e c_- &= i\mathcal{E}(t) \cos\left(\vec{k}_1 \cdot \vec{x} - (\omega_c + \omega_{ao1})t\right) c_\uparrow \\ &\quad + i\mathcal{E}(t + \Delta T) \cos\left(\vec{k}_2 \cdot \vec{x} - (\omega_c + \omega_{ao2})(t + \Delta T)\right) c_\downarrow, \end{aligned} \quad (3.59)$$

where I've set both of the energies of the symmetric and antisymmetric states equal to $\hbar\omega_e$. By transforming to rotating frame defined as,

$$\tilde{c}_\downarrow = c_\downarrow \quad (3.60)$$

$$\tilde{c}_\uparrow = c_\uparrow e^{i\omega_{HF}t} \quad (3.61)$$

$$\tilde{c}_+ = c_+ e^{i\omega_c t} \quad (3.62)$$

$$\tilde{c}_- = c_- e^{i\omega_c t}, \quad (3.63)$$

the equations of motion become,

$$\begin{aligned}
\dot{c}_\downarrow + i\omega_\downarrow c_\downarrow &= i\mathcal{E}(t)\cos\left(\vec{k}_1 \cdot \vec{x} - (\omega_c + \omega_{ao1})t\right) c_+ e^{-i\omega_c t} \\
&+ i\mathcal{E}(t + \Delta T)\cos\left(\vec{k}_2 \cdot \vec{x} - (\omega_c + \omega_{ao2})(t + \Delta T)\right) c_- e^{-i\omega_c t}
\end{aligned} \tag{3.64}$$

$$\begin{aligned}
\dot{c}_\uparrow + i(\omega_\uparrow - \omega_{HF})c_\uparrow &= i\mathcal{E}(t)\cos\left(\vec{k}_1 \cdot \vec{x} - (\omega_c + \omega_{ao1})t\right) c_- e^{-i(\omega_c - \omega_{HF})t} \\
&+ i\mathcal{E}(t + \Delta T)\cos\left(\vec{k}_2 \cdot \vec{x} - (\omega_c + \omega_{ao2})(t + \Delta T)\right) c_+ e^{-i(\omega_c - \omega_{HF})t}
\end{aligned} \tag{3.65}$$

$$\begin{aligned}
\dot{c}_+ + i(\omega_e - \omega_c)c_+ &= i\mathcal{E}(t)\cos\left(\vec{k}_1 \cdot \vec{x} - (\omega_c + \omega_{ao1})t\right) c_\downarrow e^{i\omega_c t} \\
&+ i\mathcal{E}(t + \Delta T)\cos\left(\vec{k}_2 \cdot \vec{x} - (\omega_c + \omega_{ao2})(t + \Delta T)\right) c_\uparrow e^{i(\omega_c - \omega_{HF})t}
\end{aligned} \tag{3.66}$$

$$\begin{aligned}
\dot{c}_- + i(\omega_e - \omega_c)c_- &= i\mathcal{E}(t)\cos\left(\vec{k}_1 \cdot \vec{x} - (\omega_c + \omega_{ao1})t\right) c_\uparrow e^{i(\omega_c - \omega_{HF})t} \\
&+ i\mathcal{E}(t + \Delta T)\cos\left(\vec{k}_2 \cdot \vec{x} - (\omega_c + \omega_{ao2})(t + \Delta T)\right) c_\downarrow e^{i\omega_c t}.
\end{aligned} \tag{3.67}$$

If the lowest energy state is defined to have zero energy, $\omega_\downarrow = 0$, the adiabatic approximation $\dot{c}_+ \approx \dot{c}_- \approx 0$ gives the following set of expressions for the excited

state amplitudes,

$$c_+ \approx \frac{\mathcal{E}(t)}{\Delta} \cos(\vec{k}_1 \cdot \vec{x} - (\omega_c + \omega_{ao1})t) c_{\downarrow} e^{i\omega_c t} + \frac{\mathcal{E}(t + \Delta T)}{\Delta} \cos(\vec{k}_2 \cdot \vec{x} - (\omega_c + \omega_{ao2})(t + \Delta T)) c_{\uparrow} e^{i(\omega_c - \omega_{HF})t} \quad (3.68)$$

$$c_- \approx \frac{\mathcal{E}(t)}{\Delta} \cos(\vec{k}_1 \cdot \vec{x} - (\omega_c + \omega_{ao1})t) c_{\uparrow} e^{i(\omega_c - \omega_{HF})t} + \frac{\mathcal{E}(t + \Delta T)}{\Delta} \cos(\vec{k}_2 \cdot \vec{x} - (\omega_c + \omega_{ao2})(t + \Delta T)) c_{\downarrow} e^{i\omega_c t} \quad (3.69)$$

Plugging these into the differential equations for the qubit states and making a rotating wave approximation with respect to the optical frequency yields the effective equations of motion for the qubit states,

$$\dot{c}_{\downarrow} = i \frac{\mathcal{E}(t)\mathcal{E}(t + \Delta T)}{\Delta} \left[c_{\downarrow} + \cos(\delta\vec{k} \cdot \vec{x} - \Delta\omega t + \omega_{ao2}\Delta T) c_{\uparrow} e^{-i\omega_{HF}t} \right] \quad (3.70)$$

$$\dot{c}_{\uparrow} = i \frac{\mathcal{E}(t)\mathcal{E}(t + \Delta T)}{\Delta} \left[c_{\uparrow} + \cos(\delta\vec{k} \cdot \vec{x} - \Delta\omega t + \omega_{ao2}\Delta T) c_{\downarrow} e^{i\omega_{HF}t} \right], \quad (3.71)$$

where $\Delta\omega \equiv \omega_{ao1} - \omega_{ao2}$. The factors of $\omega_{ao2}\Delta T$ inside of the cosine functions can be ignored since they act like a phase shift on one the AOMs which just acts to shift the rotation axis of the operation. Starting from Eq. (3.71),

$$\dot{c}_{\downarrow} = i \frac{\mu^2}{4\Delta} \sum_{k,k'} E_k E_{k'} e^{ik\omega_r t} e^{ik'\omega_r(t+\Delta T)} \left[2c_{\downarrow} + \left(e^{i(\delta\vec{k} \cdot \vec{x} - \Delta\omega t)} + e^{-i(\delta\vec{k} \cdot \vec{x} - \Delta\omega t)} \right) c_{\uparrow} e^{-i\omega_{HF}t} \right]. \quad (3.72)$$

The spatial dependence can be ignored for the calculation of the carrier frequency.

The resonant terms are picked out by requiring $(k+k')\omega_r + \Delta\omega - \omega_{HF} = 0$, (assuming

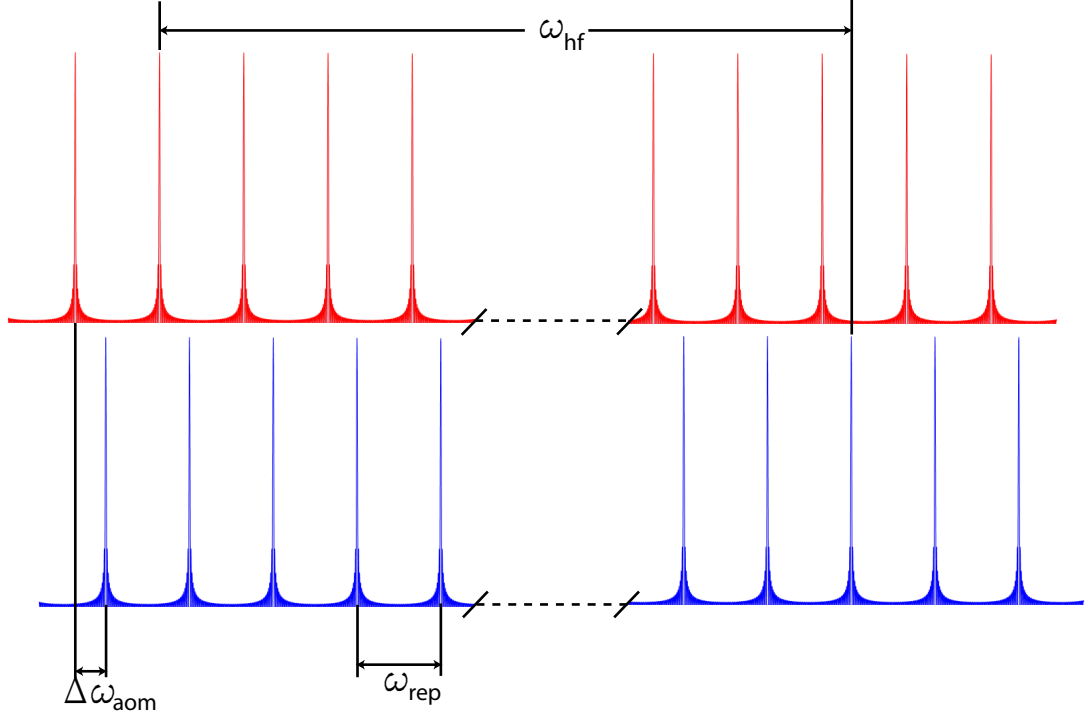


Figure 3.8: The two photon Raman transition using frequency shifted combs is illustrated. If the repetition rate of the laser is not commensurate with the desired transition frequency, the beam can be split into two and sent through separate AOM frequency shifters, (fig. 3.7), in order in order to satisfy the resonance condition in Eq. (3.75).

$(k + k')\omega_r - \Delta\omega - \omega_{HF} \neq 0$). The resonant off-diagonal coupling is then given by,

$$\frac{\Omega}{2} = \frac{\mu^2}{4\Delta} \sum_{k,k'} E_k E_{k'} \delta_{k,q'-k'} e^{ik\omega_r \Delta T} \quad (3.73)$$

$$= \frac{\mu^2}{4\Delta} \sum_k E_k E_{q'-k} e^{ik\omega_r \Delta T} \quad (3.74)$$

$$q' \equiv \frac{\omega_{\text{hf}} - \Delta\omega}{\omega_r}. \quad (3.75)$$

When the delay $\Delta T = 0$ and the parameter q' is an integer, the beat note between the two frequency combs resonantly drives the Raman transition as illustrated in fig. 3.8. As before, the sum can then be approximated by an integral if the repetition

rate is small compared to the bandwidth and $1/T$. The extra exponential factor in this expression makes the integral more difficult to evaluate analytically, but yields a simple expression for the case of Gaussian pulses as defined in table 3.1, which case the Rabi frequency is proportional to,

$$\Omega \propto e^{-\frac{1}{4}\left(\frac{\Delta T}{\tau}\right)^2}, \quad (3.76)$$

which states that the pulses must arrive at the ion simultaneously to drive the Raman transition. Eq. (3.76) is only an approximation and does not reflect the fact that the Rabi frequency should revive when the delay becomes equal to the spacing between pulses. But since the disparity between the repetition rate and the bandwidth of typical mode locked lasers is usually several orders of magnitude, Eq. (3.76) can be used to measure the bandwidth of a pulse through the measurement of the Rabi frequency as a function of the delay between the two arms as shown in fig. 3.9.

Equations (3.71) can also be derived from the following two-level Hamiltonian,

$$H_{\text{eff}} = -\frac{|\mathcal{E}(t)|^2}{\Delta} \cos\left(\delta\vec{k} \cdot \vec{x} - \Delta\omega t\right) (\sigma_- e^{-i\omega_{HF}t} + \sigma_+ e^{i\omega_{HF}t}) \quad (3.77)$$

where I've dropped the terms that describe the differential AC Stark shift. Plugging in the pulse train for the time-dependent electric field amplitude gives,

$$H_{\text{eff}} \approx -\frac{\mu^2}{4\Delta} \sum_n |f(t - nT)|^2 \cos\left(\delta\vec{k} \cdot \vec{x} - \Delta\omega t\right) (\sigma_- e^{-i\omega_{HF}t} + \sigma_+ e^{i\omega_{HF}t}) \quad (3.78)$$

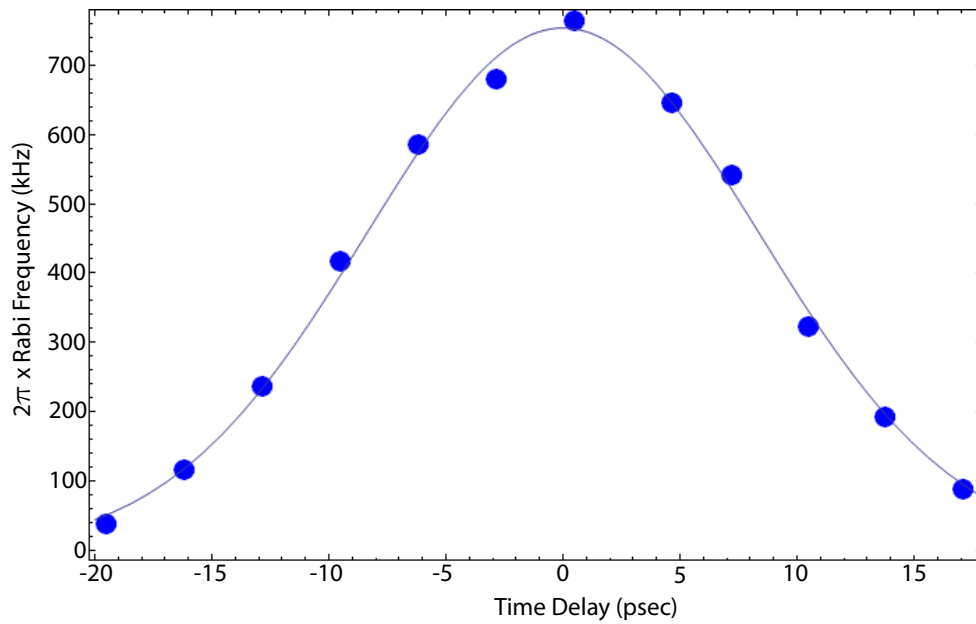


Figure 3.9: The Rabi frequency of the Raman transition on the carrier as a function of the delay between the two pulse trains introduced by a retroreflector on a movable stage as shown in fig. 3.7. The data was taken using the 355 nm Vanguard laser. A fit to the data using the function in Eq. (3.76) suggests the laser produces a pulse with a bandwidth given by $\tau \approx 6$ psec.

where the approximation is made by assuming the pulses have very little overlap. The time dependent intensity envelope $\sum_n |f(t - nT)|^2$ has a frequency spectrum of an RF comb. By assuming that q' is nearly an integer, one of the RF comb teeth can be used to make a rotating wave approximation and rewrite the Hamiltonian as,

$$H_{\text{eff}} \approx -\frac{\mu^2}{4\Delta} \sum_n |f(t - nT)|^2 (\sigma_- e^{-i(\delta\vec{k}\cdot\vec{x} - (\Delta\omega - \omega_{HF})t)} + \sigma_+ e^{i(\delta\vec{k}\cdot\vec{x} - (\Delta\omega - \omega_{HF})t)}). \quad (3.79)$$

By defining the parameter θ as the Bloch rotation angle due to a single pulse,

$$\theta = -\frac{\mu^2}{2\Delta} \int_{-\infty}^{\infty} |f(t)|^2 dt \quad (3.80)$$

$$= -\frac{\mu^2}{2\Delta} |E_0|^2 \tau \quad (3.81)$$

$$= -\frac{\Omega_0 T}{2}, \quad (3.82)$$

and changing the classical position variable to a time-dependent position operator, the Hamiltonian in Eq. (3.79) can be transformed to the Schrödinger picture to give,

$$H_s = \omega_t (a^\dagger a + 1/2) - \frac{\omega_0}{2} \sigma_z + \frac{\theta}{2} \sum_n \delta(t - nT) (\sigma_- e^{-ik\hat{x}} + \sigma_+ e^{ik\hat{x}}), \quad (3.83)$$

where we've assumed δk is along the x direction and that the pulses are short compared to the hyperfine time scale so that they can be modeled as delta pulses. To find the time evolution operator, we first write down the time evolution operator

for one delta kick at $t = 0$.

$$i \frac{\partial}{\partial t} \psi = \left(H_0 + \frac{\theta}{2} \delta(t) (\sigma_- e^{-ik\hat{x}} + \sigma_+ e^{ik\hat{x}}) \right) \psi \quad (3.84)$$

$$i \int_{-\epsilon}^{\epsilon} dt \frac{\partial}{\partial t} \psi = \frac{\theta}{2} \int_{-\epsilon}^{\epsilon} dt \delta(t) (\sigma_- e^{-ik\hat{x}} + \sigma_+ e^{ik\hat{x}}) \psi \quad (3.85)$$

If the delta function is modeled as a square pulse of width ϵ and height $1/\epsilon$ in the limit $\epsilon \rightarrow 0$, then its easy to see that the time evolved state due to one kick is given by,

$$\psi(0 + \epsilon) = e^{-i\frac{\theta}{2} Q_0} \psi(0) \quad (3.86)$$

$$Q_0 \equiv \sigma_- e^{-ik\hat{x}} + \sigma_+ e^{ik\hat{x}}. \quad (3.87)$$

Between delta kicks, the system evolves according to $H_0 = \omega_t (a^\dagger a + 1/2) - \frac{\omega_0}{2} \sigma_z$.

The time evolved state after N pulses is then,

$$|\psi(NT)\rangle = (e^{-iH_0 T} e^{-iQ_0 T})^N |\psi(0)\rangle. \quad (3.88)$$

We take the example of three pulses,

$$|\psi(3T)\rangle = e^{-iH_0T} e^{-i\frac{\theta}{2}Q_0T} e^{-iH_0T} e^{-i\frac{\theta}{2}Q_0T} e^{-iH_0T} e^{-i\frac{\theta}{2}Q_0T} |\psi(0)\rangle \quad (3.89)$$

$$= e^{-iH_0T} e^{-i2H_0T} e^{i2H_0T} e^{-i\frac{\theta}{2}Q_0T} e^{-iH_0T} e^{-iH_0T} e^{iH_0T} e^{-i\frac{\theta}{2}Q_0T} e^{-iH_0T} e^{-i\frac{\theta}{2}Q_0T} |\psi(0)\rangle \quad (3.90)$$

$$= e^{-i3H_0T} e^{-i\frac{\theta}{2}Q_2T} e^{-i\frac{\theta}{2}Q_1T} e^{-i\frac{\theta}{2}Q_0T} |\psi(0)\rangle \quad (3.91)$$

$$Q_n \equiv e^{inH_0t} Q_0 e^{-inH_0t} \quad (3.92)$$

Now the pattern is clear and we can write down the time evolved state after N pulses,

$$|\psi(NT)\rangle = e^{-iH_0NT} \prod_{n=0}^{n=N-1} e^{-i\frac{\theta}{2}Q_nT} \quad (3.93)$$

$$= e^{-iH_0NT} \sum_{k_{N-1}} \frac{(-i\frac{\theta}{2}Q_{N-1})^{k_{N-1}}}{k_{N-1}!} \dots \sum_{k_0} \frac{(-i\frac{\theta}{2}Q_0)^{k_0}}{k_0!} |\psi(0)\rangle \quad (3.94)$$

$$= e^{-iH_0NT} \sum_{k_{N-1}, \dots, k_0} \frac{(-i\frac{\theta}{2})^{k_{N-1} + \dots + k_0}}{k_{N-1}! \dots k_0!} Q_{N-1}^{k_{N-1}} \dots Q_0^{k_0} |\psi(0)\rangle \quad (3.95)$$

With this formula, it is easy to write down the time evolution operator to first order in θ ,

$$U(NT, 0) = 1 - i\frac{\theta}{2} \sum_{n=0}^{N-1} Q_n + \mathcal{O}(\theta^2). \quad (3.96)$$

To carry out the sum, we take advantage of being in the Lamb-Dicke regime and

write,

$$e^{ik\hat{x}(nT)} \approx 1 + i\eta(ae^{-i\omega nT} + a^\dagger e^{i\omega nT}) \quad (3.97)$$

$$\sum_n Q_n \approx \sum_n \sigma_- e^{-i\omega_0 nT} (1 - i\eta(ae^{-i\omega nT} + a^\dagger e^{i\omega nT})) \quad (3.98)$$

$$+ \sigma_+ e^{i\omega_{HF} nT} (1 + i\eta(ae^{-i\omega nT} + a^\dagger e^{i\omega nT})) \quad (3.99)$$

All the sums in the first order term are geometric and can be done using the formula,

$$\sum_{n=0}^{N-1} e^{i\omega nT} = \frac{\sin N\omega T/2}{\sin \omega T/2} e^{i(N-1)\omega T/2} = \frac{1 - e^{iN\omega T}}{1 - e^{i\omega T}}. \quad (3.100)$$

For example, if the offset frequency between the combs $\Delta\omega$ is tuned to satisfy the resonance condition for the red sideband, $\vartheta_r \equiv (\omega_{hf} + \Delta\omega - \omega_t)T = 2\pi j$, where j is an integer, then the sum in Eq. (3.99) is approximately given by,

$$\sum_{n=0}^{N-1} Q_n \approx i\eta \frac{\sin N\vartheta_r/2}{\sin \vartheta_r/2} e^{i\vartheta_r(N-1)/2} \sigma_+ a + \text{h.c.} \quad (3.101)$$

The coefficient in Eq. (3.101) has an amplitude ηN on resonance and the other terms in Eq. (3.99) that drive the carrier and other sideband transitions can be neglected when $N \gg (\omega_t T \eta)^{-1}$ as we now show. If we require the sideband transition amplitude to dominate the carrier then we can write,

$$\eta N \gg \frac{1 - e^{iN\omega_0 T}}{1 - e^{i\omega_0 T}}. \quad (3.102)$$

But the red sideband is in resonance, then $\omega_0 T = 2\pi q + \omega_t T$ giving,

$$\eta N \gg \frac{1 - e^{iN\omega_t T}}{1 - e^{i\omega_t T}} \approx \frac{1 - e^{i\omega_t NT}}{-i\omega_t T}, \quad (3.103)$$

where the last step was taken by assuming $\omega_t T \ll 1$. The factor $1 - e^{i\omega_t NT}$ is of order unity, so we can write the resolved sideband limit criterion as a condition on the number of pulses,

$$N \gg (\eta\omega_t T)^{-1}. \quad (3.104)$$

This result can also be derived by a more heuristic method. In order to resolve the sideband transition, it should be required that the spectral power resonant with the sideband transition is large compared to the spectral power resonant with the carrier transition. This requirement must be even more stringent given that the sideband transition is naturally weaker than the carrier transition by a factor of η . If the beat note between the comb teeth is assumed to be resonant with the sideband transition, then the spectral power that is resonant with the carrier transition can be estimated by considering a finite train of N pulses,

$$\Omega(t) \propto \sum_{n=0}^{N-1} |f(t - nT)|^2 \quad (3.105)$$

$$= \sum_{n=-\infty}^{\infty} |f(t - nT)|^2 \text{rect}\left(\frac{t - NT/2}{NT}\right), \quad (3.106)$$

where the second expression uses the rectangle function in order to eliminate the pulses outside of the window of interest. The Fourier transform of this pulse train can be

calculated using the property that products are transformed to convolutions. As shown earlier, the transform of the infinite pulse train is a sum of delta functions spaced by the repetition rate with an envelope function given by the transform of a single pulse. The transform of the rectangle function is a sinc function, meaning that the transform of a finite train is a sum of sinc functions spaced by the repetition rate with an envelope function. Considering a normalized comb tooth centered about the sideband transition frequency, the sideband transition dominates when,

$$\eta\Omega \gg \Omega \text{sinc}(\omega_t NT) \quad (3.107)$$

$$\approx \frac{\Omega}{\omega_t NT}. \quad (3.108)$$

After canceling the common factors of Ω , Eq. (3.104) is recovered. As shown in the arguments above, scanning the difference frequency of the AOM's that are used will reveal the different transitions that are possible in the qubit-oscillator system. The result from such a scan is shown in fig. 3.10.

3.1.4 Error Suppression in Raman Transitions

One source of error in the control fields is due to a fluctuating repetition rate of the pulsed laser due to small changes in the laser cavity length. This noise source can be suppressed by either a feedback method or by a feedforward method. Some pulsed lasers can have a piezo mounted behind one of the cavity mirrors, in which case monitoring of the repetition rate can be fed back to this piezo to directly stabilize the rep rate. The bandwidth of this type of lock will likely be limited to a

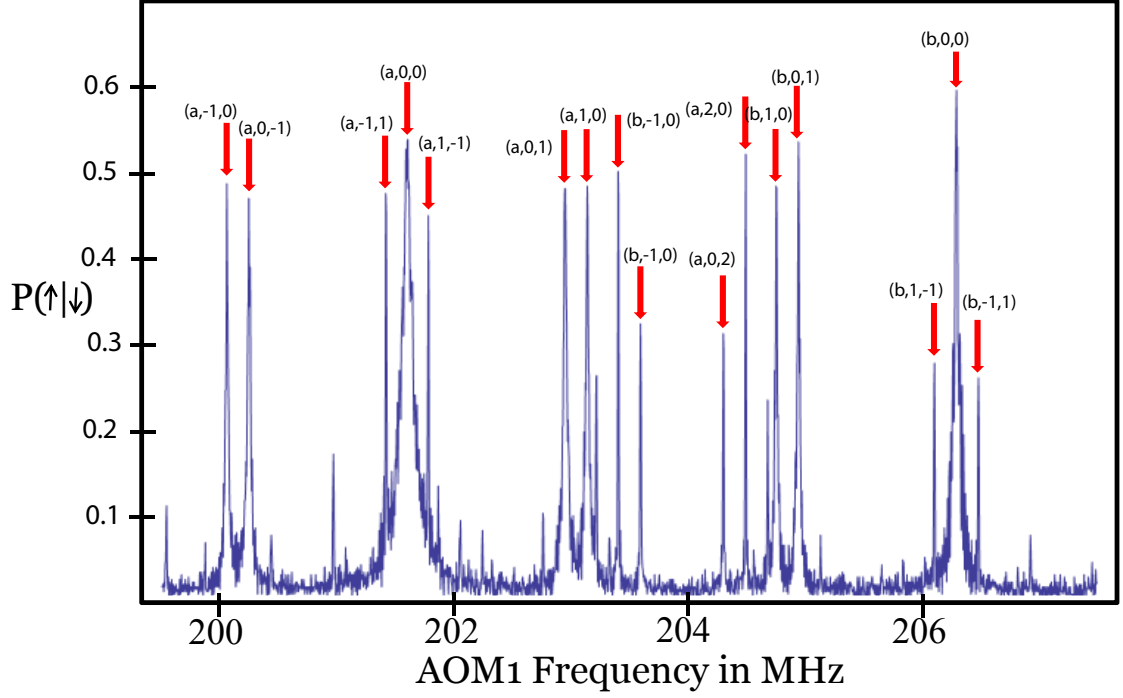


Figure 3.10: The probability of changing the qubit state is plotted as a function of the frequency of one the AOMs in the Raman beam set up shown in fig. 3.7. Using a Raman probe duration of $80 \mu\text{s}$, we can see resolved carrier and sideband transitions of a single trapped ion. The transitions are labeled, $(j, \Delta n_x, \Delta n_y)$, to indicate the carrier index and the change in the number of phonons in the two transverse modes that accompany a spin flip. The carrier indices, $a = 158$ and $b = -155$, are a reflection of the span between the different comb teeth being used as dictated by the resonance condition, $|2\pi j\nu_r + \Delta\omega_{aom}| = \omega_{hf}$.

few kHz by the response of the piezo mounted to the massive mirror. This type of lock was used in Ti:Sapph laser that is mentioned in this section. Many commercial laser systems do not allow for a piezo to mounted behind a mirror, as in the case of the 355nm Vanguard laser. In this case, a feedforward method can be used to compensate for fluctuations in the repetition rate. This method focuses on the fact that the beat note between comb teeth is crucial for clean Raman transitions and not the repetition rate alone. In order to stabilize this beat note, the repetition rate can be monitored and any deviations can be fed forward to one of the AOMs as shown in fig. 3.5. As shown in fig. 3.11, a Ramsey experiment on the carrier transition without a beat note lock in place shows a coherence time of only 2 ms, and a coherence time of 150 ms when the phase-lock-loop is switched on. The bandwidth of this lock will likely be limited by the rise time of the AOM being used which is usually on the order of half a microsecond which should be fast enough to suppress repetition rate noise caused by small changes in the laser cavity length.

Another important source of noise stems from power fluctuations in the beam. This can be corrected by taking a sample of the beam after the AOMs and feeding back to the RF drive power as shown in fig. 3.5. Because this AOM is used as an optical switch for the Raman beams, an analog PID is not used in this feedback loop. Instead, a digital PID is used so that the lock point can be stored in memory while the beam is turned off. When the beam is on, the voltage from the photodetector is sent to an FPGA chip which outputs a PID voltage that is then applied to a voltage controlled attenuator that the RF passes through. Figure 3.12 shows the suppression in intensity fluctuations on the photodetector used in the feedback loop. Because

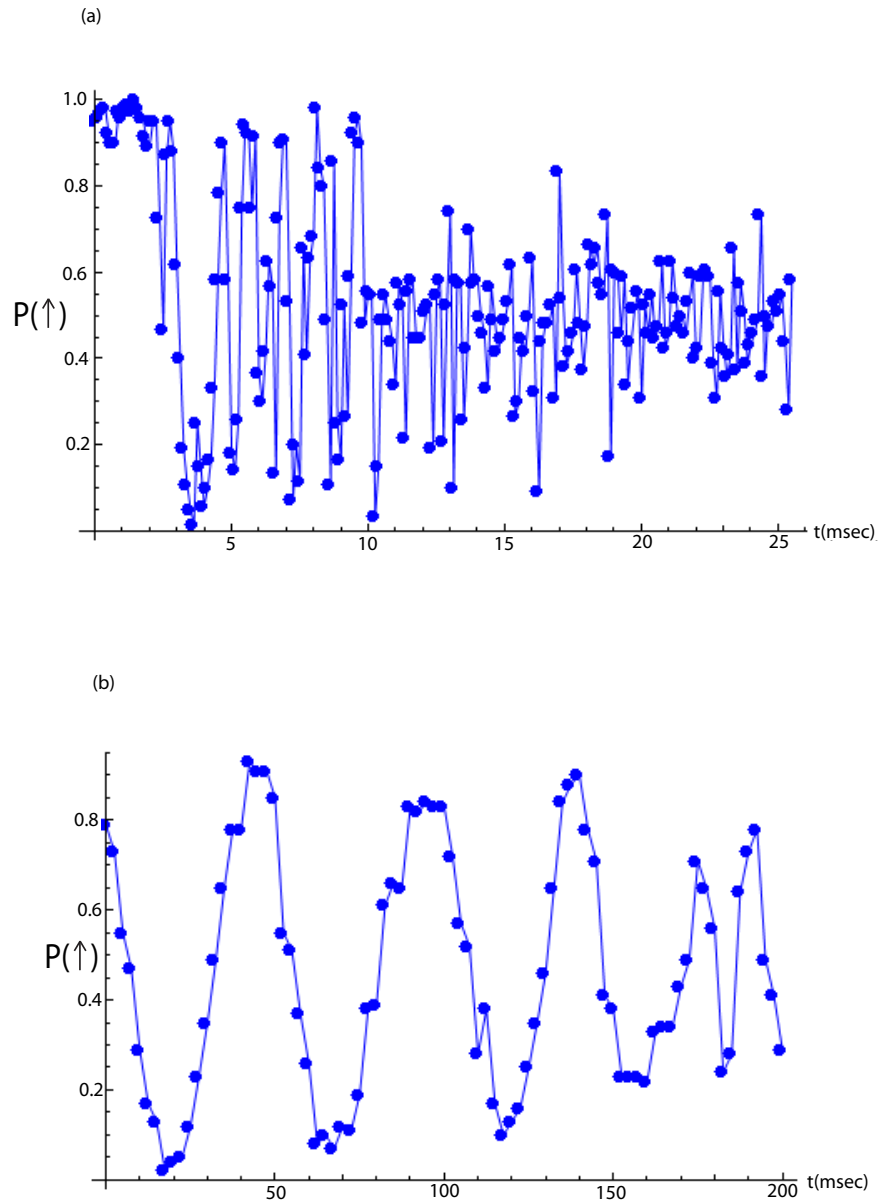


Figure 3.11: A set of Ramsey experiments are performed in a co-propagating geometry as shown in fig. 3.5. (a) The Ramsey experiment was first performed without the beat-note lock switched on and shows a coherence time of only 2 msec, implying that the noise on the rep rate of the laser has a bandwidth of approximately 1 kHz. (b) When the beat-note lock is turned on, the coherence time is seen to be extended by almost two orders of magnitude.

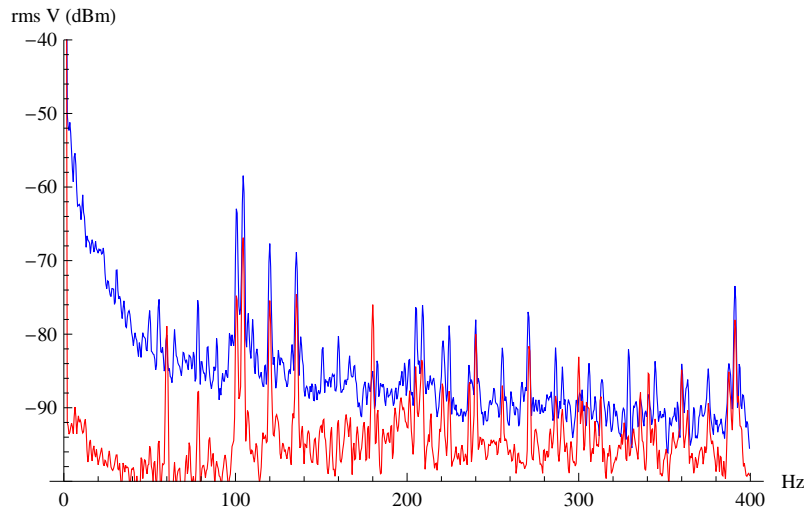


Figure 3.12: The data shows the difference in power fluctuations in the Raman beam when a noise eater is used. The sample of the beam is directed onto a photodetector that outputs a voltage that is proportional to the optical power which was plugged into a spectrum analyzer to generate the root mean square of the fluctuations in dBm. The two curves show that the noise eater reduces the low frequency intensity noise by about 20 dBm.

the voltage controlled attenuator imparts a phase shift on the RF, the noise eater is never used during the control operations but is briefly turned on immediately before the experiments begin. This system, is therefore unable to suppress noise that is fast compared to the timescale of a single experiment which is on the order of 1 ms.

Another source of noise for the control field comes from air currents which result in pressure gradients in the optical beam. This can lead to beam steering which is seen as an intensity fluctuation by the ion. This can be suppressed to some degree by using an enclosure around the Raman beams. The data shown in fig. 3.13 show the improvement in the fidelity of Rabi oscillations on the carrier transition when using the noise eater circuit and an enclosure around the Raman beam setup.

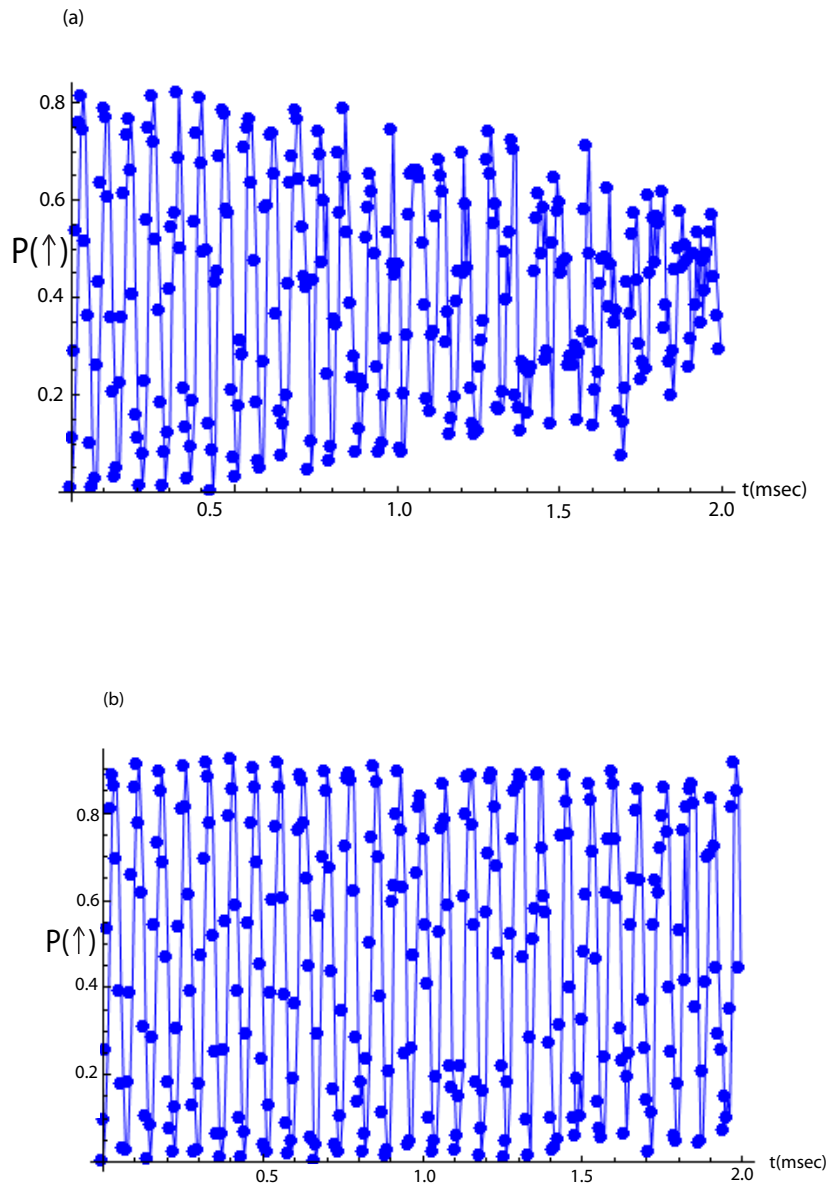


Figure 3.13: Rabi flopping on the carrier transition with and without intensity noise suppression. (a) Using a co-propagating beam geometry like the one shown in fig. 3.5, the Rabi oscillation is observed to decay substantially after approximately a 40π pulse. (b) With the noise eater circuit turned on, the HEPA filter fans over the Raman laser turned off and an enclosure around the Raman beam setup, the Rabi oscillations are seen to persist over a much longer time scale.

Besides fluctuating control fields, the other main source of error in Raman operations comes from imperfect state preparation. As discussed earlier, the initial purity of the internal state of the ion as prepared by optical pumping can be quite good, but the preparation of the motional degree of freedom is not as simple. As shown earlier, the qubit-oscillator dynamics are well described by the effective Hamiltonian in Eq. (3.77) which implies that the Rabi frequency for qubit rotations are position dependent. The most straight forward way to get around this issue is to prepare a nearly pure motional state using laser cooling. By first Doppler cooling and then sideband cooling [60], the ion can be prepared in the vibrational ground state with near unit fidelity as shown in fig. 3.14. To sideband cool to the ground state efficiently, one must take into account the vibrational level dependence of the sideband transition frequency given by,

$$\Omega_{n,n-1} = \Omega_0 e^{-\eta^2/2} \frac{1}{\sqrt{n}} \eta L_{n-1}^1(\eta^2) \approx \Omega_0 \eta \sqrt{n}, \quad (3.109)$$

where Ω_0 is the base Rabi frequency, L_n^α is the generalized Laguerre polynomial [61] and the approximation is valid when $\eta\sqrt{n} < 1^*$. The algorithm that is used to cool to the ground state then starts by optically pumping the ion(s) to $|0\rangle$, driving a π pulse on the red sideband $n \rightarrow n - 1$ transition with time being determined by Eq. (3.109), then optically pumping to $|0\rangle$, driving $n - 1 \rightarrow n - 2$ and repeating this procedure n times. If the initial π time is optimized, an ion in a 2 MHz trap can usually be cooled to the ground state in about 20 cycles as shown in fig. 3.14.

*The expression for the blue sideband transition is $\Omega_{n,n+1} = \Omega_0 e^{-\eta^2/2} \frac{1}{\sqrt{n+1}} \eta L_n^1(\eta^2) \approx \eta \sqrt{n+1}$ and the expression for the carrier transition is $\Omega_{n,n} = \Omega_0 e^{-\eta^2/2} L_n^0(\eta^2)$.

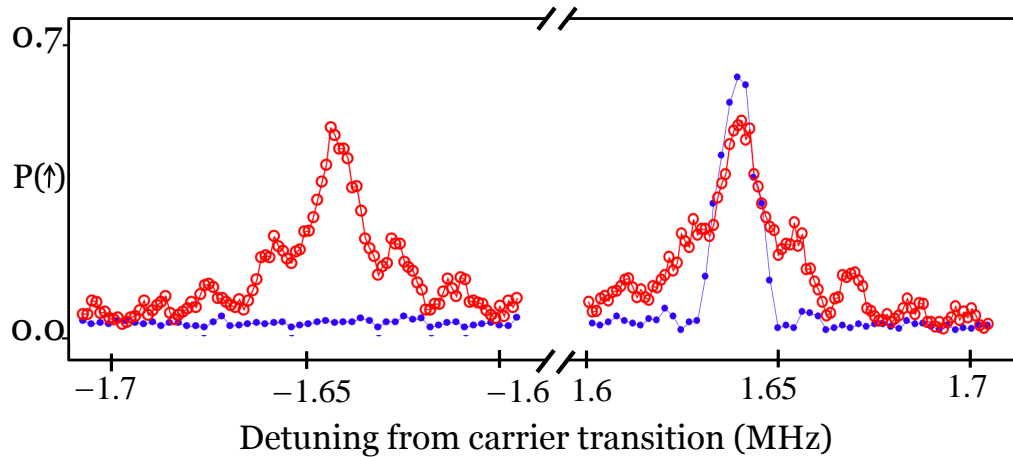


Figure 3.14: The data shows a probe of the first order sideband transitions before and after sideband cooling. The red open circles show the probability of flipping the spin on the sideband transitions after Doppler cooling. The closed blue circles show the probability of flipping the spin on the sideband transitions after sideband cooling as described in the text. After sideband cooling to the ground state, it is not possible to flip the spin on the red sideband transition and the blue sideband transition is significantly narrowed. After starting with $\bar{n} \approx 10$ after Doppler cooling, we are able to cool the ion to $\bar{n} \leq 0.03$, a measurement which is limited by the accuracy of the state detection protocol.

3.2 Light Shifts

The AC Stark shift, or light shift, is a well known effect on atomic energy levels that comes from the application of an off resonant optical field. This level shift can be calculated using second order perturbation theory and in the case of a single monochromatic beam is given by [62],

$$\langle \Delta E \rangle = \frac{|E_0|^2}{2\hbar} \sum_{k \neq g} |\mu_{gk}|^2 \frac{\omega_{gk}}{\omega_{gk}^2 - \omega^2}, \quad (3.110)$$

where the sum is taken over all atomic energy levels that are connected to the level in question through a dipole transition, μ_{gk} is the dipole matrix element, ω_{gk} is the transition frequency and E_0 and ω are the amplitude and frequency of the applied optical field. In this section I will show how to derive a similar expression for the Stark shift in the case of the optical frequency comb and show that it yields Eq. (3.110) in the appropriate limit. Take a pulse train with a carrier frequency ω_c and an electric field envelope for a single pulse $E_0 f(t)$.

$$H(t) = -\frac{\hat{\mu} E_0}{T} \cos(\omega_c t) \sum_{j=-\infty}^{\infty} \tilde{f}(\omega_j) e^{i\omega_j t} \quad (3.111)$$

$$\omega_j \equiv j\omega_r \quad (3.112)$$

The energy shift due to these off-resonant comb teeth can be calculated using perturbation theory as shown below. First, expand the wavefunction in terms of the states $\psi_k(x)$ which are eigenstates of the unperturbed Hamiltonian with energy E_k .

Consider an atom initially in the state $|g\rangle$ and the Dyson series evolution,

$$|\Psi(t)\rangle = \left(1 + \frac{1}{i\hbar} \int_{t_0}^t dt_1 V(t_1) + \left(\frac{1}{i\hbar} \right)^2 \int_{t_0}^t dt_1 \int_{t_0}^{t_1} dt_2 V(t_1) V(t_2) + \dots \right) |\Psi(0)\rangle \quad (3.113)$$

$$c_g^{(2)}(t) = 1 + \langle g | \left(\frac{1}{i\hbar} \right)^2 \int_{t_0}^t dt_1 \int_{t_0}^{t_1} dt_2 V(t_1) V(t_2) | \Psi(0) \rangle, \quad (3.114)$$

where V is the Hamiltonian in the interaction picture with respect to the unperturbed atomic Hamiltonian and $V^{gg} = 0$. Using a resolution of the identity,

$$c_g^{(2)}(t) = 1 + \sum_{k \neq g} \left(\frac{1}{i\hbar} \right)^2 \int_{t_0}^t dt_1 \int_{t_0}^{t_1} dt_2 V^{g,k}(t_1) V^{k,g}(t_2) \quad (3.115)$$

$$c_g^{(2)}(t) = 1 + \sum_{k \neq g} \left(\frac{1}{i\hbar} \right)^2 \int_{t_0}^t dt_1 \int_{t_0}^{t_1} dt_2 H_I^{g,k}(t_1) e^{-i\omega_{kg}t_1} H_I^{k,g}(t_2) e^{-i\omega_{gk}t_2} \quad (3.116)$$

If the Stark shift is denoted by ΔE ,

$$c_g(t) = |c_g(t)| e^{-i \int_{t_0}^t dt' \Delta E(t')/\hbar} \quad (3.117)$$

$$\approx 1 - \frac{1}{i\hbar} \int_{t_0}^t dt' \Delta E(t') \quad (3.118)$$

$$\Delta E(t) = -\frac{1}{i\hbar} \sum_{k \neq g} \int_0^t dt' H_I^{g,k}(t) e^{-i\omega_{kg}t} H_I^{k,g}(t') e^{-i\omega_{gk}t'} \quad (3.119)$$

Now we can plug in the Hamiltonian describing the interaction with the pulse train.

$$\Delta E(t) = -\frac{|E_0|^2}{i\hbar T} \sum_{k \neq g} |\mu_{kg}|^2 \sum_{j,n} \tilde{f}(\omega_j) f(t - nT) \cos(\omega_c t) e^{-i\omega_{kg}t} \times \quad (3.120)$$

$$\frac{i}{2} \left(\frac{e^{-i(\omega_{gk} - \omega_j + \omega_c)t} - 1}{\omega_{gk} - \omega_j + \omega_c} + \frac{e^{-i(\omega_{gk} - \omega_j - \omega_c)t} - 1}{\omega_{gk} - \omega_j - \omega_c} \right) \quad (3.121)$$

Now we can find the average Stark shift by integrating over a single pulse and multiplying by the repetition rate. If we integrate over a single pulse, we end up with 8 different terms which are all just the spectrum of the pulse evaluated at different frequencies.

$$\begin{aligned}
\langle \Delta E \rangle = & -\frac{\nu_r |E_0|^2}{4\hbar T} \sum_{k \neq g} |\mu_{kg}|^2 \sum_j \tilde{f}(\omega_j) \times \\
& \left(\frac{\tilde{f}(2\omega_c - \omega_j) + \tilde{f}(\omega_j) - \tilde{f}(\omega_c - \omega_{kg}) - \tilde{f}(\omega_c + \omega_{kg})}{\omega_{gk} - \omega_j + \omega_c} \right. \\
& \left. + \frac{\tilde{f}(\omega_j) + \tilde{f}(2\omega_c - \omega_j) - \tilde{f}(\omega_c - \omega_{kg}) - \tilde{f}(\omega_c + \omega_{kg})}{\omega_{gk} - \omega_j - \omega_c} \right) \quad (3.122)
\end{aligned}$$

Defining $\omega_c - \omega_{kg} \equiv \Delta$ and noting that terms like $\tilde{f}(\omega_c) \approx 0$ yields,

$$\langle \Delta E \rangle \approx \frac{\nu_r |E_0|^2}{2\hbar T} \sum_{k \neq g} |\mu_{kg}|^2 \sum_j \tilde{f}(\omega_j) (\tilde{f}(\omega_j) - \tilde{f}(\Delta)) \frac{\omega_{gk} - \omega_j}{(\omega_{gk} - \omega_j)^2 - \omega_c^2}, \quad (3.123)$$

which limits to Eq. (3.110) in the case of a cw laser. The differential AC Stark Shift can then be calculated to be,

$$\Delta\nu \approx \frac{\nu_r |E_0|^2}{4\hbar^2 T} \sum_{k \neq g} |\mu_{kg}|^2 \sum_j \tilde{f}(\omega_j) \left(\frac{\tilde{f}(\omega_j) - \tilde{f}(\Delta)}{\omega_j + \Delta} - \frac{\tilde{f}(\omega_j) - \tilde{f}(\Delta + \omega_{hf})}{\omega_j + \Delta + \omega_{hf}} \right). \quad (3.124)$$

This expression can be simplified further by assuming that the detuning Δ is large compared to the bandwidth of the laser, in which case $\tilde{f}(\Delta) \approx 0$.

This effect can be observed but is difficult to directly compare to theory since the shift is proportional to the intensity of the laser at the ion. A more convenient quantity to measure is the ratio of the Stark shift to the Rabi frequency since in

the case of both beams having the same intensity, both the Stark shift and Rabi frequency are directly proportional to the intensity. Using a home built Ti:Sapphire laser, we measured the differential AC Stark shift as function of the carrier frequency in a region close enough to the D_1 line that the effect of the $^2P_{3/2}$ could be ignored. In order to measure the Stark shift to Rabi frequency ratio at certain wavelength, first the carrier transition is driven and the frequency of oscillations as a function of time is measured. To measure the Stark shift, two Ramsey experiments are done. The first Ramsey experiment consists of a $\pi/2$ microwave pulse, then a delay Δt , then a second $\pi/2$ microwave pulse is applied. If the microwave frequency is slightly detuned from resonance, the final state of the qubit will oscillate as a function of the delay time between the two pulses with a frequency that is equal to the detuning from resonance. In the second Ramsey experiment, the laser was turned on during the delay time but was prepared with a polarization that does not drive Raman transitions as the Stark shift is independent of the polarization of light [59]. The difference in the two Ramsey oscillation frequencies is then interpreted as the Stark shift.

In order to calculate the theoretical curves shown in fig. 3.15, one needs to know spectrum of the pulse train being used. The center wavelength of the laser was measured using an optical spectrum analyzer and the width of a single pulse was estimated using an intensity autocorrelation measurement. As shown in fig. 3.16, the autocorrelation measurement data is well described by assuming a $\text{sinc}(t/\tau)$ pulse with $\tau = 90$ fsec, a pulse that corresponds to a flat-top spectrum in the frequency domain which is close to what was observed on the optical spectrum analyzer. The

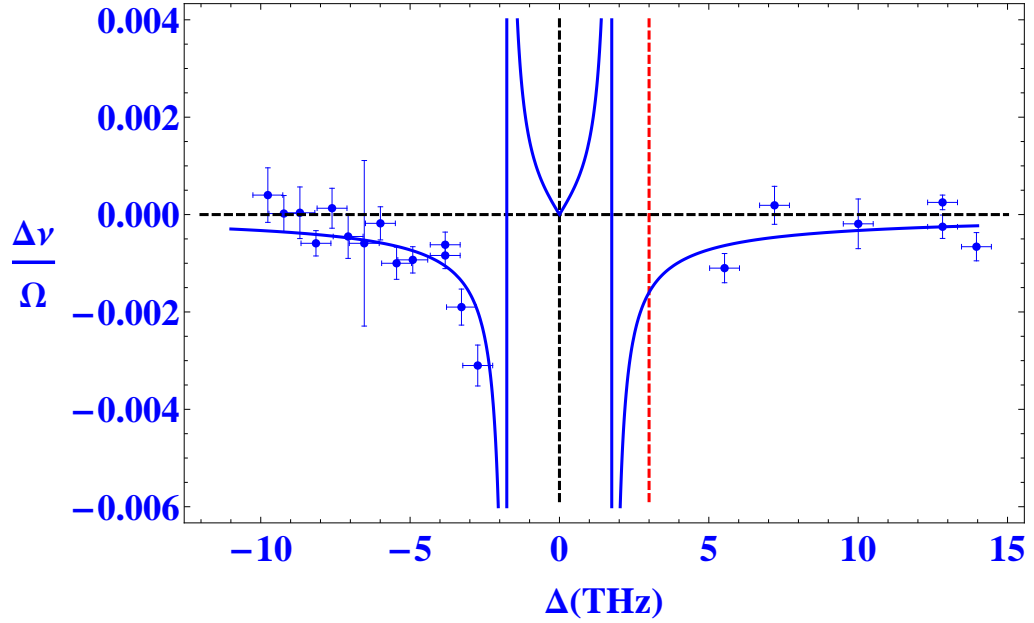


Figure 3.15: The data show the ratio of the differential Stark shift and the Rabi frequency for Raman transitions. The theory curve shown is a function computed using Eq. (3.131) with a fit parameter determined by an autocorrelation measurement. The red dotted line shows the location of a two photon resonance that can change the principal quantum number of the S shell valence electron and drive the transition $[\text{Xe}]4f^{14}6s \leftrightarrow [\text{Xe}]4f^{14}6s$. When the laser was tuned near this frequency, the ion was observed to go dark for periods of time ranging from 1 minute to 1 hour.

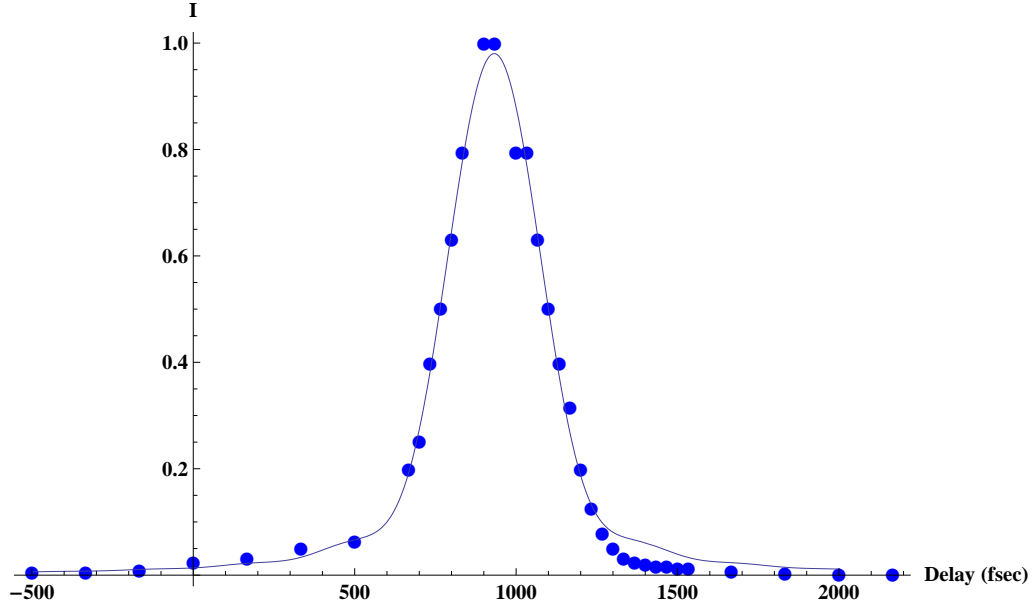


Figure 3.16: The data shows the normalized intensity autocorrelation of a single pulse produced by a Ti:Sapph laser that is then doubled using an BBO critically phase matched crystal. The function that is fit to the data is the autocorrelation of a sinc pulse as shown in Eq. (3.125).

function in the figure is given by,

$$\int_{-\infty}^{\infty} dt \operatorname{sinc}\left(\frac{t}{\tau}\right) \operatorname{sinc}\left(\frac{t-T}{\tau}\right) = \frac{\pi\tau \left(T/\tau - \cos\left(\frac{T}{\tau}\right) \sin\left(\frac{T}{\tau}\right)\right)}{\left(\frac{T}{\tau}\right)^3}. \quad (3.125)$$

If a square distribution in frequency space is assumed, which corresponds to a sinc pulse in time,

$$E(t) = E_0 \cos(\omega_c t) \sum_n \operatorname{sinc}\left(\frac{t-nT}{\tau}\right) \quad (3.126)$$

$$f(t) = E_0 \operatorname{sinc}\left(\frac{t}{\tau}\right) \quad (3.127)$$

$$\tilde{f}(\omega) = E_0 \tau \frac{\pi}{2} \operatorname{rect}(\omega\tau/2) \quad (3.128)$$

where $\operatorname{rect}(\omega\tau/2)$ is the rectangular function centered around $\omega = 0$ with a width

of $2/\tau$. Using the expressions that were derived for a 3-level atom the ratio of the Stark shift to Rabi frequency is,

$$\Omega = \frac{|\mu|^2 \sum_k E_k E_{k-q}}{\Delta} \quad (3.129)$$

$$E_k = \nu_r \tilde{f}(k\omega_r) \quad (3.130)$$

$$\frac{\Delta\nu}{\Omega} = \frac{\frac{1}{4} \sum_j \tilde{f}(\omega_j) \left(\frac{\tilde{f}(\omega_j) - \tilde{f}(\Delta)}{\omega_j + \Delta} - \frac{\tilde{f}(\omega_j) - \tilde{f}(\Delta + \omega_{hf})}{\omega_j + \Delta + \omega_{hf}} \right)}{\frac{\sum_k \tilde{f}(k\omega_r) \tilde{f}((k-q)\omega_r)}{\Delta}} \quad (3.131)$$

If we use the flat-top spectrum, the sums in Eq. (3.131) can be approximated as integrals and then done analytically as in the following example;

$$\sum_j \frac{\text{rect}\left(\frac{j\omega_r\tau}{2}\right)\text{rect}\left(\frac{j\omega_r\tau}{2}\right)}{j\omega_r + \Delta} = \sum_j \frac{\text{rect}\left(\frac{j\omega_r\tau}{2}\right)}{j\omega_r + \Delta} \quad (3.132)$$

$$\approx \int_{-\infty}^{\infty} dj \frac{\text{rect}\left(\frac{j\omega_r\tau}{2}\right)}{j\omega_r + \Delta} \quad (3.133)$$

$$= \int_{-1/\omega_r\tau}^{1/\omega_r\tau} dj \frac{1}{j\omega_r + \Delta} \quad (3.134)$$

$$= \frac{1}{\omega_r} \ln \frac{\Delta + \frac{1}{\tau}}{\Delta - \frac{1}{\tau}} \quad (3.135)$$

Note that these expressions do not include effects from unequal intensities in the two beams, but nonetheless fit to the observed data nicely as shown in fig. 3.15.

Chapter 4

Phonon mediated entanglement of ions

4.1 Spin-Dependent Forces

As mentioned in a previous chapter, engineering a spin-dependent force allows for the controlled entanglement of ions. In this chapter, I will begin by showing how to generate a spin-dependent force using stimulated Raman beams and how these forces can be studied using a single trapped ion. I will then describe the evolution of two ions under the influence of these forces and show how to measure the fidelity of these states. A variation on the standard pulse sequence will be described and shown to provide protection against uncontrolled fluctuations in the trapping frequency.

The discussion in the previous chapter shows that the pulsed laser can be used to generate effective Hamiltonians that largely confine the dynamics to the Hilbert space spanned by the tensor product of the qubit and a single mode of harmonic motion. For most of this chapter, I will assume that the ion's evolution can be described in this restricted space and that the resolved sideband limit is valid. All of the operations referred to will be engineered through combinations of the three primitive operators that are called the carrier, the red-sideband and blue-sideband. Starting with the effective Hamiltonian that drives Raman transitions in the lin-

perp-lin configuration with fields,

$$\vec{E}_1(t) = \hat{x}\mathcal{E}_1(t)e^{-i(\vec{k}_1 \cdot \vec{x} - (\omega_c + \omega_{a01})t + \phi_1)} \quad (4.1)$$

$$\vec{E}_2(t) = \hat{y}\mathcal{E}_2(t)e^{-i(\vec{k}_2 \cdot \vec{x} - (\omega_c + \omega_{a02})t + \phi_2)}, \quad (4.2)$$

the Hamiltonian is,

$$H_{\text{eff}} = -\frac{|g(t)|^2}{\Delta} \cos\left(\delta\vec{k} \cdot \vec{x} - \Delta\omega t + \Delta\phi_{1,2}\right) (\sigma_+ e^{i\omega_{hf}t} + \sigma_- e^{-i\omega_{hf}t}), \quad (4.3)$$

where,

$$g(t) \equiv \frac{\mathcal{E}(t)\mu_{g,e}}{\hbar} \quad (4.4)$$

$$\Delta\omega \equiv \omega_{a01} - \omega_{a02}, \quad (4.5)$$

where I assumed $\mathcal{E}_1 = \mathcal{E}_2 = \mathcal{E}$. If the two beams being used are derived from a single beam and a beam splitter in a Mach-Zender configuration as shown in fig. 3.7 then the relative phase $\Delta\phi_{1,2}$ is set by the relative phase of the AOM drive frequencies.

If $\delta k x_0 \sqrt{\bar{n} + 1} \equiv \eta \sqrt{\bar{n} + 1} \ll 1$, the exponential operators can be linearized to give,

$$\begin{aligned} H_{\text{eff}} \approx & -\frac{|g(t)|^2}{2\Delta} \left((1 + i\eta (ae^{-i\omega t} + a^\dagger e^{i\omega t})) e^{-i\Delta\omega t} e^{i\Delta\phi_{1,2}} \right. \\ & \left. + (1 - i\eta (ae^{-i\omega t} + a^\dagger e^{i\omega t})) e^{i\Delta\omega t} e^{-i\Delta\phi_{1,2}} \right) (\sigma_+ e^{i\omega_{hf}t} + \sigma_- e^{-i\omega_{hf}t}) \quad (4.6) \end{aligned}$$

In order to generate a Hamiltonian that drives a specific transition, the AOM frequencies are tuned to bring the corresponding operator into resonance with a

Fourier component of $|g(t)|^2$. If $|g(t)|^2$ has a Fourier component at ω_0 of strength g_0 , then tuning the AOM frequencies to be near the carrier resonance such that $\omega_0 + \Delta\omega - \omega_{HF} = \delta$, where $\delta \ll \omega_t$, generates the effective Hamiltonian,

$$H_{\text{eff}} \approx \hat{C}(t) \equiv -\frac{\Omega}{2} (\sigma_+ e^{-i\delta t} e^{i\phi_c} + \sigma_- e^{i\delta t} e^{-i\phi_c}) \quad (4.7)$$

where $\Omega \equiv \frac{g_0^2}{\Delta}$, which is the same Hamiltonian used in the previous chapter describing the interaction of a two level system interacting with a classical monochromatic source. When exciting the red or blue sideband, we get the following Hamiltonians,

$$\hat{R}(t) \equiv -i\frac{\eta\Omega}{2} (\sigma_+ a e^{-i\delta_r t} e^{i\phi_r} - \sigma_- a^\dagger e^{i\delta_r t} e^{-i\phi_r}) \quad (4.8)$$

$$\hat{B}(t) \equiv -i\frac{\eta\Omega}{2} (\sigma_+ a^\dagger e^{-i\delta_b t} e^{i\phi_b} - \sigma_- a e^{i\delta_b t} e^{-i\phi_b}). \quad (4.9)$$

As shown in [20, 63, 64], a spin-dependent force can be generated by applying the red and blue sideband operators simultaneously with a symmetric detuning $\delta_r = -\delta_b \equiv \delta$. In this case the time evolution operator can be solved for easily by considering the Magnus expansion. This expansion allows the time evolution operator to be written as the exponentiation of an operator $\sum_k \hat{O}_k$ so that,

$$U(t, t_0) = \exp \left[\sum_k \hat{O}_k \right] \quad (4.10)$$

$$\hat{O}_1 = -\frac{i}{\hbar} \int_{t_0}^t dt' H(t') \quad (4.11)$$

$$\hat{O}_2 = -\frac{1}{2\hbar^2} \int_{t_0}^t \int_{t_0}^{t'} dt' dt'' [H(t'), H(t'')]. \quad (4.12)$$

In general, the Magnus expansion has an infinite number of terms, but as will be shown, the series terminates after the second term in the case of the Mølmer-Sørensen interaction. The Mølmer-Sørensen Hamiltonian will be defined as the sum of the red and blue sideband interactions with the symmetric detuning,

$$H_{ms}(t) = \hat{R}(t) + \hat{B}(t) \quad (4.13)$$

$$\begin{aligned} &= -i\frac{\eta\Omega}{2}(\sigma_+ a e^{-i\delta_r t} e^{i\phi_r} - \sigma_- a^\dagger e^{i\delta_r t} e^{-i\phi_r} \\ &\quad + \sigma_+ a^\dagger e^{-i\delta_b t} e^{i\phi_b} - \sigma_- a e^{i\delta_b t} e^{-i\phi_b}) \end{aligned} \quad (4.14)$$

$$= -i\frac{\eta\Omega}{2}(\sigma_+ e^{i\phi_s} - \sigma_- e^{-i\phi_s})(a e^{-i\delta t} e^{i\phi_m} + a^\dagger e^{i\delta t} e^{-i\phi_m}) \quad (4.15)$$

where the spin phase $\phi_s = (\phi_r + \phi_b)/2$ and the motional phase $\phi_m = (\phi_r - \phi_b)/2$. Defining the spin operator $\hat{S} \equiv -i(\sigma_+ e^{i\phi_s} - \sigma_- e^{-i\phi_s})$, the first term in the Magnus expansion is,

$$\hat{O}_1 = \frac{\eta\Omega}{2}\hat{S} \int_{t_0}^t dt' (a e^{-i\delta t'} e^{i\phi_m} + a^\dagger e^{i\delta t'} e^{-i\phi_m}) \quad (4.16)$$

$$= \hat{S}(\alpha(t)a^\dagger - \alpha^*(t)a) \quad (4.17)$$

$$\alpha(t) = \frac{\eta\Omega}{2} \frac{e^{i\delta t} - e^{i\delta t_0}}{i\delta} e^{-i\phi_m}. \quad (4.18)$$

The second term in the Magnus expansion is given by,

$$\hat{O}_2 = -\frac{1}{2} \int_{t_0}^t \int_{t_0}^{t'} dt'' dt' [H(t'), H(t'')] \quad (4.19)$$

$$= -\frac{1}{2} \left(\frac{\eta\Omega}{2} \right)^2 \hat{S}^2 \int_{t_0}^t \int_{t_0}^{t'} dt'' dt' (e^{-i\delta(t'-t'')} - e^{i\delta(t'-t'')}) \quad (4.20)$$

$$= -\left(\frac{\eta\Omega}{2} \right)^2 \hat{S}^2 \frac{1}{i\delta} \left(t - t_0 - \frac{\sin\delta(t - t_0)}{\delta} \right). \quad (4.21)$$

All of the higher order terms in the Magnus expansion are made up of nested commutators of the Hamiltonian at different times. For example, the third order term is calculated by integrating terms like $[H(t), [H(t'), H(t'')]]$. But because the spin operator in the Mølmer-Sørensen interaction is constant and the time dependent harmonic oscillator operators have a scalar commutator, all higher order terms in the Magnus expansion are zero. This allows for the time evolution operator to be written in a simple form;

$$U_{ms}(t) = e^{-i \int dt' H(t') - \frac{1}{2} \int \int dt' dt'' [H(t'), H(t'')]} \quad (4.22)$$

$$= \exp \left[\hat{S}(\alpha^*(t)a^\dagger - \alpha(t)a) + i\hat{S}^2\Phi_0(t) \right] \quad (4.23)$$

$$\Phi_0(t) \equiv -\left(\frac{\eta\Omega}{2\delta} \right)^2 (\delta(t - t_0) - \sin\delta(t - t_0)). \quad (4.24)$$

The effect of the Mølmer-Sørensen operation can be understood as implementing a spin-dependent force which is made obvious by expressing the spin operator in its eigenbasis and examining its action on a quantum state that is routinely prepared in the laboratory, (fig. 4.1), $\rho = \sum_{\beta} P_{\beta} |\downarrow_z, \beta\rangle \langle \downarrow_z, \beta|$, where β describes the

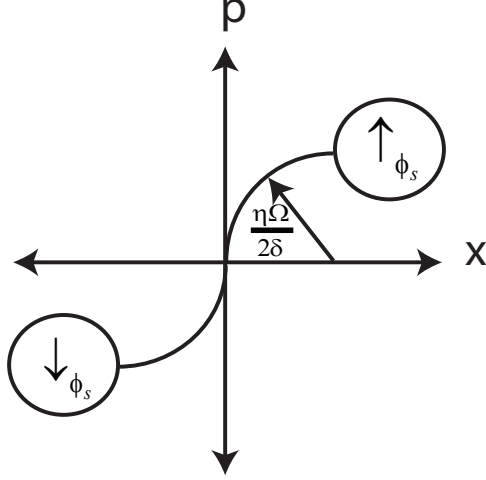


Figure 4.1: When a single ion prepared in $|\downarrow_z\rangle = |\downarrow_{\phi_s}\rangle - |\uparrow_{\phi_s}\rangle$ and subjected to the spin-dependent force, the motional wavepacket becomes entangled with the spin. For a finite detuning, the motional wavepackets execute circular trajectories in phase space and disentangle from the spin when $t = 2\pi/\delta$.

motional state of the ion. The spin operator $-i(\sigma_+e^{i\phi_s} - \sigma_-e^{-i\phi_s})$ has eigenstates $\frac{1}{\sqrt{2}}(\pm ie^{-i\phi_s}|\downarrow_z\rangle + |\uparrow_z\rangle)$ with eigenvalues ± 1 . Rewriting the time evolution operator in this basis gives,

$$\begin{aligned}
U_{ms}(t) = & \exp[(\alpha^*(t)a^\dagger - \alpha(t)a)(|\uparrow_{\phi_s}\rangle\langle\uparrow_{\phi_s}| - |\downarrow_{\phi_s}\rangle\langle\downarrow_{\phi_s}|) \\
& + i\Phi_0(t)(|\uparrow_{\phi_s}\rangle\langle\uparrow_{\phi_s}| + |\downarrow_{\phi_s}\rangle\langle\downarrow_{\phi_s}|)], \tag{4.25}
\end{aligned}$$

and its action on the state $|\downarrow_z, \beta\rangle$ is,

$$U_{ms}(t)|\downarrow_z, \beta\rangle = U_{MS}(t)(-ie^{i\phi_s}|\uparrow_{\phi_s}, \beta\rangle + ie^{i\phi_s}|\downarrow_{\phi_s}, \beta\rangle)/\sqrt{2} \tag{4.26}$$

$$\begin{aligned}
= & -\frac{i}{\sqrt{2}}e^{i\Phi_0(t)}e^{i\phi_s}(\hat{D}(\alpha(t))|\uparrow_{\phi_s}, \beta\rangle \\
& - \hat{D}(-\alpha(t))|\downarrow_{\phi_s}, \beta\rangle)/\sqrt{2}, \tag{4.27}
\end{aligned}$$

where the displacement operator is defined as $\hat{D}(\alpha(t)) = \exp[\alpha^*(t)a^\dagger - \alpha(t)a]$. The action of the displacement operator is simple in the coherent state basis as defined by $|\beta\rangle = \hat{D}(\beta)|0\rangle$, with $|0\rangle$ being the ground state of the harmonic oscillator. Note that in the case of one ion, the phase $-ie^{i\Phi_0(t)}e^{i\phi_s}$ is global and can, therefore, be ignored. Using the identity, $\hat{D}(\alpha)\hat{D}(\beta) = e^{i\varphi_{\alpha,\beta}}\hat{D}(\alpha + \beta)$, where $\varphi_{\alpha,\beta} \equiv \text{Im}[\alpha\beta^*]$, we see that the action of the spin-dependent force is expressed as,

$$U_{ms}(t)|\downarrow_z, \beta\rangle = \frac{1}{\sqrt{2}}(e^{i\varphi_{\alpha,\beta}}|\uparrow_{\phi_s}, \beta + \alpha(t)\rangle - e^{-i\varphi_{\alpha,\beta}}|\downarrow_{\phi_s}, \beta - \alpha(t)\rangle). \quad (4.28)$$

To compare this theory to an observable in the lab, we can calculate the probability of finding the the ion in $|1\rangle$ after preparing it in $|0\rangle$ and applying the spin-dependent force operation,

$$P_\uparrow(t, \delta; \beta) = \text{Tr}[|\uparrow_z\rangle\langle\uparrow_z| \rho] \quad (4.29)$$

$$= \langle\psi(t)|\uparrow_z\rangle\langle\uparrow_z|\psi(t)\rangle \quad (4.30)$$

$$= \frac{1}{4}(e^{i\varphi_{\alpha(t),\beta}}\langle\beta - \alpha(t)| - e^{-i\varphi_{\alpha(t),\beta}}\langle\beta + \alpha(t)|) \times \\ (e^{-i\varphi_{\alpha(t),\beta}}|\beta - \alpha(t)\rangle - e^{i\varphi_{\alpha(t),\beta}}|\beta + \alpha(t)\rangle) \quad (4.31)$$

$$= \frac{1}{4}(2 - 2\text{Re}[e^{2i\varphi_{\alpha(t),\beta}}\langle\beta - \alpha(t)|\beta + \alpha(t)\rangle]). \quad (4.32)$$

Using the expression for the overlap of two coherent states, $\langle\beta|\alpha\rangle = e^{-\frac{1}{2}(|\beta|^2 + |\alpha|^2 - 2\beta^*\alpha)}$, the expression for the ion brightness becomes,

$$P_\uparrow(t, \delta; \beta) = \frac{1}{2}\left(1 - \cos(4\varphi_{\alpha(t),\beta})e^{-2|\alpha(t,\delta)|^2}\right). \quad (4.33)$$

Now to consider a thermal distribution as the initial condition,

$$P_{\uparrow}(t, \delta) = \int d^2\beta P(\beta) P_{\uparrow}(t, \delta; \beta) \quad (4.34)$$

$$P(\beta) = \frac{1}{\pi\bar{n}} e^{-|\beta|^2/\bar{n}} \quad (4.35)$$

$$\int_{-\infty}^{\infty} d^2\beta e^{-|\beta|^2/\bar{n}} e^{i4\text{Im}[\alpha\beta^*]} = \pi\bar{n} e^{-4\bar{n}|\alpha|^2} \quad (4.36)$$

$$P_{\uparrow}(t, \delta) = \frac{1}{2} \left(1 - e^{-(\bar{n}+1/2)|2\alpha(t,\delta)|^2} \right) \quad (4.37)$$

In order to test this theory, we prepared a single $^{171}\text{Yb}^+$ ion in the four-rod trap and generated the spin-dependent force using the Ti:Sapph Raman laser set up discussed in the previous chapter. To generate the bichromatic force, one of the comb frequency shifters was simultaneously driven with two modulation frequencies. When these combs are tuned to drive the red and blue sidebands (in conjunction with the third frequency comb in the other beam), the ion experiences the spin-dependent force. The theoretical curve in Eq. (4.37) is compared with experimental data in fig. 4.2 and is seen to agree quite well. As seen in the figure, the periodic decoupling of the spin and motional degrees of freedom occurs with high fidelity, but is much more sensitive to the laser frequency in the case of an ion in a thermal state as compared to an ion that has been cooled to its ground state.

4.2 Two Atom Entanglement

These spin dependent forces can be used to entangle two ions. First, I'll just assume that we can isolate a single mode of motion and work with the following

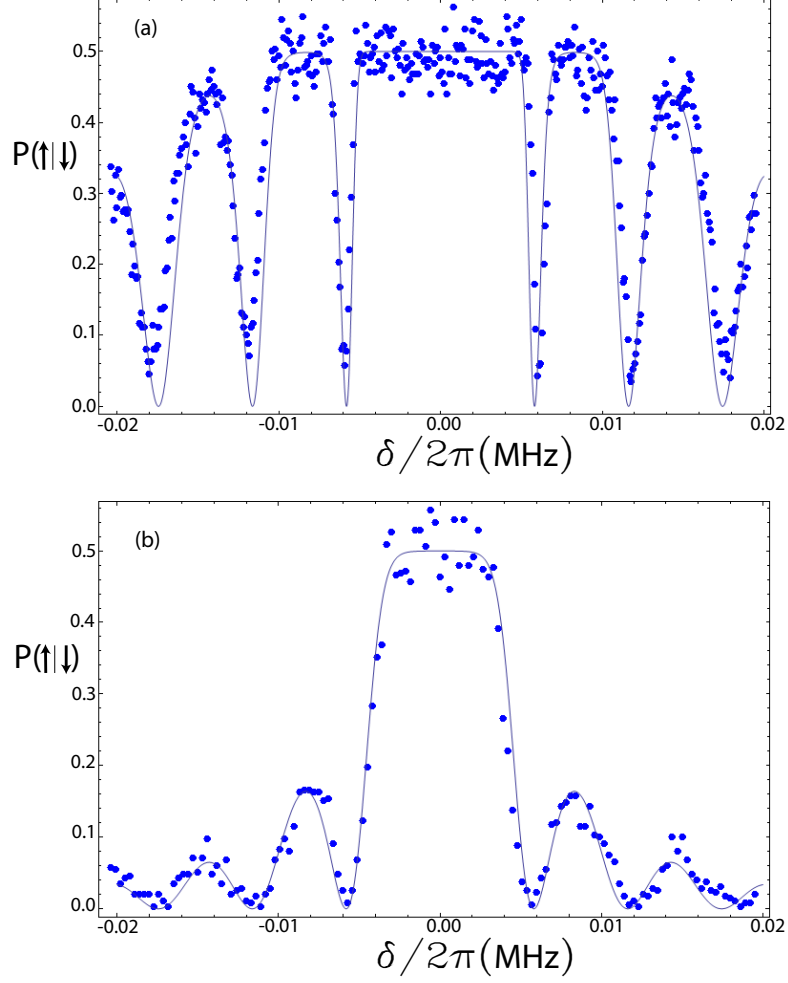


Figure 4.2: The probability of detecting $|1\rangle$ given the preparation of $|0\rangle$ and the application of the bichromatic force as function of the symmetric detuning δ . In both cases, the pulse was applied for $t_g = 172 \mu\text{sec}$. The revival of the initial spin state is seen when the symmetric detuning is equal to an integer times $1/t_g$ as evidenced by the narrow regions where the probability of detecting $|1\rangle$ is nearly zero. (a) The first data set was taken with an ion that was Doppler cooled and the theory was plotted assuming an average phonon number of $\bar{n} = 8$. (b) The second data set was taken with an ion that was sideband cooled to the ground state and the theory was plotted assuming an average phonon number of $\bar{n} = 0.01$.

Hamiltonian,

$$H = \omega_t a^\dagger a - \frac{\omega_{hf}}{2} (\sigma_z^{(1)} + \sigma_z^{(2)}) - \Omega \cos(\vec{k} \cdot \vec{x} - \Delta\omega t - \phi) (\sigma_+^{(1)} + \sigma_+^{(2)} + \sigma_-^{(1)} + \sigma_-^{(2)}) \quad (4.38)$$

A RWA can be made in the interaction picture to produce the red and blue sideband Hamiltonians just like the one ion Hamiltonians,

$$\hat{R}^{(2)} \equiv -i \frac{\eta\Omega}{2} \left((\sigma_+^{(1)} + \sigma_+^{(2)}) a e^{i\delta_r t} e^{-i\phi_r} - (\sigma_-^{(1)} + \sigma_-^{(2)}) a^\dagger e^{-i\delta_r t} e^{i\phi_r} \right) \quad (4.39)$$

$$\hat{B}^{(2)} \equiv -i \frac{\eta\Omega}{2} \left((\sigma_+^{(1)} + \sigma_+^{(2)}) a^\dagger e^{i\delta_b t} e^{-i\phi_b} - (\sigma_-^{(1)} + \sigma_-^{(2)}) a e^{-i\delta_b t} e^{i\phi_b} \right) \quad (4.40)$$

So now the Mølmer-Sørensen interaction,

$$H_{ms}^{(2)} = \hat{R}^{(2)} + \hat{B}^{(2)} \quad (4.41)$$

$$= -i \frac{\eta\Omega}{2} (\Sigma_+ e^{i\phi_s} - \Sigma_- e^{-i\phi_s}) (a e^{-i\delta t} e^{i\phi_m} + a^\dagger e^{i\delta t} e^{-i\phi_m}), \quad (4.42)$$

where $\Sigma_\pm \equiv \sigma_\pm^{(1)} + \sigma_\pm^{(2)}$ is the total spin operator. If the atoms are prepared in the state, $|\downarrow\downarrow_z\rangle$, the ideal evolution of the state is most easily calculated by assuming that the phase space trajectories close at the end of the gate operation, (fig. 4.3). In that case, the displacement operators in Eq. (4.27) limit to the identity operator so that the final state is given by,

$$U_{ms}(t) |\downarrow\downarrow_z\rangle = \frac{e^{i\hat{S}^2\Phi_0(t)} (|\downarrow\downarrow\phi_s\rangle + |\uparrow\uparrow\phi_s\rangle - |\downarrow\uparrow\phi_s\rangle - |\uparrow\downarrow\phi_s\rangle)}{2} \quad (4.43)$$

$$= \frac{e^{i4\Phi_0(t)} (|\downarrow\downarrow\phi_s\rangle + |\uparrow\uparrow\phi_s\rangle) - |\downarrow\uparrow\phi_s\rangle - |\uparrow\downarrow\phi_s\rangle}{2}. \quad (4.44)$$

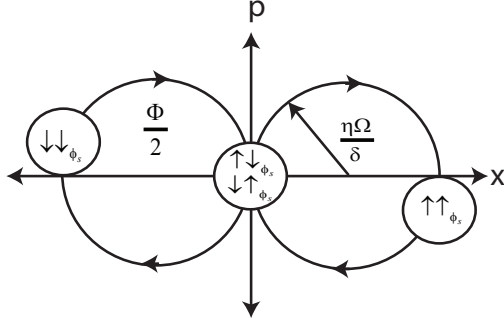


Figure 4.3: When two ions are prepared in $|\downarrow\downarrow_z\rangle = |\downarrow\downarrow_{\phi_s}\rangle + |\uparrow\uparrow_{\phi_s}\rangle - |\downarrow\uparrow_{\phi_s}\rangle - |\uparrow\downarrow_{\phi_s}\rangle$ and subjected to the spin-dependent force, the motional wavepacket splits into three components. The spin states with non-zero eigenvalues of the total spin operator execute circular trajectories in phase space and then disentangle from the motion when $t = 2\pi/\delta$. The total area swept out in phase space is equal to the relative spin phase Φ .

Using Eq. (4.24), it is easy to see that choosing a gate time $t_g = \frac{2\pi}{\delta}$ and laser power such that $\delta = 2\eta\Omega$, the accumulated phase is $e^{i4\Phi_0(t_g)} = -i$ and the final state is the maximally entangled state,

$$U_{ms}(t_g)|\downarrow\downarrow_z\rangle = e^{-i\pi/4} \frac{|\downarrow\downarrow_z\rangle - ie^{i2\phi_{ms}}|\uparrow\uparrow_z\rangle}{\sqrt{2}}. \quad (4.45)$$

4.2.1 Experimental Implementation of the Mølmer-Sørensen Gate

There are many different experimental parameters that must be calibrated in order to achieve the ideal evolution described in the previous section and we now describe some methods used in the laboratory to fine tune the system. Once two ions have been loaded into the trap, one should first make sure that the detection beam is properly adjusted. Usually the power in the detection beam is set so that a single ion prepared in $|1\rangle$ scatters an average of 10 photons, so that two ions prepared in $|11\rangle$ should scatter an average of 20 photons. To make sure that both ions are

contributing equally to the number of photons observed, one can use integrated images taken with the ICCD camera. The next step is to equalize the power being used in the red and blue sidebands. This step is complicated by the fact that most commercial combiners used to combine the two RF signals have a non-linear output whose combined frequency components usually do not have the same power ratios as the inputs*. The situation is further complicated by the frequency dependent diffraction efficiency of the AOM that is used and the different diffraction angles for the two different frequency components. In order to mitigate these effects, the optical system is designed to image the input beam of the AOM onto the ions so that the red and blue sideband beams focus at the same spot inside the vacuum chamber. The diffraction efficiency of the AOM driven with two frequencies during the operation was measured as a function of the drive frequency so that that the red and blue sideband frequencies could have equal diffraction efficiencies. By finding the peak in diffraction efficiency, the red and blue sideband frequencies can be made to straddle this peak by choosing the proper drive frequency for the other AOM that is used in the second Raman beam. Next, one should make sure that both ions will be equally illuminated by the Raman beams, which is most easily done by driving the carrier transition and mapping out the Rabi frequency as a function of the position of the final lens in the system used to focus the beam on the ion. Lastly, the power in the RF drives being used is fine tuned by measuring the red and blue sideband transition frequencies, which is most easily done with a single ion. During

*This problem might be eliminated if the two frequencies were generated together using an arbitrary waveform generator.

this last step, it is important to have both RF drives on during the measurement of the sideband transitions since the RF combiner output is non-linear in the inputs. In order to calibrate only the red sideband, the generator used to drive the blue sideband is set to a frequency that does not drive any transition but is still in the neighborhood of the blue sideband and similarly for calibrating the blue sideband transition.

Once the beams are aligned, the proper power, detuning and timing must be found. The first parameter to be calibrated is the precise frequency of the carrier transition. It is usually not sufficient to simply find the center of the carrier feature in a frequency scan such as the one shown in fig. 3.10 since the linewidth of the transition is so large compared to the necessary precision. In principle, one can decrease the power in the Raman beams in order to narrow the transition to gain more accuracy, but this method incurs the additional complexity of power dependent AC Stark shifts that must be taken into account. The easiest method found is to keep one of the RF drive frequencies fixed and detuned several linewidths red of the red sideband and then scan the other frequency blue of the blue sideband. A sharp peak should be visible in the frequency scan when the two detunings are exactly symmetric about the carrier transition. This peak is in fact where the slow version of the Mølmer-Sørensen gate would operate. Then both RF frequencies are scanned simultaneously, always staying symmetric about the carrier transition to find the correct detuning. For the symmetric detuning scan, the gate time is set to $t_g = \pi/\eta\Omega$ as measured by the sideband transition frequency. As shown in fig. 4.4, the symmetric detuning scan features reveal where the RF frequencies should be in

order to implement the ideal gate. The final step is to fix the symmetric detuning as shown in fig. 4.4 and scan the gate time in order for fine tuning as shown in fig. 4.5. These last two steps can then be iterated until the maximum gate fidelity is achieved. The theoretical predictions for the different populations are calculated in the same way as Eq. (4.37) and given by,

$$P_{\downarrow\downarrow}(t, \delta) = \frac{1}{4} \left(1 + 2e^{-|2\alpha(t,\delta)|^2(\bar{n}+1/2)} \cos(4\Phi_0(t, \delta)) + \frac{1}{2} \left(1 + e^{4\alpha(t,\delta)|^2(\bar{n}+1/2)} \right) \right) \quad (4.46)$$

$$P_{\downarrow\uparrow}(t, \delta) = P_{\uparrow\downarrow}(t, \delta) = \frac{1}{8} \left(1 + e^{4\alpha(t,\delta)|^2(\bar{n}+1/2)} \right) \quad (4.47)$$

$$P_{\uparrow\uparrow}(t, \delta) = \frac{1}{4} \left(1 - 2e^{-|2\alpha(t,\delta)|^2(\bar{n}+1/2)} \cos(4\Phi_0(t, \delta)) + \frac{1}{2} \left(1 + e^{4\alpha(t,\delta)|^2(\bar{n}+1/2)} \right) \right). \quad (4.48)$$

The gate performance is quantified by a measurement of the state fidelity. If the ideal state is $|\psi\rangle$ and the state created in the experiment is $\hat{\rho}$, then the fidelity is defined as $F = \langle\psi|\hat{\rho}|\psi\rangle$. This quantity can be found by measuring the density matrix and then calculating the overlap with $|\psi\rangle$, but a little algebra shows which measurements contain the relevant information. To see this, consider the expression for the fidelity,

$$F = \langle\psi|\hat{\rho}|\psi\rangle \quad (4.49)$$

$$= \text{Tr}[|\psi\rangle\langle\psi|\hat{\rho}] \quad (4.50)$$

$$= \frac{1}{2} \text{Tr}[(|\downarrow\downarrow\rangle + e^{i\phi}|\uparrow\uparrow\rangle)(\langle\downarrow\downarrow| + e^{-i\phi}\langle\uparrow\uparrow|)\hat{\rho}] \quad (4.51)$$

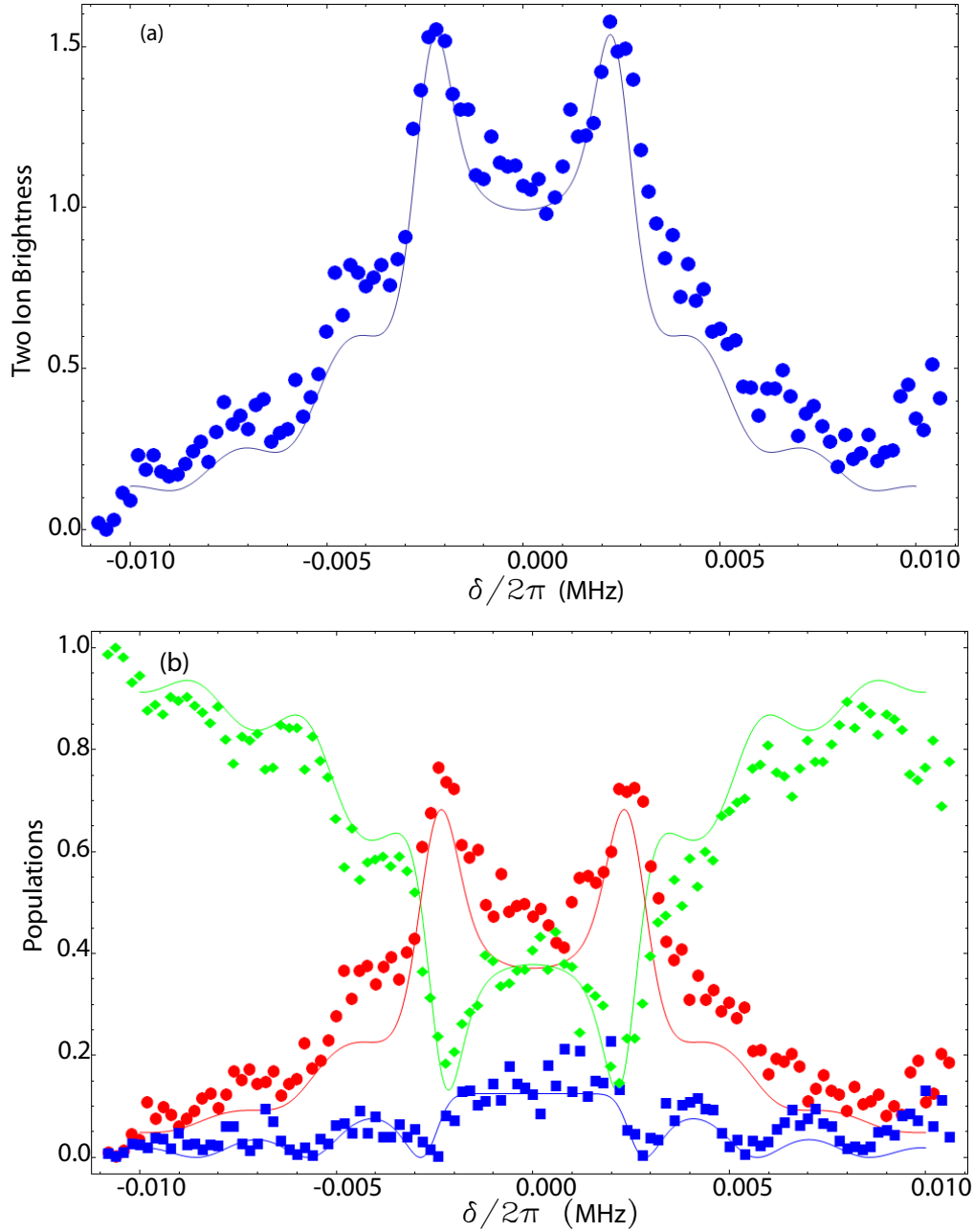


Figure 4.4: The detuning from the red and blue sidebands is symmetrically scanned using a gate time of $360 \mu\text{s}$. (a) The total ion brightness is plotted, i.e. $P(\downarrow\uparrow) + P(\uparrow\downarrow) + 2P(\uparrow\uparrow)$. At approximately ± 2.8 kHz the total ion brightness is seen to approach 1, signaling the creation of the maximally entangled state. (b) Using a fitting protocol, the different populations are plotted with $P(\downarrow\downarrow)$ represented as diamonds, $P(\uparrow\downarrow) + P(\downarrow\uparrow)$ as squares and $P(\uparrow\uparrow)$ as circles. At approximately ± 2.8 kHz the odd parity populations are seen to approach zero while the even parity populations both approach 0.5, signaling the creation of the state $|\downarrow\downarrow\rangle + e^{i\phi}|\uparrow\uparrow\rangle$. The theoretical curves plotted with the data are shown in Eqs. (4.46,4.47,4.48). The deviation from theory near $\delta/2\pi = 0.01$ is likely due to an off-resonant coupling to another motional mode.

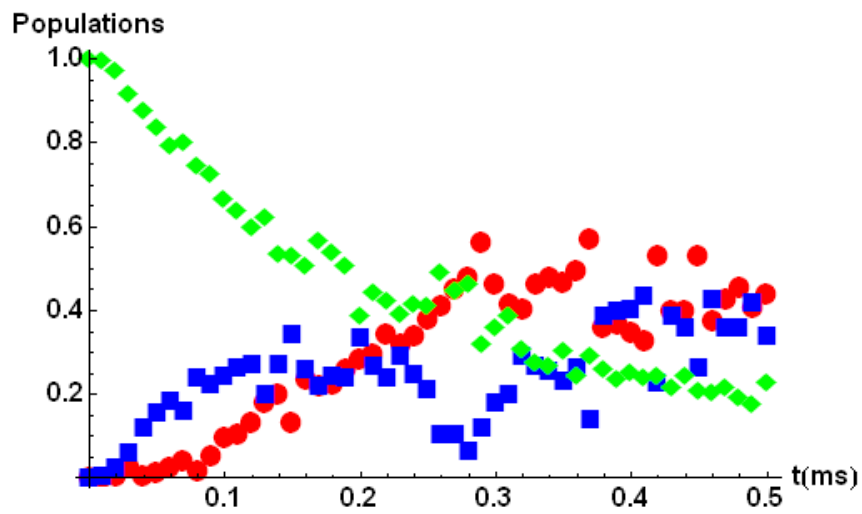


Figure 4.5: After finding the approximate ideal symmetric detuning δ , the gate time is scanned. Using a fitting protocol, the different populations are plotted with $P(\downarrow\downarrow)$ represented as **diamonds**, $P(\uparrow\downarrow) + P(\downarrow\uparrow)$ as **squares** and $P(\uparrow\uparrow)$ as **circles**. At approximately $280 \mu\text{s}$ the odd parity populations are seen to approach zero while the even parity populations both approach 0.5, signaling the creation of the state $|\downarrow\downarrow\rangle + e^{i\phi}|\uparrow\uparrow\rangle$.

The operator $|\psi\rangle\langle\psi|$ can be expanded in the Pauli operator basis,

$$|\downarrow\downarrow\rangle\langle\downarrow\downarrow| + |\uparrow\uparrow\rangle\langle\uparrow\uparrow| = \frac{1}{2}(I^{(1)}I^{(2)} + Z^{(1)}Z^{(2)}) \quad (4.52)$$

$$\begin{aligned} e^{i\phi}|\downarrow\downarrow\rangle\langle\uparrow\uparrow| + e^{-i\phi}|\uparrow\uparrow\rangle\langle\downarrow\downarrow| &= \cos\phi \frac{X^{(1)}X^{(2)} - Y^{(1)}Y^{(2)}}{2} \\ &+ \sin\phi \frac{X^{(1)}Y^{(2)} + Y^{(1)}X^{(2)}}{2}. \end{aligned} \quad (4.53)$$

This implies that the fidelity is measured as the following expectation value,

$$F = \frac{1}{4} \langle I^{(1)}I^{(2)} + Z^{(1)}Z^{(2)} + \cos\phi(X^{(1)}X^{(2)} - Y^{(1)}Y^{(2)}) + \sin\phi(X^{(1)}Y^{(2)} + Y^{(1)}X^{(2)}) \rangle, \quad (4.54)$$

where we are using the notation $\{\sigma_x, \sigma_y, \sigma_z\} = \{X, Y, Z\}$. The first term two terms are found by measuring in the standard basis and then calculating the probability of finding the two ions in the same state, i.e. $\frac{1}{4}(I^{(1)}I^{(2)} + Z^{(1)}Z^{(2)}) = \frac{1}{2}(\rho_{\downarrow\downarrow, \downarrow\downarrow} + \rho_{\uparrow\uparrow, \uparrow\uparrow})$. The second two terms are found by applying a global $\pi/2$ pulse before making a measurement. To see this, consider the $\pi/2$ rotation operator $\hat{R}(\pi/2, \varphi)$ which rotates the qubit about the $\cos\varphi X + \sin\varphi Y$ axis. If two qubits are subject to this rotation before being measured in the standard basis, then the measurement result

is given by,

$$\text{Tr}[Z^{(1)}Z^{(2)}\hat{R}^{(1)}(\pi/2, \varphi)\hat{R}^{(2)}(\pi/2, \varphi)\rho\hat{R}^\dagger(1)(\pi/2, \varphi)\hat{R}^\dagger(2)(\pi/2, \varphi)] \quad (4.55)$$

$$= \left\langle \hat{R}^\dagger(1)(\pi/2, \varphi)\hat{R}^\dagger(2)(\pi/2, \varphi)Z^{(1)}Z^{(2)}\hat{R}^{(1)}(\pi/2, \varphi)\hat{R}^{(2)}(\pi/2, \varphi) \right\rangle \quad (4.56)$$

$$= \left\langle (\cos\varphi Y^{(1)} - \sin\varphi X^{(1)}) (\cos\varphi Y^{(2)} - \sin\varphi X^{(2)}) \right\rangle \quad (4.57)$$

$$= \frac{1 - \cos 2\varphi}{2} \langle X^{(1)}X^{(2)} \rangle + \frac{1 + \cos 2\varphi}{2} \langle Y^{(1)}Y^{(2)} \rangle \quad (4.58)$$

$$- \frac{\sin 2\varphi}{2} \langle X^{(1)}Y^{(2)} + Y^{(1)}X^{(2)} \rangle. \quad (4.59)$$

The last expression shows that the measurement result as a function of φ has an amplitude that is equal to twice that of the last two terms in Eq. (4.54). We call this curve the parity, $\Pi(\varphi)$. Because the parity curve has twice the amplitude of the off-diagonal elements in the fidelity in Eq. (4.54), the contrast of the curve, Π_c , is four times bigger than the off-diagonal fidelity terms. Putting this all together implies that the fidelity is measured by,

$$F = \frac{1}{2}(\rho_{\downarrow\downarrow, \downarrow\downarrow} + \rho_{\uparrow\uparrow, \uparrow\uparrow}) + \frac{1}{4}\Pi_c \quad (4.60)$$

The data shown in fig. 4.6 shows a measurement of this operator after the preparation of an entangled state using the bichromatic force described above. Note that it is crucial that the RF used for the $\pi/2$ pulse have a well defined phase relationship to the phase ϕ_{ms} . In our case this is assured by using a set of phase locked DDSs to generate the red and blue sideband and carrier drives, which we respectively denote as $\{\nu_r, \nu_b, \nu_c\}$. Since the DDSs are digitally programmed, a stable phase relationship

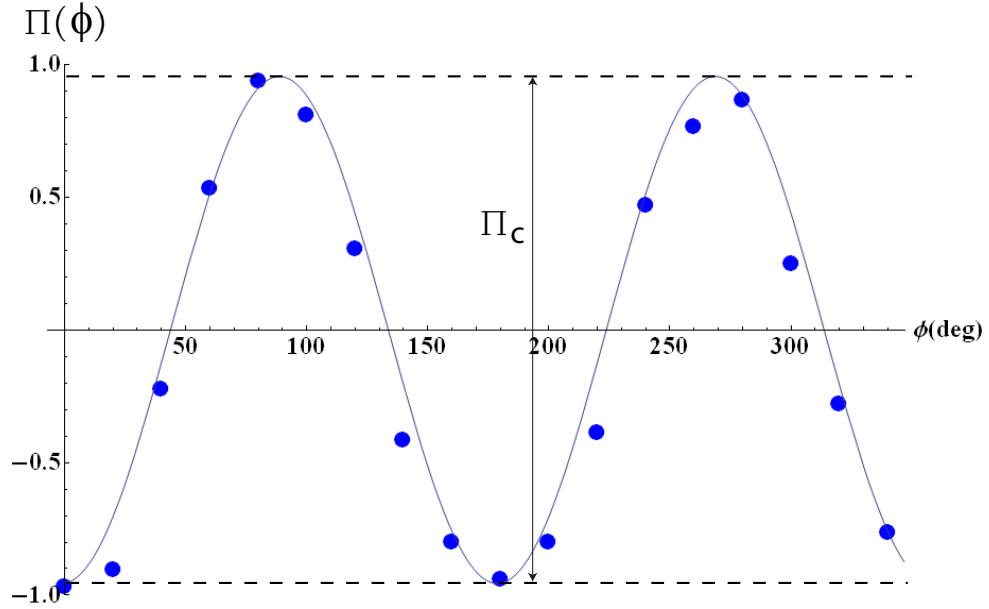


Figure 4.6: The contrast of this curve, $\Pi(\phi)$, together with a measurement in the standard basis is a measurement of the state fidelity after applying the Mølmer-Sørensen interaction. The contrast of this curve together with a measurement of the populations shows that state fidelity was $F = 0.97 \pm 0.01$.

is achieved by programming the carrier frequency to be $\nu_c = \frac{\nu_r + \nu_b}{2}$. If this frequency is not chosen precisely, the phase relationship between the gate and the analyzing will drift over the time that is needed to take the parity curve, effectively washing out the signal. The data shown in this section demonstrates that a 355 nm pulsed laser system is an effective means of executing high fidelity entangling operations between hyperfine qubits in $^{171}\text{Yb}^+$. The fidelity can likely be increased further by going to higher trapping frequencies, where the gate time can be reduced so as to further suppress heating and other noise sources.

4.3 Coherent Error Suppression in Mølmer-Sørensen Operations

Like any quantum operation, the bichromatic gate is sensitive to many potential sources of error. One source of error that is observed in the laboratory is a fluctuating detuning δ that can arise from a fluctuating trapping frequency. Because the spin and motion disentangle at times that are multiples of $2\pi/\delta$, any fluctuation in the trapping frequency will lead to residual entanglement between the spin and motion, thereby leaving the spin in a mixed state. The required level of precision grows with higher temperatures since the overlap between two states separated in phase decreases exponentially with temperature. To see this, consider a qubit under the influence of the spin-dependent force. If the initial motional state is assumed to be a Gaussian state, $\psi(x)$, with an uncertainty in position, Δx , and we describe a small detuning or timing error in the gate operation as an unintentional momentum displacement, $\hbar q$, then the overlap between the two motional states is given by $\int_{-\infty}^{\infty} dx \psi^*(x) e^{-iqx} \psi(x) = \exp[-\frac{1}{2}(q\Delta x)^2]$. For a harmonic oscillator in a thermal state, Δx increases approximately as \sqrt{T} for $k_B T > \hbar\omega$, meaning that the overlap between the two states decreases exponentially. As I will show in this section, a composite pulse can be designed that suppresses this type of error to any desired order [65].

If the trapping frequency fluctuates on a time scale that is slow compared to the gate time, then the detuning can be considered as static during a single experiment. If the detuning is given by $2\pi/t_g + \Delta$, where Δ is the fluctuation in the trap frequency, then the final displacement of the different wavepackets is

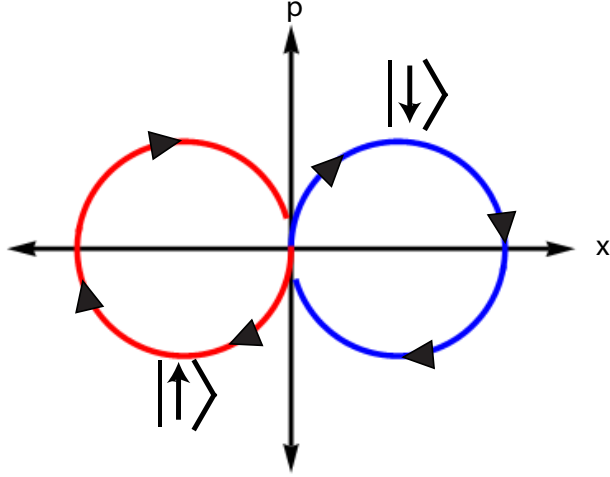


Figure 4.7: This figure is an illustration of the effect of a fluctuating trap frequency on the bichromatic force operation. In this case, the detuning, δ , is too small for the chosen gate time. This error implies that the orbits executed in phase space do not close and thereby leave the spin and motion entangled to some degree.

$\pm\alpha(t) = \mp \frac{\eta\Omega}{2(2\pi/t_g + \Delta)} (e^{i\Delta t} - 1)$ as illustrated in Fig. 4.7. The fact that $\alpha(t)$ is non-zero at the end of the operation implies some residual entanglement between the spin and motional degrees of freedom. If the parameter Δ is small compared to $2\pi/t_g$, then the fidelity of the operation can be expanded using Eq. (4.37) so that,

$$F = 1 - P_{\uparrow\downarrow}(t_g, \delta + \Delta) \quad (4.61)$$

$$= \frac{1}{2} \left(1 + e^{-\bar{n}+1/2} \left| \frac{\eta\Omega}{2(2\pi/t_g + \Delta)} (e^{i\Delta t} - 1) \right|^2 \right) \quad (4.62)$$

$$= 1 - \frac{2\pi^2 (\eta\Omega)^2 (\bar{n} + 1/2)}{\delta^4} \Delta^2 + \mathcal{O}(\Delta^3). \quad (4.63)$$

The fidelity for the one-ion operation is calculated by assuming a target state where the spin and motion are completely decoupled, which in the case of a single

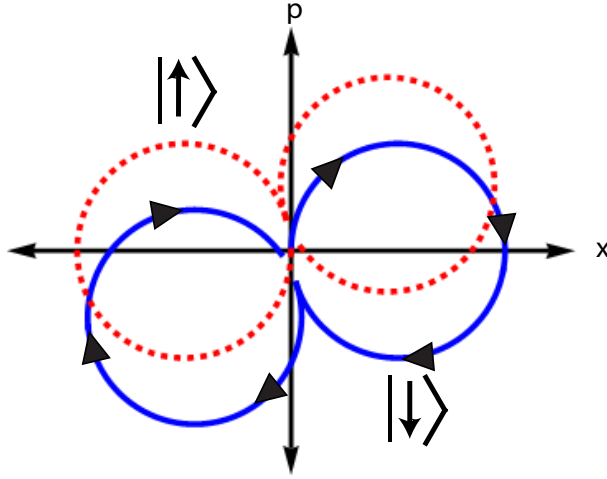


Figure 4.8: The effect of adding a second pulse to the bichromatic gate is shown here. The solid and dashed curves show the two different trajectories taken by the two different wave packets associated with spin up and spin down in the \hat{S}_ϕ basis with only the spin up trajectory being labeled for clarity. When the initial phase of the second pulse is chosen to be opposite that of the first pulse, it is clear that the final displacement from the origin is significantly reduced, thereby reducing the amount of residual entanglement between the spin and motion.

ion, implies a restoration of the initial spin state. If a second phase space trajectory is added to the operation where the initial phase of the force is opposite of the first trajectory, then the error incurred in the first operation will largely be canceled by the second operation as illustrated in fig. 4.8. Note that the direction of the spin-dependent force can be inverted by the mapping $H \Rightarrow -H$ which can be affected by either changing the spin phase $\phi_s = \frac{\phi_r + \phi_b}{2}$ by π or by changing the motional phase $\phi_m = \frac{\phi_r - \phi_b}{2}$ by π . The error suppression of this composite operation can be quantified by considering two separate spin dependent force operations. If two spin dependent force operations are applied with the first parameterized by the

displacement α_1 and the second by α_2 , then the final state is given by,

$$\hat{U}_2 \hat{U}_1 | \downarrow_z, \beta \rangle = \frac{1}{\sqrt{2}} \hat{D}_2 \left(\hat{D}(\alpha_1) | \uparrow_{\phi_s} \rangle - \hat{D}(-\alpha_1) | \downarrow_{\phi_s} \rangle \right) | \beta \rangle \quad (4.64)$$

$$= \frac{e^{i\text{Im}[\alpha_2 \alpha_1^*]}}{\sqrt{2}} \left(\hat{D}(\alpha_1 + \alpha_2) | \uparrow_{\phi_s} \rangle - \hat{D}(-\alpha_1 - \alpha_2) | \downarrow_{\phi_s} \rangle \right) | \beta \rangle. \quad (4.65)$$

If the first pulse is executed using $\phi_s = 0$ and the second is executed using $\phi_s = \pi$, the first displacement is $\alpha_1 = \frac{\eta\Omega}{2(2\pi/t_g + \Delta)} (e^{i\Delta 2\pi/\delta} - 1)$ and the second is $\alpha_2 = -\frac{\eta\Omega}{2(2\pi/t_g + \Delta)} (e^{i\Delta 4\pi/\delta} - e^{i\Delta 2\pi/\delta})$ and the fidelity is,

$$F = 1 - P_{\uparrow\downarrow}(t_g, \delta + \Delta) \quad (4.66)$$

$$= \frac{1}{2} \left(1 + e^{-(\bar{n}+1/2)} \left| \frac{\eta\Omega}{2(2\pi/t_g + \Delta)} (e^{i\Delta 2\pi/\delta} - 1 - (e^{i\Delta 4\pi/\delta} - e^{i\Delta 2\pi/\delta})) \right|^2 \right) \quad (4.67)$$

$$= 1 - \frac{8\pi^4 (\eta\Omega)^2 (\bar{n} + 1/2)}{\delta^6} \Delta^4 + \mathcal{O}(\Delta^5), \quad (4.68)$$

showing that the error has been pushed to higher order in Δ . It is straightforward to generalize this calculation to an arbitrary number of pulses. Using a thermal state for the initial motional state, the probability $P_{\uparrow\downarrow}(\alpha_1, \dots, \alpha_n)$ for n displacement operations is given by,

$$\langle | \uparrow \rangle \langle \uparrow | \rangle = \frac{1}{2} \left(1 - \exp \left[- \left| 2 \sum_{j=1}^n \alpha_j \right|^2 (\bar{n} + 1/2) \right] \right) \quad (4.69)$$

The sum in Eq. (4.69) can be rewritten as,

$$\sum_{j=1}^n \alpha_j = \frac{\eta\Omega}{2} \sum_{j=1}^n \int_{t_{j-1}}^{t_j} dt e^{-i\phi_m^{(j)} e^{i(\delta+\Delta)t}}, \quad (4.70)$$

where $t_0 = 0$ and $t_n = t_g$. If the phase ϕ_s switches between 0 and π , then the function $e^{i\phi_s}$ that appears in the time evolution operator can be replaced by a time dependent function which switches between ± 1 . Because the phase flips occur when the wave packets are near the origin of phase space, they will occur at integer multiples of $2\pi/\delta$. This allows the time dependent phase to be represented by Walsh functions, $\text{WAL}(k, t/t_g)$, so that Eq. (4.70) can be rewritten as,

$$\frac{\eta\Omega}{2} \sum_{j=1}^n \int_{t_{j-1}}^{t_j} dt e^{-i\phi_m^{(j)} e^{i(\delta+\Delta)t}} = \frac{\eta\Omega}{2} \int_0^{t_g} dt \text{WAL}(k, t/t_g) e^{i(\delta+\Delta)t}, \quad (4.71)$$

where the index k specifies the times at which phase flips occur. Walsh functions are piecewise constant functions that form a complete orthonormal set that alternate between ± 1 at times that are specified by the index k , see fig. 4.9. I will now show that by choosing specific Walsh functions for the modulation of the phase ϕ_m , the integral in Eq. (4.71) can be made arbitrarily small, thereby eliminating the residual spin-motion entanglement. The proof of this requires a precise definition of the Walsh functions. Several ways of ordering Walsh functions exist and here we use the dyadic ordering, or Payley ordering [66]. This particular ordering allows for the Walsh functions to be defined in terms of Rademacher functions, which are square waves defined as $R(n, x) \equiv \text{sign}[\sin(2^n \pi x)]$. These functions allow the Walsh

functions to be defined as,

$$\text{WAL}(k, x) \equiv \prod_{i=1}^{m+1} \text{R}(i, x)^{b_i-1}, \quad (4.72)$$

where k is expressed as a binary number $k = b_m 2^m + \dots + b_0 2^0$ and $b_i = 0$ or 1 .

With this definition it can be shown that,

$$\int_0^1 dx \text{WAL}(2^n - 1, x) e^{i2^{n+1}\pi x} \sum_{l=0}^n a_l x^l = 0, \quad (4.73)$$

where a_l are constant coefficients. A proof of Eq. (4.73) is given in appendix C.

Putting this all together gives an expression for the fidelity of a composite pulse

using the Walsh function of index $k = 2^n - 1$,

$$F_n = 1 - \langle |\uparrow\rangle \langle \uparrow| \rangle \quad (4.74)$$

$$= \frac{1}{2} \left(1 + \exp \left[- \left| 2 \sum_{i=1}^n \alpha_i \right|^2 (\bar{n} + 1/2) \right] \right) \quad (4.75)$$

$$= \frac{1}{2} \left(1 + \exp \left[-4 |\mathcal{O}(\Delta^{n+1})|^2 (\bar{n} + 1/2) \right] \right). \quad (4.76)$$

The scaling of the infidelity of the operation scales with the error Δ is found by choosing the Walsh index dependent detuning that optimizes the two ion entangling gate for speed $\delta_k = \sqrt{k+1} = 2^{n/2} \eta \Omega$, (shown in the next section), and expanding

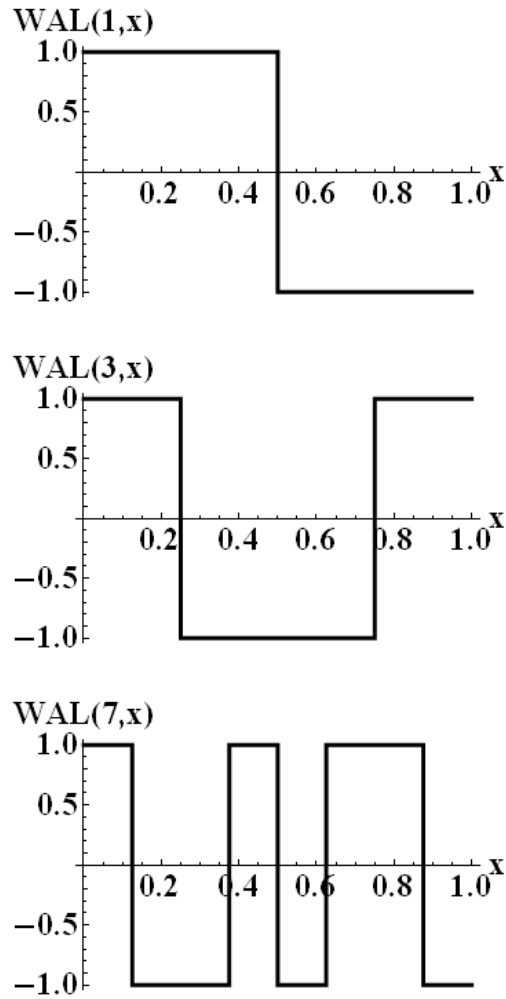


Figure 4.9: The Walsh functions $\text{WAL}(1, x)$, $\text{WAL}(3, x)$ and $\text{WAL}(7, x)$ are shown. Notice that $\text{WAL}(3, x)$ can be constructed as two sequential $\text{WAL}(1, x)$ functions with a phase flip on the second pulse. Likewise, $\text{WAL}(7, x)$ can be constructed as sequential $\text{WAL}(3, x)$ pulses with a phase flip on the second pulse.

around $\Delta = 0$ for the first few Walsh functions,

$$F_0 = 1 - \frac{2\pi^2 (\eta\Omega)^2 (\bar{n} + 1/2)}{\delta_0^4} \Delta^2 + \mathcal{O}(\Delta^3) \quad (4.77)$$

$$= 1 - (\bar{n} + 1/2) \left(\frac{\pi\Delta}{\sqrt{2}\eta\Omega} \right)^2 + \mathcal{O}(\Delta^3) \quad (4.78)$$

$$F_1 = 1 - \frac{8\pi^4 (\eta\Omega)^2 (\bar{n} + 1/2)}{\delta_1^6} \Delta^4 + \mathcal{O}(\Delta^5) \quad (4.79)$$

$$= 1 - (\bar{n} + 1/2) \left(\frac{\pi\Delta}{\sqrt{2}\eta\Omega} \right)^4 + \mathcal{O}(\Delta^5) \quad (4.80)$$

$$F_3 = 1 - \frac{128\pi^6 (\eta\Omega)^2 (\bar{n} + 1/2)}{\delta_3^8} \Delta^6 + \mathcal{O}(\Delta^7) \quad (4.81)$$

$$= 1 - (\bar{n} + 1/2) \left(\frac{\pi\Delta}{\sqrt{2}\eta\Omega} \right)^6 + \mathcal{O}(\Delta^7). \quad (4.82)$$

This effect was demonstrated using the Vanguard 355 nm laser system with a single $^{171}\text{Yb}^+$ ion in the four-rod trap with a 1.8 MHz trapping frequency. To impart the spin-dependent force, we drive one of the AOMs with two frequencies tuned close to the red and blue first order sidebands. The phase of these RF drives can be shifted on demand as triggered by a single TTL pulse. In order to change the phase of the spin-dependent force by π , without changing the spin basis that the force is diagonal in, we change both of these phases by π such that $\Delta\phi_s = \pi$ and $\Delta\phi_m = 0$. As can be seen in the data in fig. 4.10, the higher order Walsh sequences exhibit spin revivals of high purity over a much larger range of detunings in the neighborhood of $\delta = 2\pi/t_g$.

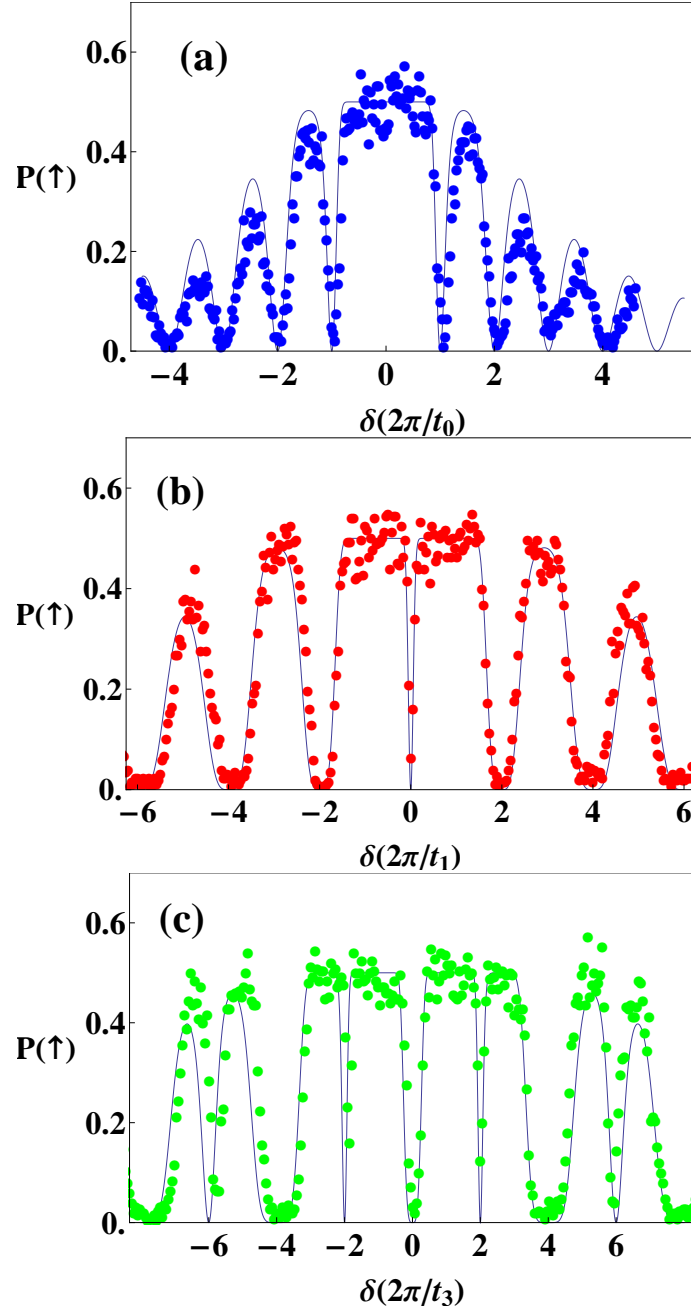


Figure 4.10: An ion prepared in $|\downarrow\rangle$ and $\bar{n} \approx 8$ is subjected to the standard and composite spin-dependent force operations. The data shown are plotted together with theoretical curves assuming an initial thermal state of motion. (a) The data show the probability of finding the ion in $|\uparrow\rangle$ as a function of the symmetric detuning δ for $t_0 = 100 \mu\text{s}$. (b) The operation is implemented using WAL(1, t/t_1) for the phase $\phi_s(t)$ with $t_1 = \sqrt{2}t_0$. (c) WAL(3, t/t_3) is used for $\phi_s(t)$ with $t_3 = 2t_0$. Note the narrow resonance at $\delta t_3/2\pi = 2$ corresponds to a trajectory where the phase flips occur when the motional wave packet is not at the origin of phase space.

4.4 Two Ion Walsh Gates

For two ions, the relative phase term $\Phi_k(t)$ must be included. We will be interested in finding the the evolution operator comprised of multiple pulses, with the evolution from a single pulse beginning at t_0 given by,

$$U(\delta, t, t_0) = D(\hat{S}\alpha_{\phi_m}(\delta, t, t_0))\exp\left[\frac{i\Omega^2\hat{S}^2}{4\delta}(t - t_0 - \frac{1}{\delta}\sin(\delta(t - t_0)))\right]. \quad (4.83)$$

The evolution due to two sequential operations is,

$$U_1U_0 = \exp\left[-\frac{i\Omega^2\hat{S}^2}{4\delta}(t_f - t_0 - \frac{1}{\delta}\sin(\delta(t_f - t_1)) - \frac{1}{\delta}\sin(\delta(t_1 - t_0)))\right]\hat{D}_1\hat{D}_0 \quad (4.84)$$

$$\hat{D}_1\hat{D}_0 = D(\hat{S}\alpha_1)D(\hat{S}\alpha_0) \quad (4.85)$$

$$= D(\hat{S}(\alpha_0 + \alpha_1))\exp\left[\frac{1}{2}\hat{S}^2(\alpha_1^*\alpha_0 - \alpha_1\alpha_0^*)\right] \quad (4.86)$$

For three pulses, the three displacement operators multiply together to give

$$D_2D_1D_0 = \hat{D}(\hat{S}\sum_{i=0}^2\alpha_i)\exp\left[\frac{1}{2}\hat{S}^2(\alpha_2^*\alpha_1 - \alpha_2\alpha_1^* + \alpha_1^*\alpha_0 + \alpha_2^*\alpha_0 - \alpha_1\alpha_0^* - \alpha_2\alpha_0^*)\right] \quad (4.87)$$

Notice that all the different phase terms add up so that the real parts cancel allowing us to redefine the spin-dependent phase for N pulses as,

$$U = e^{-i\hat{S}^2\Phi_N(t)}\hat{D}\left(\hat{S}\sum_{i=0}^N\alpha_i\right) \quad (4.88)$$

$$\Phi_N(t) \equiv \sum_{i>j=0}^N \text{Im}[\alpha_i^*\alpha_j] - \left(\frac{\eta\Omega}{2\delta}\right)^2 (\delta(t_{N+1} - t_0) - \sum_{i=0}^N \sin(\delta(t_{i+1} - t_i))) \quad (4.89)$$

Using this expression for the evolution operator, we can calculate the state fidelity for the gate assuming a detuning error Δ . We'll denote the perfect evolution operator as U and the one that describes the error as $U_\Delta \equiv U(\delta + \Delta)$ and write the fidelity as,

$$F(\Delta) = \sum_{\beta} P_{\beta} \text{Tr} \left[U_{\Delta} | \downarrow\downarrow, \beta \rangle \langle \downarrow\downarrow, \beta | U_{\Delta}^{\dagger} U | \downarrow\downarrow, \beta \rangle \langle \downarrow\downarrow, \beta | U^{\dagger} \right] \quad (4.90)$$

After some algebra the fidelity can be written as,

$$F(\Delta) = \frac{1}{4} \sum_{\beta} P_{\beta} \frac{1}{4} \left(-ie^{-i4\Phi_N} \langle \beta | D(-\sum_{i=0}^N \alpha_i) | \beta \rangle - ie^{-i4\Phi_N} \langle \beta | D(\sum_{i=0}^N \alpha_i) | \beta \rangle + 2 \right) \\ \left(ie^{i4\Phi_N} \langle \beta | D(\sum_{i=0}^N \alpha_i) | \beta \rangle + ie^{i4\Phi_N} \langle \beta | D(-\sum_{i=0}^N \alpha_i) | \beta \rangle + 2 \right) \quad (4.91)$$

$$= \frac{1}{4} \left| e^{-|\sum_{i=0}^N \alpha_i|^2(\bar{n}+1/2)} + ie^{i4\Phi_N} \right|^2, \quad (4.92)$$

where both the final displacement $\sum_{i=0}^N \alpha_i$ and the phase Φ_N depend on the detuning $\delta + \Delta$. The temperature dependence in the expression for the fidelity in Eq. (4.92) is scaled by the final displacement, which becomes more resistant to detuning errors for higher order Walsh functions as shown in the discussion of single ion composite

pulses. The other term in the expression for the fidelity that comes from the spin-dependent phase Φ_N in the evolution operator does not obey the same scaling law as the displacement term. Therefore, we are prevented from writing down a simple expression for how the fidelity scales with detuning errors as we did in the case of one ion. However, numerical evaluation of the phase Φ_N shows that it too becomes more robust to detuning errors for higher order sequences, albeit not as strongly as the displacement term. By plotting the fidelity as a function of the detuning error Δ , as in fig. 4.11, it is clear that the higher order Walsh sequences are effective in suppressing the coherent errors stemming from detuning errors.

The gate times for the composite entangling operations are not equal to the gate time for the standard operation. The spin dependent phase Φ_N is proportional to the area swept out in phase space and the number of closed circles executed when using WAL($2^n - 1$) is equal to $2^n = k + 1$. The form of the identity in Eq. (4.73) implies that the total gate time for the gate using the Walsh function of index k is $t_g^{(k)} = (k + 1)2\pi/\delta_k$. To see how the gate is to be altered, note that the total phase accumulated during the gate should be independent of which sequence is used. So for a given Rabi frequency, we can write,

$$\Phi_0 = \Phi_k \tag{4.93}$$

$$\frac{t_g^{(0)}}{\delta_0} = \frac{t_g^{(k)}}{\delta_k} \tag{4.94}$$

$$\frac{2\pi}{\delta_0^2} = \frac{(k + 1)2\pi}{\delta_k^2} \tag{4.95}$$

$$\delta_k = \sqrt{k + 1}\delta_0 = 2^{n/2+1}\eta\Omega. \tag{4.96}$$

This implies that the composite pulse gate time must be at least $t_g = 2^{n/2}\pi/\eta\Omega$ with the detuning being optimized at $\delta = 2^{n/2+1}\eta\Omega$. While the exponential nature of the gate time becomes daunting for large n , small errors can easily be corrected with a modest increase in the gate time. The increasing gate time means that increasingly complex gate sequences will eventually perform worse than simpler ones as the gate becomes sensitive to other noise sources such as laser power fluctuations or spontaneous scattering events. It is, however, worth noting that the extra time needed for performing the modulated sequence might be partially offset by the decreased sensitivity to the initial to the initial temperature of the oscillator, thereby reducing the amount of resource intensive cooling that may be needed.

The two ion Walsh gate was tested using two $^{171}\text{Yb}^+$ ions in a 1.8 MHz trap. The beat note was set to be near resonant with the tilt mode since it is less susceptible to heating than the COM mode [67]. The state fidelity measurement for the MS gate is compared for the different pulse sequences in Fig. 4.11. The increased robustness to detuning errors can be quantified by defining a characteristic width of the high fidelity region, which is referred to as the passband B_k . Since the smallest infidelity in the data sets is of order 0.1, we choose to define the passband as the range of detunings where the infidelity is always observed to be lower than 0.2 and estimate $B_0 \approx 0.5$ kHz, $B_1 \approx 0.7$ kHz, and $B_3 \approx 1.5$ kHz, demonstrating the composite sequences' tendency to suppress symmetric detuning errors. The maximum fidelities observed for the sequences $k = \{0, 1, 3\}$ are, respectively, $F_2 = \{0.91 \pm 0.02, 0.92 \pm 0.02, 0.95 \pm 0.01\}$. The relative modest increase in the maximum fidelity achieved indicates that the trapping frequency is not changing

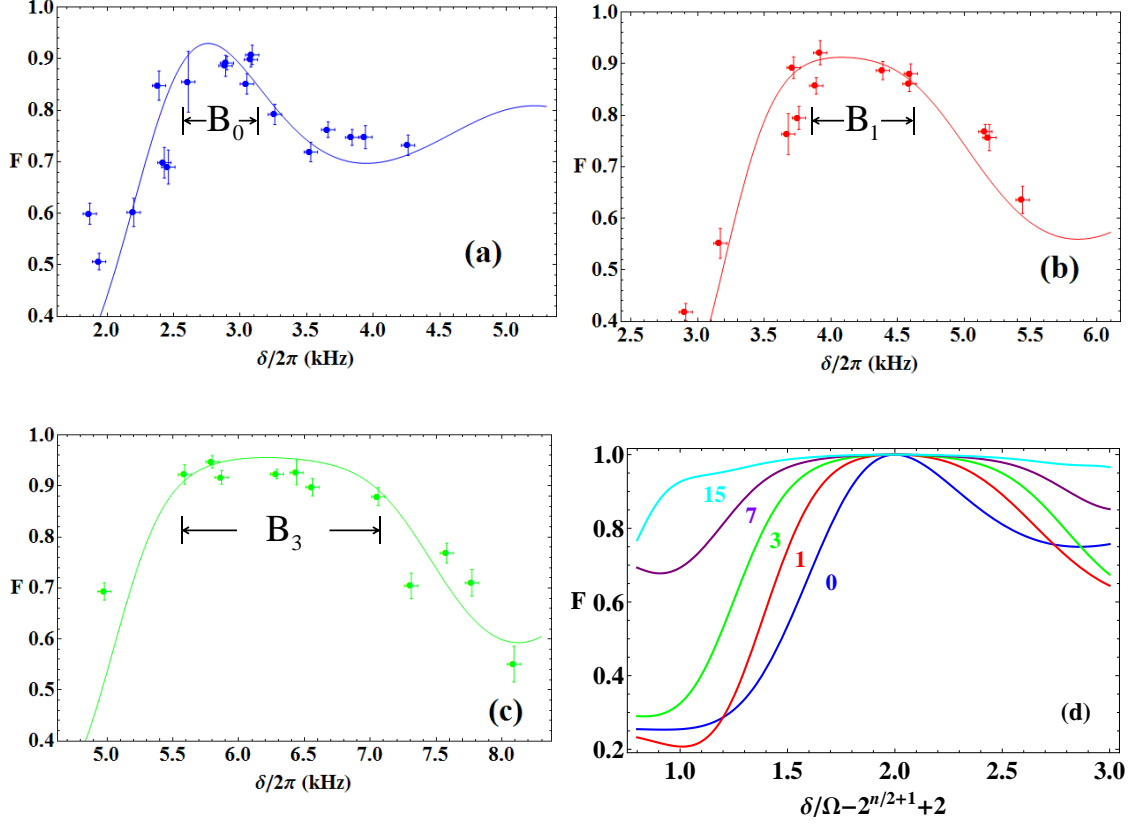


Figure 4.11: The state fidelity of a two ion MS gate as a function of the symmetric detuning δ is compared for the first three Walsh gates. In all three data sets, the ions were sideband cooled to the motional ground state before implementing the gate. In figures (a)-(c), the measured fidelity as a function of the detuning δ is compared with the theoretical curves. (d) shows the ideal fidelity curves for $W(0)$ (blue), $W(1)$ (red), $W(3)$ (green), $W(7)$ (purple) and $W(15)$ (cyan). The curves are shifted in frequency in order to facilitate comparison and highlight the increasingly large regions of high fidelity for the higher order sequences. As a guide to the eye, the ideal curves shown in (d) are fit to the data by varying $\eta\Omega$ and including an overall scale factor to account for additional experimental imperfections. The three different fit values of $\eta\Omega$ agree with each other to within 10%. The estimates for the characteristic widths of the high fidelity regions, B_k , are shown to increase rapidly with the higher order sequences.

significantly, (1 kHz), on a time scale of less than the time between recalibrations of the detuning δ , which is approximately 5 min. We observed trap frequency fluctuations of 1 kHz on a time scale of about 1 hour.

In this chapter, I have demonstrated high fidelity entangling operations between neighboring ions using spin-dependent forces generated by Raman transitions. An extension of the standard entangling operation was shown to provide protection against trap frequency fluctuations. This dynamic error suppression might prove to be crucial to the long term stability of a quantum information processor based on qubits coupled through collective harmonic oscillator modes.

Chapter 5

Photon mediated entanglement of ions

The most obvious photonic degree of freedom for encoding quantum information is the polarization [68], which forms a natural qubit, but one can also choose the frequency [69], orbital angular momentum [70] or time-bin degree of freedom [71]. There are many proposals for quantum computing with optical fields and a lot of progress has been made in demonstrating the necessary primitives including one and two qubit gates [10], but a quantum memory based on photonic qubits faces difficult challenges. In fact, many research groups are working toward photon storage inside material quantum systems [72, 73, 74]. The experiments described in this thesis do not address manipulation of quantum information stored in photon qubits, but rather they are used as an intermediary agent to create effective interactions between atomic qubits. The experiments described in this thesis use frequency encoded qubits, but a good review of how different encodings can be used in conjunction with trapped ions can be found in [75].

The underlying principle allowing the entanglement of spatially disparate atomic qubits is known as entanglement swapping. Entanglement generally requires an interaction between constituent entities, but not necessarily between every member of the group. If, for example, one can entangle two spatially separated ions with respective optical modes and then measure the state of the photons in an entangled

basis, the ions may be projected into an entangled state without ever having directly interacted with one another. The basic idea is to set up the measuring apparatus so as to erase any information that might betray the origin of the photon(s). While these protocols are extremely useful for generating remote entanglement between disparate atomic qubits, they are inherently probabilistic. Here, I review two different protocols for entangling ions using scattered photons. The first type is explained only in a theoretical setting as we have not carried out any experiments using the protocol, whereas the second protocol is described in the context of the experiments that were performed in our laboratory.

5.1 Entangling atoms by detecting a single photon

The first method of entangling ions through scattered photons, (type I), uses only one photon and a single photon detector that is incapable of discerning which atom emitted the photon [76]. In the simplest case, we consider two three-level atoms that are both initialized to their internal ground states $|0\rangle$. We then imagine simultaneously exciting the atoms with a weak laser pulse that is resonant with the transition $|0\rangle \Leftrightarrow |e\rangle$ and generates the following transformation,

$$\Psi_0 = |00\rangle \Rightarrow \Psi_1 = \sqrt{(1 - P_e)}|00\rangle + \sqrt{P_e}(|0e\rangle + |e0\rangle) + \mathcal{O}(P_e^2), \quad (5.1)$$

where P_e is the probability of a single atom absorbing a photon from the laser pulse. The state $|e\rangle$ is unstable and can decay back to $|0\rangle$ or to a third state $|1\rangle$. The detector will be placed somewhere so that the polarization of the spontaneously

emitted photon associated with the $|e\rangle \rightarrow |0\rangle$ decay channel is orthogonal to the polarization of a photon resulting from a $|e\rangle \rightarrow |1\rangle$ transition. If a polarizer is placed in front of the detector so as to block the photons resulting from the $|e\rangle \rightarrow |0\rangle$ transition, the detection of a scattered photon heralds the creation of the state,

$$\Psi_2 = \sqrt{(P_e)} (e^{i\theta_1}|01\rangle + e^{i\theta_2}|10\rangle) + \mathcal{O}(P_e^2). \quad (5.2)$$

If the excitation pulse has an intensity such that $P_e \ll 1$, then the state is approximately given by,

$$\Psi_2 \approx e^{i\theta_1}|01\rangle + e^{i\theta_2}|10\rangle, \quad (5.3)$$

showing that the detection of a single photon yields a maximally entangled state to $\mathcal{O}(P_e^2)$. If the probability of detecting a single photon is P_{det} , then the probability of successfully generating the entangled state is $P_{succ} \approx P_e P_{det}$. If the phase $e^{i\theta_1}$ is considered to be global and factored out of the state, the relative phase $e^{-i(\theta_1-\theta_2)}$ is given by the relative path lengths of the two possible photon paths in units of the transition wavelength $\lambda_{e,1}$, i.e. $e^{-i(\theta_1-\theta_2)} = e^{-i(k_{e,1}x_1 - k_{e,1}x_2)} = e^{-ik_{e,1}(x_1-x_2)}$. The interferometric stability of the path lengths required for the phase stability presents a technical challenge for the type I protocol in general. This protocol was recently demonstrated and reported on in [77].

The type I protocol can not only be used to connect distant ions, but can also be used to generate large entangled states of ions that reside in a single trap. This protocol has the advantages that large entangled states can be generated with a

single laser pulse and if the ions are in a single trap, the interferometric stability issue would largely be mitigated. In the case of N ions, the type I protocol is capable of generating what is known as a W-state, which has a single excitation that is symmetrically distributed throughout the system,

$$|\tilde{W}_N\rangle = \frac{1}{\sqrt{N}} (e^{i\theta_1}|00\dots001\rangle + e^{i\theta_2}|00\dots010\rangle + \dots + e^{i\theta_N}|10\dots000\rangle). \quad (5.4)$$

The notation $|\tilde{W}_N\rangle$ is used for the generalized W-state where the different phase factors present in the state are arbitrary, while the notation $|W_N\rangle$ will be used for a state where all of the phase factors are equal. While generating $|\tilde{W}_N\rangle$ sounds relatively simple in this protocol, proving that the state generated in the laboratory is actually the multipartite entangled W state can be quite difficult [78]. To measure the density matrix of an N qubit state requires 2^{2N} measurement settings and individual addressing in general, even though in some cases these requirements can be significantly loosened using compressed sensing [79] or other related techniques. It was, however, shown in [80] that the multipartite entanglement of the W-state can be detected by observing a negative expectation value of the witness operator $\frac{N-1}{N}\hat{\mathbb{I}} - |W_N\rangle\langle W_N|$. This implies that one simply has to measure the fidelity $F = \text{Tr}[\rho|W_N\rangle\langle W_N|]$ and get a value above $\frac{N-1}{N}$ to show that the state is multipartite entangled, a task that becomes prohibitive for large numbers of ions. By exploiting the symmetry of $|W_N\rangle$, it can be shown [81] that the witness operator can be measured by only $2N - 1$ measurement settings without the need for individual addressing, thereby significantly reducing the complexity of confirming the

multipartite entanglement of the state. The trade-off in using the witness operator instead of state tomography is that a witness operator might fail to detect multipartite entanglement if the fidelity is too low, i.e. a negative expectation value of the witness operator is a sufficient but not a necessary requirement for the verification of multipartite entanglement.

The fidelity of the W-state that can be generated in a typical ion trap setup can be calculated by drawing a parallel between the storage of coherence in the atoms through an inelastic scattering event and the coherence in the light field through an elastic scattering event. A scattering event is called elastic if the atom returns to the original internal energy state and inelastic if it ends up in a different state. The experiment described in [82], where two mercury ions in a single trap were weakly excited by a resonant laser pulse, the position where scattered photons were detected was shown to exhibit an interference pattern in elastic scattering events but no interference in inelastic scattering events. In the case of elastic scattering, because both ions will be in the same state after the scattering event, no information about which ion scattered the photon will exist, allowing the different optical paths to interfere [82, 83]. In an inelastic scattering event, one of the ions will be found in a different state upon measurement, thereby betraying the path taken by the photon and inhibiting the interference of the two possible paths. This is reminiscent of the famous discussions between Einstein and Bohr about Young's double slit experiment. In a gedanken experiment, Einstein imagined a small measuring apparatus that was capable of determining which of the two slits that a single photon had passed through, thereby showing that quantum theory must be wrong in predicting that

even single photons were somehow passing through both slits. Of course, it was subsequently shown that any such measuring apparatus would have a back-action effect on the photon in question that resulted in the interference pattern being washed out, thereby keeping quantum theory safely intact. The mercury experiment in [82] definitively demonstrates the precision of Bohr's conclusions.

The elastic scattering events yield an interference pattern with the regions of high intensity being where the photon phases $e^{-i\vec{k}\cdot\vec{R}}$ add constructively. In the case of inelastic scattering, the photon phase $e^{-i\vec{k}\cdot\vec{R}}$ gets imprinted on the ions upon detection of a photon. The ions will also pick up a dynamical phase $e^{i\omega t}$, where t is the time it takes for the photon to reach the detector, and ω is the frequency difference between $|0\rangle$ and $|1\rangle$. If the time that a photon takes to traverse the full length of the ion crystal is short compared to ω^{-1} , this dynamical factor can be ignored. If we use the $|F = 1, m_f = 0\rangle$ and $|F = 1, m_f = 1\rangle$ states in $^{171}\text{Yb}^+$, the Zeeman splitting with a magnetic field on the order of a few Gauss makes this approximation valid for ion crystals much smaller than one meter. When this approximation is valid, the regions of high intensity in the elastic case are the same points at which the detection of a photon in the inelastic case signals the creation of a W-state with all the phases being equal. Therefore, in order to identify scattering regions that herald a high fidelity W-state, it should suffice to calculate the elastic scattering cross-section for N ions in a trap and identify the high intensity region. In order to find the points of high intensity in the radiation pattern, we generalize the derivation of the scattering cross-section for two ions in a single trap [84] to N ions. Starting with the differential scattering cross-section as given by the electric

dipole Hamiltonian in second-order perturbation theory

$$\frac{d\sigma}{d\theta} = \sum_f \left| \sum_{p,j} \frac{\langle \Psi_f | \mathbf{D}_p \cdot \hat{\epsilon}_{out} e^{-i\vec{k}_{out} \cdot \mathbf{R}_p} | \Psi_j \rangle \langle \Psi_j | \mathbf{D}_p \cdot \hat{\epsilon}_{in} e^{-i\vec{k}_{in} \cdot \mathbf{R}_p} | \Psi_i \rangle}{\omega_0 - \omega_{in} + (E_j - E_i)/\hbar - i\Gamma/2} \right|^2, \quad (5.5)$$

where \mathbf{D}_p and \mathbf{R}_p are the dipole and position operators for the p^{th} ion, $\hat{\epsilon}$ is a polarization vector, \vec{k}_{in} and \vec{k}_{out} are incoming and outgoing wavevectors and the indices i and f represent the initial and final state of the ions. It is important to note that this expression only applies to elastic scattering events, since in this case the probability amplitudes for the photon scattering off different ions are added together because these processes are indistinguishable. The quantum states in the perturbation expansion are taken to be eigenvectors of the unperturbed Hamiltonian of N ions in a harmonic trapping potential and are therefore product states of the ions internal degrees of freedom and the motional state of the system.

We now examine the special case of the ion crystal axis lying in the plane defined by the incoming and outgoing wavevectors and the quantization axis being perpendicular to that plane. In this case, the dipole operator only contributes an overall scaling factor to the scattering cross-section and is therefore ignored in this calculation. As explained in [84], the denominators in Eq. (5.5) are nearly constant for the $^{171}\text{Yb}^+$ ion cooled near the Doppler limit on the 370 nm line as a consequence of the recoil frequency, 8.5 kHz, being small compared to the linewidth of 20 MHz. By considering the denominators to be nearly constant, they can be factored out of the sum allowing us to do the sums over the j and f indices via resolutions of the

identity operator, giving

$$\frac{d\sigma}{d\theta} = \langle \{n_{HO}\}_i | \sum_{p,p'} e^{-i(\vec{k}_{out}-\vec{k}_{in})\cdot(\mathbf{R}_p-\mathbf{R}_{p'})} | \{n_{HO}\}_i \rangle, \quad (5.6)$$

where $\{n_{HO}\}_i$ denotes the initial harmonic oscillator quantum numbers of the ions. Eq. (5.6) might be seen as a classical interference pattern from a diffraction grating comprised of slits that oscillate around fixed points and recoil upon deflection of light quanta. After taking the expectation value, the final scattering cross-section is given by

$$\frac{d\sigma}{d\theta} = \sum_{p,p'} e^{i\eta_\lambda(U_p-U_{p'})\Delta\hat{k}\cdot\hat{x}} \prod_{m=1}^N e^{-[(A_{p,m}-A_{p',m})\eta_a^m\Delta\hat{k}\cdot\hat{x}]^2(\bar{n}_a^m+1/2)-[(T_{p,m}-T_{p',m})\eta_t^m\Delta\hat{k}\cdot\hat{y}]^2(\bar{n}_t^m+1/2)}. \quad (5.7)$$

In the above equation, \bar{n}_a^m (\bar{n}_t^m) are the average number of axial (transverse) thermal quanta in mode m and $\eta_\lambda \equiv \left| \vec{k} \right| d$. U is a vector containing the equilibrium positions of the ions in units of length $d = (e^2/m(\omega_a^1)^2)^{1/3}$. The Lamb-Dicke parameter for the m^{th} mode in the axial (transverse) direction is $\eta_{a(t)}^m = \left| \vec{k} \right| (\hbar/(2m\omega_{a(t)}^m))^{1/2}$. The difference between incoming and outgoing wavevectors is $\Delta\hat{k} = \hat{k}_{out} - \hat{k}_{in}$, and $A_{p,m}$, $T_{p,m}$ are elements of the transformation matrices from position coordinates to axial and transverse normal coordinates, respectively.

The fidelity of the entangled state with arbitrary phase of two ions in separate isotropic harmonic traps (frequency ν and average thermal index \bar{n}) as derived in [76] is given by

$$F(\theta) = \int_0^\infty d\tau e^{-\tau} e^{-4\eta^2(\bar{n}+1/2)(1-\cos(\chi)\cos(\frac{\nu\tau}{\Gamma}))}, \quad (5.8)$$

with $\eta = k\sqrt{\hbar/2m\nu}$ and χ being the angle between the excitation beam and the emission direction. In the limit of weak confinement, $\nu \ll \Gamma$, and because the integrand decays exponentially in τ , we can approximate $\cos\left(\frac{\nu\tau}{\Gamma}\right) \approx 1$ allowing us to carry out the integration and arrive at

$$F(\theta) \approx e^{-4\eta^2(\bar{n}+1/2)[1-\cos\chi]} = e^{-8\eta^2(\bar{n}+1/2)[(\Delta\hat{k}\cdot\hat{x})^2 + (\Delta\hat{k}\cdot\hat{y})^2]} \quad (5.9)$$

This shows the relationship between Eq. (5.8) and the contrast of the fringes in Eq. (5.7). This suggests that the fringe contrast of Eq. (5.7) for $N = 2$ might be interpreted as the fidelity of the entangled state with arbitrary phase when two ions are in the same trap. Moreover, because the fringe peaks correspond to points of common phase, the full expression, (Eq. (5.7)), for $N = 2$ might be interpreted as the fidelity of the state where the relative phase is equal to zero. We contend that Eq. (5.7) should be a valid prediction of the fidelity of an N qubit W-state in the weak confinement regime, with $\eta_\lambda \gg 1$ ensuring no ion-ion photon exchange.

The emission pattern for three ions is plotted in fig. 5.1(a), clearly showing the degrading effect of recoil due to a large scattering angle. As a consequence of the ions not being evenly spaced, the scattering profile from ten ions in fig. 5.1(b) shows that the only points where radiation adds up in phase is in the forward scattering direction. This implies that in an inelastic scattering event, the only points where light detection will yield a W-state with all the terms having the same phase is in the forward scattering direction. The angular size of this spot, $\delta\theta$, in the case where the excitation pulse is along the crystal axis can be estimated by first normalizing

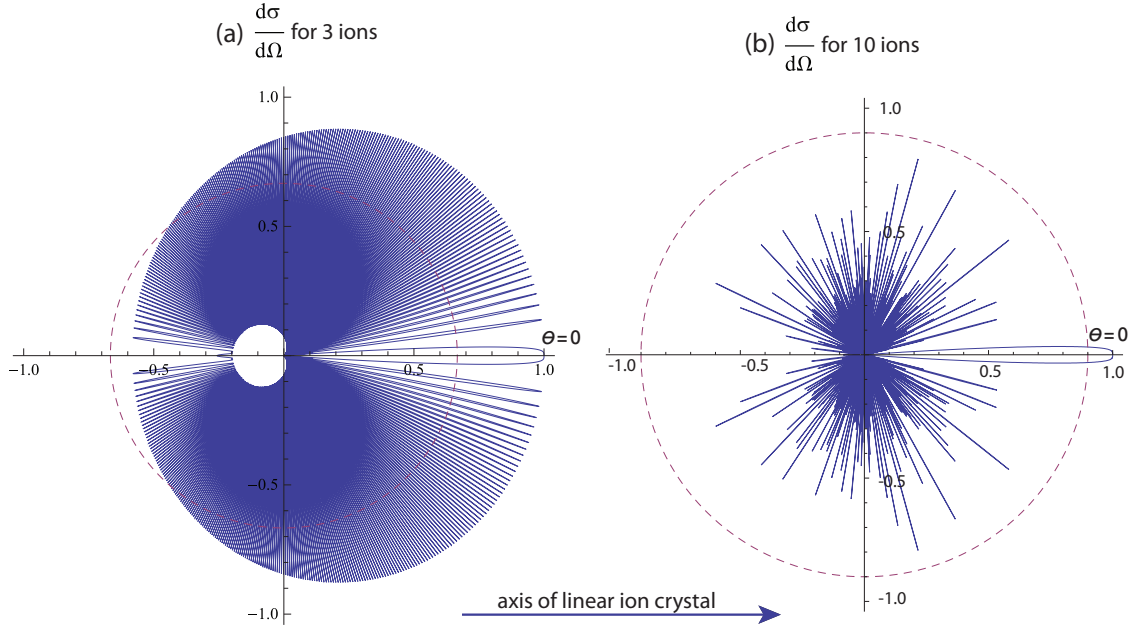


Figure 5.1: (a) The differential scattering cross section, in the plane defined by the ion crystal axis and the excitation vector, is shown in the polar plot with the excitation beam coming in along the ion crystal axis at $\theta = 0$. The dashed line represents the normalized intensity ($2/3$) required for a negative expectation value of the entanglement witness. For the example shown here, realistic trap parameters $\eta_\lambda = 600$, $\sqrt{\frac{\hbar k^2 \Gamma}{2m\omega_x^2}} = 1$ and $\frac{\omega_x}{\omega_y} = 10$ were chosen. (b) The scattering cross section for ten ions in a harmonic trap is plotted together with the required normalized intensity (0.9 , dashed circle) for a negative expectation value of the witness operator.

Eq. (5.7) by dividing by N^2 , ignoring the Debye-Waller factors and making the small scattering angle approximation, giving

$$\frac{d\sigma}{d\theta} \approx 1 - \frac{\delta\theta^4 \eta_\lambda^2}{4N^2} \sum_{p>p'} (U_p - U_{p'})^2. \quad (5.10)$$

The sum in Eq. (5.10) can be approximated by numerically solving for the equilibrium positions for different numbers of ions in a harmonic trap, which yields $\sum_{p>p'} (U_p - U_{p'})^2 \approx 0.45N^{2.87}$. We define the spot size to be the region where the intensity is at least f times the maximum and find the angular size of the spot to be approximately given by

$$2\delta\theta \approx 2 \frac{1.7(1-f)^{1/4}}{\eta_\lambda^{1/2}} N^{-0.21} \quad (5.11)$$

Remembering that the entanglement witness demands that the fidelity of the W-state be bounded by $F \geq \frac{N-1}{N}$, we set $f = \frac{N-1}{N}$. With the interpretation that the elastic scattering cross-section represents the fidelity of the W-state for an inelastic scattering event, the fraction of photons scattered into the plane of interest that will yield an N particle W-state is,

$$\frac{2\delta\theta}{2\pi} \approx \frac{0.55}{\eta_\lambda^{1/2}} N^{-0.46}. \quad (5.12)$$

Eq. (5.12) allows the estimation of an upper bound on the angle subtended by the detector being used to signal the creation of a multipartite entangled state. This scaling law shows that the efficiency with which one can create multipartite

entanglement decreases rather slowly with the number of entangled ions.

5.2 Entangling atoms through the detection of two photons

The second type of photonic interconnect, (type II), uses an entanglement swapping measurement that is triggered by the detection of two photons [85, 86]. The protocol works by first generating two photons, each of which is entangled with the internal state of a respective ion. These photons are then measured in an entangled basis which projects the ions into an entangled state. Here we describe a protocol that uses the frequency of the emitted light as the photon qubit.

Imagine two ions that are trapped in different vacuum chambers with the different positions x_1 and x_2 . The ions are first Doppler cooled and optically pumped to the state ${}^2S_{1/2}|F=0, m_f=0\rangle$, so that the state of the two ions is given by,

$$\Psi_0 = |00\rangle\psi(x_1)\psi(x_2), \quad (5.13)$$

where the functions $\psi(x_i)$ represent the motional state of the ions. Once the ions' spin state has been initialized, resonant microwaves can be used to generate arbitrary superposition spin states,

$$\Psi_1 = (\alpha|0\rangle + \beta|1\rangle)(\gamma|0\rangle + \delta|1\rangle)\psi(x_1)\psi(x_2). \quad (5.14)$$

In the next step, each ion is excited with an ultra-fast laser pulse whose center wavelength is resonant with the ${}^2S_{1/2} \leftrightarrow {}^2P_{1/2}$ transition. This laser pulse is generated by

a Ti:Sapphire mode-locked laser that generates picosecond pulses at a repetition rate $\nu_{rep} = 80$ MHz, a center wavelength near 739.05 nm and an average power of ≈ 1 W. A fast EOM is used pick a out a single pulse upon being triggered by an external TTL pulse. The single pulse is then directed through a critically phase matched BIBO crystal to generate a 369.5 nm pulse which is then directed toward one of the ions. The remaining unconverted 739 nm light is picked off using a dichroic mirror and sent through a second non-linear crystal to generate a resonant pulse for the second ion. A delay stage is inserted into the path of one of the pulses to ensure that the two pulses arrive at the two ions nearly simultaneously. In order to adjust the power and polarization of the pulses, a $\lambda/2$ waveplate followed by thin-film polarizer and another $\lambda/2$ waveplate is placed in the beam path. The first waveplate in conjunction with the polarizer is used to adjust the intensity of the pulse while the second waveplate is adjusted so that the pulse is $\hat{\pi}$ polarized. The intensity is set so that the light coherently transfers the population in the ${}^2S_{1/2}|m_f = 0\rangle$ states to the ${}^2P_{1/2}|m_f = 0\rangle$ states so that the state of the two ions becomes,

$$\Psi_2 = (\alpha|1'\rangle + \beta|0'\rangle) (\gamma|1'\rangle + \delta|0'\rangle) \psi(x_1)\psi(x_2) \quad (5.15)$$

where $|0'\rangle$ and $|1'\rangle$ are the $m_f = 0$ hyperfine levels in the ${}^2P_{1/2}$ manifold. The lifetime of the excited ${}^2P_{1/2}$ state is 8.12 nsec [87], which implies that after about 30 nsec, the ions will have spontaneously emitted photons in the random directions \vec{k}_i, \vec{k}_j . Since the excitation pulse is only 1 ps long, the probability of the ion absorbing a second photon is approximately $\frac{1 \text{ ps}}{8 \text{ ns}} \approx 10^{-4}$.

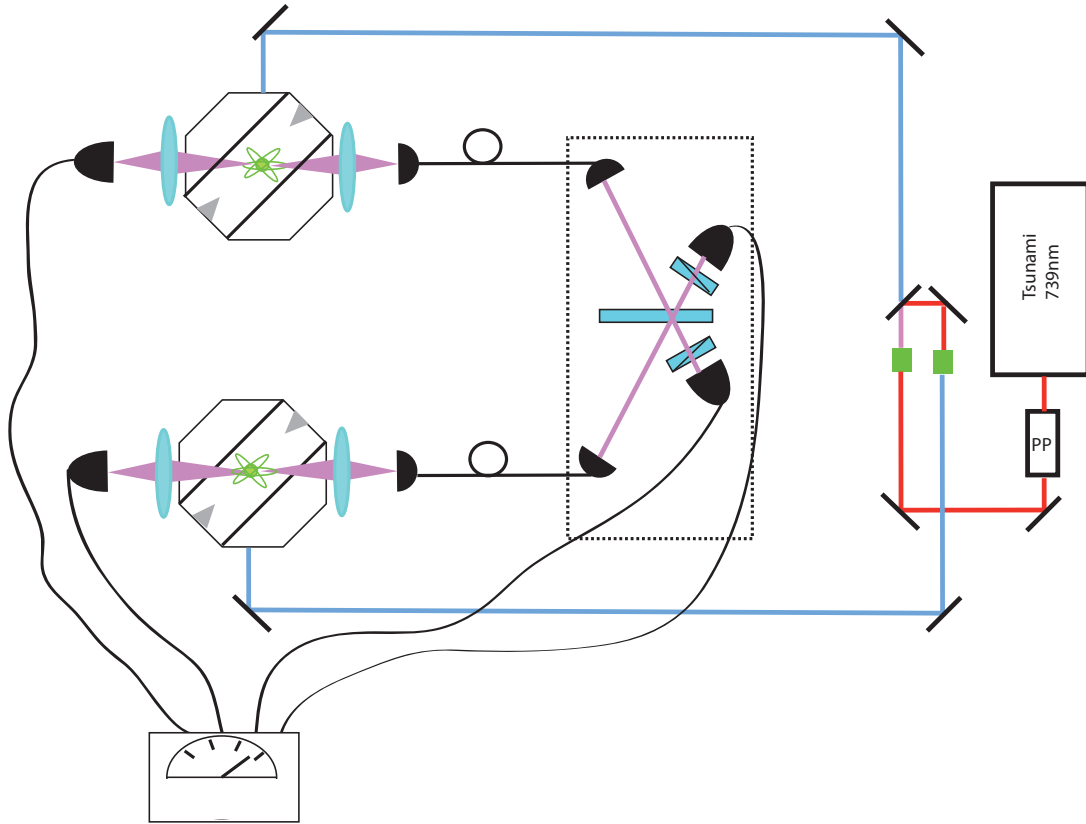


Figure 5.2: The figure shows two trapped ions that are separated by approximately 1 meter. A Ti:Sapph laser is tuned to 739 nm and directed through a pulse picker, (PP), to let through a single pulse on demand. The single pulse is frequency doubled by a non-linear crystal and then sent through a dichroic mirror to pick off the remaining 739 nm light which is then sent through a second doubling crystal. The resonant pulses are directed onto the two ions and the path lengths are adjusted so that the photons from different ions arrive at the beam splitter within about 100 psec of each other. The lens on the right hand side of the ion traps collect the single photons resulting from the resonant excitation from the Ti:Sapph and direct them into the interferometer. The entanglement of the two ions is heralded when both PMTs inside the interferometer detect a photon. The state of the ions is then read out using the PMTs on the left hand side of the ion traps.

Once the two ions have decayed, they will have produced photons whose frequency and polarization are entangled with the internal state of the ions. If the photons are then measured in an entangled basis, the ions will be projected into an entangled state. As shown in fig. 5.2, a Bell basis measurement is made on the photons by setting up collection optics near the trap which couple the scattered light into single mode fibers which are directed toward a beam splitter that erases the *which-way* information contained in the momentum vectors of the photons. Two PMTs are placed behind the beam splitter and, as we will see, the ions will be projected into an entangled state when both PMTs detect a photon. We refer to these double detection events as a coincident detection event or the heralding event. Because of the different decay channels in $^{171}\text{Yb}^+$, polarizers are used to select the emitted photons that are $\hat{\pi}$ polarized, so that the heralding event only occurs when the ions have decayed back into the qubit space instead of into a mixture that includes the $m_f = \pm 1$ states as illustrated in fig. 5.3. In the type II protocol, both ions recoil from photon emission and therefore the motional state of the ions after a scattering event does not reveal any information about which ion emitted which photon. This implies that the motional state of the ions is irrelevant and will be ignored from this point on. The single mode fibers are aligned as to select out photons in the modes \vec{k}_1 and \vec{k}_2 and due to the selection rules of the D_1 line, the frequency of the photons can either be equal to the splitting between $^2\text{S}_{1/2}|F=0\rangle$ and $^2\text{P}_{1/2}|F=1\rangle$ or the splitting between $^2\text{S}_{1/2}|F=1\rangle$ and $^2\text{P}_{1/2}|F=0\rangle$. The difference between these two frequencies is equal to the sum of the hyperfine splitting for the two electronic levels, $12.6 + 2.1 = 14.7$ GHz, which is large compared to

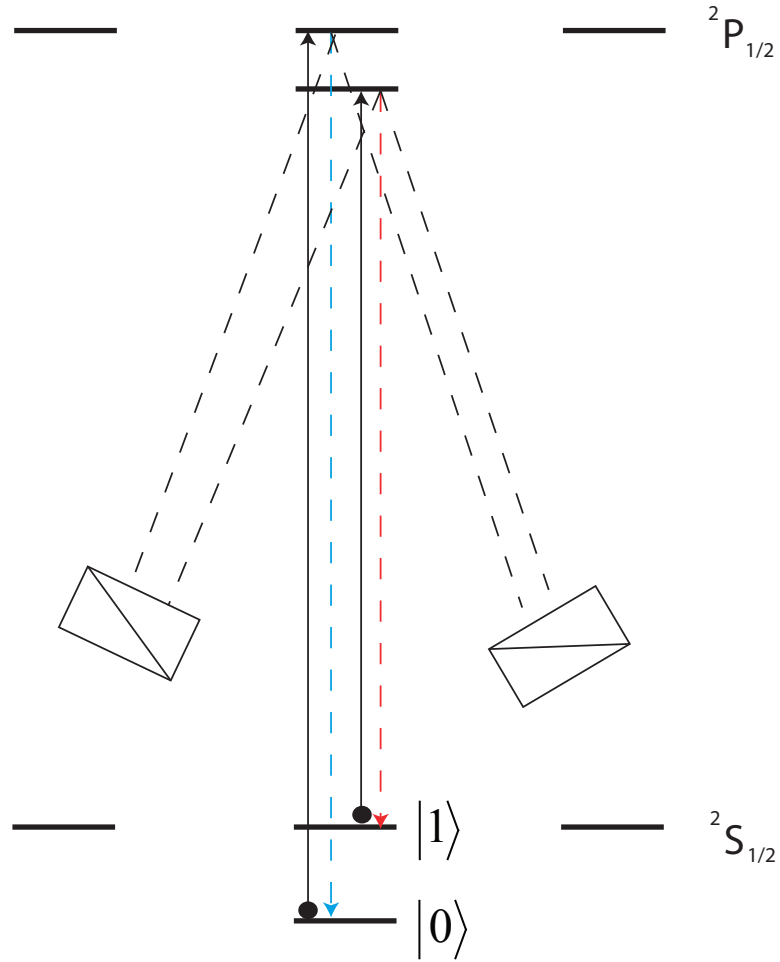


Figure 5.3: After preparing the ion in an equal superposition of the qubit states, the atom is excited to the $^2P_{1/2}$ state using a $\hat{\pi}$ polarized resonant laser pulse with sufficient bandwidth as to span the hyperfine frequency. If the spontaneously emitted photon is captured in the single mode fiber, it will pass through a polarizer to filter out the σ^\pm transition photons, thereby created the ion-photon entangled pair $|0b\rangle + |1r\rangle$.

the natural linewidth of the transition meaning that these two frequencies are well resolved and should form a good qubit. We refer to the larger frequency state as $|b\rangle$ and the smaller frequency state as $|r\rangle$. Remembering that specific wavevectors and polarizations are singled out for the operation of the gate, the post-scattering ion-photon state is,

$$\Psi_3 = \hat{\Pi} (e^{i\theta_{b,1}}\alpha|0\rangle|b_1\rangle + e^{i\theta_{r,1}}\beta|1\rangle|r_1\rangle) (e^{i\theta_{b,2}}\gamma|0\rangle|b_2\rangle + e^{i\theta_{r,2}}\delta|1\rangle|r_2\rangle), \quad (5.16)$$

where the phases included will be determined by the photon energy and the final path length and the subscripts on the photon modes refers the \vec{k} degree of freedom. The operator $\hat{\Pi}$ is a symmetry operator for the photons that is needed since they will be directed through a beam splitter that couples the modes \vec{k}_1 and \vec{k}_2 , thereby creating a situation where the indistinguishability of the photons must be taken into account. An example of how the symmetry operator enforces the Bose statistics of the photons is,

$$\hat{\Pi}|r_1\rangle|b_2\rangle = \frac{1}{\sqrt{2}} (|r_1\rangle|b_2\rangle + |b_2\rangle|r_1\rangle). \quad (5.17)$$

The action of the beam splitter is that of a rotation operator, \hat{B} , in the $\{\vec{k}_1, \vec{k}_2\}$ space and makes the following transformations,

$$\hat{B}|r_1\rangle = \frac{1}{\sqrt{2}} (|r_1\rangle + |r_2\rangle) \quad (5.18)$$

$$\hat{B}|r_2\rangle = \frac{1}{\sqrt{2}} (|r_1\rangle - |r_2\rangle), \quad (5.19)$$

with the frequency of the photon being irrelevant. We can now calculate the ion-

photon state prior to the photon detection,

$$\Psi_4 = \hat{B}\hat{\Pi} \left(\tilde{\alpha}\tilde{\gamma}|00\rangle|b_1b_2\rangle + \tilde{\alpha}\tilde{\delta}|01\rangle|b_1r_2\rangle + \tilde{\beta}\tilde{\gamma}|10\rangle|r_1b_2\rangle + \tilde{\beta}\tilde{\delta}|11\rangle|r_1r_2\rangle \right), \quad (5.20)$$

where we have redefined the coefficients by absorbing the phases present in Ψ_3 , i. e. $\tilde{\alpha} = e^{i\theta_{b,1}}\alpha$. It is straightforward to show that the action of the beam splitter ensures that half of the terms in Ψ_4 do not contribute to the coincident detection events. For example,

$$\hat{B}\hat{\Pi}|b_1b_2\rangle = \frac{1}{\sqrt{2}} (|b_1b_1\rangle - |b_2b_2\rangle), \quad (5.21)$$

showing that either both photons will be found to have momentum \vec{k}_1 or they will both be found to have momentum \vec{k}_2 , meaning that the two photons will always exit the same port of the beam splitter if they have the same frequency [88, 89]. A similar calculation shows,

$$\hat{B}\hat{\Pi}|r_1b_2\rangle = \hat{\Pi} \frac{(|r_1\rangle + |r_2\rangle)}{\sqrt{2}} \frac{(|b_1\rangle - |b_2\rangle)}{\sqrt{2}}, \quad (5.22)$$

showing that the symmetry operator and the action of the beam splitter commute when the photons are not identical. We can then calculate the state after a coincident detection event, which we represent with a projection operator \hat{P} that picks out the components where the two photons have different momenta. The final state is then,

$$\Psi_5 = \hat{P}\Psi_4 = \left(\tilde{\alpha}\tilde{\delta}|01\rangle - \tilde{\beta}\tilde{\gamma}|10\rangle \right) \hat{\Pi} (|r_1b_2\rangle - |b_1r_2\rangle), \quad (5.23)$$

showing that, when both PMTs detect a photon, the ions are projected into an entangled state in general. By carefully keeping track of the excitation time of the ions, the phase acquired while in the excited state and the path lengths from the ions to the beam splitter, it can be shown [42] that up to an overall phase factor the final state of the ions is,

$$\Psi_5 = \alpha\delta|01\rangle - e^{ic\Delta k(t_{e1}-t_{e2})}e^{i\Delta k\Delta x}\beta\gamma|10\rangle \quad (5.24)$$

where $\Delta k = k_{blue} - k_{red} = 2\pi/(2\text{cm})$ and t_{ei} is the excitation time of ion i . Because the length scale of Δk is so large, phase stability is not an issue in the type II protocol.

This mapping from Ψ_1 to Ψ_5 can be represented by the non-unitary operator $\sigma_z^{(1)}(I - \sigma_z^{(1)}\sigma_z^{(2)})$ and was shown to be useful for the creation of cluster states that might be used as a resource in one-way quantum computation [90] or a quantum repeater [37]. This gate was demonstrated using two $^{171}\text{Yb}^+$ ions separated by approximately one meter, (fig. 5.2). In order to characterize the gate, we prepared a representative set of input states as shown in table 5.1 and measured an average output state fidelity of 0.89(2) [86]. In that case, the atoms were prepared and hit with excitation pulses at a rate of 70 kHz with a coincident event being observed approximately every 11 minutes, meaning that the success probability was approximately 2×10^{-8} . The low success probability of the gate, P_{succ} , is a consequence of

Input State	Expected State	Fidelity	Events
$ 0 + 1\rangle \otimes 0 + 1\rangle$	$ 01\rangle - 10\rangle$	0.89(2)	210
$ 0 + i1\rangle \otimes 0 + 1\rangle$	$ 01\rangle - i 10\rangle$	0.86(2)	179
$ 0 - 1\rangle \otimes 0 + 1\rangle$	$ 01\rangle + 10\rangle$	0.85(1)	178
$ 0 - i1\rangle \otimes 0 + 1\rangle$	$ 01\rangle + i 10\rangle$	0.81(2)	188
$ 0 + 1\rangle \otimes 1\rangle$	$ 01\rangle$	0.86(5)	42
$ 0\rangle \otimes 0 + 1\rangle$	$ 01\rangle$	0.91(4)	52
$ 0\rangle \otimes 1\rangle$	$ 01\rangle$	0.98(2)	48

Table 5.1: Results of the remote quantum gate process. Listed are the input and expected output states of the gate, the overlap of the measured and ideal state and the number of heralding events. The success probability is 2×10^{-8} and the average state fidelity is $F = 0.89(2)$.

several factors,

$$P_{succ} = P_{Bell} P_{det}^2 = P_{Bell} (p_\pi \eta T_{fiber} T_{optics} \xi (\Delta\Omega/4\pi))^2, \quad (5.25)$$

where P_{Bell} is the probability that the photons are found to be in the correct Bell state and depends on the initialization coefficients $\alpha, \beta, \gamma, \delta$ and P_{det} is the probability of detecting a single photon emitted by an ion. p_π is the probability that ion emitted a photon with the correct polarization and is equal to 1/2 for the $^{171}\text{Yb}^+$; $\eta = 0.15$ is the quantum efficiency of each PMT; T_{fiber} is the coupling efficiency of the single mode fiber to the light that is collected from the ion was estimated to be 20%; $T_{optics} = 0.95$ is the transmission through the other optical elements and $\xi = 0.995$ accounts for the branching ratio to the $^2\text{D}_{3/2}$ state from $^2\text{P}_{1/2}$; $\Delta\Omega/4\pi = 0.02$ is the fractional solid angle subtended by the collection lens, $\text{NA} = 0.23$. These factors multiply together to give $P_{succ} \approx P_{Bell} 8.5 \times 10^{-8}$. The repetition rate of the

experiment was limited by the microwave initialization pulse of duration $30 \mu\text{sec}$.

Using these results, we can estimate how far this system could be taken toward developing novel quantum information processors. For example, a quantum repeater architecture [37] using deterministic gates between ions within a single node can use the type II photonic gate to connect different nodes in a time approximately given by $T \approx T_{succ} \ln(N-1)$ with T_{succ} being the average time needed to see a coincident event. Given that the attenuation in optical fibers for 369 nm limits the distance between nodes to a distance of about 10 meters, a 10 km network can be expected to be fully connected once every 1.3 hours. Even if the attenuation length is increased by a factor of 100, the connection time is still on the order of 24 minutes for this success rate, implying that dramatic improvements are needed in both the repetition rate of the experiment and the success probability before this platform can be considered to be a viable candidate for building a useful quantum communication network. We now explore some estimates on what connection time might be possible for this system.

The initialization of the ions begins with an optical pumping routine in which an average of 15 photons should be scattered in order to adequately purify the spin state, requiring approximately $1 \mu\text{sec}$. It was recently shown that high power off-resonant laser pulses can be used to enact ultrafast single qubit rotations [91], which would reduce the time needed to generate a coherent superposition of the qubit states to about 10 ps. The biggest uncertainty in the achievable repetition rate might come from the time that must be dedicated to keeping the ions at a reasonable temperature. For the four-rod trap, the heating rate was measured to be

7 quanta per second. If the ion can be cooled to the Doppler temperature in about 1 ms and the operations done during the experiment do not add significantly to the heating rate, then it might be possible to only dedicate 0.1% of the time to cooling. These numbers imply that the repetition rate will most likely be limited to 1 MHz as limited by the optical pumping time.

The success probability can also be improved in several ways. Most importantly, the fractional solid angle subtended by the collection lens can be increased by using a higher numerical aperture lens, reflective optics such as a parabolic mirror (see Appendix A) or high finesse cavity, or refractive optics. If for example, the numerical aperture of the lens being used is increased by a factor of 3, the fractional solid angle increases by a factor of 9, which in turn increases the success probability by a factor of 81. One might also assume an improvement in the efficiencies of PMTs by a factor of 2, as was recently reported by Hamamatsu inc., which gives an overall factor of 4 improvement in the success probability. These improvements would yield a connection time of 1 sec for a $N = 1,000$ node quantum repeater that could stretch over 10 km.

5.2.1 Errors in the Type II protocol

As discussed in [42], two known sources of error in the type II protocol are polarization mixing of the emitted photons and the mode mismatch of the interferometer. Assuming that the only error is due to the mode mismatch in the interferometer,

it can be shown [42] that the state fidelity is given by,

$$F_{mm} = \frac{1}{2 - V^2}, \quad (5.26)$$

where V is the visibility of the fringe contrast in the interferometer. The visibility is defined in terms of the intensities of incident light within the interferometer as, $V = \frac{I_{max} - I_{min}}{I_{max} + I_{min}}$, where $I_{max} = |E_1 + E_2|^2$ and $I_{min} = |E_1 - E_2|^2$. This quantity is measured by coupling laser light into the single mode fibers used for photon collection and measured to be $V > 0.98$ implying that the mode-mismatch results in a loss of fidelity of approximately 4%.

Polarization mixing errors are a result of σ^+ and σ^- transitions, that when viewed from an angle that is not in the plane perpendicular to the quantization axis, produce photons with a polarization having a component in the same direction as photons produced by π transitions. In spherical coordinates, $\hat{\pi}$ photons are always polarized along the $\hat{\theta}$ direction, no matter what the viewing angle is. If a photon with $\hat{\theta}$ polarization stemming from a σ transition is captured by the single mode fiber coupled to the ion, it will not be filtered out by the polarizers in the interferometer and could trigger a coincident event with one of the ions being in one of the $m_f = \pm 1$ states. A detailed calculation shows that the probability of σ^\pm transition producing a $\hat{\theta}$ photon is given by [42],

$$P_{\sigma,\theta}(\alpha) = \frac{\int_0^{\alpha \cos(\arcsin(\frac{1}{\alpha}(\frac{\pi}{2} - \theta)))} d\phi \int_{\pi/2}^{\pi/2 + \alpha} d\theta \sin\theta \frac{3}{8\pi} \cos^2\theta}{\int_0^{\alpha \cos(\arcsin(\frac{1}{\alpha}(\frac{\pi}{2} - \theta)))} d\phi \int_{\pi/2}^{\pi/2 + \alpha} d\theta \sin\theta \left(\frac{3}{8\pi} \cos^2\theta + \frac{3}{8\pi} \sin^2\theta \right)}. \quad (5.27)$$

This equation is the time averaged power of a radiating dipole per solid angle for σ^\pm transitions projected onto $\hat{\theta}$ integrated over of the solid angle subtended by a lens with a numerical aperture $\text{NA} = \sin\alpha$ normalized by the total radiated power projected onto $\hat{\theta}$. Because the type II protocol heralds the creation of entanglement upon detection of two photons, the probability of getting a coincident event that stems from the wrong atomic transitions is approximately $2P_{\sigma,\theta}(\alpha)$. Using the numerical aperture $\text{NA} = 0.23$ of the CVI lens used in the experiment, Eq. (5.27) can be numerically evaluated to show that the probability of erroneous coincident counts is approximately 3%.

Another source of error comes from the two photons arriving at the beam splitter at slightly different times. When the photons arrive at different times, the destructive interference associated with the photons of the same frequency is not perfect and can therefore lead to both PMTs in the interferometer registering a detection event. This effect can be quantified by considering a modification to the state in Eq. (5.16), where we now imagine that the photon coming from the second ion is delayed with respect to the first ion by a time T . We describe the photon wavepacket with momentum \hat{k}_1 as,

$$\psi_1(t) = \Theta(t)e^{-\Gamma t/2}e^{-i\omega t}\hat{k}_1, \quad (5.28)$$

where Γ^{-1} is the lifetime and ω is the transition frequency. If these wave functions are used in the above analysis, one finds that the probability of making an error due

a temporal offset of the two photon wavepackets is given by,

$$P(T) = \frac{1 - e^{-\Gamma T}}{2 - e^{-\Gamma T} \left(1 - \frac{1}{1 + \left(\frac{\omega_{r,b}}{\Gamma}\right)^2} \right)}, \quad (5.29)$$

where $\omega_{r,b}$ is the frequency difference between the *red* and *blue*. Because the two excitation pulses used to excite the two ions in our experiment are derived from the same pulse, this equation is more conveniently expressed as a path length difference instead of a temporal difference. If the expression is then expanded in terms of this path length difference L ,

$$P(L) = \left(\frac{\Gamma}{c} + \frac{\Gamma^3}{c\omega_{r,b}^2} \right) L + \mathcal{O}(L^2) \quad (5.30)$$

$$= \frac{L}{2.4\text{m}} + \mathcal{O}(L^2). \quad (5.31)$$

The path length difference is matched to approximately 1 cm in the laboratory, meaning that the error due to temporal mismatch of the photon modes comes in at the 1% level.

5.3 Bell's theorem and private random numbers

The type II experiment with distant ions is not only useful for quantum networking, but may also be used for the generation of private random numbers. The notion of *private* random numbers is a reference to the fact that a person in possession of a black box device that is supposed to generate random numbers can never

be absolutely sure that the device is truly random. Even if the numbers produced by the device pass every known randomness test available [92], one can never exclude the possibility that the numbers are stored in a memory inside the device and known by an adversary, making them deterministic. It can be shown, however, that a device that is capable of violating a Bell inequality [93] can be used to generate genuine private random numbers [94, 95]. A Bell inequality is a limit on correlations between two or more systems that is imposed by an assumption of local realism. Any system that can be described as one that obeys a hidden variable model, like a black box with a memory, will not violate a Bell inequality. A particularly simple and important Bell inequality is referred to as the CHSH inequality [96], which is named after John Clauser, Michael Horne, Abner Shimony and Richard Holt. To formulate the inequality we imagine two systems are measured by detectors A and B with the measurement settings a and b respectively. If the systems are Boolean-valued upon measurement, then we can define the two different measurement outcomes to have numerical values of ± 1 . If this is true, then at least one of the quantities $B(b, \lambda) + B(b', \lambda)$ or $B(b, \lambda) - B(b', \lambda)$ should be equal to zero if the measurement outcomes only depend on the measurement settings and the possibly hidden variable λ , while the other quantity should be equal to 2. If this is the case, then the correlation function,

$$\begin{aligned}
& A(a, \lambda)B(b, \lambda) + A(a, \lambda)B(b', \lambda) + A(a', \lambda)B(b, \lambda) - A(a', \lambda)B(b', \lambda) \\
= & A(a, \lambda) (B(b, \lambda) + B(b', \lambda)) + A(a', \lambda) (B(b, \lambda) - B(b', \lambda)) \leq 2. \quad (5.32)
\end{aligned}$$

If the expectation value of a random variable X is $E(X) = \int_{\Lambda} X(\lambda)\rho(\lambda)d\lambda$ where ρ is the probability density on the hidden parameter space Λ , then,

$$E(A(a)B(b)) + E(A(a)B(b')) + E(A(a')B(b)) - E(A(a')B(b')) \leq 2. \quad (5.33)$$

Quantum mechanics, however, admits states that are capable of violating this bound on local hidden variable models. In particular, if the singlet state $|\uparrow\downarrow\rangle - |\downarrow\uparrow\rangle$ is measured with the following measurement settings,

$$A(a) = \sigma_z \otimes I \quad (5.34)$$

$$A(a') = \sigma_x \otimes I \quad (5.35)$$

$$B(b) = \frac{1}{\sqrt{2}}I \otimes (\sigma_z + \sigma_x) \quad (5.36)$$

$$B(b') = \frac{1}{\sqrt{2}}I \otimes (\sigma_z - \sigma_x), \quad (5.37)$$

a simple calculation shows that the expectation value of the correlation function in Eq. (5.33) is equal to $2\sqrt{2}$. As shown in [95], the degree to which this inequality is violated can be used to quantify the amount of private randomness that is being generated by the system. If the two observed systems are assumed to satisfy the laws of quantum theory, separated and non-interacting during each measurement and the two measurement settings (x, y) are generated by a random process then the randomness of the measurement outcomes as quantified by the min-entropy is bounded by,

$$H_{\infty} \geq nf(\hat{I} - \epsilon), \quad (5.38)$$

with probability greater than $1 - \delta$ where $\epsilon = \mathcal{O}(\sqrt{-\log\delta/q^2n})$ is a statistical parameter and $q = \min_{x,y} P(x, y)$ is the probability of the least probable measurement setting pair. The parameter n is the number of measurements made on the system, the value \hat{I} is the observed expectation value of the correlation function in Eq. (5.33) and the function f is found using semi-definite programming and shown in fig. 5.4.

The experimental setup described in Sec. 5.2 satisfies all the requirements needed to realize this random number generator experimentally; namely that the two entangled particles can be assumed to be non-interacting during the detection process and near perfect detection of every event, i.e. the so-called detection loophole is closed. Note that the particles do not need to be space-like separated and the user must only be able to determine that the two subsystems are not capable of interacting. Because the ions are separated by such a large distance in the experiment, their mutual interaction can be safely assumed to be negligible.

The random numbers are then generated by using two $^{171}\text{Yb}^+$ ions along with the type II heralded entanglement protocol. The measurement settings are set by applying coherent microwave rotations after the heralding event and before the detection process. By using random number generators, the measurement settings were chosen from an even distribution, ($P(x, y) = 1/4$), so as to minimize the number of runs required to obtain a meaningful bound on the output entropy. After running the experiment for approximately one month, a total of 3,016 entanglement events were observed, resulting in a measured value for the correlation function of $\hat{I} = 2.414 \pm 0.058$, see table 5.2 for a summary of the measurement results. The observed CHSH violation implies that at least $H_\infty > 42$ new random bits were

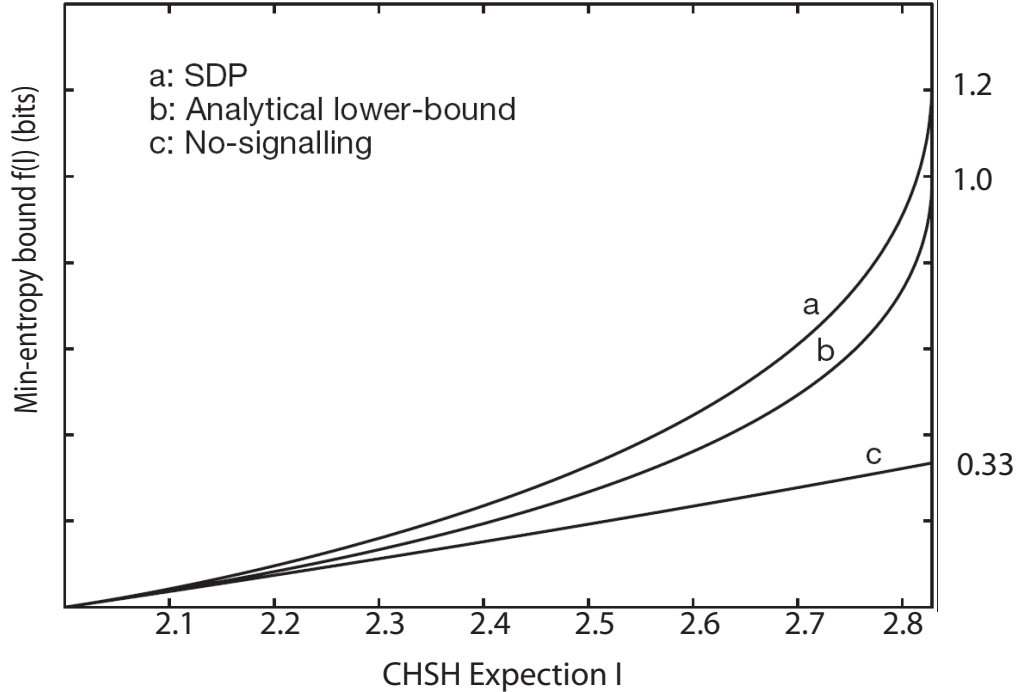


Figure 5.4: A plot of the function $f(I)$ which bounds the amount of randomness generated in a device that violates a Bell inequality. The function $f(I)$ (curve a) is found using semidefinite programming, which is a numerical method that is guaranteed to converge to the exact result. Curve b is an analytic lower-bound derived in [95] and has the form $f(I) \geq -\log_2 \left[1 - \log_2 \left(1 + \sqrt{2 - \frac{I^2}{4}} \right) \right]$. Curve c is bound on the entropy implied solely by the no-signalling principle and has the form $f(I) \geq -\log_2 (3/2 - I/4)$. By assuming the no-signalling principle, we assume that the devices cannot be used for arbitrary fast communication. The function $f(I)$ starts at zero at the local threshold $I = 2$ and implies a positive min-entropy for systems that violate the CHSH inequality.

generated in the experiment with a 99% confidence level.

(x, y)	ϕ_x, ϕ_y	$N(0, 0)$	$N(0, 1)$	$N(1, 0)$	$N(1, 1)$	Total	$P(a = b xy)$
0,0	$0^\circ, 45^\circ$	293	94	70	295	752	0.782
0,1	$0^\circ, 135^\circ$	298	70	74	309	751	0.808
1,0	$90^\circ, 45^\circ$	283	69	64	291	707	0.812
1,1	$90^\circ, 135^\circ$	68	340	309	89	806	0.195

Table 5.2: Observed number of events $N(a, b)$ for which the measurement on one atom gave outcome a and the measurement on the other atom gave outcome b , given the binary choices of the measurement bases (x, y) corresponding to $\pi/2$ qubit rotations with phase angles (ϕ_x, ϕ_y) on the equator of the Bloch sphere. The last column gives the fraction of events where $a = b$ given each input. If the experiment is interpreted as consisting of identical and independent realizations, the data then indicate a CHSH observable of $\hat{I} = 2.414 \pm 0.058$.

While it may sound circular to require that the measurement settings be chosen randomly, the small random seed that is used for the input measurement settings can be concatenated with the output of the machine, thereby establishing a randomness expansion scheme. When the number of measurements becomes large enough, a catalysis effect is possible wherein a seed string of length $\mathcal{O}(\sqrt{n} \log \sqrt{n})$ produces a much longer random output string of entropy $\mathcal{O}(n)$.

As a final remark, since the publication of Bell’s theorem in 1964, experimentalists have been hard at work trying to confirm that the universe does not obey the traditional notion of local realism [97, 98, 99, 100, 101, 102, 103, 104, 105]. All of the experiments cited here, including our experiment, have indeed violated a Bell inequality, but none have ever been able to do so in a loop-hole free manner. Most physicists consider the matter to be settled in light of the different loop-holes being closed in different instances and have accepted that local realism is in fact untenable

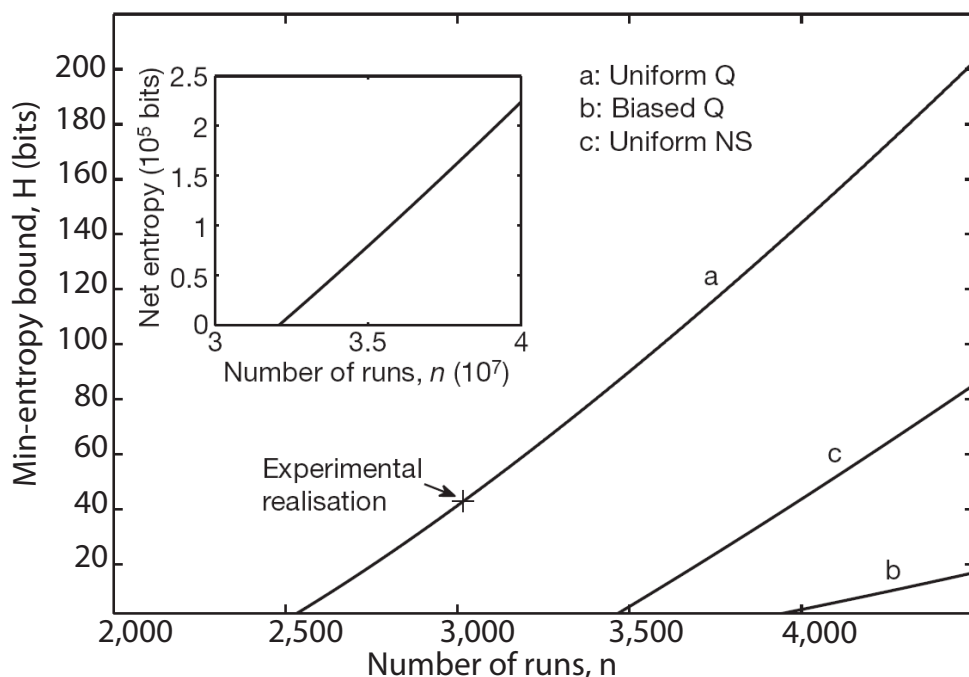


Figure 5.5: The plot shows a bound on the minimum entropy produce versus the number of trials n for an observed CHSH violation of $\hat{I} = 2.414$ and confidence level $1 - \delta = 99\%$. The bound on the entropy implied by quantum theory is for a uniform choice of inputs [$P(x, y) = 1/4$] (curve a) and for a biased choice of inputs $P(00) = 1 - 3q$, $P(01) = P(10) = P(11) = q$, where $q = \alpha n^{-1/2}$ with $\alpha = 11$ (curve b). For a given number n of uses of the device, the uniform choice of inputs leads to more randomness in the outputs. On the other hand, biased inputs require less randomness to be generated, and the net amount of randomness produced (given by the difference between the output and the input entropy) becomes positive for sufficiently large n . Curve c is the bound on the entropy implied by the no-signalling principle alone for a uniform choice of inputs. The inset shows the net amount of entropy produced for the biased choice of inputs with the observed CHSH violation.

with the laws governing the universe. On the other hand, it has been pointed out [106] that the lack of a loop-hole free violation of Bell's inequality after 40 years of trying might be akin to the search for perpetual motion machines in the 18th and 19th centuries. In that case, decades of trial and failure eventually led to the discovery of the second law of thermodynamics. Could it be that the mounting decades of searching for a system capable of violating the principle of local realism will eventually be considered as empirical evidence of the principle's sanctity and that quantum theory will have to be tweaked? Until the data comes in, the question remains open.

Chapter 6

Integrating Phonon and Photon based entangling operations

6.1 The Quantum Repeater

A quantum network that is spatially distributed will suffer from in-flight decoherence. If photons are used as flying qubits, absorption and scattering will certainly be sources of decoherence. If two quantum registers are connected through a photonic channel that has an attenuation length α , (given in dB/meter), then the probability of successfully transmitting a photon through the channel is $e^{-\alpha l_0}$ where l_0 is the length of the channel, a problem that will have to be addressed when constructing a large scale quantum communication network. A quantum repeater operates by building up entanglement between separate nodes and then using entanglement swapping measurements to connect the ends of the chain. A three node quantum repeater comprised of trapped ions and photons is shown schematically in fig. 6.1. As described in [37] the two most distant ions in the chain, (L_1 and R_2), can be entangled using a combination of the probabilistic photonic gate discussed in chapter 5 and the deterministic gate described in chapter 4. The protocol begins by preparing all of the ions in 50-50 superposition states and then exciting all of them simultaneously with resonant laser pulses. In the event that both PMTs behind one of the beam splitters register an event, two of the three nodes will then be connected. Because of the low success probability of the type II photonic en-

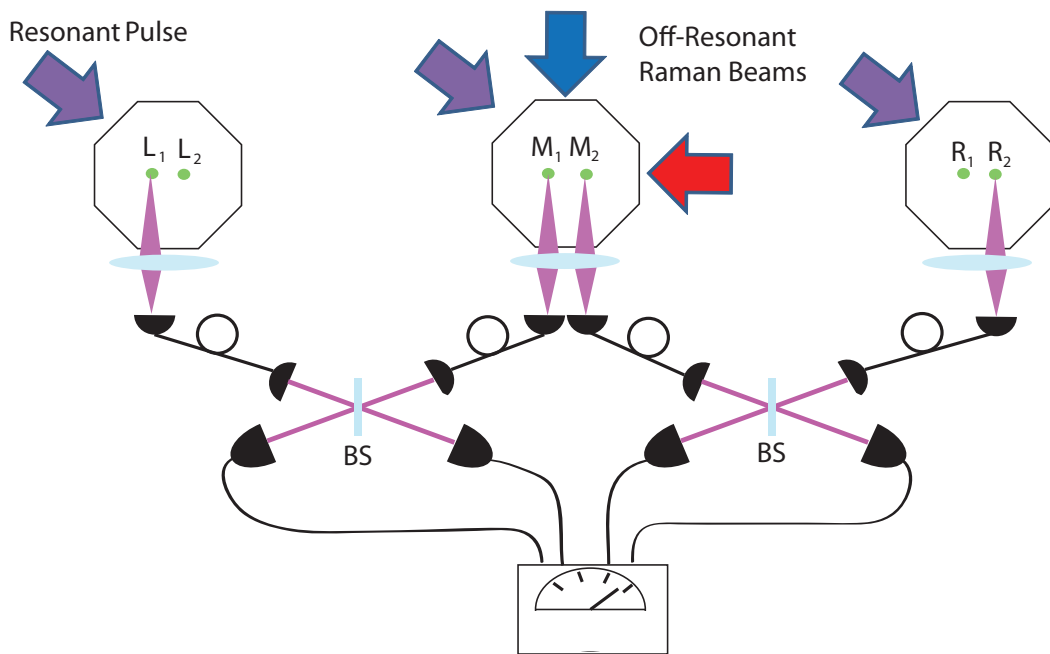


Figure 6.1: A quantum repeater architecture using ion and photons. In this hybrid approach, different nodes of the repeater are connected using a probabilistic photonic connection and the entanglement within the nodes is generated using deterministic phonon interactions.

tanglement protocol, it is extremely unlikely that both pairs of PMTs will register coincident detection events at the same time. But assuming that the other ions can be reinitialized without disturbing the entangled pair, the photonic gate can be repeatedly attempted on the unentangled ions until they are also connected. In the case that the initial $\pi/2$ pulses are done with the same phase, the resulting state of ions L_1, M_1, M_2 , and R_2 after two coincident detection events is ideally,

$$\Psi_1 = (|\uparrow\downarrow\rangle - |\downarrow\uparrow\rangle)(|\uparrow\downarrow\rangle - |\downarrow\uparrow\rangle), \quad (6.1)$$

where the ordering of the qubits is $|L_1, M_1, M_2, R_2\rangle$. If an entangling gate of the Mølmer-Sørensen type is then applied to the middle qubits, the resulting state is,

$$\begin{aligned} \Psi_2 &= |\uparrow_{L_1}\rangle U_{ms}^{M_1, M_2} |\downarrow_{M_1}\uparrow_{M_2}\rangle |\downarrow_{R_2}\rangle \\ &- |\uparrow_{L_1}\rangle U_{ms}^{M_1, M_2} |\downarrow_{M_1}\downarrow_{M_2}\rangle |\uparrow_{R_2}\rangle \\ &- |\downarrow_{L_1}\rangle U_{ms}^{M_1, M_2} |\uparrow_{M_1}\uparrow_{M_2}\rangle |\downarrow_{R_2}\rangle \\ &+ |\downarrow_{L_1}\rangle U_{ms}^{M_1, M_2} |\uparrow_{M_1}\downarrow_{M_2}\rangle |\uparrow_{R_2}\rangle \end{aligned} \quad (6.2)$$

$$\begin{aligned} &= |\uparrow_{L_1}\rangle (e^{i\pi/4} (|\downarrow_{M_1}\uparrow_{M_2}\rangle - i|\uparrow_{M_1}\downarrow_{M_2}\rangle)) |\downarrow_{R_2}\rangle \\ &- |\uparrow_{L_1}\rangle (e^{i\pi/4} (|\downarrow_{M_1}\downarrow_{M_2}\rangle - ie^{i2\phi_m} |\uparrow_{M_1}\uparrow_{M_2}\rangle)) |\uparrow_{R_2}\rangle \\ &- |\downarrow_{L_1}\rangle (e^{i\pi/4} (|\uparrow_{M_1}\uparrow_{M_2}\rangle - ie^{-i2\phi_m} |\downarrow_{M_1}\downarrow_{M_2}\rangle)) |\downarrow_{R_2}\rangle \\ &+ |\downarrow_{L_1}\rangle (e^{i\pi/4} (|\uparrow_{M_1}\downarrow_{M_2}\rangle - i|\downarrow_{M_1}\uparrow_{M_2}\rangle)) |\uparrow_{R_2}\rangle. \end{aligned} \quad (6.3)$$

Ignoring the global phase $e^{i\pi/4}$ allows the state to be rewritten as,

$$\begin{aligned}
\Psi_2 = & -|\downarrow_{M_1}\downarrow_{M_2}\rangle (|\uparrow_{L_1}\uparrow_{R_2}\rangle - ie^{-i2\phi_m}|\downarrow_{L_1}\downarrow_{R_2}\rangle) \\
& + |\downarrow_{M_1}\uparrow_{M_2}\rangle (|\uparrow_{L_1}\downarrow_{R_2}\rangle - i|\downarrow_{L_1}\uparrow_{R_2}\rangle) \\
& - i|\uparrow_{M_1}\downarrow_{M_2}\rangle (|\uparrow_{L_1}\downarrow_{R_2}\rangle + i|\downarrow_{L_1}\uparrow_{R_2}\rangle) \\
& + ie^{i2\phi_m}|\uparrow_{M_1}\uparrow_{M_2}\rangle (|\uparrow_{L_1}\uparrow_{R_2}\rangle + ie^{-i2\phi_m}|\downarrow_{L_1}\downarrow_{R_2}\rangle), \tag{6.4}
\end{aligned}$$

showing that upon measurement of M_1 and M_2 the ions L_1 and R_2 are projected into a maximally entangled state.

6.1.1 2 + 1 Quantum Repeater Elementary Unit

As discussed in Sec. 6.1, an ion-photon based quantum repeater may be constructed through the combination of probabilistic photonic gates and deterministic Coulomb interaction based gates. The minimum setup required to demonstrate the feasibility of such a setup is with two ion traps, one containing one ion and the other containing two ions, which we refer to as the 2 + 1 experiment. We refer to the two traps as the east and west trap respectively. All three ions are initially Doppler cooled and then initialized to the state $|000\rangle$, where the ordering of the ions is $\{\text{West}, \text{East}_1, \text{East}_2\}$. All three ions are then subjected to $\pi/2$ pulses, followed by a single resonant pulse to excite the atoms to ${}^2P_{1/2}$. All three atoms will then spontaneously emit photons, but only one of the two ions, say E_1 , in the east trap is coupled to a single mode fiber that directs the photon to the Bell state mea-

surement apparatus described in chapter 5. Therefore, upon coincident detection of two photons, the the W and E_1 ions are projected into an entangled state and the state of the third ion, E_2 , is mixed since the photon it emitted was not detected and is likely of the wrong polarization. Therefore, in order to purify the state, E_2 is then optically pumped to the $|0\rangle$ state with a tightly focused beam that does not significantly effect the state of E_1 . After these steps, the ions should ideally be in the state,

$$\Psi_1 = (|\uparrow\downarrow\rangle - e^{i\phi}|\downarrow\uparrow\rangle)|\downarrow\rangle, \quad (6.5)$$

where ϕ is determined by the relative phase of the $\pi/2$ pulses applied in the initialization stage. In the next step, the Mølmer-Sørensen gate is applied to the two ions in the east trap, which should ideally produce the state,

$$\Psi_2 = |\uparrow\rangle (|\downarrow\downarrow\rangle - ie^{i2\phi_m}|\uparrow\uparrow\rangle) - e^{i\phi}|\downarrow\rangle (|\uparrow\downarrow\rangle - i|\downarrow\rangle), \quad (6.6)$$

showing that a measurement in the σ_z basis should show a correlation of the spin of the single ion in the west trap with the parity of the two ions in the east trap.

6.1.2 2 + 1 Experiment

This correlation between the spin of one ion and the parity of two distant ions was demonstrated using two ions in a four-rod trap and one ion in a blade trap approximately one meter away. As depicted in fig. 6.2, the blade trap is constructed from four alumina blades that are gold coated. Similar to the four-rod trap, two

opposing blades have a large RF voltages applied to them while the other two are RF grounded through shunting capacitors. The center segments of the RF grounded blades are held at a lower voltage compared to the outer segments to provide a trap in the z direction, as is done with the needles in the four-rod trap.

The experiment consists of two loop sequences which are referred to here as the fast loop and the slow loop. As depicted in the flow diagram in fig. 6.3, the fast loop's aim is to initialize the ions and attempt to establish the photonic link between the two traps. This is done by first Doppler cooling all three ions for $50 \mu\text{sec}$, optically pumping the state to $|000\rangle$, applying a $\pi/2$ pulse on all three ions and then applying a resonant 369.5 nm pulse to both traps simultaneously. The single mode fiber is only coupled to one of the ions in the four-rod trap, meaning that a coincident event registered in the interferometer heralds the entanglement of two of the three ions while leaving the third ion in a highly mixed state. In the event that no coincident count occurs, the ions are repumped to $|000\rangle$, rotated by $\pi/2$ and excited with another resonant pulse. After repeating this sequence 20 times, the ions are recooled for $50 \mu\text{s}$. A coincident event triggers the exit of the loop sequence and begins the sequence for the implementation of the Mølmer-Sørensen gate.

After exiting the loop sequence, the first step is to purify the spin state of the third ion that is left in a mixed state after being excited by the resonant picosecond pulse. This is done using an optical pumping beam that enters through the objective lens as shown in fig. 6.4. It is crucial that this beam be focused as tightly as possible as to not disturb the spin state of the other ion in the trap. This was done by using light from a single mode fiber and a high quality output coupler from

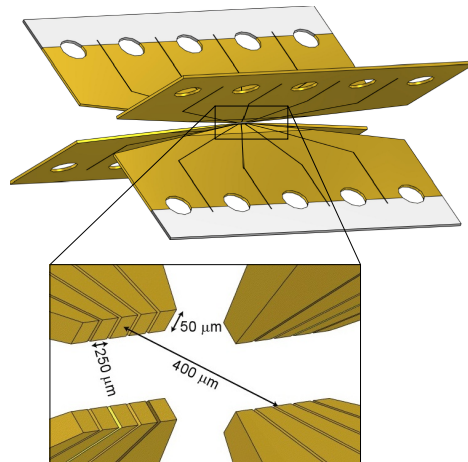


Figure 6.2: The blade trap mounted in the vacuum chamber and an up close drawing of the four blades. The high voltage RF is applied to the blades that are completely coated with gold with the other two blades being RF grounded and attached to DC voltage supplies. The five different electrodes on the DC blades allow for the possibility of creating anharmonic trapping potentials that could be used for splitting ion chains or to arrange ion crystals to have an even spacing.

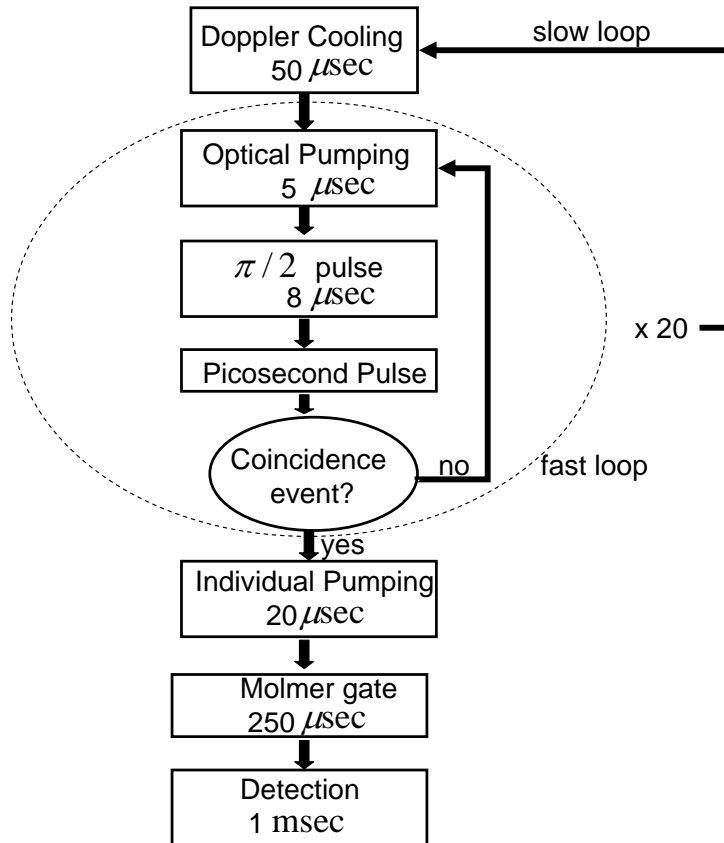


Figure 6.3: This flowchart shows how the 2 + 1 experiment is done. Because of the low photon collection efficiency, the fast loop is repeated approximately 10^8 times before a coincident event is registered.

Micro Laser Systems, Inc. The divergence of the output mode was measured and used in optical optimization software in order to calculate how far from the objective lens the fiber should reside. In order to test this individual optical pumping setup, two ions loaded in the trap were prepared in the state $|11\rangle$ and subjected to this tightly focused pumping beam. As shown in Fig. 6.5, the ion that is targeted by the beam pumps to the dark state within $50 \mu\text{s}$ while the second ion pumps down in 50 ms . In order to purify the spin state to the 1% level, the ion must scatter about 10 photons. Given that the pumping rates of the two ions in the trap differ by a factor of 1000, the ion that is not targeted will scatter a photon in about 1 – 2% of the experiments. The axial secular frequency was measured to be 300 kHz meaning that the separation between the two ions is $(\frac{e^2}{2m\omega_z^2})^{1/3} = 5 \mu\text{m}$. Assuming that the targeted ion sits at the center of a Gaussian pumping beam with an electric field profile proportional to $e^{-\frac{1}{2}(\frac{x}{\sigma})^2}$, we can infer that the width of the field is approximately $\sigma \approx \frac{5}{\sqrt{2\ln(1000)}} = 1.3 \mu\text{m}$. Given that the intensity and not the electric field is usually the measured quantity, we say that the beam waist is approximately $2 \mu\text{m}$.

The Mølmer-Sørensen gate is then applied in a way that we have not described yet. All of the discussion of the MS gate have thus far assumed the excitation of a single mode of motion, which is only valid if the gate speed is limited to be larger than $\Delta\omega^{-1}$, where $\Delta\omega = \omega_{com} - \omega_{tilt}$ is the frequency difference between the two transverse modes of motion. As discussed in chapter 2, the frequency difference between these two modes increases with the axial confinement frequency, implying that the gate speed can be increased by pushing the ions closer together which is

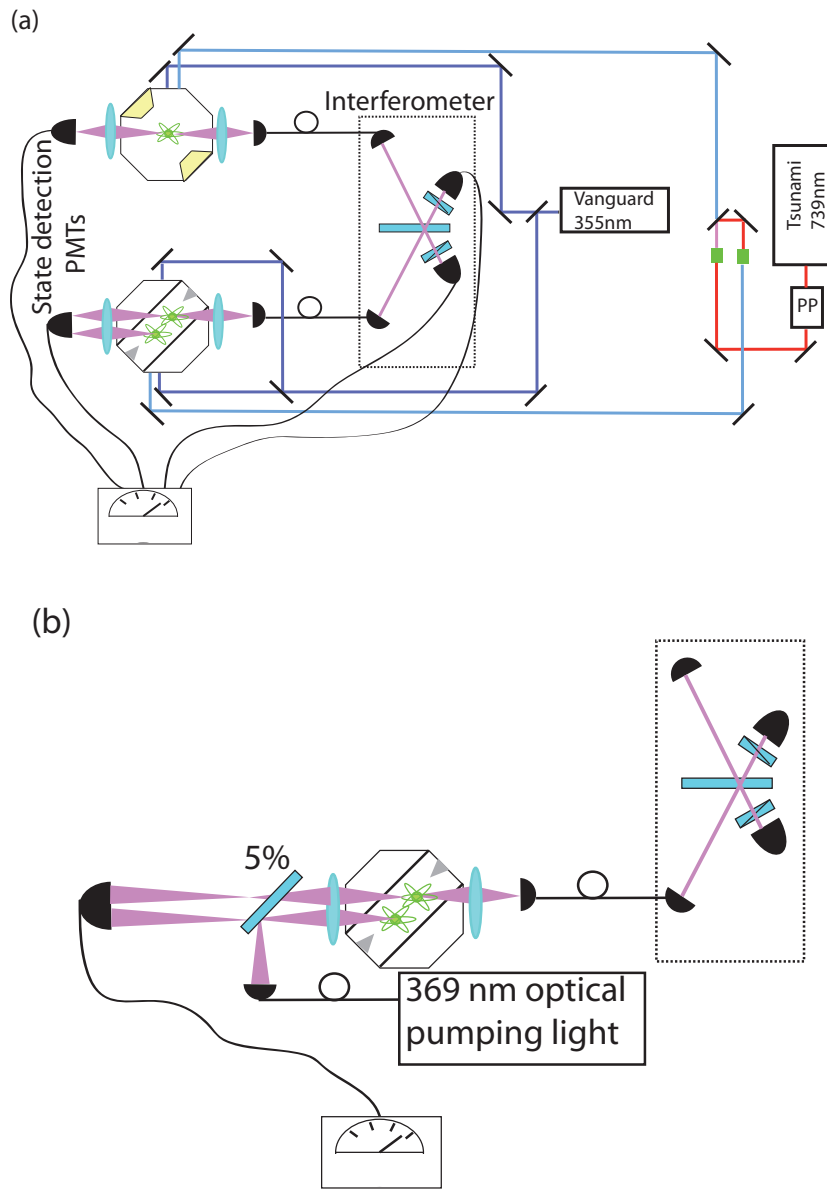


Figure 6.4: (a) A schematic of the optical setup for the 2 + 1 experiment. One ion is loaded into the blade trap and two are loaded into the four rod trap that is approximately 1 meter away. The Vanguard laser is split in half and used in a co-propagating geometry for the West trap, (fig. 3.5), and in a counter-propagating geometry for the east trap, (fig. 3.7). The entanglement swapping measurement is heralded when a coincident detection events is registered on the two PMTs inside the interferometer and the state of the of the ions is read out on the other PMTs. (b) The individual addressing optical pumping beam is brought in through a single mode fiber and directed onto the imaging lens using a 5% beam sampler and focused onto one of the ions in the four-rod trap. A 5% beam sampler is used so as to minimize the amount of light from the ion that is lost during state detection.

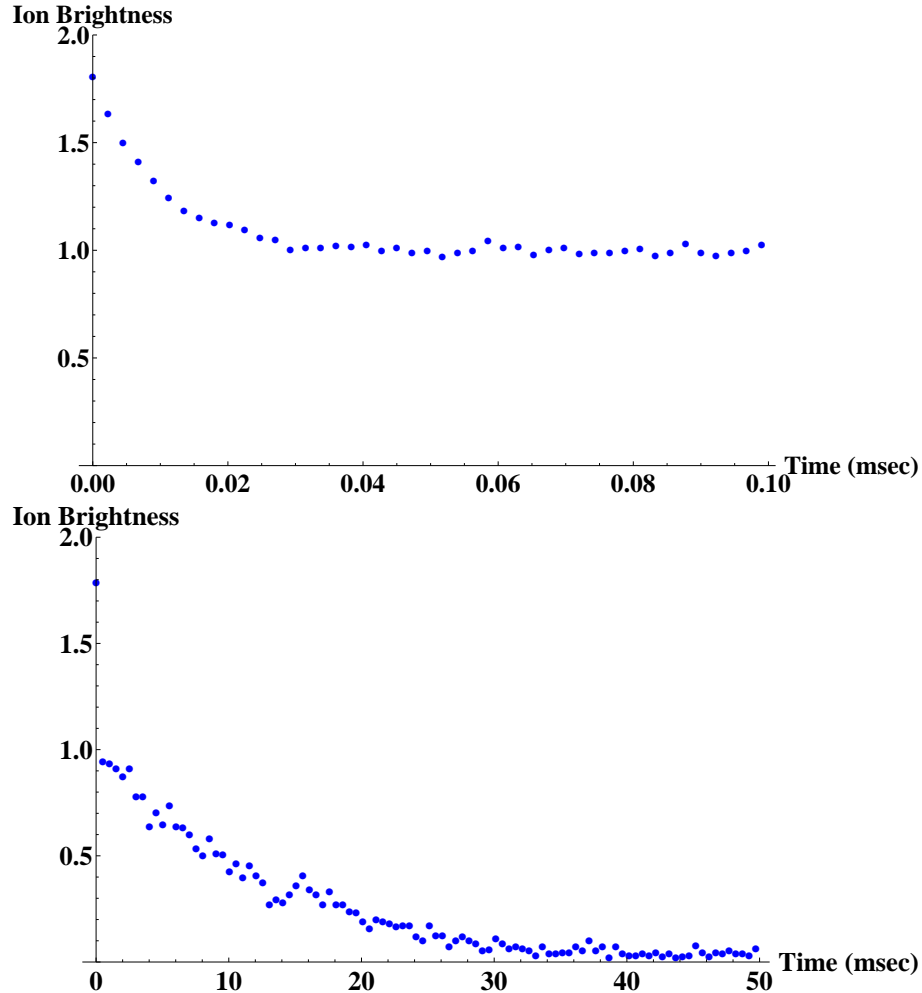


Figure 6.5: The two data sets show identical experiments done over different scales. Two ions are loaded into the four-rod trap and prepared in $|11\rangle$. The individual addressing optical pumping beam is then turned on for a variable amount of time before detecting the state of the two ions using a simple discriminator method. Notice that the first data set shows that one of the ion pumps to the dark state in approximately $40 \mu\text{s}$ while the second data set shows that the second ion eventually pumps to the dark state in approximately 40 ms, (note the first data point in the second set). With the ions being $5 \mu\text{m}$ apart, the 3 orders of magnitude discrepancy in the pumping times for the two ions implies a beam waist of approximately $1.3 \mu\text{m}$.

at odds with the desire for the ions to be far apart so that the individual pumping beam does not decohere the spin that is entangled with the ion in the other trap. Because of these opposing constraints, we implement the Mølmer-Sørensen gate in a regime that excites both the COM and the tilt mode simultaneously. If the frequency difference between the two modes is Δ , then one can drive the COM mode and the tilt mode off-resonantly with symmetric but opposite detunings so that both phase space trajectories close at the end of the gate sequence. If the difference frequency between the two modes is Δ , then the symmetric detuning δ that appears in the MS time-evolution operator is set to $\delta_{com} = \Delta/2$ and $\delta_{tilt} = -\Delta/2$. Besides allowing for further separated ions, this configuration has the added benefit of being able to entangle two ions in a shorter time for a given laser power. This is because the accumulated spin-dependent phase is proportional to the motional phase space area swept out and this configuration essentially doubles the area since two motional modes are involved. It should be noted, however, that the center of mass mode is generally more susceptible to heating [67]. In the experiment, the frequency difference between the two modes was set to 16 kHz, and a composite pulse of two 125 μ s pulses is used to for the MS gate. To keep the repetition rate of the experiment high, high fidelity in the gate operation is sacrificed by not sideband cooling. When the ions are sideband cooled to the ground state, Mølmer-Sørensen state fidelities of $\gtrsim 0.9$ are routinely seen and fidelities as high as 0.97 have been recorded. When the ions are only Doppler cooled the fidelity is usually limited to $\lesssim 0.8$ and can sometimes drift to lower values near 0.7 on the time scale of minutes. The decrease in the maximum fidelity for the Doppler cooled ions is

likely due to the effective increase in the Lamb-Dicke parameter $\eta\sqrt{\bar{n}+1}$ and a higher sensitivity to fluctuations in the trapping frequency. In the case of a single mode MS interaction, the decrease in fidelity due to the deviation from the Lamb-Dicke regime is $\eta^4 \frac{\pi^2}{4} \text{Var}(n_1)$ [107]. For an exponential distribution, the variance is equal to the square of the mean, implying that this error comes in at the 2 – 3% level for the Doppler temperature but is likely to be much higher in the 2 + 1 experiment due to the lack of sufficient laser cooling power, the cooling duty cycle of the slow loop and additional heating from the optical pumping and ps pulses. A second additional source of infidelity is likely due to an increased sensitivity to trap frequency fluctuations when the ions are not cooled to the ground state.

The experiment was run for approximately 30 hours, not including time that is taken to recalibrate the system and to reload ions after a loss, and a total of 228 coincident events were seen. As shown in fig. 6.6, the single-ion spin in the blade trap was found to be correlated with the parity of the two ions in the four-rod trap. By using a discriminator method for the state detection of the single ion in the west trap, the measurement record for the other two ions was separated into two distributions depending on the state of the west ion. By fitting sample detection histograms to the measurement records for the two cases, we can estimate the populations of the two ions and find that when the west ion is bright, the two ions in the east trap are found in an even parity state with a probability of 0.63 ± 0.04 and when the west ion is dark, the two ions are found in an odd parity state with a probability of 0.67 ± 0.04 .

The 65% spin-parity correlation that was observed is consistent with the main

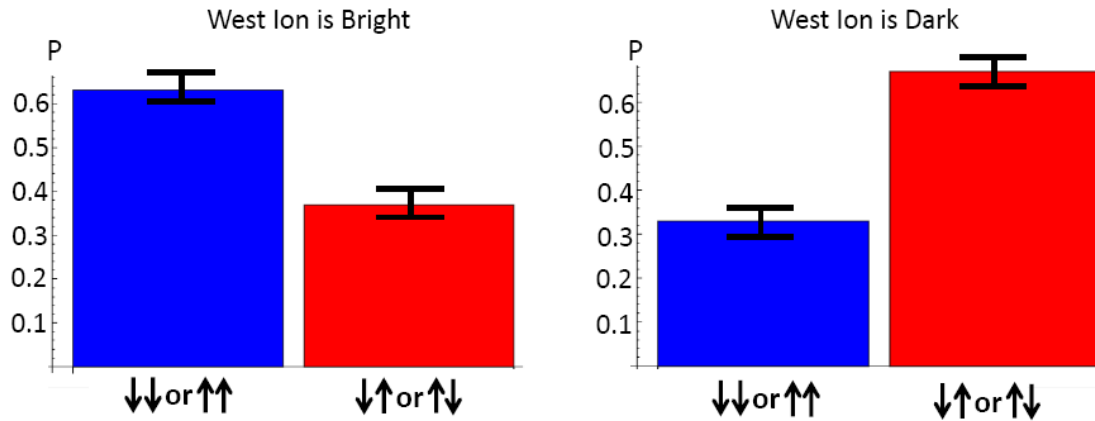


Figure 6.6: The results of the 2 + 1 data are separated into two sets according to the observed state of the West ion. When the west ion was found in the bright state, the two east ions were found to be in an even parity state with 63(4)% probability and when the west ion was found in the dark state, the two east ions were found to be in an odd parity state with 67(4)% probability.

known sources of error. Some preliminary photon interference data was taken with one ion in the blade trap and one in the four-rod trap and the ions were found to be anti-correlated in 85% of the coincident events. This figure is slightly lower than the 90% anti-correlation that was reported in [86], which likely the result of two problems. First, the pulse-picker used in the 2 + 1 experiment was not correctly calibrated and is observed to oscillate after being opened on the timescale of microseconds. Secondly, the micro-motion of the ion in the blade trap could not be fully nulled which was likely due to a shorted electrode in the trap. In order to have good photon interference at the beam splitter, it is crucial that the ion not have any micromotion in the direction in which it must emit light to couple to the fiber. Otherwise, the emitted photons will be Doppler shifted and acquire sidebands at the RF trapping frequency. We were able to null the ion's micromotion in the direction of the photon emission, but only at the cost of increasing the micromotion

amplitude in the direction of the beam that is used for state detection. This led to the state detection error in the west trap to be approximately 5%. The Mølmer-Sørensen gate fidelity for the bimodal setup without sideband cooling was usually observed to be 75%–80% while the experiment was running. Assuming these errors are uncorrelated, we expect the fidelity of the $2 + 1$ experiment to be approximately $0.8 \times 0.85 = 0.68$ if no other errors are present.

6.2 Conclusions and Outlook

The data shown in this final chapter represent the first steps toward connecting two distant trapped ion registers in an architecture that could be useful for scalable quantum computation. In order to fully demonstrate the coherence between the two registers, it will be necessary for the control fields of the two registers to be phase locked, requiring either interferometric stability of the different laser paths in the experiment, or phase insensitive gate schemes coupled with microwave controls [108]. However, for the system to be seriously considered for a distributed quantum computing network, there are two things that need to be greatly improved. First, the fidelity of the two gates that are used must be improved. The Mølmer-Sørensen gate performance can most likely be greatly improved by moving to a stronger trapping potential. A stronger trapping potential will result in a smaller variance in the initial motional excitation number and provide greater protection from stray couplings to other transitions. The main sources of error in the photonic gate were light leakage through the pulse-picker and mode mismatch in the interferometer. A

better extinction ratio for the pulse-picker might be achieved using a lock similar to the one demonstrated in [109]. The mode mismatch in the interferometer might be addressed using adaptive optics such as deformable mirrors in combination with wavefront imaging to optimize the system [110, 111, 112]. The second outstanding issue that needs to be addressed is the success rate of the photonic gate. This issue can be addressed on several fronts, including photon collection efficiency which is most easily improved by moving to high numerical aperture lens, but must be considered in the context of polarization mixing. Increasing the repetition rate of the experiment is currently limited by the optical pumping time which can not be much shorter than the microsecond time scale. One possible way around this limitation is to use many ions that are prepared off-line and then sequentially shuttled into the trapping zone that is coupled to the interferometer. Because the type II photonic gate is nearly insensitive to the motional state of the ion, the shuttling does not have to be limited by any adiabatic time scales imposed by the trap.

Assuming these improvements can be made, one must eventually confront another technical challenge stemming from the addressing errors in the application of the resonant pulses used to generate single photons. In order to allow for long computations in a distributed ion-trap processor, the quantum information stored in the registers must be protected from the decoherence that would be induced by the resonant pulses used to generate the single photons. Because the success rate is so low and we require many resonant pulses to establish the photonic link, any cross-talk to untargeted ions will destroy the stored information. One attractive method around this problem is to use one ion for the memory qubits and a second

ionic species for establishing a photonic link. Since the transition frequencies can vastly different, the absorption probability for the memory ions will be drastically reduced. Phonon based quantum logic gates between different ion species have been already been demonstrated using $^{27}\text{Al}^+$ and $^9\text{Be}^+$ in spectroscopy experiments [113]. Although the quantum logic used in these experiments is more similar to that proposed by Cirac and Zoller [19], it should also be possible to implement the more robust Mølmer-Sørensen gate between different species. While there may be pitfalls in the road ahead, the road exists and there is a visible horizon. The construction of a fully functional ion-photon network will be a difficult task and may require a little luck, but as Thomas Jefferson said, “I’m a big believer in luck, and I find the harder I work the more I have of it.”

Appendix A

Paraboloidal Ion Trap

This appendix shows that a paraboloidal electrode configuration is capable of creating a trapping region located at the focus of a paraboloid.

The trap design to be described is perhaps closest in spirit to a ring-and-fork quadrupole trap where an AC voltage is applied to a ring electrode with cylindrical symmetry and capping DC voltages are applied to electrodes on the top and bottom of the ring. Our design shown in Fig. A.1 consists of a paraboloidal surface segmented as to form three distinct electrodes with cylindrical symmetry. Similar to the ring-and-fork trap, an AC voltage is applied to the ring shaped middle electrode and then DC capping voltages are applied to the electrodes above and below the ring. Unlike the ring-and-fork trap, there is an asymmetry in the direction of the axis of symmetry which will be reflected in the form of the potential. This implies that the minimum of the trapping potential will not in general be located at the center of the AC electrode.

Constraints on the dimensions of the different segments of the trap can be found by requiring the trapping potential minimum to be located at the focus of the paraboloid. These constraints are found by solving Laplace's equation with the

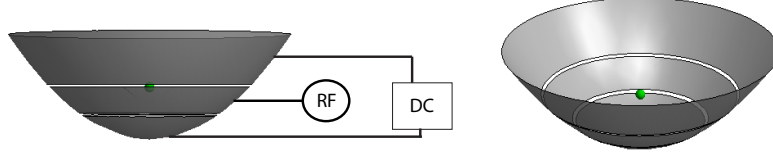


Figure A.1: The proposed paraboloidal ion trap design is shown schematically, with the DC voltages being applied to the top and bottom regions and an AC voltage being applied to the middle region.

potential being piece-wise constant on the conducting surface defined by,

$$z(\rho, f) = \frac{\rho^2}{4f} - f. \quad (\text{A.1})$$

Laplace's equation is separable in paraboloidal coordinates defined as,

$$x = \alpha\beta\cos\phi \quad (\text{A.2})$$

$$y = \alpha\beta\sin\phi \quad (\text{A.3})$$

$$z = \frac{1}{2}(\alpha^2 - \beta^2), \quad (\text{A.4})$$

with $0 \leq \alpha < \infty$, $0 \leq \beta < \infty$, $-\pi < \phi \leq \pi$. In these coordinates, paraboloids with

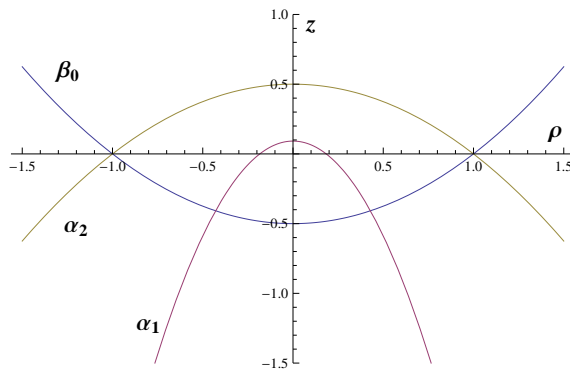


Figure A.2: The parabolic coordinates β_0 , α_1 and α_2 are shown. β_0 defines the surface of the ion trap while α_1 and α_2 define the segmentation dimensions. The points of intersection define the Cartesian coordinates z_1 and z_2 .

an axis of symmetry along the z axis are described by surfaces of constant α or β . If the electrodes are symmetric with respect to the polar angle ϕ , the potential does not depend on ϕ and the general solution to Laplace's equation is given by,

$$\phi_{int}(\alpha, \beta) = M_\lambda J_0(\lambda\alpha) I_0(\lambda\beta) \quad (\text{A.5})$$

$$\phi_{ext}(\alpha, \beta) = M_\lambda J_0(\lambda\alpha) K_0(\lambda\beta) \quad (\text{A.6})$$

with M_λ being an arbitrary non-negative constant determined by the boundary conditions [114]. J_0 is a Bessel function of the first kind and I_0 and K_0 are modified Bessel functions of the first and second kind. In general, the potential will be a super-position of the these and for simplicity we only write the solution for the interior region,

$$\phi(\alpha, \beta) = \int_0^\infty d\lambda M_\lambda J_0(\lambda\alpha) I_0(\lambda\beta). \quad (\text{A.7})$$

The average potential seen by the ion is calculated by separately considering the contributions of the AC and DC potentials. On the boundary $\beta = \beta_0 = \sqrt{2f}$, the application of the AC voltage to the central segment while grounding the top and bottom and segments gives a boundary potential of the form,

$$\phi_{AC}(\alpha, \beta_0) = V(\theta(\alpha - \alpha_1) - \theta(\alpha - \alpha_2)) \cos \Omega t, \quad (\text{A.8})$$

where V is a voltage, Ω is the drive frequency, θ is the Heaviside function and α_1 and α_2 are the positions of the segment cuts in parabolic coordinates as shown in

fig.A.2. To solve for M_λ , we use Hankle's integral relation,

$$f(r) = \int_0^\infty J_\nu(\lambda r) \lambda d\lambda \int_0^\infty f(\rho) J_\nu(\lambda \rho) \rho d\rho. \quad (\text{A.9})$$

Application of Eq. (A.9) with the boundary conditions stated in Eq. (A.8) gives,

$$M_\lambda = V \cos \Omega t \int_{\alpha_1}^{\alpha_2} d\alpha \alpha \lambda \frac{J_0(\lambda \alpha)}{I_0(\lambda \beta_0)}. \quad (\text{A.10})$$

The integral over α can be done, giving the following exact formula for the amplitude of the AC potential,

$$\phi_{AC}(\alpha, \beta) = V \int_0^\infty d\lambda \lambda \frac{J_0(\lambda \alpha) I_0(\lambda \beta)}{I_0(\lambda \beta_0)} (-\alpha_1 J_1(\lambda \alpha_1) + \alpha_2 J_1(\lambda \alpha_2)). \quad (\text{A.11})$$

If the DC potential is defined by the application of a common voltage on the top and bottom of the paraboloid and grounding the center segment so that the DC boundary potential is given by,

$$\phi_{DC}(\alpha, \beta_0) = U(\theta(\alpha_1 - \alpha) + \theta(\alpha - \alpha_2)), \quad (\text{A.12})$$

then a similar analysis shows that the potential in the interior region due to the DC voltages is given by,

$$\phi_{DC}(\alpha, \beta) = U \int_0^\infty d\lambda \lambda \frac{J_0(\lambda \alpha) I_0(\lambda \beta)}{I_0(\lambda \beta_0)} (\alpha_1 J_1(\lambda \alpha_1) - \alpha_2 J_1(\lambda \alpha_2)). \quad (\text{A.13})$$

We now solve for the conditions on α_1 and α_2 to ensure the ion is trapped at the focus of the paraboloid. For the pseudo-potential to have a minimum at the focus, the amplitude of the AC potential must have an extremum at the focus [38]. Setting $x = y = 0$ and requiring the derivative with respect to z to be zero in the limit of $z \rightarrow 0$ gives,

$$\int_0^\infty d\lambda \lambda^2 \frac{\alpha_1 J_1(\lambda\alpha_1) - \alpha_2 J_1(\lambda\alpha_2)}{I_0(\lambda\beta_0)} = 0. \quad (\text{A.14})$$

Eq. (A.14) gives the required relationship between α_1 and α_2 in order for the parabolic ion trap to have a minimum at the optical focus. This transcendental equation must be solved numerically or graphically, with the former method being illustrated in figure A.3. To satisfy Eq. (A.14), one can plot the function $s(z)$ defined as,

$$s(z) = \int_0^\infty d\lambda \lambda^2 \frac{\alpha J_1(\lambda\alpha)}{I_0(\lambda\beta_0)} \Big|_{\alpha=\sqrt{2z+\beta_0^2}}, \quad (\text{A.15})$$

and then graphically find two segment positions z_1 and z_2 by finding two intersection points of $s(z)$ and a horizontal line. As Fig. A.3 implies, there are an infinite number of ways to segment the paraboloidal ion trap so as to give a potential minimum at the optical focus. This allows one to choose a segmentation that optimizes the characteristics of the potential and geometry of the electrodes according to any desiderata. For example, in order to have optical access to the ion, one might design a trap so that the gap between the middle and top segments is at the same height as the focus. Fig. A.3 also shows that the trapping region can be placed above the

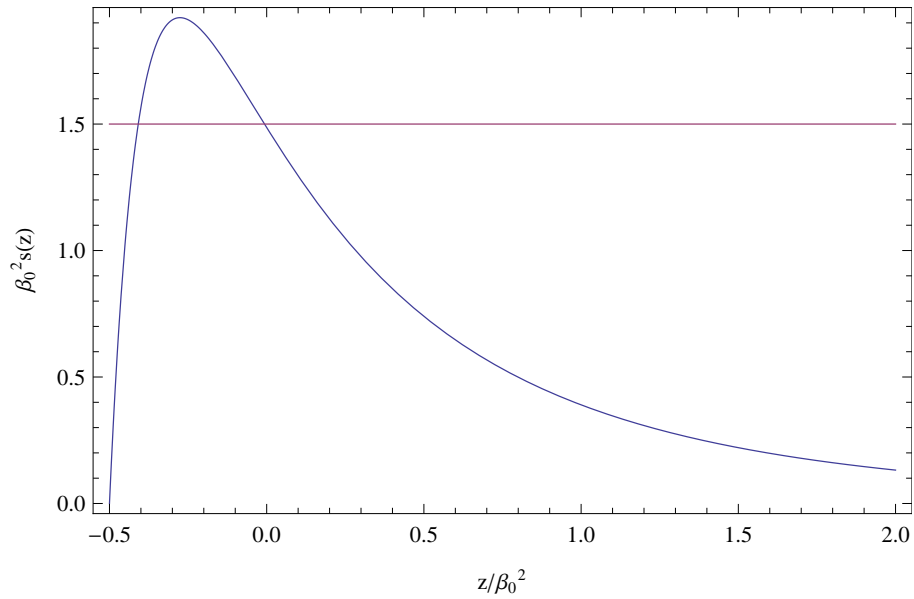


Figure A.3: The dimensionless function $\beta_0^2 s(z)$ is plotted as well as the horizontal line used to find values of z_1, z_2 that give rise to an extremum in the trapping potential at the focus of the paraboloid. The particular line drawn in the figure gives a value of z_2 that is equal to the focal length, meaning that one of the cuts in the paraboloid will be at the same height as the trapping region. Having z_2 be at the same height as the trapping region would allow one to gain laser access to the ion without having to drill additional holes in the paraboloid.

middle segment or within the middle segment, but never below the middle segment.

Appendix B

Probability amplitude for Raman transitions in a three-level atom using an optical frequency comb

Assume the dipole operator $\mu(r)$ couples $|1\rangle$ to $|3\rangle$ and $|2\rangle$ to $|3\rangle$. If the solution to the time-dependent Schrödinger equation is expanded in the eigen-basis of H_0 the probability amplitudes are governed by the following equations of motion,

$$\psi = \sum_n c_n(t) |n\rangle \quad (\text{B.1})$$

$$\dot{c}_1 + i\omega_1 c_1 = \frac{i}{2} \sum_k \tilde{E}_k [e^{i\omega_k t} + e^{-i\omega_k t}] \mu_{1,3} c_3 \quad (\text{B.2})$$

$$\dot{c}_2 + i\omega_2 c_2 = \frac{i}{2} \sum_k \tilde{E}_k [e^{i\omega_k t} + e^{-i\omega_k t}] \mu_{2,3} c_3 \quad (\text{B.3})$$

$$\dot{c}_3 + i\omega_3 c_3 = \frac{i}{2} \sum_k \tilde{E}_k [e^{i\omega_k t} + e^{-i\omega_k t}] (\mu_{3,1} c_1 + \mu_{3,2} c_2), \quad (\text{B.4})$$

where $\tilde{E}_k = E_k/\hbar$. Now make the following transformations:

$$\tilde{c}_1 = c_1 \quad (\text{B.5})$$

$$\tilde{c}_2 = c_2 e^{i\omega_{hf} t} \quad (\text{B.6})$$

$$\tilde{c}_3 = c_3 e^{i\omega_c t}, \quad (\text{B.7})$$

where $\omega_{hf} = \omega_2 - \omega_1$. The new equations of motion are,

$$\dot{\tilde{c}}_1 = \frac{i}{2} \sum_k \tilde{E}_k [e^{i\omega_k t} + e^{-i\omega_k t}] \mu_{1,3} \tilde{c}_3 e^{-i\omega_c t} - i\omega_1 \tilde{c}_1 \quad (\text{B.8})$$

$$\dot{\tilde{c}}_2 = \frac{i}{2} \sum_k \tilde{E}_k [e^{i\omega_k t} + e^{-i\omega_k t}] \mu_{2,3} \tilde{c}_3 e^{-i(\omega_c - \omega_{hf})t} - i(\omega_2 - \omega_{HF}) \tilde{c}_2 \quad (\text{B.9})$$

$$\dot{\tilde{c}}_3 = \frac{i}{2} \sum_k \tilde{E}_k [e^{i\omega_k t} + e^{-i\omega_k t}] (\mu_{3,1} \tilde{c}_1 e^{i\omega_c t} + \mu_{3,2} \tilde{c}_2 e^{i(\omega_c - \omega_{hf})t}) - i(\omega_3 - \omega_c) \tilde{c}_3. \quad (\text{B.10})$$

These transformations get rid of the fast oscillations in the probability amplitude for the excited state. If the laser is far from resonance so that the population of the excited is small, this transformation allows the adiabatic approximation $\dot{\tilde{c}}_3 \approx 0$. Using this approximation and defining $\omega_1 \equiv 0$ “sea-level,” the equations become,

$$\dot{\tilde{c}}_1 = \frac{i}{4\Delta} \sum_{k,k'} \tilde{E}_k \tilde{E}_{k'} [e^{i\omega_k t} + e^{-i\omega_k t}] [e^{i\omega_{k'} t} + e^{-i\omega_{k'} t}] |\mu_{1,3}|^2 (\tilde{c}_1 + \tilde{c}_2 e^{-i\omega_{hf} t}) \quad (\text{B.11})$$

$$\dot{\tilde{c}}_2 = \frac{i}{4\Delta} \sum_{k,k'} \tilde{E}_k \tilde{E}_{k'} [e^{i\omega_k t} + e^{-i\omega_k t}] [e^{i\omega_{k'} t} + e^{-i\omega_{k'} t}] |\mu_{2,3}|^2 (\tilde{c}_1 e^{i\omega_{hf} t} + \tilde{c}_2), \quad (\text{B.12})$$

where $\Delta = \omega_3 - \omega_c$. In order to proceed, we want to make a rotating-wave approximation, but is this allowed with a frequency comb? In the equations of motion for \tilde{c}_1 and \tilde{c}_2 there are terms that look like $e^{i(2\omega_c + (k+k')\omega_R)t}$. In our case ω_c is hundreds of THz, while ω_R is around 100 MHz. In general, this term can not be thrown out, but in our case we can use the shape of the pulse to argue for the validity of the RWA. In

our case $f(t)$ has a width of around 1 picosecond. This means that $\tilde{f}(\omega)$ has a width of about 1 THz. The term $e^{i(2\omega_c+(k+k')\omega_R)t}$ oscillates rapidly unless $\omega_R(k-k') \approx -2\omega_c$, but the coefficients $\tilde{E}_k\tilde{E}_{k'}$ die off exponentially. $\tilde{E}_k \propto \tilde{f}(k\omega_R)$. The stationary terms are around $k \sim \omega_c/\omega_R$ which have coefficients $\tilde{E}_k \propto \tilde{f}(\omega_c) \sim \tilde{f}(800THz) \sim 0$, allowing these terms to safely be ignored. In this approximation, the equations of motion become,

$$\dot{\tilde{c}}_1 = \frac{i}{4\Delta} \sum_{k,k'} \tilde{E}_k \tilde{E}_{k'} \left[e^{i(k-k')\omega_R t} + e^{-i(k-k')\omega_R t} \right] |\mu_{1,3}|^2 (\tilde{c}_1 + \tilde{c}_2 e^{-i\omega_{HF}t}), \quad (\text{B.13})$$

and the equation for \tilde{c}_2 is similar. By picking out the stationary terms one arrives at the following differential equation,

$$\dot{\tilde{c}}_1 = \frac{i|\mu_{e,g}|^2}{4\Delta} \left(2 \sum_k |\tilde{E}_k|^2 \tilde{c}_1 + \left(\sum_k \tilde{E}_k \tilde{E}_{k-q} + \sum_k \tilde{E}_k \tilde{E}_{k+q} \right) \tilde{c}_2 \right), \quad (\text{B.14})$$

where $q \equiv \omega_{HF}/\omega_R$ is assumed to be an integer. In the case of symmetric pulses, \tilde{f} is an even function, which implies that $\tilde{E}_k = \tilde{E}_{-k}$ and the final result becomes,

$$\dot{\tilde{c}}_1 = \frac{i|\mu_{e,g}|^2}{2\Delta} \left(\sum_k |\tilde{E}_k|^2 \tilde{c}_1 + \sum_k \tilde{E}_k \tilde{E}_{k-q} \tilde{c}_2 \right) \quad (\text{B.15})$$

$$\dot{\tilde{c}}_2 = \frac{i|\mu_{e,g}|^2}{2\Delta} \left(\sum_k |\tilde{E}_k|^2 \tilde{c}_2 + \sum_k \tilde{E}_k \tilde{E}_{k-q} \tilde{c}_1 \right). \quad (\text{B.16})$$

Now we can define the Rabi frequency Ω and a coefficient for the Stark shift δ ,

$$\delta \equiv \frac{|\mu|^2 \sum_k |\tilde{E}_k|^2}{2\Delta} \quad (\text{B.17})$$

$$\frac{\Omega}{2} \equiv \frac{|\mu|^2 \sum_k \tilde{E}_k \tilde{E}_{k-q}}{2\Delta}. \quad (\text{B.18})$$

The expressions in Eq. (B.18) involve a sum over the different spectral components in the frequency comb which should be able to be approximated by an integral in the case where the repetition rate is small compared to the bandwidth of a single pulse. In this approximation, Eq. (B.18) states that the Rabi frequency is proportional to the autocorrelation of the field envelope evaluated at the hyperfine frequency.

Appendix C

Walsh function Identity

This appendix provides an inductive proof of the following identity,

$$\int_0^1 dx \text{WAL}(2^n - 1, x) e^{i2^{n+1}\pi x} \sum_{l=0}^n a_l x^l = 0. \quad (\text{C.1})$$

The construction of the Walsh functions is simple in terms of the elementary sequences known as Rademacher functions $R(n, t) = \text{sign}[\sin(2^n \pi t)]$. The dyadic ordering of the Walsh functions allow them to be defined in terms of the Rademacher functions as $\text{WAL}(n, t) = \prod_{i=1}^{m+1} R(i, t)^{b_i-1}$ when n is expressed as a binary number $n = b_m 2^m + \dots + b_0 2^0$ and $b_i = 0$ or 1 . With this definition, it is easy to see that choosing the index $2^n - 1$ for the Walsh function means that all the b_i coefficients are 1. We now prove the base case, $n = 1$.

$$\int_0^1 dx \text{WAL}(1, x) e^{i4\pi x} \sum_{l=0}^1 a_l x^l \quad (\text{C.2})$$

$$= \int_0^1 dx R(1, x) e^{i4\pi x} \sum_{l=0}^1 a_l x^l \quad (\text{C.3})$$

$$= a_1 \int_0^1 dx R(1, x) e^{i4\pi x} x \quad (\text{C.4})$$

$$= a_1 \left(\int_0^{1/2} dx e^{i4\pi x} x - \int_{1/2}^1 dx e^{i4\pi x} x \right) \quad (\text{C.5})$$

$$= a_1 \int_0^{1/2} dx e^{i4\pi x} (x - (x + 1/2)) = 0. \quad (\text{C.6})$$

The inductive step is taken by assuming that Eq. (C.1) is true and looking at the $2^{n+1} - 1$ case:

$$\begin{aligned} & \int_0^1 dx \text{WAL}(2^{n+1} - 1, x) e^{i2^{n+2}\pi x} \sum_{l=0}^{n+1} a_l x^l \\ &= \int_0^1 dx \text{R}[1, x] \dots \text{R}(n+1, x) e^{i2^{n+2}\pi x} \sum_{l=0}^{n+1} a_l x^l \end{aligned} \quad (\text{C.7})$$

$$= \frac{1}{2} \int_0^2 dx \prod_{i=1}^{n+1} \text{R}(i, x/2) e^{i2^{n+1}\pi x} \sum_{l=0}^{n+1} a_l \left(\frac{x}{2}\right)^l \quad (\text{C.8})$$

$$\begin{aligned} &= \frac{1}{2} \int_0^1 dx \prod_{i=1}^{n+1} \text{R}(i, x/2) e^{i2^{n+1}\pi x} \sum_{l=0}^{n+1} a_l \left(\frac{x}{2}\right)^l \\ &+ \frac{1}{2} \int_1^2 dx \prod_{i=1}^{n+1} \text{R}(i, x/2) e^{i2^{n+1}\pi x} \sum_{l=0}^{n+1} a_l \left(\frac{x}{2}\right)^l. \end{aligned} \quad (\text{C.9})$$

The next step is taken by noting that for an integer $n \geq 0$, $\text{R}(n+1, x/2) = \text{R}(n, x)$, which allows the expression to be written as,

$$\begin{aligned} &= \frac{1}{2} \int_0^1 dx \prod_{i=0}^n \text{R}(i, x) e^{i2^{n+1}\pi x} \sum_{l=0}^{n+1} a_l \left(\frac{x}{2}\right)^l \\ &+ \frac{1}{2} \int_1^2 dx \prod_{i=0}^n \text{R}(i, x) e^{i2^{n+1}\pi x} \sum_{l=0}^{n+1} a_l \left(\frac{x}{2}\right)^l \end{aligned} \quad (\text{C.10})$$

$$\begin{aligned} &= \frac{1}{2} \int_0^1 dx \prod_{i=1}^n \text{R}(i, x) e^{i2^{n+1}\pi x} \sum_{l=0}^{n+1} a_l \left(\frac{x}{2}\right)^l \\ &- \frac{1}{2} \int_1^2 dx \prod_{i=1}^n \text{R}(i, x) e^{i2^{n+1}\pi x} \sum_{l=0}^{n+1} a_l \left(\frac{x}{2}\right)^l. \end{aligned} \quad (\text{C.11})$$

We now make the substitution $x' = x - 1$ and take advantage of the fact that $R(n, x + 1) = R(n, x)$ for $n \geq 1$.

$$\begin{aligned}
&= \frac{1}{2} \int_0^1 dx \text{WAL}(2^n - 1, x) e^{i2^{n+1}\pi x} \sum_{l=0}^{n+1} \frac{a_l}{2^l} x^l \\
&- \frac{1}{2} \int_0^1 dx \text{WAL}(2^n - 1, x) e^{i2^{n+1}\pi x} \sum_{l=0}^{n+1} \frac{a_l}{2^l} \sum_{k=0}^l \binom{m}{k} x^k \tag{C.12}
\end{aligned}$$

$$= \frac{1}{2} \int_0^1 dx \text{WAL}(2^n - 1, x) e^{i2^{n+1}\pi x} \sum_{l=0}^n b_l x^l, \tag{C.13}$$

which is zero by assumption since b_l is a constant, thus concluding the proof.

Bibliography

- [1] C. Monroe, D. M. Meekhof, B. E. King, W. M. Itano, and D. J. Wineland, “Demonstration of a fundamental quantum logic gate,” *Phys. Rev. Lett.*, vol. 75, 1995.
- [2] J. P. Home, D. Hanneke, J. D. Jost, J. M. Amini, D. Leibfried, and D. J. Wineland, “Complete methods set for scalable ion trap quantum information processing,” *Science*, vol. 325, 2009.
- [3] K. Kim, M.-S. Chang, S. Korenblit, R. Islam, E. E. Edwards, J. K. Freericks, G. D. Lin, L.-M. Duan, and C. Monroe, “Quantum simulation of frustrated ising spins with trapped ions,” *Nature*, vol. 465, 2010.
- [4] A. Friedenauer, H. Schmitz, J. T. Glueckert, D. Porras, and T. Schaetz, “Simulating a quantum magnet with trapped ions,” *Nature Physics*, vol. 4, 2008.
- [5] R. Gerritsma, G. Kirchmair, F. Zahringer, E. Solano, R. Blatt, and C. F. Roos, “Quantum simulation of the Dirac equation,” *Nature*, vol. 463, 2010.
- [6] T. Monz, P. Schindler, J. T. Barreiro, M. Chwalla, D. Nigg, W. A. Coish, M. Harlander, W. Hansel, M. H. M., and R. Blatt, “14-qubit entanglement: Creation and coherence,” *Phys. Rev. Lett.*, vol. 106, 2011.
- [7] A. Negretti, P. Treulein, and T. Calarco, “Quantum computing implementations with neutral particles,” *Quan. Inf. Proc.*, vol. 10, 2011.
- [8] V. Cerletti, W. A. Coish, O. Gywat, and D. Loss, “Recipes for spin-based quantum computing,” *Nanotechnology*, vol. 16, 2005.
- [9] H. Paik, D. I. Schuster, L. S. Bishop, G. Kirchmair, G. Catelani, A. P. Sears, B. R. Johnson, M. J. Reagor, L. Frunzio, L. I. Glazman, S. M. Girvin, M. H. Devoret, and R. J. Schoelkopf, “Observation of high coherence in Josephson junction qubits measured in a three-dimensional circuit qed architecture,” *Phys. Rev. Lett.*, vol. 107, 2011.
- [10] P. Kok, W. J. Munro, K. Nemoto, T. C. Ralph, J. P. Dowling, and G. J. Milburn, “Linear optical quantum computing with photonic qubits,” *Rev. Mod. Phys.*, vol. 79, 2007.
- [11] C. W. Chou, D. B. Hume, J. C. J. Koelemeij, D. J. Wineland, and T. Rosenband, “Frequency comparison of two high-accuracy Al^+ optical clocks,” *Phys. Rev. Lett.*, vol. 104, 2010.
- [12] V. Boyer, A. M. Marino, R. C. Pooser, and P. D. Lett, “Entangled images from four-wave mixing,” *Science*, vol. 321, 2008.

- [13] R. Ursin, F. Tiefenbacher, T. Schmitt-Manderbach, H. Weier, T. Scheidl, M. Linderthal, B. Blausteiner, T. Jennewin, J. Perdigues, P. Trojek, B. Omer, M. Furst, M. Meyenburg, J. Rarity, Z. Sodnik, C. Barbieri, H. Weinfurter, and A. Zeilinger, “Entanglement based quantum communication over 144 km,” *Nature Physics*, vol. 3, 2007.
- [14] G. Vidal, J. I. Latorre, E. Rico, and A. Kitaev, “Entanglement in quantum critical phenomena,” *Phys. Rev. Lett.*, vol. 90, 2003.
- [15] W. Hendrik, “<http://www.quantenblog.net/physics/moores-law-quantum-computer>,” 2011.
- [16] D. P. DiVincenzo, “The physical implementation of quantum computation,” *Fortschr. Phys.*, vol. 48, 2000.
- [17] P. W. Shor, “Fault-tolerant quantum computation,” *Proc. 37th Annual Symposium on Foundations of Computer Science, IEEE Computer Society Press*, pp. 56–65, 1996.
- [18] P. T. H. Fisk, M. J. Sellars, M. A. Lawn, and C. Coles, “Accurate measurement of the 12.6 GHz ‘clock’ transition in trapped $^{171}\text{Yb}^+$ ions,” *IEEE Trans. Ultrasonics, Ferroelectrics, and Frequency*, vol. 44, 1997.
- [19] J. I. Cirac and P. Zoller, “Quantum computations with cold trapped ions,” *Phys. Rev. Lett.*, vol. 74, 1995.
- [20] K. Mølmer and A. Sørensen, “Multiparticle entanglement of hot trapped ions,” *Phys. Rev. Lett.*, vol. 82, 1999.
- [21] C. Sackett, D. Kielpinski, Q. Turchette, V. Meyer, M. Rowe, C. Langer, C. Myatt, B. King, W. M. Itano, D. J. Wineland, and C. Monroe, “Experimental entanglement of four particles,” *Nature*, vol. 404, 2000.
- [22] D. Kielpinski, C. Monroe, and D. Wineland, “Architecture for a large-scale ion-trap quantum computer,” *Nature*, 2002.
- [23] W. K. Hensinger, S. Olmschenk, D. Stick, D. Hucul, M. Yeo, M. Acton, L. Deslauriers, C. Monroe, and J. Rabchuk, “T-junction ion trap array for two-dimensional ion shuttling, storage and manipulation,” *App. Phys. Lett.*, vol. 88, 2006.
- [24] R. Bowler, J. Gaebler, Y. Lin, T. R. Tan, D. Hanneke, J. D. Host, J. P. Home, D. Leibfried, and D. J. Wineland, “Coherent diabatic ion transport and separation in a multizone trap array,” *Phys. Rev. Lett.*, vol. 109, 2012.
- [25] C. Monroe, R. Raussendorf, A. Ruthven, K. R. Brown, P. Maunz, L.-M. Duan, and J. Kim, “Large scale modular quantum computer architecture with atomic memory and photonic interconnects,” *arXiv*, vol. 1208, 2012.

- [26] P. Shor, “Polynomial-time algorithms for prime factorization and discrete logarithms on a quantum computer,” *SIAM J. Comput.*, vol. 26, 1997.
- [27] C. H. Bennett and G. Brassard, “Quantum cryptography: Public key distribution and coin tossing,” *Proceedings of the IEEE International Conference on Computers, Systems, Signal Processing*, 1984.
- [28] M. A. Nielsen and I. L. Chuang, *Quantum Computation and Quantum Information*. Cambridge University Press, 2000.
- [29] S. Ritter, C. Nolleke, C. Hahn, A. Reiserer, A. Neuzner, M. Uphoff, M. Mücke, E. Figueroa, J. Bochmann, and G. Rempe, “An elementary quantum network of single atoms in optical cavities,” *Nature*, vol. 484, 2012.
- [30] A. D. Boozer, A. Boca, R. Miller, T. E. Northup, and H. J. Kimble, “Reversible state transfer between light and a single trapped atom,” *Phys. Rev. Lett.*, vol. 98, 2007.
- [31] J. D. Sterk, L. Luo, T. A. Manning, P. Maunz, and C. Monroe, “Photon collection from a trapped ion-cavity system,” *Phys. Rev. A*, vol. 85, 2012.
- [32] A. Golla, B. Chalopin, M. Bader, I. Harder, K. Mantel, R. Maiwald, N. Lindlein, M. Sondermann, and G. Leuchs, “Generation of a wave packet tailored to efficient free space excitation of a single atom,” *Eur. Phys. J. D*, vol. 66, 2012.
- [33] M. K. Tey, Z. Chen, S. A. Aljunid, B. Chng, F. Huber, G. Maslennikov, and C. Kurtsiefer, “Strong interaction between light and a single trapped atom without the need for a cavity,” *Nature Physics*, vol. 4, 2008.
- [34] D. L. Moehring, P. Maunz, S. Olmschenk, K. C. Younge, D. N. Matsukevich, L.-M. Duan, and C. Monroe, “Entanglement of single-atom quantum bits at a distance,” *Nature*, vol. 449, 2007.
- [35] C. H. Bennett, F. Bessette, G. Brassard, L. Salvail, and J. Smolin, “Experimental quantum cryptography,” *Journal of Cryptology*, vol. 5, 1992.
- [36] W. K. Wootters and W. H. Zurek, “A single quantum cannot be cloned,” *Nature*, vol. 299, 1982.
- [37] L.-M. Duan, B. B. Blinov, D. L. Moehring, and C. Monroe, “Scalable trapped ion quantum computation with a probabilistic ion-photon mapping,” *Quantum Information and Computation*, vol. 4, 2004.
- [38] H. G. Dehmelt, “Radiofrequency spectroscopy of stored ions i: Storage,” *Adv. At. Mol. Phys.*, vol. 3, 1967.
- [39] W. Paul, “Electromagnetic traps for charged and neutral particles,” *Rev. Mod. Phys.*, vol. 62, 1990.

- [40] S. Olmschenk, D. Hayes, D. N. Matsukevich, P. Maunz, D. Moehring, and C. Monroe, “Quantum logic between distant trapped ions,” *Int. J. Quant. Inf.*, vol. 8, 2010.
- [41] W. M. MacAlpine and R. O. Stratton, “Coaxial resonators with a helical inner core,” *Proc. IRE*, vol. 2099, 1959.
- [42] S. Olmschenk, *Quantum Teleportation Between Distant Matter Qubits*. PhD thesis, University of Michigan, 2009.
- [43] D. Das, S. Barthwal, A. Banerjee, and V. Natarajan, “Absolute frequency measurements in Yb with 0.08 ppb uncertainty: Isotope shifts and hyperfine structure in the 399-nm $^1S_0 \leftrightarrow ^1P_1$ line,” *Phys. Rev. A*, vol. 72, 2005.
- [44] R. D. Cowan, *The Theory of Atomic Structure and Spectra*. University of California Press, 1981.
- [45] M. Roberts, P. Taylor, G. P. Barwood, W. R. C. Rowley, and P. Gill, “Observation of the $^2S_{1/2} \leftrightarrow ^2F_{7/2}$ electric octupole transition in a single $^{171}\text{Yb}^+$ ion,” *Phys. Rev. A*, vol. 62, 2000.
- [46] E. D. Black, “An introduction to Pound-Drever-Hall laser frequency stabilization,” *American Journal of Physics*, vol. 69, 2001.
- [47] S. Olmschenk, K. C. Younge, D. L. Moehring, D. N. Matsukevich, P. Maunz, and C. Monroe, “Manipulation and detection of a trapped Yb^+ hyperfine qubit,” *Phys. Rev. A*, vol. 76, 2007.
- [48] M. Acton, K.-A. Brickman, P. C. Haljan, P. J. Lee, L. Deslauriers, and C. Monroe, “Near-perfect simultaneous measurement of qubit register,” *Quantum Inf. Comp.*, vol. 6, 2006.
- [49] C. Langer, *High Fidelity Quantum Information Processing with Trapped Ions*. PhD thesis, University of Colorado, 2006.
- [50] A. H. Myerson, D. J. Szwer, S. C. Webster, D. T. C. Allcock, M. J. Curtis, G. Imreh, J. A. Sherman, D. N. Stacey, A. M. Steane, and D. M. Lucas, “High-fidelity readout of trapped-ion qubits,” *Phys. Rev. Lett.*, vol. 100, 2008.
- [51] A. H. Burrell, D. J. Szwer, S. C. Webster, and D. M. Lucas, “Scalable simultaneous multiqubit readout with 99.99% single-shot fidelity,” *Phys. Rev. A*, vol. 81, 2010.
- [52] K. C. Young and K. B. Whaley, “Qubits as spectrometers of dephasing,” *Phys. Rev. A*, vol. 86, 2012.
- [53] A. Steane, “The ion trap quantum information processor,” *Applied Physics B*, vol. 64, 1997.

- [54] S.-L. Zhu, C. Monroe, and L.-M. Duan, “Trapped ion quantum computation with transverse phonon modes,” *Phys. Rev. Lett.*, vol. 97, 2006.
- [55] D. Hayes, D. N. Matsukevich, P. Maunz, D. Hucul, Q. Quraishi, S. Olmschenk, W. Campbell, J. Mizrahi, C. Senko, and C. Monroe, “Entanglement of atomic qubits using an optical frequency comb,” *Phys. Rev. Lett.*, vol. 104, 2010.
- [56] S. T. Cundiff and J. Ye, “Colloquium: Femtosecond optical frequency combs,” *Rev. Mod. Phys.*, vol. 75, 2003.
- [57] S. K. Son and S. I. Younge, “Many-mode Floquet theoretical approach for coherent control of multiphoton dynamics driven by intense frequency-comb laser fields,” *Phys. Rev. A*, vol. 77, 2008.
- [58] D. F. James and J. Jerke, “Effective Hamiltonian theory and its applications in quantum information,” *Canadian Journal of Physics*, vol. 85, 2011.
- [59] D. J. Wineland, M. Barrett, J. Britton, J. Chiaverini, B. DeMarco, W. M. Itano, B. Jelenkovic, C. Langer, D. Leibfried, V. Meyer, T. Rosenband, and T. Schatz, “Quantum information processing with trapped ions,” *Phil. Trans. R. Soc. Lond. A*, vol. 361, 2003.
- [60] C. Monroe, D. M. Meekhof, B. E. King, S. R. Jefferts, W. M. Itano, D. J. Wineland, and P. Gould, “Resolved-sideband raman cooling of a bound atom to the 3d zero-point energy,” *Phys. Rev. Lett.*, vol. 75, 1995.
- [61] P. J. Lee, *Quantum Information Processing with Two Trapped Cadmium Ions*. PhD thesis, University of Michigan, 2006.
- [62] B. H. Bransden and C. J. Joachain, *Physics of Atoms and Molecules*. Prentice Hall, 2nd ed., 2003. page 466.
- [63] E. Solano, R. L. de Matos Filho, and N. Zagury, “Deterministic Bell states and measurement of the motional state of two trapped ions,” *Phys. Rev. A*, vol. 59, 1999.
- [64] G. J. Milburn, S. Schneider, and D. F. V. James, “Deterministic Bell states and measurement of the motional state of two trapped ions,” *Fortschr. Phys.*, vol. 48, 2000.
- [65] D. Hayes, S. M. Clark, S. Debnath, D. Hucul, I. V. Inlek, K. W. Lee, Q. Quraishi, and C. Monroe, “Coherent error suppression in multiqubit entangling gates,” *Phys. Rev. Lett.*, vol. 109, 2012.
- [66] K. G. Beauchamp, *Applications of Walsh and Related Functions*. Academic Press Inc., New York, 1984.
- [67] B. E. King, C. S. Wood, C. J. Myatt, Q. A. Turchette, D. Leibfried, W. M. Itano, C. Monroe, and D. J. Wineland, “Cooling the collective motion of trapped ions to initialize a quantum register,” *Phys. Rev. Lett.*, vol. 81, 1998.

- [68] B. B. Blinov, D. L. Moehring, L.-M. Duan, and C. Monroe, “Observation of entanglement between a single trapped atom and a single photon,” *Nature*, vol. 428, 2004.
- [69] S. Olmschenk, D. N. Matsukevich, P. Maunz, D. Hayes, L.-M. Duan, and C. Monroe, “Quantum teleportation between distant matter qubits,” *Science*, vol. 323, 2009.
- [70] E. Nagali, F. Sciarrino, F. D. Martini, L. Marrucci, B. Piccirillo, E. Karimi, and E. Santamato, “Quantum information transfer from spin to orbital angular momentum of photons,” *Phys. Rev. Lett.*, vol. 103, 2009.
- [71] I. Marcikic, H. Riedmatten, W. Tittel, V. Scarani, H. Zbinden, and N. Gisin, “Time-bin entangled qubits for quantum communication created by femtosecond pulses,” *Phys. Rev. A*, vol. 66, 2002.
- [72] H. P. Specht, C. Nolleke, A. Reiserer, M. Uphoff, E. Figueroa, S. Ritter, and G. Rempe, “A single-atom quantum memory,” *Nature*, vol. 473, 2011.
- [73] C. Clausen, F. Bussieres, M. Afzelius, and N. Gisin, “Quantum storage of heralded polarization qubits in birefringent and anisotropically absorbing materials,” *Phys. Rev. Lett.*, vol. 108, 2012.
- [74] M. Gundogan, P. M. Ledingham, A. Almasi, M. Cristiani, and H. de Riedmatten, “Quantum storage of a photonic polarization qubit in a solid,” *Phys. Rev. Lett.*, vol. 108, 2012.
- [75] L. Luo, D. Hayes, T. A. Manning, D. N. Matsukevich, P. Maunz, S. Olmschenk, J. D. Sterk, and C. Monroe, “Protocols and techniques for a scalable atom-photon quantum network,” *Fortschritte der Physik*, vol. 57, 2009.
- [76] C. Cabrillo, J. I. Cirac, P. Garcia-Fernandez, and P. Zoller, “Creation of entangled states of distant atoms by interference,” *Phys. Rev. A*, vol. 59, 1999.
- [77] L. Slodicka, G. Hetet, N. Rock, P. Schindler, M. Hennrich, and R. Blatt, “Atom-atom entanglement by single-photon detection,” *arXiv:1207.5468*, 2012.
- [78] H. Haffner, W. Hansel, C. F. Roos, J. Benhelm, D. Chekalkar, M. Chwalla, T. Korber, U. D. Rapol, M. Riebe, P. O. Schmidt, C. Becher, O. Gühne, W. Dur, and R. Blatt, “Scalable multiparticle entanglement of trapped ions,” *Nature*, vol. 438, 2012.
- [79] D. Gross, Y.-K. Liu, S. T. Flammia, S. Becker, and J. Eisert, “Quantum state tomography via compressed sensing,” *Phys. Rev. Lett.*, vol. 105, 2010.
- [80] M. Bourennaneand, M. Eibl, C. Kurtsiefer, S. Gaertner, H. Weinfurter, O. Gühne, P. Hyllus, M. L. D. Bruß, and A. Sanpera, “Experimental detection of multipartite entanglement using witness operators,” *Phys. Rev. Lett.*, vol. 92, 2004.

- [81] O. Gühne, C. Lu, W. Gao, and J. Pan, “Toolbox for entanglement detection and fidelity estimation,” *Phys. Rev. A*, vol. 76, 2007.
- [82] U. Eichmann, J. C. Berquist, J. J. Bollinger, J. M. Gilligan, W. M. Itano, D. J. Wineland, and M. G. Raizen, “Young’s interference experiment with light scattered from two atoms,” *Phys. Rev. Lett.*, vol. 70, 1993.
- [83] M. O. Scully and K. Druhl, “Quantum eraser: A proposed photon correlation experiment concerning observation and delayed choice in quantum mechanics,” *Phys. Rev. A*, vol. 25, 1981.
- [84] W. M. Itano, J. C. Berquist, J. J. Bollinger, and D. J. Wineland, “Complementarity and Young’s interference fringes from two atoms,” *Phys. Rev. A*, vol. 57, 1998.
- [85] C. Simon and W. Irvine, “Robust long-distance entanglement and a loophole-free Bell test with ions and photons,” *Phys. Rev. Lett.*, vol. 91, 2003.
- [86] P. Maunz, S. Olmschenk, D. Hayes, D. N. Matsukevich, L.-M. Duan, and C. Monroe, “A heralded quantum gate between remote quantum memories,” *Phys. Rev. Lett.*, vol. 102, 2009.
- [87] S. Olmschenk, D. Hayes, D. N. Matsukevich, P. Maunz, D. L. Moehring, K. C. Younge, and C. Monroe, “Precision measurement of the lifetime of the $6p^2P_{1/2}$ level of Yb^+ ,” *Phys. Rev. A*, vol. 91, 2009.
- [88] C. K. Hong and Z. Y. Ou, “Measurement of subpicosecond time intervals between two photons by interference,” *Phys. Rev. Lett.*, vol. 59, 1987.
- [89] Y. H. Shih and C. O. Alley, “New type of Einstein-Podolsky-Rosen-Bohm experiment using pairs of light quanta produced by optical parametric down conversion,” *Phys. Rev. Lett.*, vol. 61, 1988.
- [90] R. Raussendorf and H. J. Briegel, “A one-way quantum computer,” *Phys. Rev. Lett.*, vol. 86, 2001.
- [91] W. C. Campbell, J. Mizrahi, Q. Quraishi, C. Senko, D. Hayes, D. Hucul, D. N. Matsukevich, P. Maunz, and C. Monroe, “Ultrafast gates for single atomic qubits,” *Phys. Rev. Lett.*, vol. 105, 2010.
- [92] M. Matsumoto and T. Nishimura, “Mersenne twister: a 623-dimensionally equidistributed uniform pseudo-random number generator,” *ACM Trans. Model. Comput. Simul.*, vol. 8, 1998.
- [93] J. S. Bell, “On the Einstein-Podolsky-Rosen paradox,” *Physics*, vol. 1, 1964.
- [94] R. Colbeck, *Quantum and Relativistic Protocols for Secure Multi-Party Computation*. PhD thesis, University of Cambridge, 2007.

- [95] S. Pironio, A. Acyn, S. Massar, A. B. de la Giroday, D. N. Matsukevich, P. Maunz, S. Olmschenk, D. Hayes, L. Luo, T. A. Manning, and C. Monroe, “Random numbers certified by Bells theorem,” *Nature*, vol. 464, 2010.
- [96] J. Clauser, M. Horne, A. Shimony, and R. Holt, “Proposed experiment to test local hidden-variable theories,” *Phys. Rev. Lett.*, vol. 23, 1969.
- [97] S. J. Freedman and J. F. Clauser, “Experimental test of local hidden-variable theories,” *Phys. Rev. Lett.*, vol. 28, 1974.
- [98] A. Aspect, “Experimental tests of realistic local theories via Bell’s theorem,” *Phys. Rev. Lett.*, vol. 47, 1981.
- [99] A. Aspect, J. Dalibard, and G. Roger, “Experimental test of Bell’s inequalities using time-varying analyzers,” *Phys. Rev. Lett.*, vol. 49, 1983.
- [100] W. Tittel, J. Brendel, B. Gisin, T. Herzog, H. Zbinden, and N. Gisin, “Experimental demonstration of quantum correlations over more than 10 km,” *Phys. Rev. A*, vol. 57, 1998.
- [101] G. Weihs, T. Jennewein, C. Simon, H. Weinfurter, and A. Zeilinger, “Violation of Bell’s inequality under strict Einstein locality conditions,” *Phys. Rev. Lett.*, vol. 81, 1998.
- [102] M. A. Rowe, D. Kielpinski, V. Meyer, C. A. Sackett, W. M. Itano, C. Monroe, and D. J. Wineland, “Experimental violation of a Bell’s inequality with efficient detection,” *Nature*, vol. 409, 2001.
- [103] D. Salart, A. Baas, J. A. W. van Houwelingen, N. Gisin, and H. Zbinden, “Spacelike separation in a Bell test assuming gravitationally induced collapses,” *Phys. Rev. Lett.*, vol. 100, 2008.
- [104] D. N. Matsukevich, P. Maunz, D. L. Moehring, S. Olmschenk, and C. Monroe, “Bell inequality violation with two remote atomic qubits,” *Phys. Rev. Lett.*, vol. 100, 2008.
- [105] M. Ansmann, H. Wang, R. C. Bialczak, M. Hofheinz, E. Lucero, M. Neeley, A. D. O’Connell, D. Sank, M. Weides, A. N. Clealand, and J. M. Martinis, “Violation of Bell’s inequality in Josephson phase qubits,” *Nature*, vol. 461, 2009.
- [106] E. Santos, “Bell’s theorem and the experiments: Increasing empirical support for local realism?,” *Studies in History and Philosophy of Modern Physics*, vol. 36, 2005.
- [107] A. Sørensen and K. Mølmer, “Entanglement and quantum computation with ions in thermal motion,” *Phys. Rev. A*, vol. 62, 2000.

- [108] P. J. Lee, K.-A. Brickman, L. Deslauriers, P. C. Haljan, L.-M. Duan, and C. Monroe, “Phase control of trapped ion quantum gates,” *Journal of Optics B*, vol. 7, pp. S371–S383, 2005.
- [109] C. Yin, L. Liu, A. Lv, and Y. Li, “EOM bias control scheme in BOTDR system,” *ICEMI*, 2009.
- [110] S. M. Jobling and P. G. Kwiat, “A virtual-interferometer technique for surface metrology,” *Optics Express*, vol. 18, 2010.
- [111] S. Bonora, I. Capraro, L. Poletto, M. Romanin, C. Trestino, and P. Villoresi, “Wavefront active control by a digital-signal-processor-driven deformable membrane mirror,” *Rev. Sci. Instrum.*, vol. 77, 2006.
- [112] F. G. A. Courteville and R. Dandliker, “Optimization of a single-mode fiber coupling efficiency with an adaptive membrane mirror,” *Opt. Eng.*, vol. 41, 2002.
- [113] P. O. Schmidt, T. Rosenband, C. Langer, W. M. Itano, J. C. Bergquist, and D. J. Wineland, “Spectroscopy using quantum logic,” *Science*, vol. 309, 2005.
- [114] N. N. Lebedev, *Special Functions and Their Applications*. Dover, 1972.